DIGITAL FRACTOGRAPHIC IMAGING ANALYSIS

By

RICHARD HORACE MCSWAIN

A DISSERTATION PRESENTED TO THE GRADUATE SCHOOL
OF THE UNIVERSITY OF FLORIDA IN
PARTIAL FULFILLMENT OF THE REQUIREMENTS
FOR THE DEGREE OF DOCTOR OF PHILOSOPHY

UNIVERSITY OF FLORIDA

1985

Copyright 1985

by

Richard Horace McSwain

ACKNOWLEDGMENTS

I am deeply indebted to a number of people for their consistent support and encouragement during my program of study for the Ph.D degree. The indebtedness begins with Ms. F. M. Goodrich of the Naval Air Rework Facility, Pensacola, Florida, who assisted me in obtaining Navy long-term training, and to Mr. J. G. Ruff, Mr. J. H. Whittington and Mr. B. T. DeArmon of NARF Pensacola, who made the training a reality. I am also appreciative of my supervisors and co-workers for their patience and assistance. I am grateful to Mr. J. F. Collins of the Naval Air Systems Command and Mr. C. D. Beachem and Mr. D. A. Meyn of the Naval Research Laboratory for their interest and support of this research.

I am appreciative of the University of Florida and my graduate committee for giving me the opportunity to pursue one of the goals of my life. I am thankful for Mr. A. B. Gregalot whose experience in image processing made this work possible. I am especially appreciative of Dr. E. D. Verink, Jr., who encouraged me over the years to pursue this degree and to my chairman, Dr. R. W. Gould, for his constant encouragement and motivation to always seek the positive.

I am grateful to my friends who reminded me that I could complete what had been started, especially Rev. and Mrs. J. B.

Findlay and to Ms. S. S. Hammer, who not only provided encouragement, but also assisted in preparation of this dissertation as well.

I am grateful to my mother and my late father who encouraged me to be inquisitive and to seek my limits.

Most of all I am indebted to my family; to my wife, Wanda, for her untiring support, for taking my place many times in my responsibilities as a father, and for her many hours of word processing. I am also grateful to my children, Rachel and John, who suffered the most in my absence.

I thank my Father, God, who gifted me with the desire to understand His creation.

The Naval Air Systems Command provided support for this work under Contract N000-14-83-K-2035.

TABLE OF CONTENTS

Page

ACKNOWLEDGMENTS iii

ABSTRACT viii

CHAPTER

1 INTRODUCTION 1

1.1 Fractography 2

1.1.1 Historical Development 2
1.1.2 Fracture Mode Analysis 7
1.1.3 Quantitative Fractography 9

1.2 Digital Imaging Analysis 14

1.2.1 Image Processing and Analysis 14
1.2.2 Imaging Applications 21

2 THEORETICAL FOUNDATIONS 31

2.1 Fracture Features and Mechanisms 31

2.1.1 Microvoid Coalesence Fracture 32
2.1.2 Transgranular Cleavage Fracture 41
2.1.3 Fatigue Fracture 48
2.1.4 Decohesive Rupture 57

2.2 Imaging Analysis 74

2.2.1 Optical Image Characterization 74
2.2.2 Optical Diffraction Pattern Formation . . . 75
2.2.3 Optical Fourier Transform Analysis 81
2.2.4 Digital Fourier Transform Analysis 90
2.2.5 Fourier Transform Image Characterization . 112

3 EXPERIMENTAL PROCEDURE 126

3.1 Fractograph Generation and Calibration 126

3.1.1 Scanning Electron Microscopy 128
3.1.2 Instrumental Variable Analysis 135
3.1.3 Fractographic Specimens 142
3.1.4 Theoretical Fractographic Models 158

3.2 Image Processing Software 163

3.2.1 Digital Image Acquisition 163
3.2.2 Image Matrix Size 165
3.2.3 Image Window Selection 166
3.2.4 Fourier Transform Processing 167

3.2.5 Fourier Transform Sampling 169
3.2.5.1 Spatial Frequency Pattern 168
3.2.5.2 3D Surface Plot 171
3.2.5.3 Radial Plot 172
3.2.5.4 Ring Plot 175
3.2.5.5 Wedge Plot 175

4 RESULTS AND DISCUSSION 179

4.1 Data Window Function Analysis 179
4.2 Scanning Electron Microscope Variable Analysis . . 182
4.3 Fractographic Image Feature Calibration 205
4.4 Digital Fractographic Pattern Classification . . . 248

4.4.1 Microvoid Coalesence Dimples 252
4.4.2 Cleavage Planes 260
4.4.3 Fatigue Striations 267
4.4.4 Intergranular Facets 272

4.5 Digital Fractographic Pattern Characterization . . 282

4.5.1 Fatigue Striation Density 282
4.5.2 Dimple Rupture Shear Component 285
4.5.3 Cleavage vs. Quasicleavage 306
4.5.4 Hydrogen Assisted Cracking vs. Stress Corrosion Cracking 312

5 CONCLUSIONS AND RECOMMENDATIONS 324

APPENDIX 328

REFERENCES 334

BIOGRAPHICAL SKETCH 358

Abstract of Dissertation Presented to the Graduate School
of the University of Florida in Partial Fulfillment of the
Requirements for the Degree of Doctor of Philosophy

DIGITAL FRACTOGRAPHIC IMAGING ANALYSIS

By

Richard Horace McSwain

August, 1985

Chairman: Dr. Robert W. Gould
Major Department: Materials Science and Engineering

Fractographic analysis of fracture surfaces is inherently subjective. The fractographer interprets fracture features based on recognized and categorized patterns. The potential for misinterpretation and conflicting opinions is strong.

In an effort to reduce subjectivity in fractographic analyses, the use of digital imaging analysis techniques for fractographic image classification and characterization was investigated. The two-dimensional Fourier transform, which has had extensive application in other fields of imaging analysis, was applied to four major fracture modes. These modes included microvoid coalescence, cleavage, fatigue and decohesive rupture. The imaging analysis precedure was successful in classifying the four primary modes and characterizing features inherent to each of the modes. The presence of repeat features in the fracture patterns provided the basis for the Fourier transform analysis. The technique was also used to determine the presence of directionality in fracture patterns such as elongated shear dimples and cleavage river patterns. The potential for quantitative measurement of fracture features including striation spacing, dimple size and intergranular facet size was also demonstrated.

CHAPTER 1

INTRODUCTION

Fractography, as a critical part of failure analysis, relates fracture surface morphology to the mechanism of fracture. Without it as a diagnostic tool, failures would inevitably be repeated without hope of prevention. Fractography as practiced today, however, is inadequate. The fractographer must use a combination of experience and reference fractographs to identify specific fracture surface features. For fracture features that fit a recognized pattern, the process is simple. In the case of those fractures that do not fit a recognized pattern, the process may be extremely difficult. The problems that are sometimes encountered are microstructural features that appear as fracture patterns and alteration of expected fracture surface features by environmental attack.

The fractographic process in these difficult cases can become excessively subjective. To reduce the subjectivity, an effort was undertaken to develop a technique of computer-assisted fractographic analysis. Computerized imaging techniques have been applied in the past to numerous areas of technology, including earth resource sensing, military target acquisition, medical analysis, business transactions, microstructural analysis, and industrial inspection.

Image processing techniques have also been applied in electron microscopy for image enhancement and improvement of image quality. Based on the success of digital imaging analysis in these areas, an investigation was undertaken to examine the feasibility of applying digital Fourier transform techniques to fractographic imaging analysis.

1.1 Fractography

1.1.1 Historical Development

An appreciation of the problems in characterizing fractographic images may be gained by a review of the development of the field of fractography. The study of fracture surfaces dates to antiquity. The reference book, Fractography and Atlas of Fractographs (1974), provides an excellent review of the early development of fractography. As metalsmiths learned to form metals, they discovered that the appearance of a fracture surface provided information about the quality of the metal. One of the earliest reported uses of visual fracture surface analysis was in De La Pirotechnia (Biringuccio, 1540). It described the use of fracture surface appearance as a means of determining the quality of ferrous and nonferrous alloys. A work that followed, De Re Metallica (Agricola, 1556), described techniques for fracture of ferrous specimens and examination of the fracture surfaces to determine if an alloy was iron or steel. Ercker (1574) discussed the use of fracture surface examination to evaluate the quality of copper, brass, and silver.

Fractures were classified as brittle or ductile and sources of the brittleness were investigated.

The development of the optical microscope provided a new means for fracture surface evaluation. The first scientific study of fracture surfaces using visual and optical microscopy techniques was published by de Reaumur (1722). His book contained engravings that classified macroscopic and microscopic features observed in iron and steel fractures. Gellert (1750) described the use of fracture tests and fracture surface appearances to distinguish between steel, wrought iron, and cast iron. His tests were also applied to the evaluation of carburization heat treatment and embrittlement of steel. Mallet (1856) used fracture surface analysis to characterize cannon barrels. He related fractures in barrel castings to solidification features and provided an early example of failure analysis. Tunner (1858) developed a list of casting defects that produced characteristic fracture patterns. Percy (1861) described the six general classes of fracture patterns that had been observed to that date as crystalline, granular, fibrous, silky, columnar, and vitreous. Martens (1878a, 1878b) performed the first studies that combined metallography with fracture surface analysis. His publications contained comparative drawings of microstructures and related fracture surfaces. Martens (1887) later published fracture surface images produced by photography and illustrated radial fracture lines that showed crack propagation direction. He also analyzed fracture surfaces produced in tension, torsion, bending and fatigue and concluded in each case that radial lines diverge from the fracture origin.

Because of a strong interest in metallography, little additional attention was given to fracture surface analysis until the 1920s. At that time special fracture tests were developed. Shepherd (1923, 1924) used fracture surface analysis to further quantify the quality of steel. His work led to fracture tests that rated the prior austenite grain size in hardened tool and die steels. The most significant development in modern fractography was the work of Zapffe in the 1940s. He investigated the role of dissolved hydrogen in generating flake-type fissures in hardened steel (Zapffe and Moore, 1943) and was able to photograph facets created by hydrogen damage. This initiated the field of microfractography. In later work on stainless steels, he explored the characteristics of brittle fracture surfaces and the resulting publication coined the name fractography (Zapffe and Clogg, 1945a). With the newly developed field of study, numerous fracture surface analysis problems were attacked and multiple publications resulted. Zapffe evaluated alloy toughness by cleavage plane analysis (Zapffe et al., 1948), transgranular cleavage facets in molybdenum (Zapffe et al., 1948), tungsten fractures (Zapffe and Landgraf, 1949), and fatigue fractures (Zapffe and Worden, 1951). Zapffe's techniques of light-microscope fractography are very similar to those used today.

Problems with limited depth of field in the optical microscope led to a search for other techniques for fractographic observations. The development of the transmission electron microscope (TEM) provided the means to continue the fractographic exploration. The first practical TEMs were described by von Borries and Ruska (1939) and by Prebus and Hillier (1939). The first application of the TEM to fractography was in a written discussion by Barrett and Derge following a paper by Zapffe and Moore (1943). As commercial TEMs appeared in about 1945 (Murr, 1982), the use of TEMs in fractography quickly spread. Various laboratories began intense studies of fracture surface markings and nomenclature was applied to each of the distinct classes. The U.S. Naval Research Laboratory was a predominant leader in the field with a tremendous contribution to fractography being made by Beachem and Meyn.

A number of review articles have been prepared which discuss the early stages of fractography (Beachem, 1962a; McMillian and Pelloux, 1962; Warke and McCall, 1964, 1965; Burghard and Davidson, 1965; Beachem and Pelloux, 1965; Beachem, 1965, 1966a). The U.S. Air Force published the first atlas of fractographs, the Electron Fractography Handbook, in 1965 based on the work of Phillips et al. of Douglas Aircraft Company. That was followed by a number of symposia held by the American Society for Testing and Materials on fractography which have continued to this date. These proceedings were published in book format and some are listed as follows: Electron Fractography, ASTM STP 436 (1968), Electron Microfractography, ASTM STP 453 (1968), Application of Electron Microfractography to Materials Research, ASTM STP 493 (1971), Fractography-Microscopic Cracking Processes, ASTM STP 600 (Beachem and Warke, 1976), Fractography in Failure Analysis, ASTM STP 645 (Strauss and Cullen, 1978), Fractography and Materials Science, ASTM STP 733 (Gilbertson and Zipp, 1981), Fractography of Ceramic and Metal Failures, ASTM STP 827 (Mecholsky and Powell, 1984).

The fractography performed in the 1960s was based on analysis with the TEM. The typical procedure for preparation of a TEM fractograph, as given by Phillips et al. (1965), involved replication of the fracture surface with a plastic media. The plastic was coated with a combination of carbon and metal followed by removal of the plastic. The remaining carbon-metal replica was inserted into the TEM for examination. The process was tedious and often introduced artifacts into the image. The advent of the scanning electron microscope (SEM) opened the way for better fractographic interpretation because the actual fractured specimen was examined.

The first SEM was designed by Knoll (1935) in Germany. A second instrument was completed shortly thereafter by von Ardenne (1938a, 1938b). The first SEM to be developed in the United States was in 1942 (Zworykin et al., 1942). The improvements that followed led to an instrument capable of imaging surface topography and morphology with unprecedented depth of field (McMullan, 1953; Smith and Oatley, 1955; Oatley et al., 1965). The improved signal collection and amplification led to the commercial development of the SEM. The first reported fractographic results from the SEM were by Tipper et al. (1959) who examined cleavage in iron. McGrath et al. (1962) published the first SEM examination of fatigue and impact fractures. Comparisons of fractographic results from the SEM and TEM have been presented by Johari (1968), Pelloux et al. (1970), and Russ (1971a, 1971b). The general techniques of SEM fractography have been discussed by Ashbury and Baker (1967), Lifshin et al. (1969), Meny et al. (1970), Almond et al. (1970), and by McCall (1972).

1.1.2 Fracture Mode Analysis

Fractography has become an essential part of failure analysis for fracture mode identification. The standard texts referred to for failure analysis reference are Failure Analysis and Prevention (1975), Case Histories in Failure Analysis (Riederer, 1979), Failure Analysis--The British Engine Technical Reports (Hutchins and Unterweiser, 1981), and Understanding How Components Fail (Wulpi, 1985). Each of these texts relies heavily on SEM fractography for fracture mode analysis. The Metals Handbook Desk Edition (Boyer and Gall, 1985) provides a general procedure for failure analysis investigations. The process begins with a visual examination of the fractured component for gross mechanical abuse and indications of excessive corrosion and deformation. The fracture surface is also examined to determine if an origin can be identified. The direction of crack propagation is then determined and the presence of secondary fractures is evaluated. The fracture is examined with the stereomicroscope to gain insights into the details of the fracture process. Metallography is performed to evaluate the microstructural contributions to the fracture process. Finally, the fracture surface is examined directly with the SEM or with replicas in the SEM or TEM to determine the fracture mode. Boyer and Gall (1985) list the principal categories of fracture features as cleavage facets, quasicleavage facets, dimples, tear ridges, fatigue striations, separated grain facets, mixed fracture features such as binary combinations of cleavage, dimples, tear, fatigue striations and intergranular facets, and finally features resulting from chemical and thermal environments.

SEM fractography of metals is routine when the fracture mode is unique. However, the nonunique fracture and fractures in new engineering materials such as composites offer a challenge to the fractographer. Fractography of polymers, ceramics and composites is rapidly developing. Hertzberg and Manson (1980) have published a text on fatigue in engineering plastics. Rimnac et al. (1981) evaluated the fatigue fracture surface morphology of polyvinyl chloride as a function of molecular weight, plasticizer content, and residual orientation. Engel et al. (1981) have published An Atlas of Polymer Damage which depicts various SEM fractographs of polymer fractures and surface damage. Fractography of ceramics has been discussed in an ASTM book edited by Mecholsky et al. (1978). Govila et al. (1981) have performed a detailed fractographic study of several high temperature structural ceramics, hot pressed silicon nitride, silicon carbide, sialons, and lithium-aluminum-silicate glass ceramics. Mecholsky and Freiman (1981) have performed fractographic investigations on glass and ceramics that failed under constant load after a fixed time. Frechette (1984) has attempted to classify the fracture modes observed fractographically in ceramics. Michalske (1984) has evaluated the fractographic markings associated with environmental effects in the fracture of glass. Rice (1984) has summarized the commonly observed fracture features in ceramics and their associated mechanisms. Fractography of composites is even more complex than that of polymers and ceramics, because of the structural mixtures. Hancock (1975) examined fatigue mechanisms and features in composites. Stinchcomb and Reifsnider (1979) have also reviewed the mechanism of fatigue in fiber-reinforced composites. There have been numerous conferences on failure modes in composites. These have resulted in publications describing composite fractography (Toth, 1973; Fleck and Mehan, 1974; Chiao and Schuster, 1976; Cornie and Crossman, 1979). Liechti et al. (1982) have published an atlas of fractographs of polymer matrix composites. As metal matrix composites have been developed, fractographic investigations have also been performed. Stoloff and Duquette (1979) have examined the high cycle fatigue behavior of several nickel and cobalt base eutectic composites. Kim et al. (1981) have evaluated fractures occurring in tungsten fiber reinforced aluminum composites. Finello et al. (1984) have investigated fractographic features in both aluminum matrix and titanium matrix composites.

Fractography in polymers, ceramics and composites appears to be more complex than in metals. The complexity of these fractures and the difficulties associated with metal fractures that do not fit a particular class are driving forces to evaluate new techniques of fractographic interpretation. Advanced approaches to fractographic analysis have generally fallen into the category of quantitative fractography.

1.1.3 Quantitative Fractography

Quantitative fractography is an attempt to translate fracture features into parametric form. It originated in the 1970s with the first theoretical work of significance being performed by El-Soudani (1974). Chermant and Coster (1979) published the first review of quantitative fractography. A second review by Coster and Chermant (1983) provided further information concerning the areas of investigation in quantitative fractography.

The simplest form of quantitative fractography has been striation counting in fatigue fractures to determine microscopic crack propagation rates. Abelkis (1978) used striation counting to study spectrum loading in fatigue failures. Madeyski and Albertin (1978) and Au and Ke (1981) correlated fatigue crack growth rates with striation spacing. Danity (1984) used marker blocks of constant amplitude load in fatigue testing to mark fatigue surfaces between groups of random load cycles. The entire growth history of a fatigue crack was accounted for from the counted striations.

A more sophisticated form of quantitative fractography involves stereology which extends a two-dimensional image to a three-dimensional structure. This technique was extended from quantitative metallography. The basis of quantitative metallography has been described by DeHoff and Rhines (1968), Underwood (1970), and Exner and Hougardy (1981). The quantitative microscopy techniques typically define the volume fraction Vv, the surface area per unit volume Sv, the length per unit volume, Lv, and the number per unit volume, Nv, as fundamental parameters. Other parameters may be used to describe curvature. The fundamental volumetric parameters may also be related to surface and lineal measure. Rhines (1979) proposed the use of quantitative microscopy techniques for the study of fatigue fracture and recommended that the fundamental quantitative parameters be applied to fractographic analysis.

The application of quantitative fractography is difficult due to fracture surface roughness. To simplify the surface roughness problem, El-Soudani (1974) proposed a mean fracture plane concept. The mean plane is an idealized surface plane parallel to the fracture surface that intersects the fracture surface peaks so that the volume of fractured material above the plane equals the volume of material below the plane. Fracture features may then be classified as ideally flat, nominally flat, random curved, stepped, and zigzagged.

A simple technique to analyze surface roughness is the examination of vertical or profile sections. Profile sections of a fracture surface reveal the five types of fracture surfaces classified by El-Soudani (1974). The experimental methods which have been used to obtain the surface profiles are fracture through a brittle material with polished edges, precision sectioning transverse to the fracture surface, and thin slices taken from a thick replica of the fracture surface. The precision sectioning technique may be extended to multiple parallel sections in a technique known as serial sectioning. Kerr et al. (1976) have used precision sectioning to correlate microstructural features with fracture features in titanium alloys. Van Stone and Cox (1976) have used precision sectioning to study fractures deformed to various levels. They defined the microstructural features which controlled a given fracture process. Precision sectioning, like striation counting, however, is not a direct indication of fracture surface morphology.

The early work on quantitative fractography to develop a single descriptive fracture surface feature parameter began with the surface roughness profile (Coster and Chermant, 1983). The linear roughness parameter, R_L, related the length of a profile to its projection on the mean fracture plane along the direction of crack propagation. This technique stereologically related the two-dimensional structure to the actual three-dimensional surface. The roughness parameter alone was insufficient to describe the morphology of a profile, and thus other techniques were required to define surface morphology. El-Soudani (1974, 1978) defined the true area of the fracture surface, the surface fraction of a feature, and the volume fraction of some identifiable feature from sections. He concluded that stereological techniques could be applied to fracture surfaces by lineal analysis, areal analysis, volumetric analysis, feature count analysis and orientation analysis. Underwood and Starke (1979) proposed the use of stereological methods to analyze microstructural effects in fatigue. They developed techniques to quantify elongated structures, lamallar systems, gradients, and locational characteristics of particles, as each related to the fatigue process. Underwood and Chakrabortty (1981) expanded the use of stereological techniques to describe fracture surfaces. They examined the faceting characteristics and subsurface cracking of fatigue in a titanium alloy. They were able to classify fracture features in terms of true length, roughness, degree of orientation, true surface area and type of surface. Passoja and Psioda (1981) applied one-dimensional Fourier transform techniques to a sectioned fracture to isolate the spatial frequencies occurring in the fracture.

Another approach to profile analysis of the fracture surface has been the use of fractals. Fractals were first proposed by Mandelbrot (1977) as a new approach to dimensional analysis. The basis of fractals is that linear dimensions are dependent on the measurement device. The finer the measuring device, the better able it is to exactly replicate a surface. The technique establishes the fractal dimension as a measure. The measured dimension is plotted on a log-log scale against the measuring device step size. If a linear plot results, the fractal dimension may be calculated and becomes a characteristic feature of the object being measured. Wright and Karlsson (1983) applied both fractal analysis and stereological evaluation to microstructures. Banerji and Underwood (1983) have applied fractal and stereological techniques to fractured 4340 steel by sectioning. Automated measurements of the fracture surface profile were made and the linear roughness parameter, R_L, the profile roughness parameter R_R, and the fractal dimension, D, were calculated. The fracture demonstrated fractal character for certain fractal step lengths. The fractal dimension was used to distinguish between dimples and facets on the fracture surface.

Computer simulations have been used to model and quantify fracture surfaces. Underwood and Underwood (1982) developed a simulation to model sections through a nonplanar faceted fracture surface. The technique allowed the determination of the best analytical method for estimating true fracture surface area.

Another technique for stereological fracture surface analysis has been the use of stereoscopic views and parallax measurements. Kobayashi et al. (1984) used a stereometric approach for matching sites on conjugate fracture surfaces to perform topographical characterizations. They were able to determine the crack tip opening stretch, fracture process zone size, and deformation of grains in the fracture process. Kobayashi and Shockey (1984) were able to apply the stereometric techniques to environmentally assisted fatigue fractures in steel to determine the crack growth mechanism.

The quantitative parameters used to classify fracture surfaces have been listed by Chermant and Coster as the linear roughness index, the waviness index, the fractal dimension, the absolute mean curvature, the mean convex curvature, and the mean concave curvature. Apart from the roughness characterization, no linear parameter has been able to suitably establish a surface morphology parameter. Even the fractal dimension cannot be related to the actual character of the fracture surface. The only successful approach to date has been the use of linear roughness, stereologically extended to a surface roughness parameter (Coster and Chermant, 1983).

Though fractographic techniques have become standardized and much effort has been applied to extracting quantitative information concerning a fracture surface, no practical means exists for fracture surface morphological pattern analysis. Imaging analysis techniques have been applied in a variety of other fields of study, but rarely to fractography. The goal of this work was to investigate the feasibility of the use of the Fourier transform as a means to characterize and classify fracture surface features.

1.2. Digital Imaging Analysis

1.2.1 Image Processing and Analysis

Image processing has as its goal the improvement of an image to aid in information extraction and interpretation. Digital image processing developed simultaneously with the space exploration program and was driven by requirements to analyze less than optimum images from space. Digital processing of remotely sensed images has been extensively reviewed by Moik (1980) and the following summary is based on his work. Image processing assumes that information of concern to the observer can be characterized in terms of the properties of perceived objects or patterns. The extraction of that information involves detection and recognition of image patterns. It usually requires considerable human interaction because of the complexity of the analysis and the lack of precise digital algorithms for automatic processing. Even though the human visual system has extraordinary pattern recognition capability, it is limited in ability to extract all the information in an image in the presence of image degradations. The primary purpose of most image processing is then to remove distortions and aid in the visual extraction of information from an image. It can be done digitally, optically, or photographically, but digital techniques usually offer greater flexibility and accuracy. Hall (1979) has examined digital image processing techniques in detail.

Most image analysis involves image restoration, enhancement, or information extraction and requires a combination of man and machine. Huang (1979) has reviewed the restoration and enhancement process as related to lunar and planetary imaging. Image restoration is required when some definite degradation exists, such as defocusing. Enhancement is a broader technique that involves improvement of image appearance. Lunar and planetary images are often degraded by random noise, interference, contrast loss and blurring. Blurring is usually a linear degradation that is uniform over the image, caused by the introduction of unwanted information. Fourier analysis techniques have been applied to identify the unwanted image information as it exists in the spatial frequency domain, to filter the unwanted information, and to restore the image in a more focused condition. Fourier techniques may also be applied to remove spherical abberations caused by lenses and to remove translational motion of a camera with respect to an object. Enhancement techniques may be applied to the restored image to make the image more visually appealing and to emphasize certain types of data.

Visual interpretation of an image is based on properties of perceived objects or patterns. The properties are determined by observable psychophysical parameters such as contrast, contour, texture, shape, and color. Visual interpretation consists of a sequence of visual processing stages that begin with initial detection and end in final recognition. Objects and patterns can only be detected visually when they can be distinguished from their surroundings utilizing psychophysical parameters. Recognition depends not necessarily on the information present in an image, but on the prior experience of the observer.

The two primary parameters that describe an image feature are contrast and contour. Contrast is a local difference in luminence. It may be defined as the ratio of the average gray level value of an object to the average gray level of its background. The sensitivity of the human visual system depends logarithmically on the light intensities entering the eye. Thus, the greater the brightness, the greater the contrast required between objects to detect differences.

The apparent brightness of an object depends on the local background intensity. Objects with equal intensities can appear different because of differences in background intensity levels. The ability of the visual system to detect sharp edges that define contour is known as acuity. The eye possesses a lower sensitivity for slowly and for rapidly changing patterns than for patterns with midrange spatial frequencies.

Color is another parameter that describes an image. The varying wavelengths of light cause a change in the perceived color from violet (the shortest wavelength) through blue, green, yellow, orange to red. Color can be further described by the attributes of hue, saturation, and brightness. The eye can simultaneously discriminate 20 to 30 gray levels but many more color differences.

Texture is a combination of brightness, color, size, and shape that further defines an image. The local subpatterns in an image determine the texture character as perceived lightness, coarseness, and directionality. Texture may be defined based on regular repetitions of subpatterns or in terms of spatial frequency of local image properties.

Image enhancement involves manipulation of the visual perception parameters transmitted to the analyst in image information extraction and interpretation. Enhancement is achieved by emphasis of features or patterns of interest, and by use of display techniques that are especially adapted to the properties of the human visual system. The techniques of enhancement may be divided into contrast enhancement (gray scale modification), edge enhancement, color enhancement (pseudocolor or false color) and multi-image enhancement. Contrast enhancement has as its goal the production of an image that fully uses the dynamic range of the display device. The device may be a CRT screen, photographic media, or any other equipment used to display an image. Edge enhancement may be used to correct minor blurring by use of a differentiation process. However, the process may increase overall image noise since differentiation amplifies high frequency components. Color enhancement, with simultaneous use of brightness and chromatic variations, provides additional levels of detail distinguishable by the eye. Conversion of a black and white image to color may be achieved by pseudocolor techniques. Different gray levels are assigned specific colors so the final image has color distinguished contrast. False color may be used to display multispectral information with color assignments having no relationship to the actual colors represented in the patterns. Multi-image enhancement is performed by imaging in more than one spectral band or by monitoring an object over a period of time. The multiple images may be ratioed or differenced to enhance specific features.

Image analysis is concerned with the description of images in terms of properties of objects or regions in the image and the relationship between them. The result of image analysis is a description of the input image. The description may be a list describing the properties of objects of interest, such as location, size, shape, relational structure, and directionality. The described image is usually segmented with parts determined by homogeneity with respect to a given gray level or to a geometric property. Regions of approximately constant gray level or approximately uniform texture may represent objects. For images with a characteristic range of gray levels, thresholding may be used to segment desired image components from the undesirable.

Images may also be segmented based on discontinuity of gray levels caused by edges or surface texture. Regions of constant texture usually denote an object. Current texture analysis techniques are based either on statistical analysis by pattern matching or Fourier transform techniques to extract frequency components. Texture is often qualitatively described as coarseness and is related to the spatial frequency period of a local structure with a large period implying a coarse texture. Texture properties such as coarseness and directionality can be obtained from the two-dimensional Fourier transform of the image.

Once an image has been segmented into regions it may be described in terms of regional properties and relationships. A special case of image description is classification. In classification a name of the class to which the image belongs is applied. The properties used to classify an image may be gray level, texture measure, Fourier transform coefficients, or the description of size and shape of a region within the image. Image property values for a given point may combine to form a pattern. However, the use of patterns may not lead to efficient classification because similar patterns may be difficult to distinguish. Feature analysis is more useful in classification and is used to determine those measurements that are most effective for classification. Features are sets of combined or selected measurements derived from originally measured image properties. One approach to classification is to perform the optical or digital Fourier transform on an image and use the resulting frequency power spectrum as a feature. This approach is often simpler than classification of the actual image.

The potential of the Fourier transform for pattern analysis as well as image restoration and enhancement has led to the development of specific instrumentation for performing the Fourier transform. Ginsburg (1976) developed and patented a technique for Fourier transforming an image, spatially filtering the image, and classifying the image. The spatial filter extracted one-, two-, or three-dimensional patterns from spatial frequency subsets to determine general form, edge, texture, and depth information. Speiser and Whitehouse (1976) developed and patented a hardware apparatus for the generation of the two-dimensional discrete Fourier transform. Moss et al. (1983) developed an on-line image analysis technique based on the Fourier transform. A transformed image arranged in polar coordinate form is stored in digital memory. Comparisons of image transforms to the stored transforms are made for image classification. Radial and circular profiles of the Fourier transform are used to further classify the image.

Once an image classification technique is finalized, pattern recognition techniques may be applied. The techniques are usually either statistical, based on a distribution of features, or syntactical, based on pattern structure and pattern element relationships (Mundy and Jarvis, 1982). The intent of this work is to evaluate fractographic image analysis for characterization and classification but not automatic recognition. For further information on digital image and waveform analysis and pattern recognition the works of Hall (1979), Chen (1982), and Fu (1982) are recommended.

1.2.2 Imaging Applications

Digital imaging analysis has become a powerful tool in diverse areas of technology. Stucki (1979) has reviewed many of these areas and has detailed them as industrial applications, earth resources applications, business applications, and medical applications. These and two other areas, military applications, and microstructural applications will now be considered. Most of the industrial imaging has been related to inspection during manufacturing. Lieberman (1979) has described machine vision systems for part recognition, inspection, and verification in an industrial environment. Specific techniques involved in automatic visual inspection have been described by Mundy and Jarvis (1982). In these applications, part lighting is critical, with the most common technique being backlighting to produce a silhouette. Spatial modulation techniques for surface detail detection are sometimes used by applying bands of light to a part being inspected, causing surface relief to be enhanced. Directional contour lighting may be applied from multiple sources with the object profile being extracted from variations in intensity with direction. Diffuse sources are used on highly reflective sources such as solder on printed circuit boards. One of the most significant lighting sources is coherent laser radiation. The technique produces an object diffraction pattern which is the two-dimensional Fourier transform of the object outline shape. The Fourier transform power spectrum is a unique signature pattern for the component and simple classification techniques may be performed. Array detectors may also be placed behind the part being inspected to collect the transform power spectrum image. Sampling techniques may be applied to evaluate the pattern for radial and rotational features which further simplifies classification.

Much industrial imaging has been applied to printed circuit board inspection. Fridge et al. (1984) and Skaggs (1984) have described techniques for circuit board inspection for defects. Most of the requirements in this area have been for line width measurements and the presence, or absence, of a line in an image at a specific location. Harris et al. (1984) described a system to monitor the quality of the microlithographic process in wafer manufacture. Most of the techniques are again dimensionally oriented. Other, more exotic, industrial imaging applications that have been reported are a system to detect apple bruises (Taylor and Rehkugler, 1985), and a system to detect glass fragments in food jars (Dykes, 1985).

Earth resource and space monitoring have had extensive application of imaging analysis techniques. Moik (1980) has thoroughly reviewed the principles and applications of remotely sensed imaging analysis. These techniques have generally fallen into two categories: multispectral analysis and Fourier imaging analysis. Multispectral earth resource monitoring began with the Landsat I satellite in 1972 (Triendl, 1979). It was designed to respond to earth reflected sunlight in four spectral bands. The colors emitted by various types of earth features such as trees, rocks, water, etc. are unique. Various combinations of spectral reflectances from these objects may be used to classify earth features. Triendl (1979) listed some of the multispectral applications as crop acreage and yield assessment, water resource monitoring and management, mineral and petroleum exploration and land use mapping and monitoring. Fox (1980) was able to distinguish, for a given area, the percentage distribution of redwood, Douglas fir, mixed conifer, hardwood, brush, grasslands, soil, water, and other features using multispectral analysis. The second approach, Fourier transform analysis, is based on repeat patterns instead of wavelength variations. Bajcsy (1972) described techniques for analysis of outdoor scenes involving grass, trees, water and clouds. Image descriptors were obtained from the Fourier transform power spectrum using directional and nondirectional components. Mason (1977) described Fourier transform techniques for analysis of cloud structure and was able to detect straight, uniform with globular texture, and broken cover cloud textures.

Business imaging analysis has found primary application in optical character recognition (Stucki, 1979). Ullman (1982) described imaging analysis techniques for automatic character recognition in banking, mail sorting, commercial data processing and newspaper typesetting. McHargue (1976) has described a Fourier transform spatial frequency analysis technique for recognition of Russian alphabet characters.

Medical imaging analysis has developed concurrently with new biomedical imaging techniques and with digital processing of information obtained from existing techniques. Kinsinger (1984) has reviewed medical imaging and found primary applications in digital radiography, computed radiography, nuclear medicine, and ultrasound.

Digital radiography uses digital techniques for image enhancement such as image subtraction. Fourier transform techniques are appropriate for spectral frequency component analysis, but radiologists have been slow to transition from more familiar techniques. Computed radiography (CAT Scan) uses attenuation of transmitted multi-angle x-ray beam intensities to form an image of internal body structure. Nuclear medicine uses radioactive dyes inserted into the body to image specific body components. Both techniques require digital imaging analysis for image intensification. An alternate approach, ultrasound imaging, is rapidly advancing because it is nondestructive to body tissue. It also uses digital techniques for image enhancement. One of the most recent advances in medical imaging is based on nuclear magnetic resonance. Ching (1981) has described a technique for three-dimensional nuclear magnetic resonance imaging of the body with the use of Fourier transform techniques for image reconstruction. Most medical imaging techniques involve image processing and enhancement but little image classification. The primary area of image classification has been in blood cell analysis. Preston (1979, 1982) has discussed image analysis and classification of blood cells by spectral reflectance and by morphological features.

Military imaging analysis has focused primarily on target acquisition and weapons guidance. Most of the work in this area is classified or has limited distribution and cannot be reported here. Multispectral image analysis and Fourier transform image analysis are the two most common forms of image analysis used in target acquisition. Aggarwal et al. (1980) have described infrared image target screeners used with forward looking infrared radar systems on high performance aircraft. Richard and Hemami (1972) have demonstrated the feasibility of a method of identification of a three-dimensional target from its boundary silhouette. The Fourier transform of the silhouette is calculated and descriptors are then applied to each silhouette. Classification techniques may then be used to identify the three-dimensional object and estimate the object's position and attitude with respect to a reference position. The method has been tested for the identification of four different aircraft. French (1978) described the evaluation and use of the two-dimensional Fourier transform for extracting spatial frequency components from acoustic data images. He found that in the presence of poor signal-to-noise ratios the Fourier transform provided no significant benefits. For good signal-to-noise ratios, the Fourier transform was clearly superior to the original image for systematic measurement and ranking of periodic spatial features in the image. Hannigan (1980) patented a method and apparatus for measuring the extent of camouflage applied to a target. The apparatus included a direct electronic Fourier transform device for producing frequency spectra from the camouflage. Duke et al. (1980) used the Fourier transform power spectrum and the log of the power spectrum for target enhancement and detection.

Microstructural analysis applications for imaging analysis have been quantitative metallography, particle analysis, and electron microscopy. Quantitative metallographic techniques have been developed to extract visual information from a two-dimensional image (Saltykov, 1958; DeHoff and Rhines, 1968; Underwood, 1970; DeHoff, 1968a, 1968b; Wiebel, 1980; Exner and Hougardy, 1981). Quantitative stereology techniques have been developed for extension of two-dimensional image data obtained in metallography to three-dimensional features (DeHoff, 1968). The types of features routinely investigated in quantitative metallography have been listed by Vander Voort (1984). These are grain size (including fracture surface grain size), inclusion analysis, line length, object spacing (mean free path and mean spacing), contiguity, anisotropy, and shape. Manual, semiautomatic, and automatic techniques have been developed to extract these kinds of information. Automated instrumentation for quantitative metallography has been described by Cole (1971), Moore (1972), Gahm (1973), Hougardy (1974, 1975, 1976), Underwood (1974), and Exner (1978). There have been no significant reports of use of Fourier transform methods to metallographic analysis.

Microscopic particle analysis is closely related to fractographic feature analysis and has seen significant use of Fourier transform techniques. Approaches to particle characterization have been provided by Beddow and Meloy (1980) and Beddow (1984). Tou (1980) has discussed specific techniques for computer-based particle shape analysis. Classification is typically based on type and number of particles, size distribution for each type, shapes, and texture of particles. Shapes have been described by distance measurements between parallel tangents of a particle, comparison of particles to an equivalent sphere, by intercept lengths, and by Fourier transform techniques. Computer classification of particles may be performed by local morphology of individual particles or by global morphology of groups of particles.

Features for classification are boundaries, centroids, area, size, moments, symmetry, elongation, major axis direction and cluster patterns. For single particle analysis, boundary, textural, and three-dimensional characteristics are critical. For an aggregate of particles, contour patterns, textural and three-dimensional characteristics are critical. Kaye (1984) has discussed the use of fractal analysis for individual particle characterization based on the particle perimeter profile. Lieberman (1984) analyzed individual particle perimeters using one-dimensional Fourier transform techniques. The vector magnitude of the particle profile from its centroid to its perimeter was taken as a function of angle, resulting in a waveform. The Fourier analysis of the waveform extracts the characteristic frequency components. A sharply textured particle will have high frequency components and a smooth particle will be void of high frequency components. Luerkens et al. (1984) reviewed particle morphological analysis based on Fourier descriptors. They listed the primary techniques for particle shape analysis utilizing different methods of acquiring particle perimeter data. Ehrlich and Full (1984) in applying the Fourier shape analysis technique found that higher harmonics isolated by Fourier analysis were due to specific shape features with increasing harmonic detail. Lenth (1984) also performed similar analyses but found digital resolution to be critical when particle profiles are obtained automatically. Lack of resolution caused smoothing of particle features and overfitting added particle features which were not in the original image. Bezdek and Solomon (1984) extended the Fourier analysis methods of particle shape analysis for prediction of features.

Image analysis in electron microscopy has been concerned primarily with improvement of image quality. Fourier transform imaging techniques have been applied in transmission electron microscopy for ultrahigh resolution imaging but also for analysis of periodic features. Most of the analysis has been performed optically, using the optical transform power spectrum version of the Fourier transform. Taylor and Lipson (1951, 1964) provided the early basis for optical transform analysis of periodicities in electron micrographs. Markham et al. (1963) and Klug and Berger (1964) demonstrated that the optical transform was applicable for determination of spacings and angles in electron micrographs. Erickson and Klug (1971) used the optical transform for removal of imaging defects such as defocusing and aberrations by optical reconstruction techniques. In optical transform filtering, the transform of the image is taken, the unwanted frequency components causing the image degradation are physically filtered and the image is reconstructed to a higher quality. Crowther and Klug (1975) established digital techniques of image reconstruction for electron micrographs using the Fourier transform. Yokota et al. (1981) developed an on-line system for performing the Fourier transform in analysis of atomic resolution electron micrographs. Tejeda and Dominguez (1985) have reviewed the available techniques for computer processing of high resolution electron micrographs.

Image processing in scanning electron microscopy is used to maximize information content. Jones and Smith (1978) have reviewed many of the current possibilities available for image processing with the scanning electron microscope. The type processing selected is dependent on the requirements established for the image; numerical data extraction, or an improved visual image. For numerical or analytical image processing, information such as the number of particles, size distribution, or orientation distribution can be obtained. In the case of visual image improvement, the image may have been degraded by some instrumentation factor such as noise, blurring, poor resolution, or lack of contrast. Image enhancement may be used to obtain a more satisfying image. More complex image restoration is used to correct for specific degradation processes. The Fourier transform is the most common technique for image restoration as in other types of imaging.

Scanning electron microscopy image processing techniques may be divided into two categories, analog processing and digital processing. Analog processing is usually for image enhancement only. It involves the time dependent form of the image, and thus filtering and differentiation are effective only in the line scan direction. Digital image processing may be used for image enhancement, but more importantly for image restoration. Digital processing is able to correct for geometric distortion by use of a test object with known dimensions. Numerical image modification allows for distortion correction based on known object dimensions and image dimensions. Gray scale modification may be performed digitally by black level subtraction, contrast expansion, and gamma control. Gray level histogram modification can be performed for image matching studies. A homomorphic filter may be used for gray scale improvement and at the same time enhancement of high spatial frequency detail. Digital filters can remove systematic distortion such as line scan noise by use of the Fourier transform filtering and image reconstruction. Particle counting, area and perimeter assessment and feature extraction may all be performed. Contour analysis may be performed using parallex and stereoscopic techniques, and texture analysis may be performed by analysis of degree of alignment of particles in an image. Pattern classification of scanning electron micrographs has been performed by optical transform techniques by Tovey and Wong (1978). They were able to quantify scanning electron micrograph features for size, shape, micromorphology, distribution and geometric arrangement using the optical transform and calibrated input images.

The success of digital imaging for image enhancement and analysis makes it a logical choice for application to fractographic investigations. The Fourier transform is a proven technique for repeat feature analysis. Because fracture surfaces are typically a collection of repeat patterns, the Fourier transform is the logical technique for classification and characterization of fracture surface features.

CHAPTER 2

THEORETICAL FOUNDATIONS

2.1 Fracture Features and Mechanisms

Fractographic analysis is possible because a given failure mechanism usually produces the same fracture surface features in a specific material. The identification of the failure mechanism requires a knowledge of the material's structure and its properties, the loading characteristics and the environment. The four major classes of failure mechanisms are microvoid coalescence, transgranular cleavage, fatigue and decohesive rupture (Beachem, 1979).

The approach for this work was the application of digital Fourier transform imaging techniques to the four major classes of fracture patterns. The effort attempted to determine what information could be extracted about the fracture surface features by digital imaging analysis. There are many other fracture surface features that could be explored, but not in the context of this work. Digital imaging analysis techniques offer a means of classifying fracture features and a way to measure fracture pattern deviations due to material, loading and environmental variables.

The present practical technique of fractography is based on the previous identification and labeling of typical fracture patterns and collection of the patterns into handbooks. Some of the primary references used for fractographic identification are An Atlas of Metal Damage (Engel and Klingele, 1981); IITRI Fracture Handbook, Failure Analysis of Metallic Materials (Bhattacharyya et al., 1979); SEM/TEM Fractography Handbook (1975); Fractography and Atlas of Fractographs, Metals Handbook, Vol. 9, 8th Edition (1974); and the Electron Fractography Handbook (Phillips et al., 1965). All of these references provide descriptions of the primary fracture features and the fracture mechanisms that created them. Many other references contain additional information on the theories of fracture mechanisms (Tetelman and McEvily, 1967; Broek, 1974; LeMay, 1978; Ewalds and Wanhill, 1984).

An understanding of fracture mechanisms is important in making an accurate assessment of a failure mode. Each of the four major classes of fracture features will now be reviewed with primary reference to the features outlined in the IITRI Fracture Handbook (Bhattacharyya et al., 1979). This will illustrate the types of features that are distinguishable and provide a foundation for classification of the features based on their mechanism of formation.

2.1.1 Microvoid Coalescence Fracture

Metallic materials that are fractured by application of a massive overload, either in tension, in shear, or by tearing, will contain numerous small depressions on their fracture surfaces. These depressions have been given the name dimples and the fractographic classification applied is dimple rupture (Beachem, 1962b). The dimples form by a process of microvoid nucleation at sites in the material where plastic deformation is high. These sites are typically microscopic inhomogeneities such as precipitates, inclusions, and grain boundaries (Crussard et al., 1959). With increasing strain due to the applied massive overload, the microvoids grow and coalesce, producing rupture of the material. Thus the name microvoid coalescence is applied to the fracture mode. Figure 2.1 shows a typical dimple rupture fracture pattern produced by microvoid coalescence.

The type of loading and extent of microvoid nucleation determine the shape and size of the dimples (Beachem, 1962b, 1962c). For extensive nucleation, the growth of the microvoids is limited by impingement with adjacent voids. In this case, a high density of small dimples will result on the fracture surface. If only a few microvoids are nucleated, they will grow to larger sizes before coalescence occurs, producing large isolated dimples. The number and spacing of microscopic particles control the nucleation of microvoids (Gurland and Plateau, 1963). If particles are not present, as in high purity materials, then other inhomogeneities such as grain boundaries control microvoid nucleation. If an overstressed material is hard, the dimples will usually be shallow and if the material is soft, the dimples will usually be deep. Microscopic dimples indicating microscopic ductility may appear on a fracture surface even if there are no indications of macroscopic ductility or deformation.

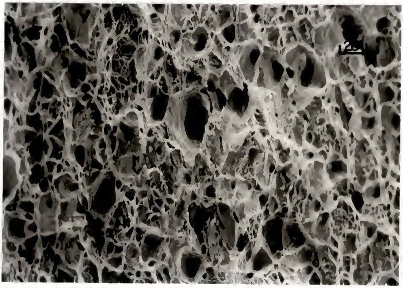

Figure 2.1 Scanning electron fractograph of tensile dimples in plain carbon steel. 500X

The state of stress in overload determines the shape of dimples formed (Beachem, 1963). For uniaxial tensile loading, as shown in Figure 2.2a, equiaxed dimples will result with complete rims at the outer edges of the dimples. For shear loading, as shown in Figure 2.2b, elongated dimples result but with incomplete rims as shown in Figure 2.3. For tensile tearing, as in Figure 2.2c, elongated dimples are also produced, as shown in Figure 2.4. The direction of elongation of the dimples is an indicator of the direction of crack propagation (Beachem, 1962b). For a shear failure, the dimples on the mating fracture faces will point in opposite directions. For a tear failure the dimples on the mating surfaces will point in the same direction. Other microvoid coalescence features that may also appear in an overload fracture are the oval dimple, serpentine glide, ripples and stretched areas (Beachem and Meyn, 1968). The oval dimple is caused by a large void impinging a smaller void, resulting in an oval shaped dimple with a complete rim. Serpentine glide is composed of an interwoven pattern of glide plane decohesion steps resulting from extensive slip (Beachem and Meyn, 1964). Ripples are formed by partly smoothed out areas of serpentine glide that result from continued deformation of a serpentine glide pattern (Beachem and Meyn, 1964). A stretched area is a flat featureless zone that results from further deformation of ripples (Beachem and Meyn, 1964).

Numerous authors have proposed mechanisms for microvoid coalesence, including causes for microvoid formation, coalesence, and final rupture. A complete review of all of these mechanisms is not warranted to establish a theoretical basis for digital characterization of fractographic features. However, a brief review

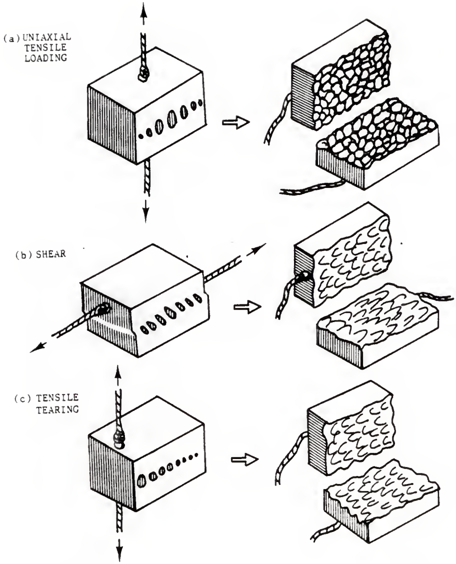

Figure 2.2 Dimple formation from uniaxial loading showing (a) tensile dimples, (b) shear dimples and (c) tearing dimples. (Ewalds and Wanhill, 1984, adapted)

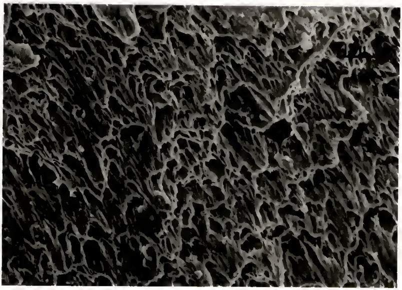

Figure 2.3 Scanning electron fractograph of shear dimples in plain carbon steel. 750X

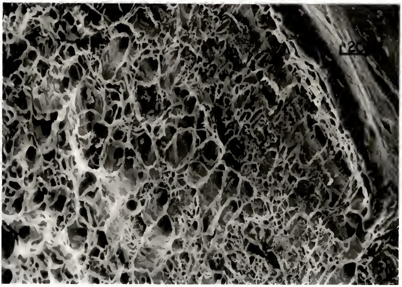

Figure 2.4 Scanning electron fractograph of tensile tear dimples in plain carbon steel. 500X

will aid in an understanding of the uniqueness of each of the features.

The most common source of dimple initiation in microvoid coalescence is intermetallic particles and inclusions (Beachem and Pelloux, 1964). Figure 2.1 shows dimples that nucleated around particles. Puttick (1959), Crussard et al. (1959), and Rogers (1960) were some of the first investigators to isolate intermetallic particles and inclusions as the initiation site for microvoids. Broek (1982) has classified the typical alloy second phase particles by size and origin. He concluded that the largest particles (1-20 microns) are usually brittle and cannot support plastic deformation imposed by a surrounding deforming matrix; therefore they fracture early in the deformation process. Broek (1970, 1971, 1973) demonstrated the formation of microvoids at these large particles. Dundurs and Mura (1969) have proposed a dislocation-particle interaction model as the void initiator at the particle-matrix interface. Broek (1971, 1972, 1973) has attributed the final fracture mechanism to the intermediate submicron size particles. The intermediate particles cannot deform as easily as the matrix and lose coherence. Small voids are formed at the particle-matrix interface and grow by slip. These voids coalesce to produce the final fracture. As an overload crack progresses, large particles ahead of the advancing crack tip will fail as shown in Figure 2.5 (Spitzig et al., 1968). Thus, a distribution of dimple sizes may be observed on the final fracture surface due to the size of the particles initiating the microvoids.

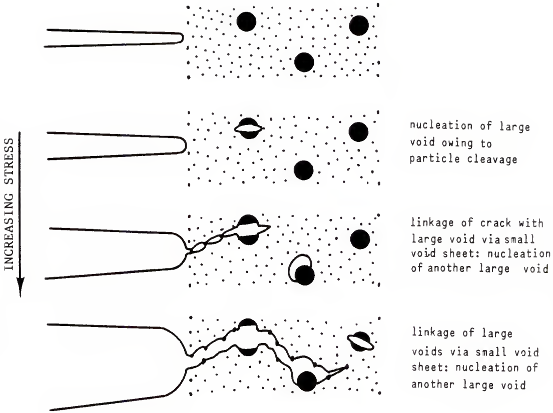
INCREASING STRESS
nucleation of large void owing to particle cleavage
linkage of crack with large void via small void sheet: nucleation of another large void
linkage of large voids via small void sheet: nucleation of another large void

Figure 2.5 Crack extension by transgranular microvoid coalescence with large particle fracture ahead of the crack tip.
(Ewalds and Wanhill, 1984, adapted)

Beachem (1975) has proposed fourteen ways in which microvoids may coalesce to produce different size and shape dimples. Mating fracture surfaces will rarely have matching dimple shapes due to differences in plastic flow on either side of the crack tip during crack growth (Beachem, 1975). Dimple distribution and shape may also vary due to nonuniform distribution of microscopic particles and anisotropy of particle shape (Sailors, 1976).

The primary fractographic feature of interest in classifying microvoid coalesence is the dimple or shear dimple.

2.1.2 Transgranular Cleavage Fracture

Fracture by transgranular cleavage is usually considered brittle on both the macroscopic and microscopic levels (Zappfe and Clogg, 1945b). Cleavage exhibits little or no macroscopic deformation and occurs by atomic separation on low index, well defined crystallographic planes (Low, 1959). It is specific to body centered cubic and hexagonal close packed lattice materials. It may appear in face centered cubic materials under the right environmental conditions such as cracking of aluminum in the presence of mercury, the stress corrosion cracking of brass and the corrosion fatigue of some alloys (Forsyth et al., 1961).

Cleavage is favored under conditions of high triaxial stress, such as at the root of a notch, at high deformation rates, and at low temperatures in ferrous alloys. Cleavage has been responsible for many catastrophic failures in steel that occurred without warning, especially at low temperatures.

Steels and other ferrous alloys have a transition temperature, separating microscopic ductile and brittle behavior. Above the transition temperature the fracture will be predominantly ductile, resulting in microvoid coalescence. Below the transition temperature the fracture will be predominantly brittle, resulting in cleavage.

Cleavage cracks proceed along low index planes and thus in polycrystalline materials, the fracture changes directions at grain boundaries as shown in Figure 2.6. The direction may also change at subgrain boundaries, precipitates, inclusions, and dislocations.

A typical cleavage fracture pattern is shown in Figure 2.7. The features that are used to characterize cleavage are low index crystallographic plane facets, steps separating portions of facets at different heights and river patterns of steps converging in a "downstream" manner (Beachem, 1979). These are shown in Figure 2.7 and schematically in Figure 2.8. Other features sometimes found are the cleavage tongue and herringbone patterns (Friedel, 1959; Dahlberg, 1962; Dahlberg and Beachem, 1963; and Burghard and Stoloff, 1968). Because the cleavage crack follows a specific crystallographic plane, when the crack crosses a grain boundary it will be forced to propagate into the new grain with a different orientation. If the boundary is a tilt boundary, as in Figure 2.8a, the cleavage features will continue from one grain or subgrain into the next. This occurs because of planar registration across the boundary. The river patterns will always converge downstream in the direction of the propagating crack. If the grain or subgrain boundary is a twist boundary, as shown in Figure 2.8b, cleavage crack propagation will not continue across the boundary because of lack of

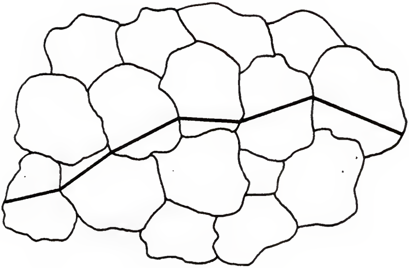

Figure 2.6 Transgranular cleavage crack propagation through a polycrystalline material. (Broek, 1982, adapted)

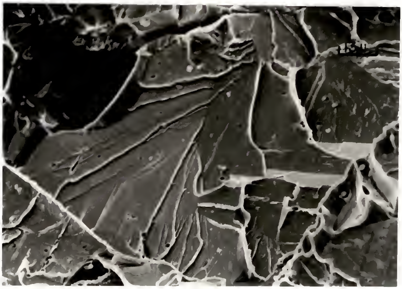

Figure 2.7 Scanning electron fractograph of cleavage in plain carbon steel. 750X

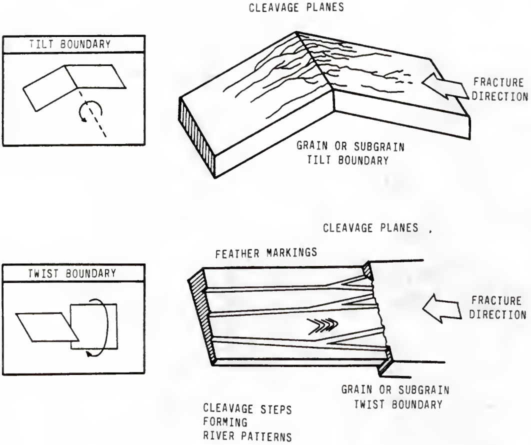

Figure 2.8 Typical fractographic features associated with transgranular cleavage cracking. (Ewalds and Wanhill, 1984, adapted)

registration. Thus new cleavage cracks must be initiated at the interface for the crack to propagate.

Other cleavage features as listed by Ewalds and Wanhill (1984) are cleavage steps, feather markings, herringbone patterns, cleavage tongues and wallner lines. The cleavage step is due to height differences between two cleavage facets as shown in Figure 2.8b. Feather markings, which are fine, fan like, markings that open into the crack propagation direction are also shown in Figure 2.8b. Herringbone patterns are flat narrow strips that have a central flat zone in the fracture direction with angled facets on each side arranged in a herringbone formation. Cleavage tongues are fine slivers of metal on cleavage facets that form at the intersection of a crack with a microtwin (Berry, 1959 and Beachem, 1966b). Wallner lines are distinct "v" shaped fracture patterns observed in brittle materials by the intersection of two groups of parallel cleavage steps (Schardin, 1954 and Limb and McNeil, 1964).

Quasicleavage is a form of cleavage that occurs in quenched and tempered steels (Beachem et al., 1963). The cleavage facet size does not correspond to the grain size so the name quasicleavage has been applied. The facet size may be smaller (micro-quasicleavage) or larger than the prior austenite grains. Instead of a few growing crack fronts in cleavage, micro- quasicleavage has multiple crack fronts that result in many small cleavage facets. Figure 2.9 shows a typical micro-quasicleavage fracture in a quenched and tempered steel.

The mechanism of initiation of cleavage cracks has been studied extensively by Kitajima and Futagami (1969). Cleavage initiation in

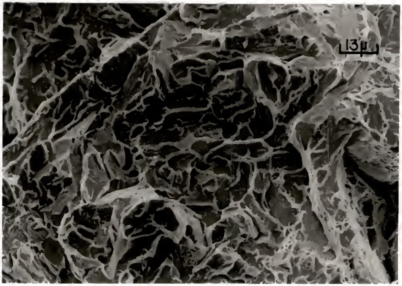

Figure 2.9 Scanning electron fractograph of quasicleavage in 17-4 PH carbon steel. 750X

a mild steel has been, in one theory, related to the fracture of brittle intergranular carbides at a grain boundary (Smith, 1966). An applied tensile stress results in a shear stress within the ferrite grains. The shear stress leads to a dislocation pileup at the grain boundary which results in fracture of the brittle intergranular carbide. The carbide crack is then propagated into the surrounding grains and instantaneous fracture occurs. Berry (1959) and Low (1959) have shown that parallel cleavage cracks, once initiated, will overlap to form a vertical cleavage step either by secondary cleavage or by shear. Low (1959), Friedel (1959) and Plateau et al. (1965) have shown that cleavage steps can also be initiated by the passage of a screw dislocation. Beachem (1978) has proposed in an alternate theory that cleavage actually occurs by microplasticity and not by brittle decohesion of atoms.

The primary fractographic feature for classifying transgranular cleavage is flat grain facets with superimposed river patterns of cleavage steps.

2.1.3. Fatigue Fracture

Fatigue fractures result from repeated cyclic loading. Zapffe and Worden (1951) first reported observing parallel macroscopic lines on fatigue fracture surfaces. The fatigue fracture process is composed of two distinct events, fatigue crack initiation and fatigue crack propagation. The mechanisms that operate are determined by the material, the crystallographic orientation, material homogeneity, cyclic load frequency, alternating stress amplitude, environment, and section thickness (Bhattacharyya et al., 1979). There are three stages to a fatigue fracture as shown in Figure 2.10: stage I which is initiation and initial crack propagation, stage II which is crack propagation, and stage III which is final overload, usually by microvoid coalescence (LeMay, 1978).

The characteristic fracture feature of fatigue is microscopic striations (Beachem, 1969). Striations were first observed by Thompson et al. (1956) and appear as multiple microscopic parallel ridges oriented transverse to the crack direction. Figure 2.11 shows a typical fatigue fracture with striations. Each striation represents one load cycle. The striations are mutually parallel and are usually bowed out in the direction of local propagation. Because two mating fracture surfaces are not stressed equally, striations are not equally sharp on both fracture surfaces (Beachem, 1967). The appearance and spacing of striations is dependent on the ductility of the material, the stress level at which the crack propagated, the stress state, and the environment (Beachem, 1969). Fatigue of aluminum in a vacuum may result in no striations being formed (Meyn, 1967). Alloys with moderate strength and good ductility, such as aluminum and corrosion resistant steel, typically produce well defined striations. High strength materials, such as quenched and tempered steels, rarely produce well defined striations. Striations, if well formed, may be counted to determine the number of cycles to failure (Pelloux, 1964; Abelkis, 1978). Striations may be brittle or ductile (Forsyth et al., 1959, 1961). Au and Ke (1981) have demonstrated the ability to count striations even in high strength steel.

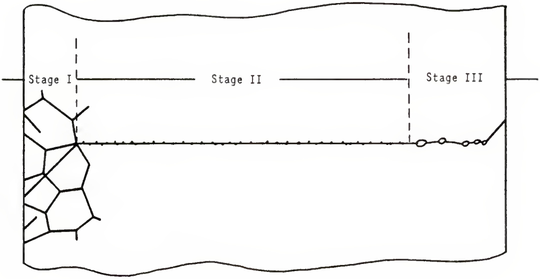

Figure 2.10 Three stages of fatigue fracture.
(LeMay, 1978, adapted)

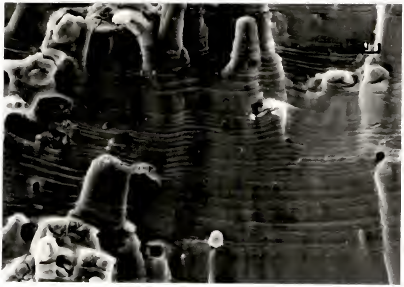

Figure 2.11 Scanning electron fractograph of fatigue striations in wrought aluminum 2024-T3. 750X

The fracture in Stage I fatigue is by slip plane movement and striations rarely occur. With the onset of Stage II fatigue, many parallel plateaus are produced with striations present. The plateaus are separated by longitudinal ridges that radiate in the direction of crack propagation. Regions in the Stage II fracture may not show striations due to rubbing or corrosion. High cycle fatigue typically produces closely spaced and well defined striations. Random loading in high cycle fatigue may cause the one-to-one ratio of load cycle to striation to no longer exist. Low cycle fatigue may produce striations or may act as a step-progressive overload fracture, producing bands of dimples as the crack steps forward.

Other features associated with fatigue as listed by Bhattacharyya et al. (1979) are beach marks, ratchet marks, secondary cracks and tire tracks. Beach marks are crescent shaped markings emanating out of a fatigue origin and are caused by arrests in crack propagation. Ratchet marks are macroscopic step marks that occur along the fracture origin due to cracks initiating on multiple planes. Secondary cracks are microscopic cracks that are parallel to fatigue striations and are a result of cracking aligned perpendicular to the primary crack. Tire tracks are microscopic features observed in high cycle fatigue caused by repeated impacting of the fracture surfaces, causing indentations in the fracture surface by second phase particles (Beachem, 1966c; Broek, 1969; Koterazawa et al., 1973).

The mechanism of fatigue initiation has been reviewed by a number of authors (Grosskreutz, 1971a, 1971b; Coffin, 1972; Fong, 1979; Laird, 1979; Lankford et al., 1983) and is related to cyclic plastic deformation. The applied stress may be well below the elastic limit, but the local stress level may be above it due to stress concentrations at inclusions and surface defects. Several early models based on the presence of fatigue striations (Forsyth and Ryder, 1961) were proposed to explain the initiation of fatigue cracks by local plastic deformation (Cottrell and Hull, 1957; Wood, 1958; and Mott, 1958). The fatigue initiation model developed by Wood (1958) is shown in Figure 2.12. During the rising-load part of the cycle, slip occurs on favorably oriented slip planes. In the falling-load part of the cycle, slip occurs in the reverse direction on a parallel slip plane. This reversal occurs because slip on the first plane is inhibited by strain hardening and by oxidation of the newly created free surface. The first cyclic slip can result in an extrustion or intrusion at the surface. An intrusion can grow into a crack by continued plastic deformation from continued cyclic loading. This mechanism continues to operate even if the cyclic loading is tension-tension because the plastic deformation occurring at increasing load will result in residual compressive stresses during load release. Figure 2.12 also shows surface extrusions and intrusions that result from cyclic loading.

Once a fatigue crack initiates, it can grow by a mechanism of reverse slip as proposed by Forsyth (1961, 1963), Laird and Smith (1962), McEvily and Boettner (1963), Pelloux (1969, 1970), Bowles and Broek (1972), and Neumann (1973). Figure 2.13 shows the stages of growth of the advancing fatigue crack tip. A sharp crack in a tensile stress field causes a large stress concentration at its tip under conditions of easy slip. The material above the crack (stages

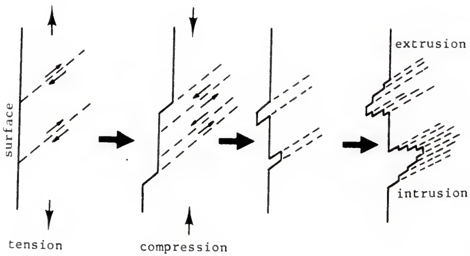

Figure 2.12 Extrusion-intrusion model of fatigue crack initiation. (Wood, 1958, adapted)

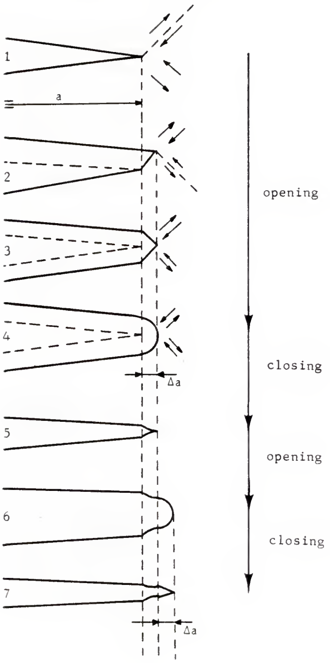

Figure 2.13 Reverse slip model for fatigue crack propagation. (Broek, 1982, adapted)

1 and 2 in Figure 2.13) may slip along a favorable slip plane in the direction of maximum shear stress. The slip from the rising load cycle causes the crack to open and to extend in length by an amount Δa. Slip then becomes operable on another plane (stage 3). Work hardening and increasing stress activate other parallel slip planes which leads to a blunt crack tip (stage 4). Plastic deformation occurs in a small region surrounded by elastic material as the crack progresses. During load release the elastic surroundings contract and the plastically deformed region, which has become too large, will no longer fit into its surroundings. In order to accommodate the deformed material the elastic region will exert compressive stresses on the plastic region. The compressive stresses will be above yield at the crack tip so that reverse plastic deformation occurs, closing and resharpening the crack tip (stage 5). The cyclic opening and closing movement at the crack tip (Stages 1-5 and 6-7) develops a pattern of fracture surface ripples or striations as shown in Figure 2.11. Every new load cycle adds a new striation. The formation of striations, however, is dependent on the ductility of the matrix.

Fatigue crack initiation can be influenced by inclusions and second phase particles (Pelloux, 1964; Eylon and Kerr, 1978). For smooth specimens, inclusions are sites of stress concentrations. McEvily and Boettner (1963), Grosskreutz and Shaw (1969), and Bowles and Schijve (1973) have shown that fatigue cracks can initiate at such particles. If mechanical stress concentrations such as notches are present, the particles have less importance in crack initiation. Likewise, particles have little influence on slow fatigue crack propagation. This has been shown experimentally by Broek (1969) and El-Soudani and Pelloux (1973). For slow crack growth rates, the crack front will approach a large particle and contact it before the particle fails. For high crack growth rates, on the order of one micron per cycle or greater, a high stress intensity exists at the crack tip. Particles in front of the crack tip may cleave or lose coherence with the matrix creating a large void (Broek, 1969; El-Soudani and Pelloux, 1973). The remaining material between the void and crack tip will then rupture by ductile tearing as shown in Figure 2.5, providing a local jump of the crack front.

At high crack growth rates, the effect of inclusions cannot be neglected. Broek (1969) has shown a discrepancy between striation spacing and measured crack growth rate as measured during testing, due to small amounts of static fracture. The static fracture is by dimple rupture originating at particles. At extremely high growth rates, striations disappear entirely and dimples appear. Thus particle effect in fatigue fractures is limited to extremely high crack growth rates or the final portion of crack propagation. At extremely slow growth rates, striations may be replaced by facets with a cleavage appearance (Hertzberg and Mills, 1976).

The primary fractographic feature for classifying fatigue fractures is the fatigue striation.

2.1.4 Decohesive Rupture

Decohesive rupture is the separation of fracture surfaces along weak fracture paths, usually grain boundaries. The two main factors that contribute to the occurrence of this mode of fracture are morphological variables and environmental attack. The morphological variables are typically the presence of large amounts of grain boundary precipitates, formation of low strength phases and defect structures along grain boundaries, and formation of grain boundary precipitate free zones. The environmental factors are those which promote material-environment interactions such as hydrogen assisted fracture and stress corrosion cracking. The most common form of decohesive rupture is intergranular fracture. This is due to the fact that grain boundaries are numerous in polycrystalline materials and because they are an easily accessible microstructural inhomogeneity in the material.

Intergranular fracture surfaces typically display microscopic grain facets. The facets may be flat and free from any other features, as in some hydrogen assisted cracking as shown in Figure 2.14a, they may show the presence of corrosion product as in some stress corrosion cracking fractures, or they may have superimposed dimples, as shown in Figure 2.14b, due to weak grain boundary phases such as that caused by a precipitate free zone.

The two primary forms of intergranular decohesion fracture of interest in this work are hydrogen assisted cracking and stress corrosion cracking. The features produced by both fracture modes are sometimes identical. Some of the proposed fracture modes are nearly identical as well. Figure 2.15 shows a typical fractograph of a hydrogen assisted cracking fracture and Figure 2.16 shows a typical fractograph of a stress corrosion cracking fracture. Both fractures are in the same type material and the fractographs appear identical.

(a)

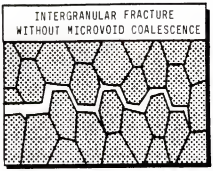

(b)

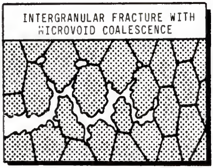

Figure 2.14 Decohesive rupture in a polycrystalline material producing (a) intergranular facets and (b) intergranular facets with superimposed dimples. (Ewalds and Wanhill, 1984, adapted)

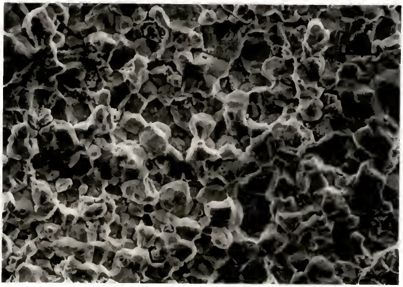

Figure 2.15 Scanning electron fractograph of hydrogen assisted cracking in 4340 steel. 750X

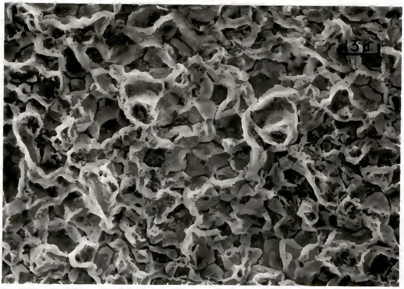

Figure 2.16 Scanning electron fractograph of stress corrosion cracking in 4340 steel. 750X

The proposed hydrogen assisted cracking mechanisms are numerous. Many of the mechanisms have been presented by Bernstein and Thompson (1974). Recent reviews of the mechanisms of hydrogen damage have been published by Nelson (1983) and Gibala and Hehemann (1984). One of the most common sources of hydrogen accumulation and resulting damage in high strength steels is during chemical and electrochemical processing such as pickling, electroplating, and stripping. Sufficient internal hydrogen pressure can lead to blisters and cracks at internal interfaces such as grain boundaries and inclusions, resulting in delayed failure. Hydrogen assisted cracking can also occur as a result of exposure of a component to a hydrogen bearing environment, as was first reported by Van Ness and Dodge (1955). The mechanism of hydrogen assisted cracking is complex and may result from a single mechanism or a number of different mechanisms. The exact process involved depends on the origin of the hydrogen, the change in behavior of the alloy, and the transport reactions and hydrogen-metal interaction mechanisms that occur between the two. The presence of hydrogen in a metal lattice can degrade properties by dislocation interactions, lattice-bond interactions, internal pressure formation and hydride precipitation. The first two involve hydrogen below the solid solution solubility limit and the latter two above the limit.

The hydrogen-dislocation interaction mechanism for hydrogen damage makes the assumption that a hydrogen field can change the mobility of a dislocation. Dislocation mobility determines the nature of plasticity in a structural alloy, thus influencing its fracture behavior. Bastien and Azou (1951) were the first to propose that hydrogen would associate itself with dislocations. They theorized that hydrogen can form a Cottrell-type atmosphere around dislocations, exerting a drag force and making dislocation movement more difficult. This acts to harden and embrittle the alloy. A reduction in dislocation mobility can change fracture behavior by increasing the difficulty for deformation at a crack tip. Reduced deformation will result in a sharper crack tip and crack growth at lower applied stress.

An alternate hydrogen effect, slip-softening, by hydrogen-enhanced dislocation motion has been proposed by Beachem (1972). The hydrogen weakens the matrix by making dislocation motion easier. This has led to the nomenclature hydrogen-assisted cracking. The mechanism is based on fractographic observations that indicate extreme microscopic plasticity can occur in hydrogen enhanced "brittle" fracture in a high strength martensitic steel. Beachem (1972) proposed that a high hydrogen concentration just ahead of the crack tip aids microstructural deformation in the area of high hydrogen concentration. Failure occurs when a critical strain is achieved in the localized region. Lynch (1979) has proposed a similar mechanism, but suggested that chemisorbed hydrogen at the crack-tip surface facilitates the nucleation of dislocations and softens the region around the crack tip.

Lattice-bond interactions that are affected by hydrogen were first proposed by Petch and Stables (1952) as the adsorption mechanism of hydrogen embrittlement. They suggested that hydrogen, when adsorbed on a metal surface, would lower the free energy of the surface. A lower surface free energy causes a reduction in the work required to break the cohesive bonds across a crystallographic plane, making fracture easier. Barnett and Troiano (1959) considered a similar model in which subsurface hydrogen would result in a localized reduction in the cohesive strength of the lattice. The model is sometimes referred to as the decohesion mechanism of hydrogen embrittlement. In this model, hydrogen interacts to weaken the lattice bonds ahead of a crack tip, at the point of maximum stress. A subsurface crack nucleates ahead of the crack tip and propagates backward to the already existing crack tip. The process is repeated and propagation occurs in a discontinuous manner. In effect, the adsorption mechanism and decohesion mechanism are identical and both depend on a hydrogen-induced reduction in the metal lattice cohesive strength. The only difference is the proposed location of strength degradation, at the crack tip or ahead of the crack tip. Oriani (1978) advanced the decohesion mechanism by considering both a thermodynamic and transport kinetics argument.

The oldest of all the currently accepted mechanisms of hydrogen degradation is the internal pressure formation mechanism, first proposed by Zapffe and Sims (1941), to explain embrittlement of steels by electrolytic hydrogen charging. Subsequent modifications made to the mechanism by De Kazinczy (1954), Bilby and Hewitt (1962), and Tetelman and Robertson (1962) have resulted in a general mechanism of embrittlement in an alloy containing a nonequilibrium supersaturated concentration of hydrogen. The excess hydrogen attempts to leave the metal lattice by forming molecular hydrogen at an external or internal surface. Hydrogen precipitates as molecular hydrogen at internal surfaces, such as the interface between an inclusion and the metal lattice. As the lattice hydrogen concentration is reduced by the formation of molecular hydrogen at interfaces, more hydrogen will diffuse into the region. The result is additional molecular hydrogen formation at the interface and increased hydrogen pressure within the newly created internal cavity. The hydrogen assisted cracking process is the result of cavity creation and microcrack formation at subsurface locations in the alloy. An additive effect occurs from the internal cavity pressure which lowers the required applied stress for cavity growth. In high strength steels, the cavity growth may be made easier by other hydrogen-metal interactions such as a dislocation interaction or lattice decohesion at the tip of an internal microcrack. An applied stress is not required for the nucleation and growth of microcracks by molecular hydrogen. Even if hydrogen is removed by diffusion with time or by baking, the cavities will remain, resulting in irreversible hydrogen embrittlement.

Hydrogen concentrations above the solid-solution solubility limit will react with many alloys to form a hydrogen-rich second phase known as a hydride. The hydrides are usually less dense than the host lattice and are brittle. The hydride mechanism of embrittlement was first proposed by Wood and Daniels (1965) and Westlake (1969). The number of elements which will form stable metallic hydrides is limited. Certain transition metals such as titanium, zirconium, and niobium and other rare earths readily form embrittling hydrides. The primary mechanism of the embrittlement is the premature failure of the brittle hydride in the ductile metal lattice.

Nelson (1983) has provided an overall summary of the effects of hydrogen. Hydrogen may result in degradation of mechanical properties, including strain hardening rate, elongation to failure, reduction of area, tensile strength, and fracture toughness. The influence of hydrogen in general is either on plastic behavior by hydrogen-dislocation interaction or fracture behavior of an alloy. Fracture of an alloy in hydrogen occurs by crack initiation and slow crack growth, followed by rapid unstable failure. The initiation stage generally requires significant dislocation movement (plasticity) on a local scale and consists of nucleation and initial growth of a microcrack. The crack growth stages occur when the microcrack becomes sufficiently long that continued growth can occur from an interaction with a chemical or thermal environment and the stress field at the tip of the microcrack. Hydrogen can affect all three stages of fracture depending on the type alloy, processing history, and service conditions. The final unstable crack growth is a near instantaneous process and is independent of most influences of hydrogen. If load is applied rapidly to a susceptible alloy containing hydrogen, mechanical degradation will be rapid and hydrogen degradation will not have time to occur. If the load is applied slowly and held constant, the hydrogen transport has time to occur, and the hydrogen-metal interactions can influence the crack initiation and slow crack growth stages of fracture.

The fractographic features that result from the hydrogen damage are dependent on the many variables that operate during the process. If no sharp cracks are present at a surface, hydrogen cracks will typically initiate at subsurface sites where triaxial stresses are highest (Phillips et al., 1965). In quenched and tempered steels, the hydrogen assisted crack usually follows prior austenite grain boundaries producing an intergranular fracture surface as shown in Figure 2.14. Hydrogen damage may also result in dimples on grain facets as in Figure 2.14 or in transgranular cracking by quasicleavage (Kikuta et al., 1978).

The fracture produced by hydrogen assisted cracking may exhibit intergranular facets with tear ridges, secondary cracking or transgranular quasicleavage (Beachem, 1969). The fine scale fracture features produced by hydrogen assisted cracking and stress corrosion cracking in quenched and tempered high strength steels are very similar. Phillips et al. (1966) and Beck et al. (1971) have shown that the fractures may be distinguished not by the presence of a certain type feature but by the relative proportions of the features. They found that more tear ridges were present in hydrogen cracked surfaces than in stress corrosion surfaces, and more secondary cracking was found in stress corrosion surfaces than in hydrogen cracked surfaces.

Engel and Klingele (1981) have reviewed many of the features associated with a hydrogen assisted fracture and concluded that the fractures may be either intergranular or transgranular relative to the prior austenite grains. For martensitic steels, the transgranular fracture propagates either transverse-to or parallel-with the lath structure. If the fracture is parallel to the laths, the fracture facets are smaller than the prior austenite grains, resulting in micro-quasicleavage which resembles curved leaves and micropores. The most common appearance of transgranular hydrogen cracking is with hydrogen flakes and "fisheyes" which surround subsurface nonmetallic inclusions.

Intergranular hydrogen assisted cracking will display intergranular secondary cracks, ductile tear ridges and micropores. The tear ridges form during grain boundary separation and represent small areas of plastic deformation. The tear ridges often branch to form "crows feet" markings. Figure 2.15 shows a typical hydrogen induced fracture in a high strength quenched and tempered steel.

Stress corrosion cracking is an environmentally assisted fracture process that occurs in the presence of an applied or residual tensile stress and a specific corrosive environment. Logan (1966), Craig (1972, 1976), and Brown (1972), as well as papers in the publication edited by Gibala and Hehemann (1984) have summarized the characteristics of a stress corrosion cracking fracture. A tensile stress is required which may result from service loads, cold work, mismatch in fit-up, heat treatment, or by the wedging action of corrosion products. In general, only alloys are susceptible and only a few chemical environments are effective in causing stress corrosion in a given alloy. The chemical environment does not have to be available in large quantities or in high concentrations. For some alloy-chemical environment combinations such as titanium and crystalline sodium chloride, or austenitic stainless steel and chloride solutions, temperatures well above room temperature may be required to activate stress corrosion. A stress corrosion prone alloy is usually almost inert in a stress free chemical environment that would otherwise cause stress corrosion. There appears to be a threshold stress below which stress corrosion cracking does not occur in some systems. Stress corrosion cracks are brittle in appearance.

Brown (1972) has also provided a review of the typical sequence of events that occur in stress corrosion cracking. A corrosion pit will form with a porous cap of corrosion product present. The cap resists flow of corrosive media, external and internal to the pit, but permits inward migration of anions such as chloride. The inward migration which causes growth of the stress corrosion crack is essentially "uphill diffusion" of anions. The driving force is the active metal surface. The pH of the environment inside the corrosion pit will be altered from that of the external environment. The pit in general changes the solution chemistry inside the pit and establishes the conditions required for stress corrosion cracking. The crack will propagate by combined stress and chemical attack mechanisms until the structure can no longer support the applied tensile load. At that point massive overload occurs.

Ford (1984) has reviewed the spectrum of mechanisms currently in existence to explain observed stress corrosion behavior. He has distinguished three broad categories of stress corrosion mechanisms: pre-existing active-path mechanisms, absorption-related mechanisms, and strain-assisted active-path mechanisms.

The pre-existing active-path theories (Dix, 1940; Mears et al., 1945; and Dix, 1950), have had application primarily to intergranular cracking of ductile alloys in aqueous environments. They relate crack propagation to preferential dissolution of chemically active regions at the grain boundaries. Some of the metallurgical sources of active grain boundaries are segregation of alloying elements to the grain boundary and the formation of low solute concentration regions at the grain boundary that accompany grain boundary precipitation. The purpose of the applied tensile stress is to keep the crack open, allowing electrolyte access to the crack tip for continued preferential dissolution.

The adsorption-related mechanisms place emphasis on the stress component and associate crack propagation with a decrease in mechanical integrity of the crack tip area. Numerous specific mechanisms for the crack tip mechanical property degradation have been proposed in various texts and conference proceedings (Bastien, 1972; Bernstein and Thompson, 1974; Hirth and Johnson, 1976; Beachem, 1977; and Staehle et al., 1977). The mechanisms are either based on surface energy reduction or on decohesion. In the surface-energy models (Petch and Stables, 1952; Petch, 1955, 1956; Ulig, 1959; Coleman et al., 1961; and Heady, 1977), the atom-atom rupture occurs at the crack-tip surface with the process affected by changes in surface energy due to adsorption of chemical species from the environment. In the decohesion models (Troiano, 1960; Oriani and Josephic, 1974; Yoshino and McMahon, 1974), the atom-atom rupture occurs subsurface to the crack tip. The fracture process is dependent on adsorption and transport of hydrogen atoms to regions of high triaxial stress. The mechanism that is operating is essentially hydrogen assisted cracking.

The strain-assisted active-path theories place equal importance on the chemical and mechanical contributions to crack propagation. The earliest theories (Hines and Hoar, 1958; Hoar and West, 1962; Hoar, 1963), proposed that crack advance was associated with strain-enhanced dissolution of the bare crack tip. This concept was modified by slip-dissolution models (Logan, 1952: Scully, 1968;

Staehle, 1971; Hoar, 1971; Vermilyea, 1972), and brittle film models (Forty and Humble, 1963; McEvily and Bond, 1967; Pugh, 1971). Both of the modifications proposed that the crack surfaces had to be protected by a thermodynamically stable oxide layer to maintain a high aspect ratio propagating crack instead of massive corrosion attack. The crack tip advances by either dissolution or film growth followed by repetitive film rupture which produces incremental crack growth.

The complexity of the proposed mechanisms is as vast as the number of researchers investigating the problem. A simplified strain-assisted active path mechanism from LeMay (1978) is shown in Figure 2.17. Corrosion is localized at the tip of an intergranular or transgranular propagating crack. The surface of the crack becomes passivated by formation of a protective oxide film. The film is ruptured by slip at the crack tip, leaving a fresh metal surface exposed. The surface is attacked by the corrosive environment and repassivated, resulting in overall crack growth. The process continues on a stepwise basis, resulting in a fracture morphology that may show macroscopic beach marks and even microscopic striations.

In steel and aluminum, stress corrosion crack propagation is primarily along grain boundaries (Beachem, 1969). Intergranular stress corrosion cracking in aluminum usually results in considerable branching of the propagating crack front. The intergranular cracking in aluminum may show very flat facets in forged products (Alex, 1972). Titanium alloys also show intergranular stress corrosion cracks but with some grains failing by cleavage (Phillips et al.,

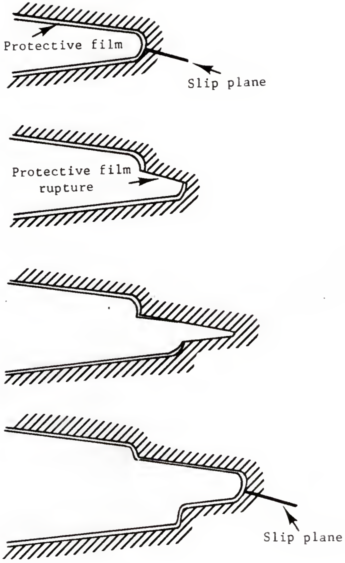

Figure 2.17 Mechanism of stress corrosion crack propagation by repeated rupture of protective film. (LeMay, 1978, adapted)

1965). Figure 2.16 shows a typical stress corrosion crack in high strength steel that is free of corrosion product.

The primary fractographic feature for classifying decohesive rupture is the intergranular facet. Finer scale features are used to identify differing mechanisms of decohesive rupture.

In summary, the four primary fractographic modes of interest are microvoid coalesence which produces dimples, cleavage which produces cleavage facets, fatigue which produces striations, and decohesive rupture which produces intergranular facets. For most of the features the fractographer can easily distinguish the fracture mode. However, complexities exist that can be confusing, such as hydrogen assisted cracking and stress corrosion cracking fractures with identical features. Other fracture modes can produce confusing combinations of fracture features such as fatigue in a high strength precipitation hardening stainless steel that results in intergranular fracture, stress corrosion cracking that results in crack arrest "striations" and microstructural platelets in titanium that can be confused with fatigue striations. These complexities have often led to controversy and reveal the need for an objective tool for fractographic analysis. The most appropriate technique is digital imaging analysis based on the Fourier transform. The success of the Fourier transform in other image classification and characterization applications make it an equally viable solution to the problem of fractographic image characterization.

2.2 Imaging Analysis

One method of image analysis and characterization as presented in the introduction is isolation of frequency components from an image. Because optical image formation is a linear process where individual spatial frequencies combine to produce a consolidated image, techniques may be applied to unfold the frequency components. This has been done through optical diffraction techniques for numerous types of images (Lipson and Taylor, 1958; Taylor and Lipson, 1965; Lipson, 1972; Steward, 1983). The process utilizes a laser light source passed through a transparency of the image and projected through a lens to produce a diffraction spot pattern. The spots represent the spatial frequencies in the image transparency. The physical process of diffraction spot formation is mathematically equivalent to the calculated Fourier transform. Digital Fourier transform processing of images to extract frequency components has been applied in a similar manner to the optical processing for numerous types of images (Peterson and Dobrin, 1966; Andrews, 1970; Moik, 1980). The basic property of the Fourier transform in imaging analysis, whether performed optically or digitally, is the isolation of image frequency components. Each technique offers specific advantages for particular applications in imaging analysis.

2.2.1 Optical Image Characterization

The process of image characterization and recognition is extremely complex. Harmon (1974) in an attempt to develop computerized techniques for facial recognition concluded that the human mind operates on a data base composed of unique facial features that occupies a 21-dimensional matrix. Multiple combinations of eye, ear, nose, mouth, chin and hair features must be simultaneously evaluated by the brain in order to recognize a face. The work of Lendaris and Stanley (1970) has given other insights into how the human mind performs pattern recognition. The process is dynamic in that general information is sought first and a context is established. Then more specific information is sought, step by step, with each step being more detailed, until the desired identification is made. Specifically, a relative scale would first be established, then quick scanning of the eye is performed to locate characteristic features. Once a feature is recognized, a finer detail search is begun to locate features typical of the anticipated image. After a sufficient number of features have been identified, the image is recognized.

In the pattern recognition process the presence of repeat features in the image simplifies the effort. The mind readily detects the presence of a repeat pattern and disruptions of such patterns. Isolation of spatial frequency components becomes a logical basis for simplifying the computerized image characterization process. Spatial frequency extraction is equally valid in applications of optical Fourier transform analysis.

2.2.2 Optical Diffraction Pattern Formation

The formation of diffraction spots is a naturally occurring optical phenomenon. It is simply the interaction of electromagnetic radiation with an aperture or aperture-like device to produce a projected image. The diffraction spot pattern is an intermediate step in the image formation process which typically occurs between two lenses in a projection system employing coherent light.

Steward (1983) has reviewed the historical development of optical diffraction spot formation based on electromagnetic wave theory. The initial experiment that provided crucial evidence for the wave theory of light was performed by Young (1802). In his experiment, as detailed in Figure 2.18, Young allowed sunlight to pass through a pinhole, S, and illuminate an aperture mask some distance away. The mask or screen contained two closely separated pinholes, B, and C, separated by distance, D. A third screen was located at about the same distance of separation as the first two screens, distance L. At the final screen, light and dark fringes were observed in the regions of geometrical shadow around 0 with a spacing, Δ. Neither pinhole alone could have produced the fringes and their existence was interpreted as interference between light diffracted at the two pinholes and traveling paths A_1 and A_2. This phenomena supported the wave theory of light earlier developed by Huygens in 1690 which described the progression of waves in a medium (Steward, 1983). Huygens' principle stated that every advancing wavefront is composed of an array of secondary wavelets with the same velocity as the primary wavefront. The profile of the combined wavelets forms the advancing wavefront as shown in Figure 2.19a. When the wavefront is intercepted by a screen containing an aperture,

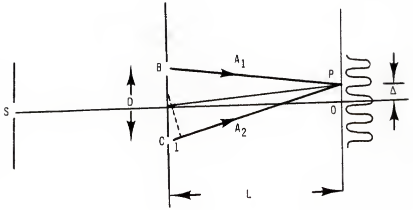

Figure 2.18 Young's experiment demonstrating optical diffraction. (Steward, 1983, adapted)

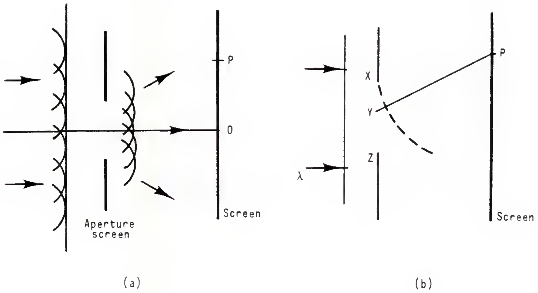

Figure 2.19 Huygen's wavelets spreading into geometrical shadow due to diffraction by an aperture. (Steward, 1983, adapted)

diffraction occurs. The wavelets passing through the aperture have a wavefront envelope that spreads into the region that would be unilluminated according to the ray theory of geometrical optics (pre-electromagnetic wave theory). Figure 2.19a can be considered as representing one of the apertures in Young's experiment. At any point, P, which is in the geometrical shadow region for direct ray optics, the illumination is the result of interference. The wavelets arriving there from all points across the aperture, arrive with different phases due to the different path lengths they have traveled. Figure 2.19b shows a wavefront leaving the aperture at position y and striking the screen at P. The diffraction pattern produced on the final screen is the result of interference between the light diffracted from various positions in the aperture. If the light source or final screen is sufficiently close to the aperture screen, the curvature of the wavefront becomes significant and the diffraction is known as near field or Fresnel diffraction. If the light source and final screen are at sufficient distance from the aperture screen the wavefront remains parallel and the diffraction is known as far field or Fraunhofer diffraction. The Fraunhofer diffraction is equivalent to the Fourier transform and is of primary interest for imaging analysis.

To demonstrate Fraunhofer diffraction a lens is used to focus the far field diffraction pattern to a focal plane. Figure 2.20 illustrates the Fraunhofer diffraction process as an intermediate step in image formation. If the diffracted light waves with wavelength λ leave the aperture screen at apertures B and C and pass through a lens, the pattern will be focused at the diffraction plane

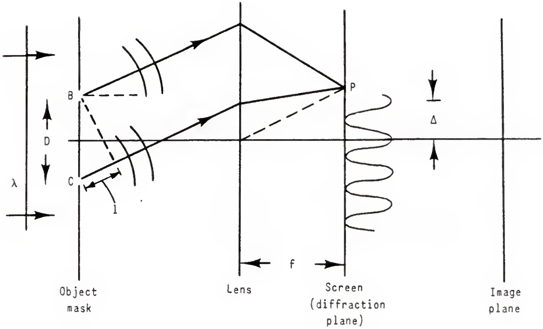

Figure 2.20 Diffraction an an intermediate step in image formation. (Steward, 1983, adapted)

at point P. A resulting pattern of light and dark areas with spacing will be formed due to the interference of the diffracted waves. If the waves are allowed to pass through another lens, an image will be formed at the image plane. Figure 2.21a shows a single-slit Fraunhofer diffraction pattern produced by light from a far source being diffracted by an aperture of width a. The diagram in 2.21b illustrates the aperture function f(x), which is a line profile description of the aperture shape.

Fraunhofer diffraction by a single slit will produce a pattern known as a sinc function as shown in Figure 2.22a. The amplitude of the pattern, given by $\frac{\sin \alpha}{\alpha}$ is shown on the left with horizontal axis units of wave displacement. The units listed on the second level below the horizontal axis are inverse distance or spatial frequency. The spatial frequency is in reciprocal space with units of 1/distance. The pattern in Figure 2.22b is the intensity plot of the sinc function and represents a photographic display of the amplitude squared. Photographic media and the eye are incapable of observing negative amplitudes and thus the intensity or amplitude squared is utilized for visualizing diffraction patterns. The amplitude squared is known as the Fourier transform power spectrum.

2.2.3 Optical Fourier Transform Analysis

The Fourier transform power spectrum provides a means for image characterization, recognition, and even manipulation. The manipulation often takes the form of image restoration by filtering the optical transform. A basic arrangement of optical components for coherent optical filtering is shown in Figure 2.23. The image formed

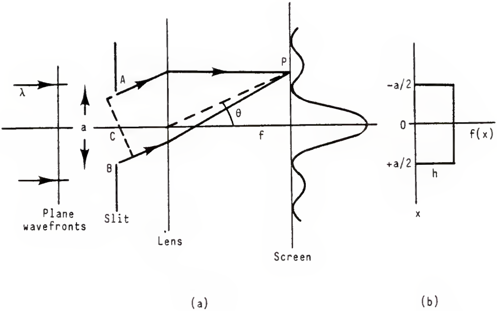

Figure 2.21 Single-slit parallel optic Fraunhofer diffraction. (Steward, 1983, adapted)

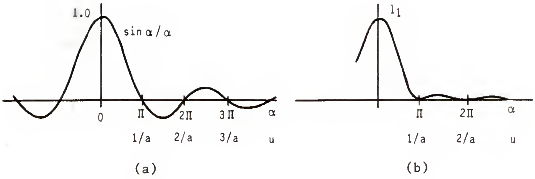

(a)

(b)

Figure 2.22 Single rectangular slit optical diffraction pattern displayed as, (a) amplitude (sinc function), and (b) intensity or amplitude squared. (Steward, 1983, adapted)

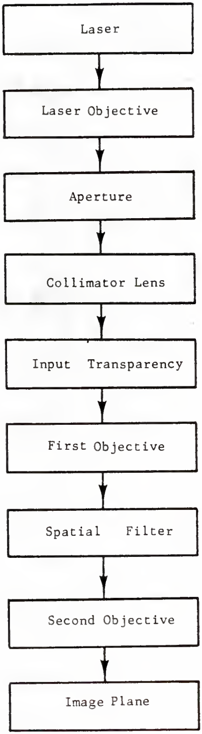

Figure 2.23 Optical Fourier transform image production. (Pincus, 1978, adapted)

at the diffraction plane is a spatial frequency representation of the image at the object plane. The frequency of two-dimensional repeat features in the object plane establishes the location of diffraction intensity spots in the diffraction plane. The input plane as shown in Figure 2.23 is in the form of an image transparency that transmits a complex amplitude f(x), similar to the aperture function. The transparency is illuminated at normal incidence with light from a laser and beam expander combination to produce plane wave coherent illumination. A diffraction image is produced at the diffraction plane and a restored image is produced at the image plane. The patterns produced are usually recorded photographically. The resulting pattern is dependent on the shape of the aperture used at the object plane and the features in the image transparency. The pattern produced is also two-dimensional, as opposed to the one-dimensional patterns previously illustrated.

A rectangular aperture and its corresponding optical Fourier transform power spectrum from Lendaris and Stanley (1970) are shown in Figure 2.24. The intensity of the transform along the direction corresponding to the width of the rectangle has an intensity form of $((\sin x)/x)^2$ and is the sinc function as previously shown. The sinc function is characteristic of diffraction by a single rectangular slit.

A circular aperture and resulting optical transform, known as an Airy pattern, are shown in Figure 2.25. The two-dimensional Fourier transform power spectrum preserves circular symmetry as shown by the expanding ring pattern. The pattern intensity has the form of a first-order Bessel function. The pattern is identical to the wave pattern produced by dropping an object into a body of water.

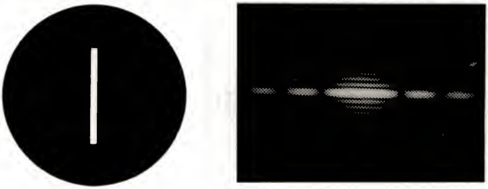

Figure 2.24 Rectangular aperture and resulting optical Fourier transform. (Lendaris and Stanley, 1970, with permission)

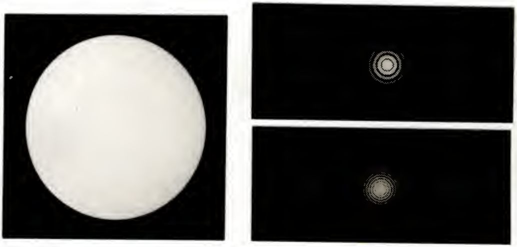

Figure 2.25 Circular aperture and resulting optical Fourier transforms for radius R (top) and radius 2R (bottom). (Lendaris and Stanley, 1970, with permission)

A typical optical Fourier transform power spectrum is shown in Figure 2.26 which was produced from an aerial photograph of a ship at sea. The transform pattern contains all the information in the aerial photograph but in a reciprocal space spatial frequency format. The repeat frequency of the wave structure is given by the elongated bands extending from the center spot or optical axis of the transform. The ship's wake is represented as the orthogonal spikes at the ends of the elongated bands. Thus, significant optical image characterization data is readily available and can be extracted from the optical Fourier transform image.

The optical Fourier transform spot pattern contains a complete description of the image. If noise is present, it may have unique spots in the pattern. Removal of the spots carrying the noise information will remove the noise from the reconstructed image. The removal of certain unwanted diffraction spots is known as spatial filtering. Figure 2.27 shows an optical instrument similar to the one shown in Figure 2.23, but with the addition of a spatial filter. If an optical image were obtained with a superimposed set of narrow parallel lines such as raster lines from a video monitor, the resulting Fourier transform power spectrum would contain extra spots corresponding to the noise. The spots would be located equidistant on either side of the optical axis and correspond to the parallel superimposed lines. If the spots were physically removed by blocking or filtering them with an opaque material, the resulting final image would be free of the parallel lines. This form of image reconstruction, filtering the Fourier transform, has been performed on high resolution electron micrographs to resolve periodicities by

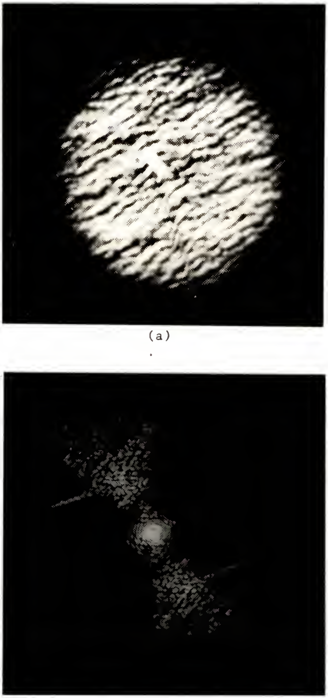

(a)

(b)

Figure 2.26 Typical optical Fourier transform produced by ship at sea (a) and resulting transform power spectrum (b). (Lendaris and Stanley, 1970, with permission)

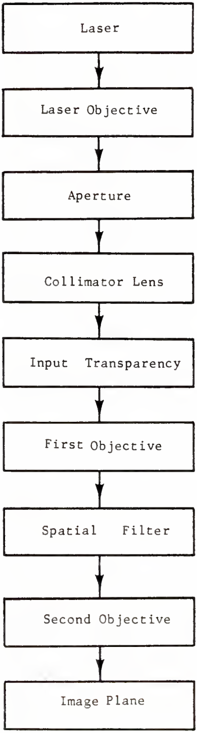

Figure 2.27 Optical Fourier transform filtering. (Pincus, 1978, adapted)

many investigators (Fitch and Holmes, 1967; Erickson and Klug, 1971; Moody, 1971). The filtering process may be applied to both the optical transform by physical filtering and to the digital transform by numerically inhibiting the unwanted spots.

2.2.4 Digital Fourier Transform Analysis

The digital Fourier transform to the nonuser may seem complex and abstract. However, its counterpart in nature is quite common. The previous sections have described the Fourier transform process in optical image formation. Another example of a natural Fourier transform process is the optical glass prism. As white light enters the prism a transform occurs and a spectrum of colors exit, separated into frequencies or wavelengths. The ear also performs a type of Fourier transform. Sound is complex, containing many superimposed frequencies. The ear (brain) decomposes the sound into specific frequencies so that separated tones, harmonies, overtones, etc. are heard. Examination of natural processes thus aids in comprehending the properties of the Fourier transform.

For phenomena that alternate with time or distance, a modeling process may be performed to simulate the changes. This is best done with the trigonometric sine or cosine function. Figure 2.28a shows that a cosine wave can be produced by tracking the perimeter of a rotating unit circle, (radius equals 1). As the circle is rotated counterclockwise and its amplitude is measured with time, a cosine wave is traced as in Figure 2.28b. If the angular position of a spot on the circle is tracked, then distance from an origin can be described by the phase angle or degrees of rotation from the origin.

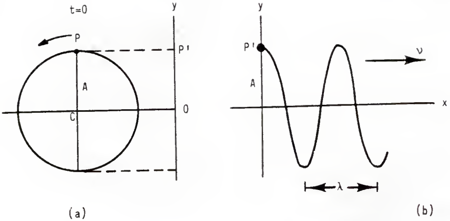

Figure 2.28 Scalar wave approximation of electromagnetic radiation. (Steward, 1983, adapted)

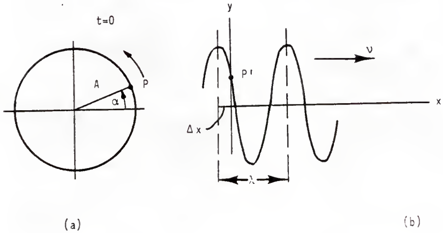

Figure 2.29 Scalar wave approximation of electromagnetic radiation with phase delay. (Steward, 1983, adapted)

Figure 2.29a shows a circle with a phase angle α that corresponds to a displacement of the cosine wave by ΔX in Figure 2.29b. If the cosine wave is shifted 90 degrees about the origin, a sine wave results. The cosine wave is 90 degrees ahead of the sine wave (90 degrees phase shift) but has the identical shape of the sine wave. The sine and cosine waves can thus be combined to produce a complex waveform.

The basic principle of Fourier waveform analysis is that arbitrary repeating signals can be expressed as the infinite sum of many sine waves of differing frequencies, amplitudes, and phase shifts. Figure 2.30 shows a Fourier representation of a periodic function f(x) as the combination of two distinct waves of differing frequency, amplitude, and phase shift. The combination of the two waves superimposes to produce the single wave shown at the top of the figure. The frequency components for analysis of infinitely repeating functions, such as these, are typically calculated with the Fourier series. Imaging analysis usually involves imperfectly repeating patterns so the Fourier transform must be utilized.

The basic equation for calculation of the one-dimensional Fourier transform, given by Steward (1983), is

$$f(x) = \int_{-\infty}^{\infty} F(u)\exp(2\pi iux)du \qquad (2.1)$$

and the inverse Fourier transform is

$$F(u) = \int_{-\infty}^{\infty} f(x)\exp(-2\pi iux)dx \qquad (2.2)$$

The function f(x) is spatial based and the function F(u) is frequency based. The product of u and x is dimensionless.

The two-dimensional continuous Fourier transform, given by Moik (1980), is

$$f(x,y) = \int_{-\infty}^{\infty}\int_{-\infty}^{\infty} F(u,v)\exp[2\pi i(ux+vy]dudv \qquad (2.3)$$

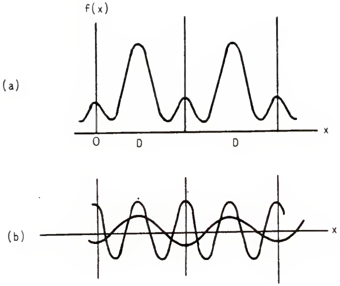

Figure 2.30 Fourier analysis of a complex function, f(x), in (a), resulting in separation of function into two cosine waves in (b). (Steward, 1983, adapted)

and the inverse Fourier transform is

$$F(u,v) = \int_{-\infty}^{\infty}\int_{-\infty}^{\infty} f(x,y)\exp[-2\pi i(ux+vy)]dxdy \qquad (2.4)$$

The exponential notation has a real component R(u,v) and an imaginary component I(u,v). The calculated transform used for visual display as a combination of the two in the form of the modulus squared is

$$|G(u,v)|^2 = R(u,v)^2 + I(u,v)^2 \qquad (2.5)$$

If the Fourier transform is to be calculated by digital computer, the transform must be performed in a stepwise manner and the discrete Fourier transform, given by Moik (1980), is used:

$$f(j,k) = \sum_{m=0}^{M-1}\sum_{n=0}^{N-1} F(m,n)\exp[2\pi i(\frac{jm}{M} + \frac{kn}{N})]$$

$$j = 0,1,\ldots\ldots\ldots M-1 \qquad (2.6)$$

$$k = 0,1,\ldots\ldots\ldots N-1$$

The inverse discrete Fourier transform is given as:

$$F(m,n) = \frac{1}{MN}\sum_{j=0}^{M-1}\sum_{k=0}^{N-1} f(j,k)\exp[-2\pi i(\frac{jm}{M} + \frac{kn}{N})]$$

$$m = 0,1,\ldots\ldots\ldots M-1 \qquad (2.7)$$

$$n = 0,1,\ldots\ldots\ldots N-1$$

These equations are implemented in an algorithm for computer calculation.

The Fourier transform has several features that make it extremely useful for image analysis which are due to the nature of the transform. The features describe the relationship between the input image and the resulting transform image and are summarized from Lendaris and Stanley (1970) as follows:

1. The Fraunhofer diffraction pattern of an aperture is equivalent to the two-dimensional optical or digital Fourier transform of the transmission function of that aperture.

2. The Fourier transform of any function is independent of translation of that function except for a linear phase factor.
3. The Fourier transform preserves rotation; if the input image is rotated, the Fourier transform is rotated about its optical axis and is otherwise unchanged. A constant directional relationship exists between the direction of repeat units in the input image and spot location in the transform.
4. The Fourier transform of a scan area is a spatial frequency representation. Since physical sensors such as the eye, film, photoelectric cells, etc., sense intensity and not simply the amplitude of light, the phase factor from sample translation disappears. Thus the Fourier transform as observed by these sensors is equivalent to the power spectrum of the scan area's transmission function. The modulus squared of the Fourier transform is useful for visualizing or measuring its features.
5. The center of the Fourier transform corresponds to a spatial frequency of zero. Any other point in the plane of the transform corresponds to a spatial frequency proportional to the distance from the point to the origin. The radial position of a point in the transform plane corresponds to the orientation of repeat features in the image plane. An intense low spatial frequency indication (close to the

center) in a given direction in the transform plane corresponds to an input pattern with a large repeat dimension in that direction. Similarly, an intense high-frequency indication (far from the optical axis of the transform) along a given direction in the transform plane corresponds to an input pattern with a small repeat dimension in that direction.

6. The modulus of the Fourier transform is symmetric with respect to the origin; every spot in the transform plane has an identical counterpart which is located on the same radial direction line, on the opposite side of the optical axis, and the same distance from the origin.

Distinct patterns in the image plane produce distinct patterns in the Fourier transform frequency plane. Figure 2.31a shows a rectangular function and its corresponding Fourier transform, a sinc function. If the Fourier transform is taken on the complete sinc function, the initial rectangular function is restored as in Figure 2.31b. Figure 2.32 shows several patterns and their resulting Fourier transform in the frequency domain. The single spike, or delta function, in Figure 2.32a results in a horizontal line extending in both directions to infinity. A square wave in Figure 2.32b results in a sinc function. Uniformly spaced delta functions in Figure 2.32c result in uniformly spaced lines with a reciprocal spacing of 1/d. Uniformly spaced square waves in Figure 2.32d result in a sinc function. A cosine wave in Figure 2.32e results in a single frequency, or a dual spikes. The double spike is due to the symmetry principle of the Fourier transform. The three input

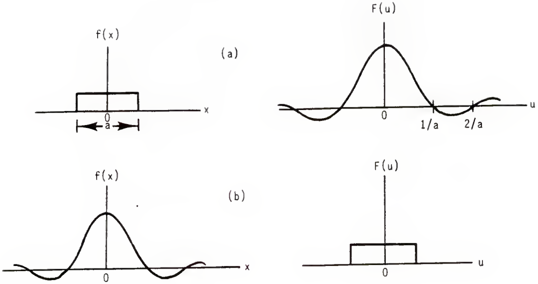

Figure 2.31 Fourier transform pairs, f(x) and F(u).
(Steward, 1983, adapted)

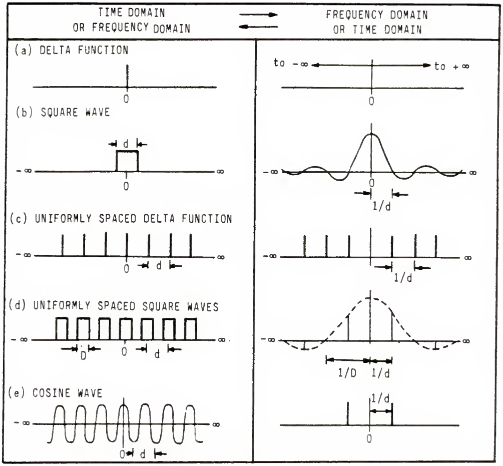

Figure 2.32 Fourier transform pairs. The left column shows the input function and the right column shows the transformed function. (Peterson and Dobrin, 1966, adapted)

functions in Figure 2.32 (c), (d), and (e) have the same fundamental frequency (d) as revealed by the identical transform spacing 1/d.

In order to perform the Fourier transform on a set of repeat features, a finite number of features must be selected for evaluation. This is done by a process called windowing, with all data outside the window assumed to be zero. The process of windowing, as illustrated in Figure 2.33, is essentially the multiplication of the window and the input data in the spatial domain. The Fourier transform of the windowed function is the convolution of the Fourier transform of the input function and the Fourier transform of the window. Figure 2.34 shows a set of delta functions f(x) to be convolved by a rectangular function g(x). The result of the convolution is a set of rectangular functions, h(x), with features due to both the delta function and the rectangular window. Convolution in this case has the effect of modifying the original data by the window used to examine the data. Therefore the selection of the window used to isolate a given set of data from the whole data for the Fourier transform calculation is extremely critical. Convolution may be mathematically described as

$$h(x) = \int_{-\infty}^{\infty} f(u)g(x-u)du \qquad (2.8)$$

Other names for convolution are folding product, Faltung, composition product and superposition integral. The Fourier transform of the window function, g(x), is known as a smoothing or blurring function, line spread function, and in two dimensions the point spread function.

Figure 2.35 (left) shows three sets of functions, a rectangular window used to isolate portions of each function and the

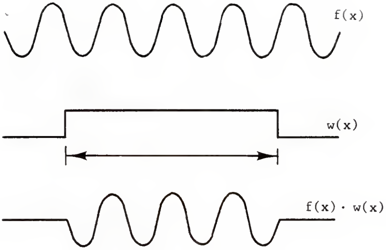

Figure 2.33 The windowing of a semi-infinite wave pattern f(x), by a rectangular window, w(x) resulting in the windowed function f(x)•w(x). (Bergland, 1969, adapted)

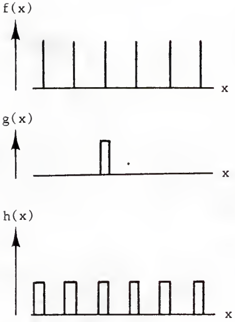

Figure 2.34 The convolution of an input function, f(x), and a window function, g(x), resulting in the convolved function, h(x). (Steward, 1983, adapted)

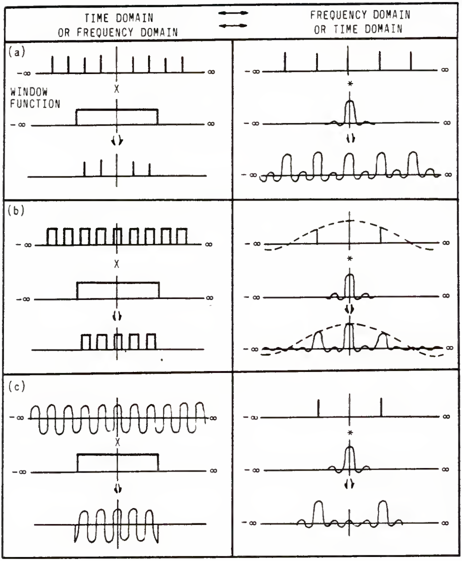

Figure 2.35 Fourier transform patterns of windowed functions. The input function, the rectangular window and the windowed function are shown on the left. The theoretical transform, the window transform convolution are shown on the right. (Peterson and Dobrin, 1966, adapted)

rectangularly windowed form of each of the functions. Figure 2.35 (right) shows the Fourier transform of each step. In Figure 2.35a (right) the five frequency spikes convolved with the sinc function from the rectangular window, results in a set of five sinc functions with the same spacing as the frequency spikes. Figure 2.35b shows a similar process that results in the formation of multiple sinc functions. Figure 2.35c shows two frequency spikes convolved with the single sinc function from the window to produce two sinc functions. The resulting transforms now reflect both the shape of the input function and the shape of the window function and demonstrate that convolution in the frequency domain corresponds to multiplication in the spatial domain. The final transform in each case takes on features of both the input data and the rectangular window. Again, window selection is extremely critical in digital Fourier transform imaging analysis because window selection controls the appearance of the final transform product.

Fourier transform analysis by digital computer has been extensively reviewed by Bergland (1969) who demonstrated its usefulness for characterizing linear systems and for identifying the frequency components of continuous waveforms. When a waveform is to be analyzed by a computer, the finite or discrete version of the Fourier transform (DFT) must be used. Most properties of the continuous Fourier transform (CFT) are retained, but the differences that result are due to the fact that the DFT must operate on a sampled waveform that is defined over a finite interval. The fast Fourier transform (FFT) is simply an algorithm for computing the DFT. The FFT can replace the continuous Fourier transform only to the extent that the DFT can, but with the benefit of substantial reduction in processing time. The first formally reported FFT algorithm was developed by Good (1958). However, the FFT was brought into prominence by Cooley and Tukey (1965). The Cooley-Tukey fast Fourier transform software has become widespread and it is readily available for a number of computer systems. Alternate techniques for calculating the fast Fourier transform have been reported (Bergland, 1967, 1968a, 1968b, 1969; Brenner, 1967; Cooley, 1966a, 1966b; Pease, 1968; Yarne, 1968). However, the Cooley-Tukey FFT algorithm remains the most widely accepted and used algorithm.

The evolution of the Fourier transform has progressed in the past 25 years from hand calculation, to large digital computers calculating the discrete Fourier transform to implementation of high speed algorithms such as the Cooley-Tukey to implementation of the routines for minicomputers, and to development of high speed array processors for hardware processing of the Fourier transform. The Digital processing of the Fourier transform has resulted in two often encountered problems: aliasing and leakage. The discrete Fourier transform is applied in numerical analysis because it approximates the continuous Fourier transform and its calculation is straightforward. However, the process of windowing and sampling the data to be analyzed can result in a misleading analysis. In Figure 2.36 the effect of windowing and sampling of a cosine waveform is shown. The analysis, however, can be applied to any function expressed as a sum of sine and cosine waves. Figure 2.36a shows the input signal, s(x) and its continuous Fourier transform that consists of two impulse frequency functions symmetric about the zero frequency

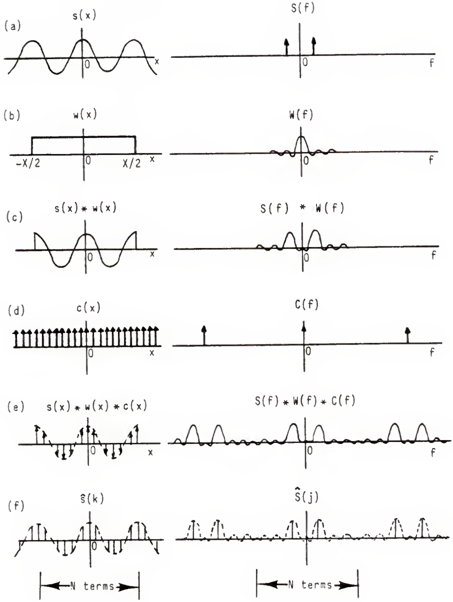

Figure 2.36 The effects of windowing and digital sampling on the Fourier transform of a continuous cosine wave pattern. (Bergland, 1969, adapted)

axis. In order to analyze the continuous function s(x), a sample must be extracted through a data window of unity amplitude shown in Figure 2.36b. The rectangular window has a continuous Fourier transform which is in the form of the sinc function, as previously shown. The extracted position of initial waveform s(x) that is to be analyzed is shown as the product of the whole data s(x) and the window w(x) in Figure 2.36c, left. The corresponding product or convolution in the frequency domain results in a blurring of the Fourier transform into two sinc function pulses as shown in Figure 2.36c, right. Thus the display of S(f) as two distinct spikes is now seriously corrupted so that the spikes appear as wider peaks. In order to perform a digital analysis, the windowed data must be sampled to obtain discrete values. This process is equivalent to multiplying the sampling function c(x), which is a finite train of pulses, as shown in Figure 2.36d, left, with the windowed portion of the curve in Figure 2.36c, left. The windowed and sampled input function is shown in Figure 2.36e, left, as the function product, $s(x)*w(x)*c(x)$. The resulting Fourier transform consists of multiple sets of sinc function peaks separated by low amplitude ripples. The transform has the features of the window and the sampled function. By considering N terms of the sampled function as in Figure 2.36f, left, a Fourier transform analysis of the N terms results in the limited frequency domain area of N terms in Figure 2.36f, right. Thus the discrete Fourier transform is simply a reversible mapping of N terms of $\hat{S}(k)$ from the distance domain into N terms of $\hat{S}(j)$ in the frequency domain.

The illustration given in Figure 2.36f yields a very accurate representation of the continuous transform by the discrete transform because the sampling was performed at exactly the peaks and valleys of the original windowed function. The sampled data resulted in a perfect resemblance of the original data. If the sampling were at intermediate points, the coarseness of the sampling would have led to a false representation of the data and an erroneous transform. This undersampling, known as aliasing, results in a high frequency function appearing to be a low frequency function, as shown schematically in Figure 2.37. A uniform sampling rate results in a smooth function with no clue that the original sampled function was a high frequency function. To avoid aliasing, the sampling rate must be high enough for the highest frequency present to be sampled at least twice during each cycle. This is described by the sampling theorem (Elliott and Rao, 1982) which states that if a signal is sampled at two times its highest frequency sinusoidal, then the signal can be completely reconstructed. The sampling frequency, fs, then is two times the highest frequency component. The folding frequency, f_f, also known as the Nyquist frequency, is equal to half the sampling frequency, or fs/2. For a given input function, sampling will be correct if its highest frequency component is any value less than the folding frequency f_f or fs/2. A time based frequency 5Hz higher than the folding frequency will impersonate a frequency 5Hz lower than the folding frequency. Any frequency components higher than the folding frequency are aliased (or folded) into the frequency range equidistant below the folding frequency. To avoid aliasing, the signal must either be sampled at twice the

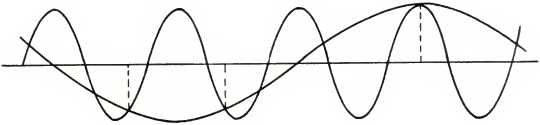

Figure 2.37 The phenomena of aliasing as shown by a low frequency sine wave resulting from undersampling a higher frequency sine wave. (Bergland, 1969, adapted)

highest frequency component as stated previously or if the frequencies can be restricted by filtering a sampling rate may be selected accordingly. Thus, analog filtering may be used to eliminate high frequency components allowing a sampling frequency to be selected that is twice the filter cutoff point.

The other source of error, leakage, is inherent in the Fourier analysis of any finite set of data. The set is established by windowing an actual signal over a fixed distance and by neglecting everything outside that windowed region. As previously stated, this is equivalent to multiplying the signal by a rectangular data window of unity value. If an unwindowed cosine waveform is processed by the continuous Fourier transform, the result would be a single spike on the frequency axis as shown in Figure 2.38. The data must, however, be windowed and the Fourier transform of the window, if rectangular, is the sinc function. The multiplication of the input signal by the data window in the distance domain is equivalent to performing a convolution of the frequency domain of the single spike and the sinc function, resulting in a sinc function centered about the zero frequency. The sinc function has a wide central peak and a series of sidelobes which decrease from the central peak. This spreading may be considered as "leakage". The usual correction for leakage consists of applying a data window whose transform has lower sidelobes in the frequency domain than the rectangular data window. Numerous data windows have been evaluated and typically involve some technique of smoothing the sharp sides of the window. A common window, as shown in Figure 2.39, is the extended cosine-bell. A

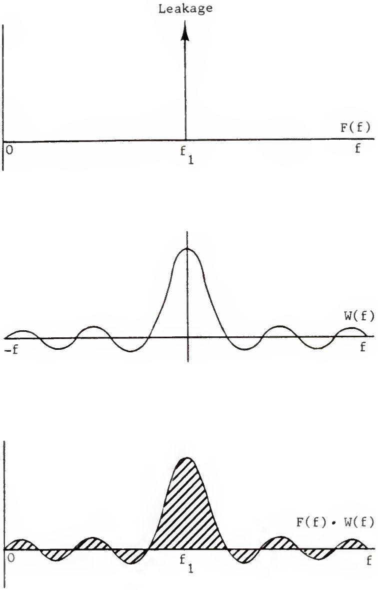

Figure 2.38 The phenomena of leakage that results from convolving a single input frequency, F(f), with a window function, w(f), to produce a product F(f) W(f). The information in the central spike of F(f) is spread (leaked) into the sidelobes of F(f) W(f). (Bergland, 1969, adapted)

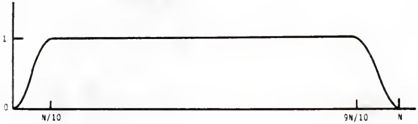

Figure 2.39 Extended cosine bell data window used to minimize leakage caused by windowing. (Bergland, 1969, adapted)

raised cosine wave is applied to all but the first and last 10 percent of the data.

2.2.5 Fourier Transform Image Characterization

The optical and digital Fourier transform has tremendous power for analysis and characterization of all types of images. Pincus (1978) was interested in geological microstructures and analyzed microscope images by use of the optical Fourier transform using micrograph negatives and directly through a modified microscope. To analyze the effects of grain elongation he prepared three arrangements of rhombic stacked ovals as shown in Figure 2.40. (These patterns are very similar to those observed for dimple rupture fracture, with and without shear present.) The associated optical Fourier transform power spectra are also shown in Figure 2.40. The uniform stacking of circles resulted in a uniform transform with no directionality. The vertical elongation of ovals resulted in a horizontal spread in the transform. The horizontal elongation of ovals resulted in a vertical spread in the transform. By use of a calibration grid and its transform, the spot spacing from the ovals were directly correlated to the average diameter of the ovals. The spot patterns were a result of equal sized ovals in the input image. Figure 2.41 shows three distinct patterns that model geological structures and their associated transforms produced by Power (1973). Figure 2.41 (a) and (b) show idealized drainage patterns. (Figure 2.41a is very similar to cleavage river patterns.) Figure 2.41c, which has a variable gray scale, depicts a rock surface. The Fourier transform power spectra for Figure 2.41a indicated the presence of

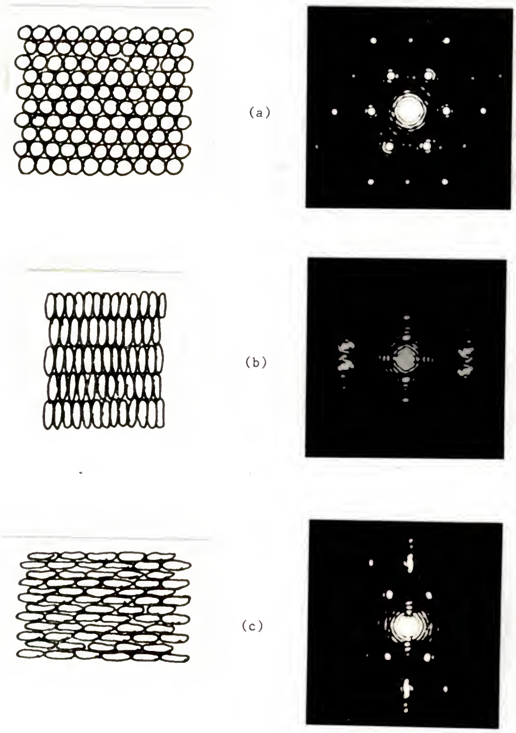

Figure 2.40 Theoretical models of equiaxed and elongated ovals and resulting optical Fourier transform power spectra. (Pincus, 1969, with permission)

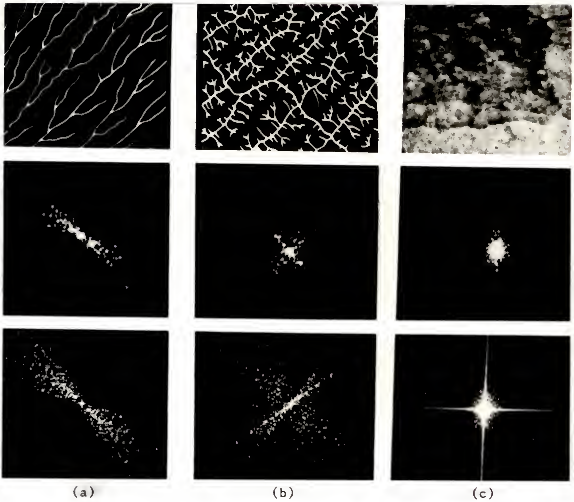

Figure 2.41 Geological structure input patterns and resulting optical Fourier transform power spectra. Middle spectra are microtransforms produced directly in microscope. Bottom spectra are macrotransforms produced from transparencies. (Power, 1975)

parallel lines in one diagonal direction in the input image which established the linear spatial frequency pattern. Line branching in the input image resulted in the spread of the transform pattern. The transform power spectrum in Figure 2.41b showed the presence of dominant lines in two diagonal directions in the input image which produced perpendicular lines in the transform. The transform in Figure 2.41c displayed less directionality but still detected the presence of some banding in the input image. The cross in the macrotransform was a two-dimensional sinc function due to a rectangular aperture.

Pincus (1978) also performed optical Fourier transform analysis on geological microstructures using the optical microscope and optical bench techniques as shown in Figure 2.42. As the magnification of the input image was increased, the image became coarser and the Fourier transform power spectrum shrank. Pincus was able to detect preferred orientation in the microstructure, deformation effects, particle shapes and other features. His work demonstrated the feasibility of use of the Fourier transform to characterize microscopic features.

Lendaris and Stanley (1970) applied a similar approach of optical Fourier transform analysis to aerial photographs for image characterization. Figure 2.43a shows a circular windowed natural terrain on the left and its optical Fourier transform power spectrum on the right. The transform shows essentially a random structure. Figure 2.43b shows an orchard with two-dimensional regularity and image rotation with respect to the horizontal. The transform shows a

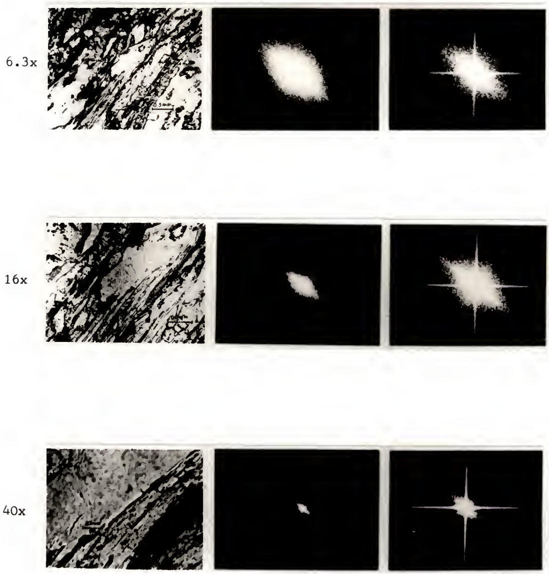

Figure 2.42 Geological microstructures at three magnifications and resulting macro- and micro-optical Fourier transforms. (Pincus, 1970, with permission)

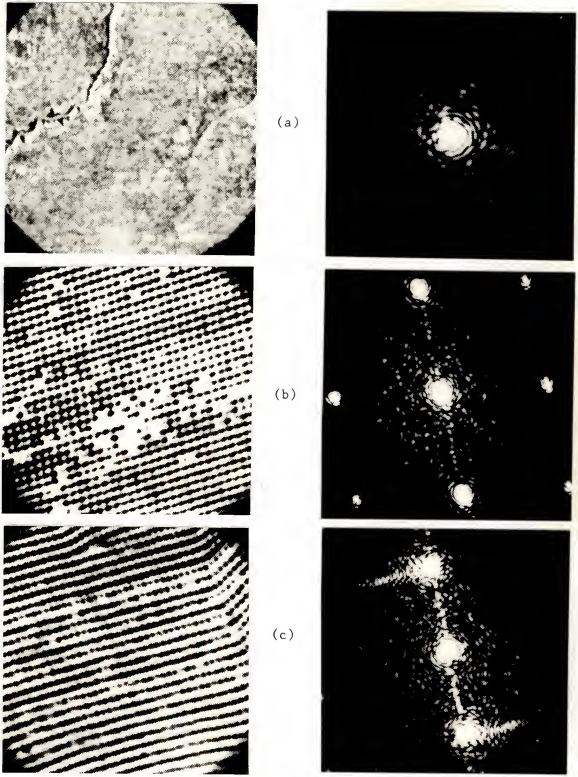

Figure 2.43 Aerial photographs and optical Fourier transform spectra of (a) natural terrain, (b) an orchard and (c) an orchard on a hillside. (Lendaris and Stanley, 1970, with permission)

spot pattern and illustrates the rotation present in the windowed image. Figure 2.43c shows an orchard on a hillside with curvature on the parallel lines. The resulting transform has perpendicular smears due to the input image line curvature.

Lendaris and Stanley (1970) found that the process of obtaining the Fourier transform of a windowed image greatly simplified the pattern characterization process. The transforms displayed patterns that were representative of certain type structures. By sectioning or sampling the two-dimensional Fourier transform power spectrum, the pattern classification process was simplified. The Fourier transform decomposes the image into basic building block patterns (primatives) with the contribution of each centered on the optical axis of the transform, no matter where the pattern is located within the scan area. The optical axis thus provides the reference point for evaluation of the transform. A windowed image alone will not possess such a reference point. Because of the building block and centering properties of the two dimensional transform, sampling geometries can be developed which are rotation invariant, size invariant, or both. The ultimate purpose of the sampling is to reduce the transform into a smaller set of numbers which becomes a sample signature. The sampling is especially useful for revealing linear features, and one- and two-dimensional periodicity.

Lendaris and Stanley (1970) developed several sampling patterns as shown in Figure 2.44. They were using optical transforms so the sampling consisted of measuring the light intensity in a given region of the transform. The sampling pattern shown in Figure 2.44a is a set of annular rings which sample the transform periodically at a

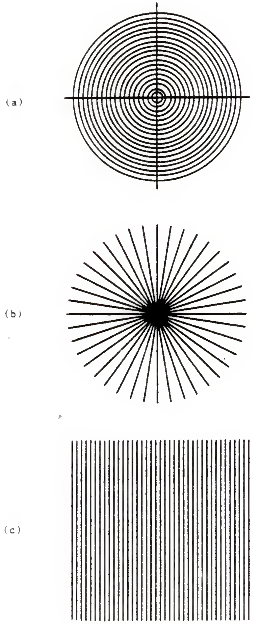

Figure 2.44 Sampling patterns for evaluating Fourier transform power spectra; (a) annular ring, (b) wedge, (c) parallel-slit. (Lendaris and Stanley, 1970, adapted)

given radial distance from the optical axis. Because a given point in the transform frequency plane represents a spatial frequency in the image, the radial sampling pattern emphasizes the spatial frequency content. The periodic radial sampling over a given finite distance tends to reduce the effects of minor variations caused by image noise. Figures 2.45a and 2.45b show images with one- and two-dimensional repeat frequencies. (Figure 2.45a is similar to fatigue striations and Figure 2.45b is similar to dimple rupture fracture.) The associated transforms are shown in Figures 2.45c and 2.45d. Figures 2.45e and 2.45f show radial plots from annular ring sampling of the two transforms. The input image on the left in Figure 2.45a has one-dimensional periodicity composed of parallel lines which results in a transform with two symmetric spatial frequency spots. The radial plot in Figure 2.45e shows a predominant outer spike which corresponds to the spots in the transform pattern. The input image on the right in Figure 2.45b shows two-dimensional periodicity composed of a two-dimensional array of spots. Its transform in Figure 2.45d is a symmetric array of spots located about the optical axis. Its radial plot, Figure 2.45f, produces spikes at the location of the primary spots. Figures 2.45g and 2.45h show the result of sampling the same two transforms with a wedge shaped sampling device, Figure 2.44b. The wedge sampling requires that any point in the transform frequency plane correspond to a direction in the image plane. That direction can be determined by drawing a radius vector from the origin to the point in the frequency plane. A radial line in the transform corresponds to a single direction in the image and includes all frequencies. Thus by integrating all the

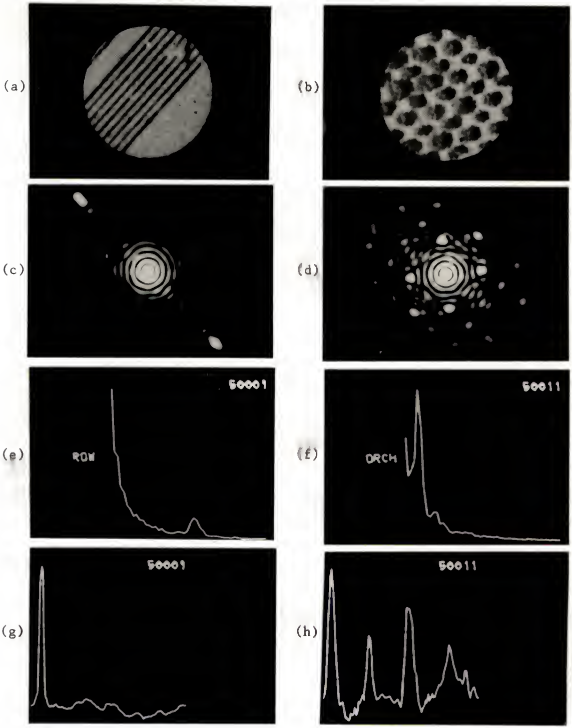

Figure 2.45 Circular window aerial photographs of (a) one-dimensional and, (b) two-dimensional structure. Optical Fourier transform spectra are shown in (b) and (c) with radial sampling in (e) and (f) and wedge sampling in (g) and (h). (Lendaris and Stanley, 1970, with permission)

intensity in a given radial wedge, the total contribution from a given direction in the input image is obtained, independent of frequency or object size. For the transforms in Figures 2.45c and 2.45d, wedge sampling geometry is especially useful for distinguishing one-dimensional regularity from two-dimensional regularity, as shown in Figures 2.45g and 2.45h. The radial plot is thus used to detect regularity and the wedge plot shows principle directions. Another approach to transform sampling is shown in Figure 2.44c, a parallel-slit sampling geometry. A frequency profile is produced along any desired direction by placing a small slit aperture at or near the origin and moving it along the desired direction.

Lendaris and Stanley (1970) showed that the Fourier transform provides not only a means for detecting regularity, but also a means for obtaining quantitative dimensional information about an image. If an array of objects is present in the input image, it provides information about the lattice-like properties of the array, which is useful in pattern classification. Figure 2.46 shows a collection of parked aircraft and their associated transform. The radial plot signatures of the transform were sampled with coarse rings and fine rings, resulting in a number of localized peaks. The relative peak spacing in the sampled transform indicated aircraft engine nacelle separation, wing-to-horizontal stabilizer separation, and wing and horizontal stabilizer lengths all useful for aircraft classification. The use of annular ring sampling (radial plot) made the dimensional information independent of the orientation or position of the parked aircraft and made the transform sampling useful for both object

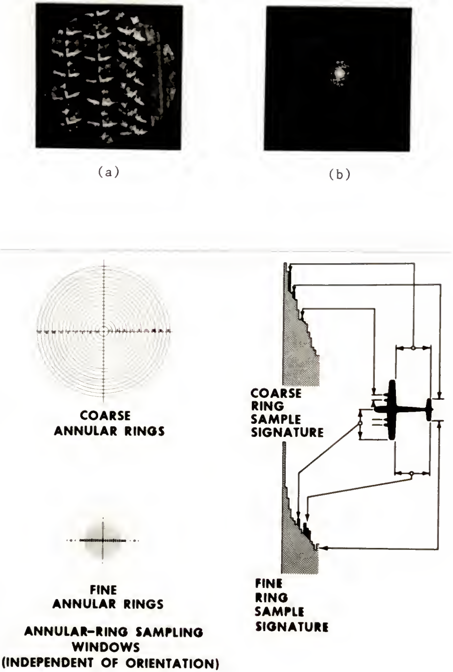
(a) (b)

(c)

Figure 2.46 Aerial photograph of aircraft on runway (a), resulting optical Fourier transform power spectrum (b), and sampled spectrum (c). (Lendaris and Stanley, 1970, with permission)

detection and object identification. Lendaris and Stanley were thus able to use aerial photographs, which were two-dimensional projections of three-dimensional objects and perform pattern classification and characterization by use of the sampled Fourier transform.

The Fourier transforms shown to this point were obtained by optical means. Figure 2.47a shows a satellite image with superimposed parallel noise lines. Its digital Fourier transform is shown in Figure 2.47b. The vertical row of spots represents the horizontal lines on the input image. If the spots are numerically removed and the inverse digital Fourier transform is calculated, the resulting image is noise free as shown in Figure 2.47c. There are no significant differences between Fourier transform power spectra produced optically or digitally. The optical process is faster, but an appropriate optical bench is not as readily available as digital computers and fast Fourier transform algorithms. The sampling processes for simplification of the transform are also more easily performed digitally. The analysis of the fracture surfaces in this work was therefore performed digitally.

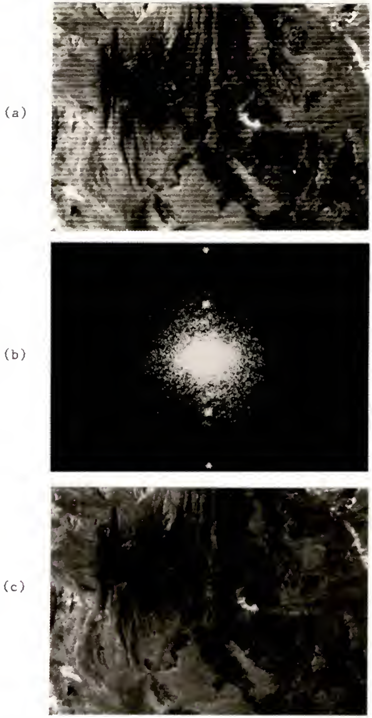

Figure 2.47 (a) Satellite image of earth with superimposed noise, (b) digital Fourier transform power spectrum of noisy image and (c) reconstructed image with spots in power spectrum removed. (Moik, 1980, with permission)

CHAPTER 3

EXPERIMENTAL PROCEDURE

3.1 Fractograph Generation and Calibration

Fractographic investigations usually employ the scanning electron microscope (SEM) for fracture surface analysis. The SEM has as its advantage a wide range of magnifications, as shown in Figure 3.1, compared to other microscopic tools used for fracture surface analysis. It also has the ability to examine the actual fracture surface and to produce a three-dimensional appearing image which aids in fractographic interpretation. The SEM was selected as the instrument to produce the fractographs used in this work. Instrument variables were evaluated and carefully controlled to allow comparison of fractographs.

Fractures used in the investigation were primarily from Navy helicopters and jets. The fractures could have been laboratory generated but duplication of exact field conditions would have been questionable. Additional theoretical fractographic models were computer generated to produce simplified cases of fracture features.

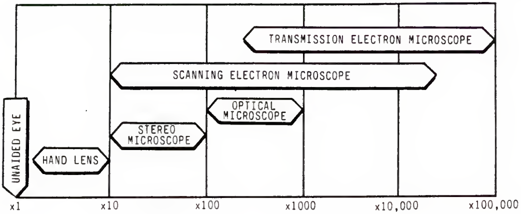

Figure 3.1 Approximate ranges of magnification for imaging instruments used in fractography. (Ewalds and Wanhill, 1984, adapted)

3.1.1 Scanning Electron Microscopy

The function and operation variable effects of the SEM must be considered to produce optimum images for digital fractographic analysis. Numerous authors have described the scanning electron microscope: Murr (1970), Wells (1974), Goldstein et al. (1975), Goldstein et al. (1981), and Murr (1982).

The principles of operation of the SEM as described by Bowen and Hall (1975) concern primarily the mechanics of scanning an electron beam over the surface of a specimen point by point and monitoring the results. As the fine high energy electron beam is focused to a point on the specimen, electrons are emitted from the material. The emitted electrons are collected and amplified to produce an electrical signal. The signal is used to modulate the intensity of a beam of electrons in the view and record cathode ray tubes (CRT). The scan raster applied to the beam interacting with the specimen surface is identical to the raster applied to the CRT's. Thus a point of high emission on the specimen surface corresponds to a bright spot on the CRT. Magnification is controlled by the area of beam scan and is usually variable from 20X to 100,000X. Resolution in the SEM is defined as resolvable edge to edge separation of two points on a specimen surface and is much more important than magnification. Ultimate resolution in the SEM is typically 5 nm (50 Å), compared to 300 nm for an optical microscope. Resolution in the SEM depends critically on the nature of the specimen surface and the mode of operation of the instrument.

Specimen preparation for a conducting material is relatively simple for the SEM. A careful cleaning is usually the only requirement. Electrically insulating materials accumulate charge from the primary electron beam which deflects the incident beam and emitted electrons, resulting in a grossly distorted image. Charging may be eliminated either by using a reduced accelerating potential or by coating the specimen surface with a thin layer of conducting material such as gold or carbon.

The application of the SEM is primarily in a range of magnifications between the optical microscope and the transmission electron microscope. The SEM is useful for relatively rough surfaces such as produced by fracture, but not so useful for examination of flat or polished surfaces. Because actual specimens are used instead of replicas, as in the transmission electron microscope, the imaging process is much simpler. Imaged specimen features are easily related to specimen geometry.

The design and construction of a typical SEM is shown in Figure 3.2. The essential components are:

(a) An electron gun to produce a narrow beam of electrons accelerated through a potential of up to about 50KV,

(b) Two or three lenses to focus the electron beam as finely as possible,

(c) A system to deflect the beam through a raster over the specimen surface,

(d) A specimen stage permitting lateral movement, tilt, and rotation of the specimen,

(e) A collector and amplifier for the emitted electrons,

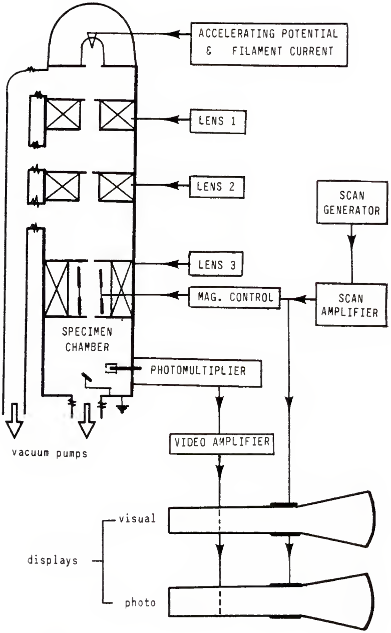

Figure 3.2 Schematic diagram of a scanning electron microscope. (Bowen and Hall, 1975, adapted)

(f) Cathode-ray-tubes to display the image,

(g) Electronic circuits to supply and control the electron gun, accelerating voltage, lens current, scan generator, and signal amplifier, and

(h) A high capacity vacuum system to maintain pressures below 10E-5 torr and permit rapid evacuation of the specimen chamber.

There are a number of factors in the SEM which affect image quality and thus the results obtained in the Fourier transform frequency analysis. Those factors are listed as follows:

(1) Accelerating Voltage. A high accelerating voltage gives improved resolution, but a tradeoff exists due to other imaging effects. The higher accelerating voltage also leads to loss of detailed information about surface structure due to beam penetration and unnecessary subsurface generated signals. A high operating voltage causes larger emission of electrons from edges on the specimen surface. This improves the image for frequency component analysis unless the effect is so severe that image detail is lost. Higher operating voltages also cause greater possibility of specimen charging, and greater specimen damage by the electron beam. A relatively high operating voltage, 20-30KV, is typically used in fractography of metal fractures. In general, any minor loss of surface detail from a higher operating voltage results in a form of analog filtering. This limits the high spatial frequency components in the image and helps prevent aliasing in the digital sampling process. Specimen charging is not a serious problem at the 20KV operating voltage for clean metal specimens; metal specimens typically undergo no beam damage at 20KV.

(2) Probe Current. The current in the electron beam is controlled by the condenser lens. For high resolution a large condenser lens current is required, leading to a small beam current and spot size. However, small beam currents result in poor signal-to-noise ratios and reduced contrast. The poor signal-to-noise ratio tends to increase the high frequency image components in the form of noise. Reduced contrast inhibits the detectability of a given spatial image frequency in the Fourier transform processing. A relatively high condenser lens current setting is commonly used for producing fractographs that balance high resolution with minimal noise.

(3) Focal Depth. The focal depth becomes important in electron fractography when the fracture surface has extreme peak to valley ratios. Extreme parts of the image may be out of focus if the focal depth is not correct. The depth of focus is controlled by a combination of final aperture size and working distance. A final aperture size of 200 μm and a working distance of 11 mm typically produces satisfactory fractographs. If surface peaks or valleys in the image become defocused due to limited depth of focus, the effect is loss of high frequency components in the area. The result will not be deleterious to the Fourier transform if there are other areas in the image with the same high frequency components present. The loss of some of the high frequency only reduces the amplitude of the transform for that frequency.

(4) Astigmatism. Astigmatism causes a loss of image sharpness and directional distortion. It becomes more critical at high magnifications, above 5,000X, and is corrected by proper adjustment

of the astigmatism phase and amplitude controls. Astigmatism can be critical in Fourier transform image analysis because of defocusing effects, causing loss of all high frequency components, and because of linear distortion which produces directionality in the Fourier transform.

(5) Contrast and Brightness. The contrast and brightness in fractography are typically adjusted subjectively to produce the best quality image. Excessive brightness or darkness will cause loss of image detail in the fractograph. Excessive high or low contrast produces the same result on the Fourier transform, loss of spatial frequency components from the regions affected. If sufficient unaffected representative regions are still present in the input image the only effect will be loss of amplitude for the affected frequencies in the transform. Most SEM's offer techniques for reproducibly setting the image contrast and brightness. Once the levels are established for producing a high quality image then all following fractographs will have suitable exposures.

(6) External Disturbances. Two types of external disturbances typically affect the SEM; mechanical vibration and magnetic fields. Mechanical vibration produces horizontal lines on the fractograph that are particularly noticeable at specimen edges, but do not usually appear below 20,000X. Magnetic fields cause nonuniform image smearing and distortion. Both disturbances are dependent on instrument and facility design. Residual magnetism in a specimen may also cause image distortion. The problem is corrected by proper demagnetism of the specimen. External disturbances are not a problem for a high quality and properly installed SEM. However, if not

properly corrected, vibration and magnetic fields will introduce defects into a fractograph that will be detected by the Fourier transform analysis and result in a false frequency component analysis.

(7) Image Distortion. The most common type of image distortion is due to specimen tilt which results in foreshortening. Tilt is usually required to improve emission from a sample. Increasing tilt decreases beam penetration and generation of subsurface signals. However, the tilt causes linear dimensions in the direction of tilt to become shortened. The result is that squares begin to appear as rectangles. The distortion can be corrected electronically by amplification of one orthogonal image direction more than another. It can also be corrected by using a zero tilt on the specimen stage. However, higher magnification fractographs become difficult to produce because of beam-specimen interaction. At magnifications typically under 5,000X, a zero tilt specimen has no loss of image detail. The effects of linear distortion on the Fourier transform are extremely critical, making the use of zero tilt or some form of tilt correction imperative.

(8) Beam-Aperture Alignment. Beam alignment affects the number of electrons passed down the SEM column to the specimen surface. Improper beam alignment results in decreased signal-to-noise ratio. Objective lens aperture alignment controls the sharpness of the fractograph image. Proper alignment of the electron beam and objective aperture allows for the best signal-to-noise ratio and image sharpness, assuming other instrument variables are properly set. If the signal-to-noise ratio is degraded, the image becomes

noisier and the Fourier transform will detect the false high frequency components from the noise. If the image sharpness is degraded, high frequency components in the specimen will not appear in the image and a false Fourier transform will result. The same result will exist from improper focusing.

The test of proper SEM instrument settings and external conditions is the quality of the fractograph produced. Any distortion that has occurred will be visible in the fractograph, and if distortion or image defects are present, then the image is unsuitable for Fourier transform imaging analysis.

3.1.2 Instrumental Variable Analysis

The SEM micrographs produced in this work were made on an Etec Omniscan Scanning electron microscope at the Naval Air Rework Facility, Pensacola, Florida. The instrument is routinely used for fractography and is capable of producing high quality electron micrographs at magnifications ranging from 10X to 20,000X. The instrumental variables controlling image quality and digital imaging analysis were evaluated by production of SEM micrographs with operating parameter variations. A gold test grid was selected as a specimen because the repeat units in the grid produce a known Fourier transform pattern. Figure 3.3 shows the test grid at two magnifications, 75X and 250X. The micrographs were produced at instrument settings routinely used to generate high quality fractographs from aircraft failures. The instrument settings were adjusted to preclude the problems discussed in the previous section. An accelerating voltage of 20KV was selected because it produces an

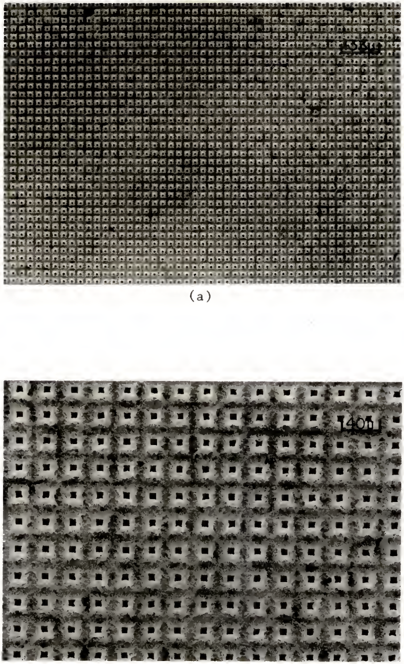

(a)

(b)

Figure 3.3 Scanning electron micrographs of gold test grid at (a) 75X and (b) 250X.

optimum image in scanning electron fractography. The signal-to-noise ratio was acceptable because the operating voltage was sufficiently high. Surface image detail was not lost because the beam penetration was not excessive from too high an operating voltage. The probe current was set for production of high resolution micrographs, without obvious noise. The focal depth was set by an objective aperture size of 200 m and a working distance of 11 mm. The aperture size was one that was routinely used in fractography with the Etec Omniscan and one that produced an optimum balance of beam size and focal distance. The working distance of 11 mm was an optimum setting for magnifications of up to about 5,000X with the Omniscan. The aperture-working distance combination resulted in adequate depth of focus. The astigmatism was adjusted to produce maximum image sharpness and minimum distortion. The contrast and brightness were adjusted to produce an optically pleasing micrograph. Good image quality was bounded by contrast and brightness settings to force the regions with minimum emission to appear black and those with maximum emission to appear white. The ranges in between appeared as some intermediate gray scale. External disturbances to the instrument were minimal. There were no detectable magnetic field effects and no indications of mechanical vibration. Image distortion (foreshortening) caused by specimen tilt was avoided by use of a zero tilt condition. The beam and apertures were aligned to ensure optimum image sharpness. These same instrument settings were duplicated for all of the fractographs in this work as well as the test grid shown in Figure 3.3.

The test grid served two purposes; a means of evaluating instrument settings on the Fourier transform and also a method to calibrate the Fourier transform power spectrum for quantitative measurements. Figure 3.3 shows the test grid at two magnifications. Other magnifications were obtained by altering the television camera focal length during digitization.

The instrument variables evaluated with the test grid were brightness, contrast, and condenser lens setting. Figure 3.4 shows the test grid at 250X with two extremes in brightness. The top micrograph was made with the brightness level significantly greater than the normal setting, and the bottom micrograph with the brightness significantly less than the normal setting. Figure 3.5 shows the same test grid with high and low contrast settings. The low contrast setting resulted in a drop in the image bright level and loss of much of the image detail. Figure 3.6 shows the grid at two extreme condenser lens settings. The higher setting resulted in greater image noise but higher resolution due to the smaller beam size.

All the SEM test micrographs and fractographs produced in this work were photographed on Polaroid Type 55 positive/negative film. The negative was used in the Fourier transform analysis because of its finer grain (higher resolution) than the positive. It also had better digitizing characteristics because of the availability of uniform backlighting which precluded the problems of unwanted reflections from a positive image. All the photographs were processed identically to avoid any image variations due to processing variables.

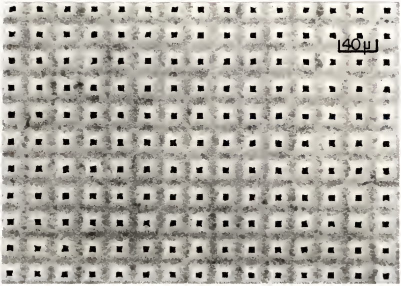

(a)

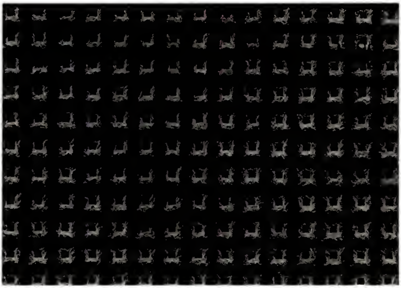

(b)

Figure 3.4 Scanning electron micrographs of gold test grid in (a) high brightness condition and (b) low brightness condition. 250X

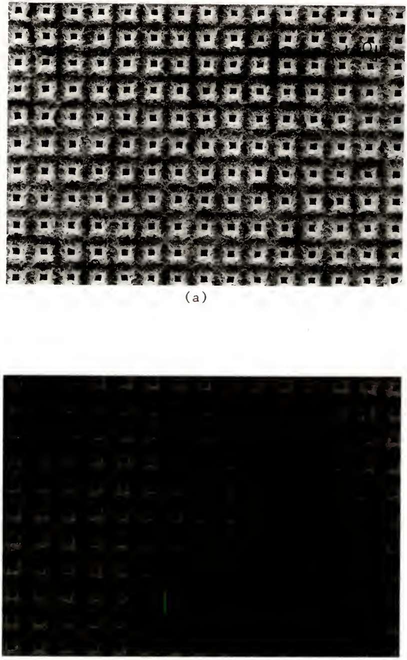

(a)

(b)

Figure 3.5 Scanning electron micrographs of gold test grid in (a) high contrast condition and (b) low contrast condition. 250X

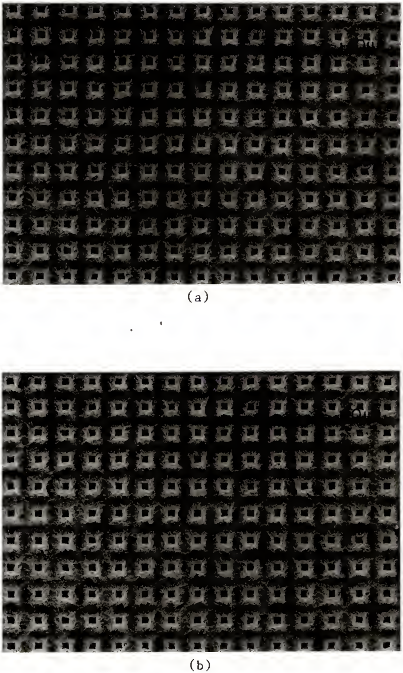

(a)

(b)

Figure 3.6 Scanning electron micrographs of gold test grid in (a) high condenser current condition and (b) low condenser current condition. 250X

3.1.3 Fractographic Specimens

The fractures used in this study were primarily from engineering investigations performed at the Naval Air Rework Facility, Pensacola. The fractographs were produced in a manner similar to that used in routine failure analysis investigations. Some additional specimens were included in the study to cover a broader range of material properties and fracture features.

The samples used for the fractographs and basic property information are given in Table 3.1 The alloys selected represented an extremely broad range in materials, from high strength quenched and tempered steel used in an attack aircraft tailhook to a century old steel used to produce a Florida Keys railroad bridge. The alloys used for evaluation of dimple rupture features were a C1117 plain carbon steel from an attack helicopter bolt insert, a C1008 plain carbon steel from a wood screw and a 4340 steel from a tailhook. The alloys for evaluation of cleavage facets were a 1020 plain carbon steel with high phosphorus and sulfur from a Florida Keys railroad bridge built in the 1880s, and a 17-4 PH precipitation hardening stainless steel in a brittle high strength condition from a failed helicopter collective control stick. The alloys for fatigue striation evaluation were a 2024-T3 aluminum from a ground support equipment hydraulic cylinder failed in fatigue and a 2014-T6 aluminum from a helicopter main rotor blade spar that failed in fatigue. The alloys for the decohesive rupture evaluation were a chrome plated high strength 4340 quenched and tempered steel used as a helicopter main landing gear axle that failed due to hydrogen assisted cracking,

Table 3.1 Fractographic Spacimen Alloy Data

Component	Alloy	Microstructure	Strength	Fracture Feature
Helicopter Rotor Head Bolt Insert	C1117 Steel	Ferrite/ Pearlite	93 KSI (641 MPa)	Tensile Dimples and Tear Dimples
Wood Screw	C1008 Steel	Ferrite	89 KSI (614 MPa)	Shear Dimples
Attack Aircraft Tailhook	4340 Steel	Tempered Martensite	290 KSI (200 MPa)	Tensile Dimples
Florida Keys Railroad Bridge	1020 Steel	Banded Ferrite/ Pearlite	74 KSI (510 MPa)	Cleavage Facets (high velocity fracture)
Helicopter Collective Control Stick	17-4 PH CRES Steel	Tempered Martensite	237 KSI (1640 MPa)	Micro-Quasicleavage Facets
Hydraulic Cylinder	2024-T3 Aluminum	Wrought Aluminum	70 KSI (483 MPa)	Fatigue Striations
Helicopter Main Rotor Blade Spar	2014-T6 Aluminum	Wrought Aluminum	75 KSI (517 MPa)	Fatigue Striations
Helicopter Main Landing Gear Axle	4340 Steel	Tempered Martensite	290 KSI (200 MPa)	Intergranular Facets (hydrogen assisted cracking)
Attack Aircraft Tailhook	4340 Steel	Tempered Martensite	290 KSI (2000 MPa)	Intergranular Facets (stress corrosion cracking)
Washer from Helicopter Main Rotor Blade Pitch Control	H-11 Tool Steel	Tempered Martensite	255 KSI (1760 MPa)	Intergranular Facets (stress corrosion cracking)

a 4340 quenched and tempered steel from an attack aircraft tailhook and an H-11 tool steel from a helicopter main rotor blade pitch control washer that failed in stress corrosion cracking. The strengths of each of the alloys are also given in Table 3.1.

The fracture surfaces for all the specimens were cleaned with a high pressure spray of 1-1-1 trichloroethane solvent to remove surface contaminants. No other cleaning was required.

The microstructures and fractographs for each of the components investigated are shown at 250X in each of the following micrographs. The C1117 plain carbon steel bolt insert, used in the analysis of tensile and tearing dimple rupture fracture, failed due to over-torque while a bolt was being installed into the insert. The center of the insert displayed tensile dimples and the outer edge had tear dimples, probably due to a bending component. The microstructure of the C1117 plain carbon steel insert is shown in Figure 3.7a. The structure consisted of ferrite grains and pearlite with small globular inclusions present. The fractograph, Figure 3.7b, showed a dimple rupture pattern with a range of dimple sizes present. The larger dimples had oval shapes and initiated from the globular inclusions seen at the base of the dimples. Figure 3.8 shows a fractograph of a high strength 4340 steel that failed in overload, resulting in fine equiaxed dimples. The fracture occurred in an attack aircraft tailhook that failed from a preexisting stress corrosion crack. The tailhook microstructure is shown in Figure 3.16a. The plain carbon steel insert, Figure 3.7, also showed tear dimples at the fracture origin as shown in Figure 3.9.

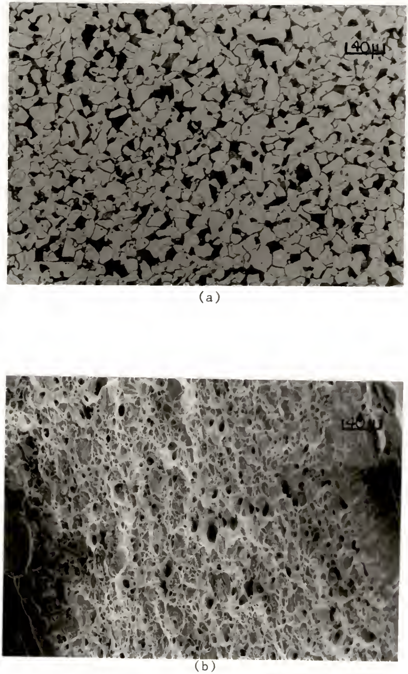

(a)

(b)

Figure 3.7 Tensile overload fracture specimen.
(a) Microstructure of C1008 plain carbon steel bolt insert from helicopter rotor head etched with 5% Nital. 250X
(b) Fractograph of tensile overload fracture in bolt insert showing mixed dimple sizes and large oval dimples. 250X

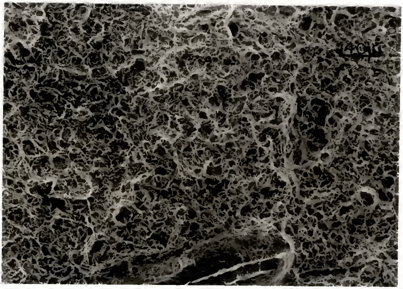

Figure 3.8 Fractograph of tensile overload fracture in 4340 steel tailhook showing fine equiaxed dimples. 250X

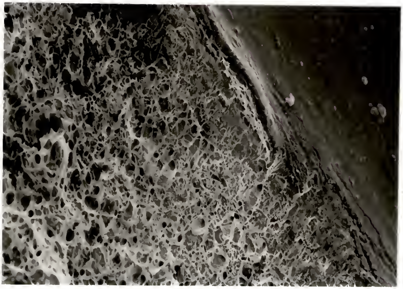

Figure 3.9 Fractograph of edge of fracture in steel bolt insert showing tear dimples. 250X

The C1008 plain carbon steel wood screw, used in the analysis of shear dimple rupture fracture, was being installed to support a ceiling fan when torsional overload occurred. The microstructure of the wood screw is shown in Figure 3.10a. The structure consisted of ferrite grains with finely distributed carbide particles. The fractograph, Figure 3.10b, showed shear dimples.

The 1020 plain carbon steel, used in the analysis of cleavage fracture, was taken from a Florida Keys railroad bridge and machined into charpy specimens. The specimen was fractured by a rifle bullet impact, producing ultrahigh velocity fracture. The microstructure shown in Figure 3.11a consisted of alternating bands of ferrite and pearlite. The fractograph, Figure 3.11b, showed distinct cleavage facets.

The 17-4 PH precipitation hardening stainless steel used in the analysis of quasicleavage fracture was from a helicopter collective control stick that underwent a brittle fracture and separated in the pilot's hand. The microstructure shown in Figure 3.12a consisted of coarse tempered martensite due to the H900 heat treat condition. The fractograph, Figure 3.12b, showed micro-quasicleavage facets.

The 2024-T6 wrought aluminum used in the analysis of coarse fatigue striations was from a hydraulic cylinder assembly. The microstructure shown in Figure 3.13a consisted of wrought aluminum grains and intermetallic particles. The fractograph, Figure 3.13b showed coarse fatigue striations and perpendicular fracture plane ridges.

The 2014-T6 wrought aluminum used in the analysis of fine fatigue striations, was from a helicopter main rotor blade spar that

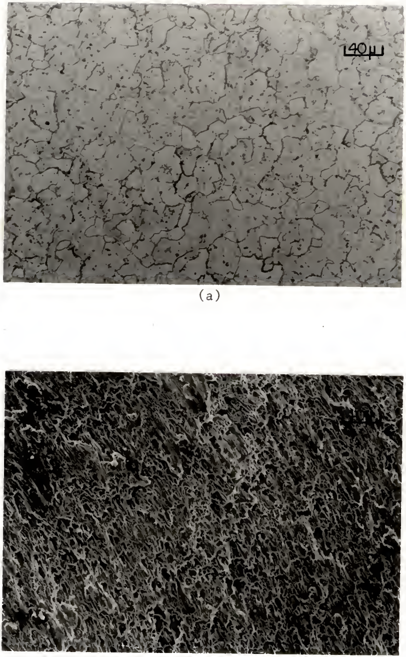

(a)

(b)

Figure 3.10 Torsional overload fracture specimen.
(a) Microstructure of C1008 plain carbon steel wood screw etched with 5% Nital. 250X
(b) Fractograph of torsional overload fracture in screw showing shear dimples. 250X

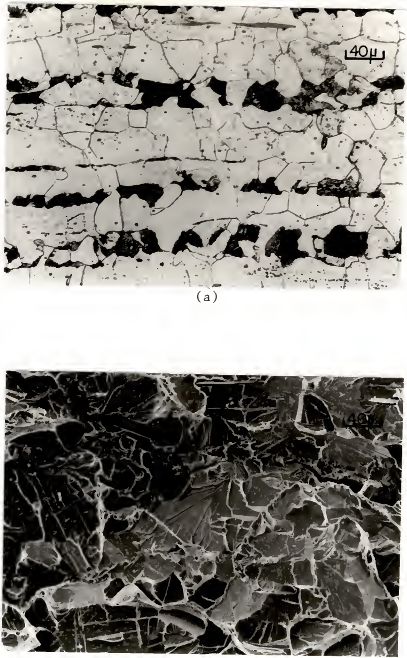

(a)

(b)

Figure 3.11 Cleavage fracture specimen.
(a) Microstructure of banded 1020 plain carbon steel from Florida Keys railroad bridge etched with 5% Nital. 250X
(b) Fractograph of inpact fracture in bridge steel specimen showing cleavage facets. 250X

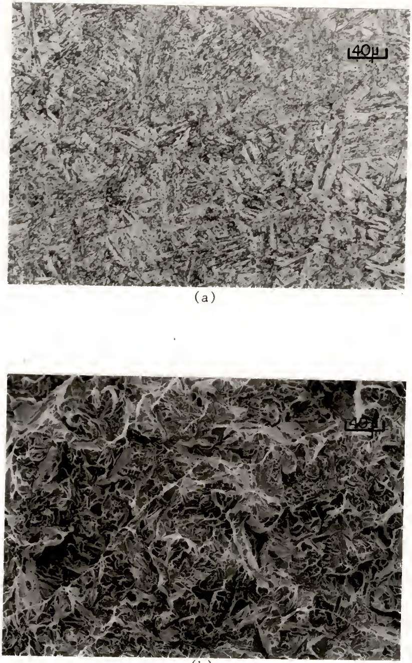

Figure 3.12 Quasicleavage fracture specimen.
(a) Microstructure of 17-4 PH precipitation hardening stainless steel from a helicopter collective stick etched with 5% Nital. 250X
(b) Fractograph of brittle fracture in collective stick showing quasicleavage facets. 250X

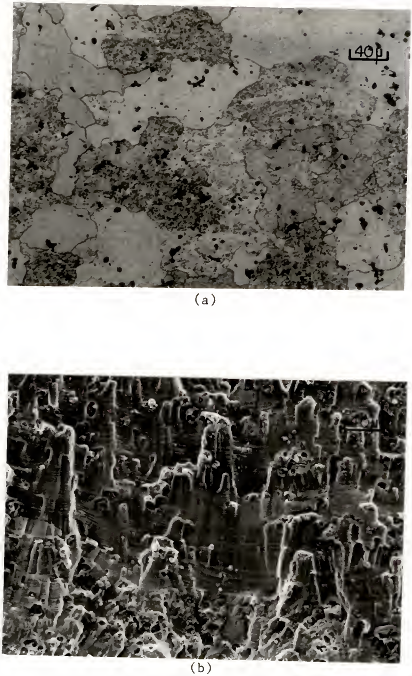

Figure 3.13 Fatigue fracture specimen.
(a) Microstructure of 2024-T3 wrought aluminum from hydraulic cylinder, Keller's etched. 250X
(b) Fractograph of fatigue fracture in cylinder showing fatigue striations. 250X

failed in fatigue and partially separated in flight. The microstructure shown in Figure 3.14a consisted of wrought grains of aluminum and intermetallic particles. The fractograph, Figure 3.14b, showed poorly defined striations and a noisy image due to high magnification.

The 4340 steel axle used in the analysis of hydrogen assisted cracking was from a helicopter main landing gear. The axle was chrome plated, resulting in subsurface hydrogen crack initiation below the chrome plating. The microstructure shown in Figure 3.15a consisted of fine tempered martensite. The fractograph, Figure 3.15b, showed intergranular facets with little evidence of any surface corrosion.

The 4340 steel tailhook, used in the analysis of stress corrosion cracking, was from an attack aircraft. The tailhook had developed a stress corrosion crack, and on contact with the arresting wire during landing, split in overload. The microstructure as shown in Figure 3.16a consisted of fine tempered martensite. The fractograph, Figure 3.16b, showed intergranular facets with little evidence of surface corrosion.

The H-11 tool steel, also used in the analysis of stress corrosion cracking, was from a helicopter main rotor blade pitch control bolt washer. The washer failed by formation of multiple stress corrosion cracks that initiated on one face of the washer. The microstructure, as shown in Figure 3.17a, consisted of fine carbide particles in a matrix of tempered martensite. The fractograph, Figure 3.17b showed intergranular facets with some of

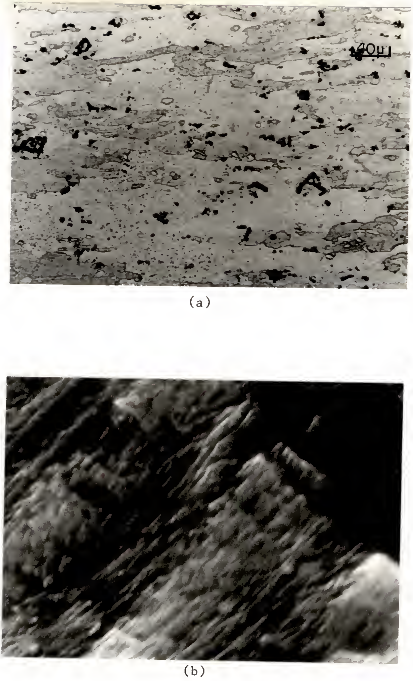

Figure 3.14 Fatigue fracture specimen.
(a) Microstructure of 2014-T6 wrought aluminum from helicopter main rotor blade spar, Keller's etched. 250X
(b) Fractograph of fatigue fracture fracture in spar showing fatigue striations. 13,500X

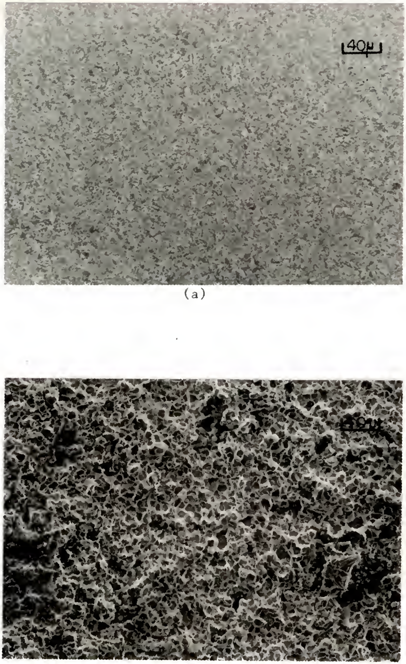

Figure 3.15 Intergranular fracture specimen.
(a) Microstructure of 4340 quenched and tempered steel from helicopter main landing gear axle etched with 5% Nital. 250X
(b) Fractograph of hydrogen assisted fracture in axle showing intergranular facets. 250X

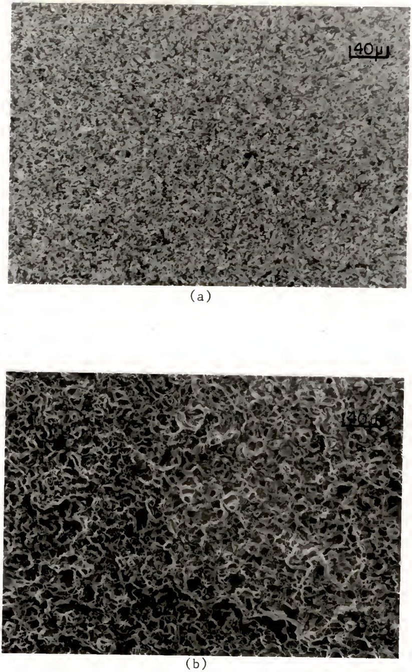

(a)

(b)

Figure 3.16 Intergranular fracture specimen.
(a) Microstructure of 4340 quenched and tempered steel from attack aircraft tailhook etched with 5% Nital. 250X
(b) Fractograph of stress corrosion fracture in tailhook showing intergranular facets. 250X

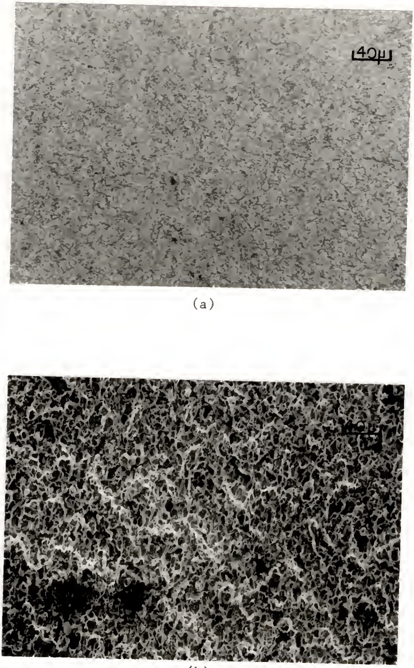

(a)

(b)

Figure 3.17 Intergranular fracture specimen.
(a) Microstructure of H-11 quenched and tempered tool steel from helicopter main rotor blade pitch control washer etched with 5% Nital. 250X
(b) Fractograph of stress corrosion fracture in washer showing intergranular facets. 250X

corrosion present as evidenced by the charging nonmetallic material in the lower left of the fractograph.

3.1.4 Theoretical Fractographic Models

Computer generated fracture feature models were also prepared for digital imaging analysis. The four most pronounced features observed in the four primary fracture modes (dimples, cleavage facets, fatigue striations and intergranular facets) were straight lines, curved lines, and multifaceted cellular structures. Figure 3.18 shows a computer generated theoretical model for fatigue fracture. The model was composed of bands of parallel lines produced by a computerized plotter and made into a transparency for digital imaging analysis. The lines had a fine spacing of 1 mm and a coarse spacing of 12 mm. Figure 3.19 shows two sets of parallel lines with two degrees of single curvature. These lines simulated a bowed fatigue crack front. Figure 3.20 shows two sets of parallel lines with double curvature and two spacings, 2.0 mm and 2.5 mm. Both simulated curved fatigue fronts. Figure 3.21 shows the multifaceted cellular models, ASTM grain size charts, used to simulate fracture facets and dimples. The chart in Figure 3.21a is ASTM grain size 2 which has a nominal average grain diameter of 0.180 mm. The average grain diameter was measured from the chart at 100X using a computerized digitizer pad. The longest grain diameters were averaged, which resulted in an average grain diameter of 19.79 mm. Figure 3.21b shows the ASTM grain size 4 chart. The nominal average grain diameter was 0.090 mm and the measured average grain diameter

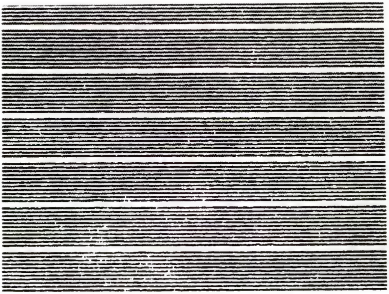

Figure 3.18 Computer generated theoretical model of fatigue fracture shown as parallel groups of straight lines.

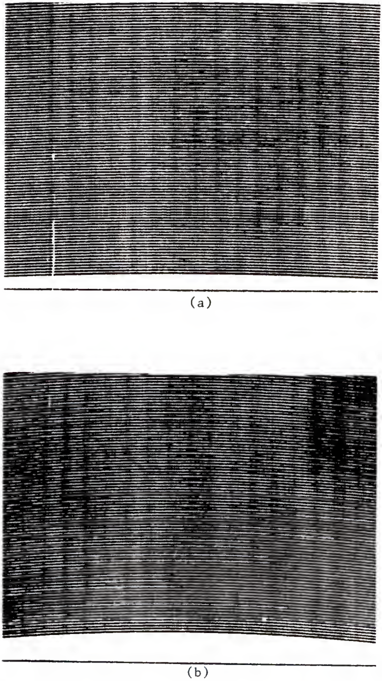

Figure 3.19 Computer generated theoretical models of fatigue fracture with equispaced lines. Plot (a) has single radius of curvature which is greater than radius of curvature of (b).

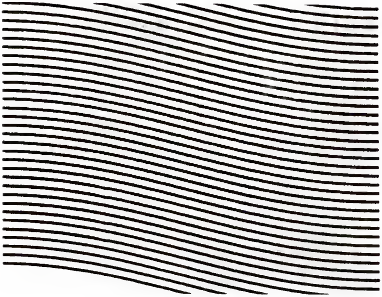

(a)

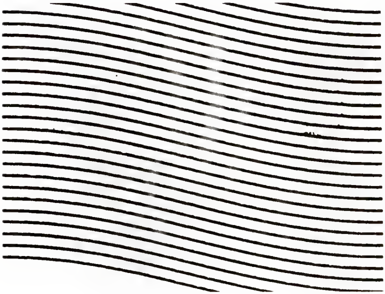

(b)

Figure 3.20 Computer generated theoretical models of fatigue fracture with double curvature; (a) has spacing of 2.5 mm and (b) has spacing of 3 mm.

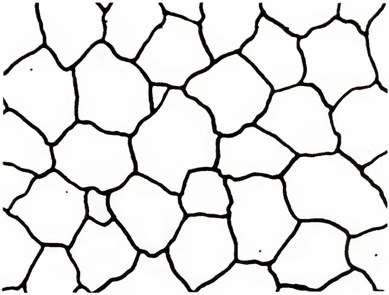

(a)

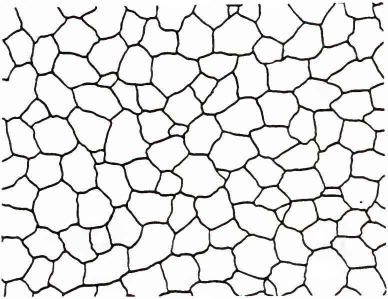

(b)

Figure 3.21 ASTM grain size charts used as theoretical models of dimples, cleavage facets, and intergranular facets; (a) is ASTM grain size 2 and (b) is ASTM grain size 4.

from the chart at 100X is 12.39 mm. Figure 3.22a shows the ASTM grain size 6 chart and Figure 3.22b shows ASTM grain size 7. The nominal average grain diameters were 0.045 mm and 0.032 mm, respectively. The measured average grain diameters from the charts at 100X were 7.7 mm and 5.17 mm, respectively. The average of the longest dimension was consistently larger than the reported nominal average grain diameter for the grain size charts.

The computer generated models and ASTM grain size charts served as a means for spatially calibrating the Fourier transform. They also served as a way to correlate input image features with the resulting Fourier transform power spectrum.

3.2 Image Processing Software

The conversion of a fractographic image into a Fourier transform power spectrum is performed by a sequence of operations. The image is digitized, an area is selected for analysis and windowed, the fast Fourier transform is calculated, and the input image and power spectrum are photographed. The data is further arranged into circular arrays to aid in computer display and sampling. The sampling is performed to produce a radial plot, ring plot and wedge plot for pattern classification and characterization.

3.2.1 Digital Image Acquisition

The negative transparency of the SEM fractograph was digitized using an EyeCom II picture digitizer and display system produced by Spatial Data Systems. A backlighting system was used for projecting

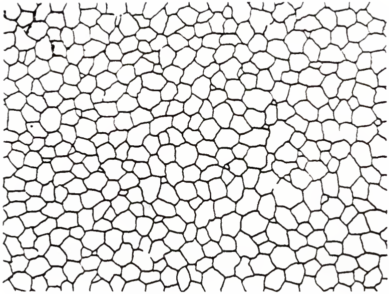

(a)

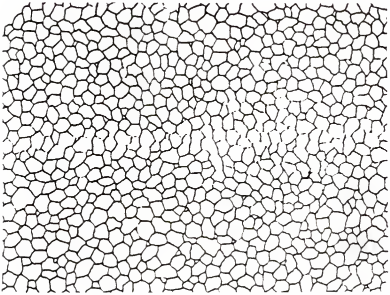

(b)

Figure 3.22 ASTM grain size charts used as theoretical models of dimples, cleavage facets, and intergranular facets; (a) is ASTM grain size 6 and (b) is ASTM grain size 7.

the images which produced 1% flat illumination. A vidicon television camera with variable aperture and focal length was used for digitization. The system produced a high resolution image composed of 640 x 480 pixels with 256 gray levels in a digitization time of 1/30 second. The camera was focused for each image and the lens aperture was adjusted so that the bright level was just below saturation. For the test grids with varying SEM instrument settings the camera was adjusted for the normal image and the remaining test micrographs were digitized with the same standard setting. All of the digitization was performed at a one-to-one magnification ratio except in the case of the test grid patterns used to produce a range of magnifications.

3.2.2 Image Matrix Size Selection

A reduced area of the digitized 640 x 480 pixel image was selected for Fourier transform analysis. The matrix size for the reduced area was initially evaluated as a 128 x 128 pixel array. However, the coarseness of the array was inadequate to resolve the detail of interest. A 256 x 256 pixel array was evaluated and found to produce satisfactory resolution. The array size was critical in that too coarse of an array could result in aliasing. An array that is too fine, such as a 1024 x 1024, requires an unrealistically long fast Fourier transform calculation time. Processing of one 256 x 256 array required approximately 15 minutes.

To evaluate the potential for aliasing with the 256 x 256 array, a fine structure composed of parallel lines with 1 mm spacing was analyzed. The digitizing camera system was barely able to resolve the fine lines using the 256 x 256 pixel array. The rule for digitizing fine structure, the sampling theorem, requires that data be sampled at twice the highest frequency component present to prevent aliasing. Thus the highest repeat pattern that could be tolerated without aliasing would complete 128 cycles in one direction of the 256 x 256 array. For the 1 mm spaced lines and a window size of 75 mm diameter, 75 cycles would be completed in the 75 mm distance, below the maximum of 128. For an even smaller window of 25 mm diameter, as used for the fractographic analysis, there would be 25 cycles completed, approximately 5 times below the maximum of 128. Thus, there was no possibility for aliasing based on the analog filtering effect of the Eyecom II camera system, the imaging matrix size selected, and the window sizes used.

3.2.3 Imaging Window Selection

The shape of the window used in Fourier transform imaging analysis is critical, as previously shown. Because the Fourier transform of the window is convolved with the Fourier transform of the input image data, the window transform pattern must be controlled to minimize leakage. A square window was initially examined but found to cause strong lobes in the transform pattern. A circular window produced the least amount of degrading effects in the final transform pattern. To eliminate the step created by the edge of the window, a softening function was applied to the data at the window interface by a DEC PDP 11/34 computer interfaced to the EYECOM II. The softening function was a 10% cosine taper which was initiated at the outer boundary of the data, 127 pixels from the center of the image. The cosine taper ended at a point approximately 106 pixels from the center of the image. The window diameter varied for the theoretical patterns but was 25 mm in diameter for all of the fractographic images. The window size was selected to correspond to typical regions of uniform fracture shown in the 4 x 5 inch negative at the magnifications of interest. The windowed data was stored on hard disk and transported to a DEC VAX 750 system for fast Fourier transform processing.

3.2.4 Fourier Transform Processing

The fast Fourier transform program used to process the image data was the Cooley-Tukey algorithm software known as HARM. The HARM subroutine is listed in the appendix. The time required to process a single 256 x 256 array image on the VAX 750 was approximately 15 minutes. The processed data was stored in a 256 x 256 array as the Fourier transform power spectrum which is the sum of the squares of the real and imaginary parts of the Fourier transform, or the modulus squared. The power spectrum data was displayed on a CRT and photographed onto 35 mm high resolution black and white film for photographic reproduction of the Fourier transform patterns. The data was also converted into a ring format to aid in sampling, as shown in Figure 3.23. The data in the circumferential area covered by the first 4 radial pixel positions was ignored because it was composed only of the zero frequency central dc spike from the image background intensity. The sum of the data contained in the radial pixels located between positions 5 and 9 were stored in ring 1. Each ring was further segmented into 40 angular sectors. All the data

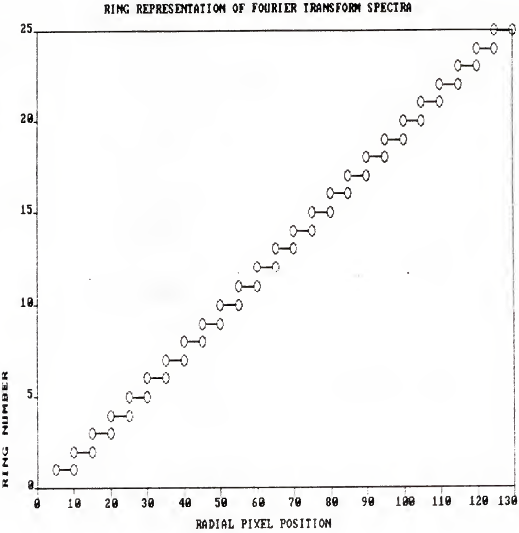

Figure 3.23 Sampling technique used to collect Fourier transform power spectrum data into plotting format.

within a sector was combined and averaged to produce a single value representing the sector. The data in radial positions 10 to 14 were averaged and stored in ring number 2 for each of the 40 sectors. This process was continued until the final data contained 25 rings with 40 sectors for each ring. The data was stored on 5-1/4 inch floppy disks and analyzed on an IBM PC computer for classification and characterization of the fractographic patterns.

3.2.5 Fourier Transform Sampling

The Fourier transform power spectra were analyzed in six primary formats: the spatial frequency pattern photograph, the three-dimensional surface plot, the radial plot, the first difference of the radial plot, the ring plot and the wedge plot.

3.2.5.1 Spatial frequency

The primary format for visual display of the Fourier transform power spectrum is the photographic two-dimensional image of the data. Figure 3.24 shows a typical Fourier transform power spectrum for the theoretical fatigue model shown in Figure 3.19b. The theoretical model contains parallel, equally spaced, lines with a single radius of curvature. The transform pattern contains the repeat frequency information from the input image. The centrally located white spot at the center of the transform pattern represents a background frequency of zero and is known as the dc power spike. It is primarily due to the window function and the background gray level of the input image. The two outer large spots are due to the presence of the parallel lines in the input image. Their distance from the

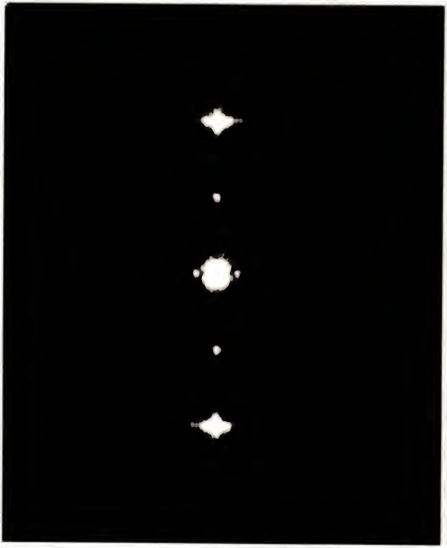

Figure 3.24 Fourier transform power spectrum of theoretical fatigue model shown in Figure 3.19b.

optical axis is directly correlated to the line spacing or repeat frequency in the input image. The two outer spots are nonsymmetrical, distorted horizontally. This indicates curvature of the parallel lines in the input image. The degree of curvature is reflected in the amount of distortion in the spots. The location of the two major spots along the vertical axis of the transform power spectrum indicates that the repeat pattern direction in the input image was also along the vertical axis. The two low intensity spots on the vertical axis were due to the fact that some of the lines in Figure 3.19b have joined, resulting in halving of the repeat frequency and moving the Fourier transform power spectrum spots half the distance to the dc spike. The high intensity spots also have harmonics located twice their distance from the dc spike, beyond the edge of the photograph. The harmonics have frequencies that are multiples of the fundamental frequency and thus have positions in the transform pattern that are multiples of the primary spot locations. The two spots located in the horizontal axis of the transform pattern are a result of the perpendicular, vertical lines in the input image. The brightness of the spots in the transform pattern indicates the number of repeat features present in the input image. The greater the number of repeat features, the brighter the spot. Thus, visual analysis of the Fourier transform power spectrum is extremely valuable in extracting descriptive data concerning the input image features.

3.2.5.2 3D surface plot

The rectangular 3D surface plot provides a means for viewing the Fourier transform power spectrum from an angle to better visualize the relative positions and heights of the spatial frequency data. Figure 3.25 shows the three steps in the production of the 3D surface plot. The top view is the transform power spectrum data in ring format, as viewed in the transform photograph. The central white spot represents the area removed corresponding to the core of the dc spike. The dark lobes and spots represent data. The ring is divided into five sectors for simplicity. In order to produce the rectangular representation of the 3D surface plot, the ring data is split and opened, creating a rectangular surface as shown in the middle drawing of Figure 3.25. This requires expansion of the inner sector area and compaction of the outer sector area, a process that is reasonable because of the positionally varying density of data within the sectors. If the middle drawing is then rotated back on a horizontal axis, it becomes a rectangular 3D surface plot of the Fourier transform power spectrum. The relative intensities of features in the spectrum now become height variations in the surface plot. The heights were not calibrated for specific numbers of repeat patterns, but serve as a means of comparing input images. The two outer rings of data were dropped from the surface plot because the ring sampled data was taken from a square matrix, causing loss of data at the outer edges.

3.2.5.3 Radial plot

The radial plot, as shown in Figure 3.26, is a technique of sampling the Fourier transform power spectrum data so that it is directionally insensitive. Figure 3.26 shows a sample spectrum with

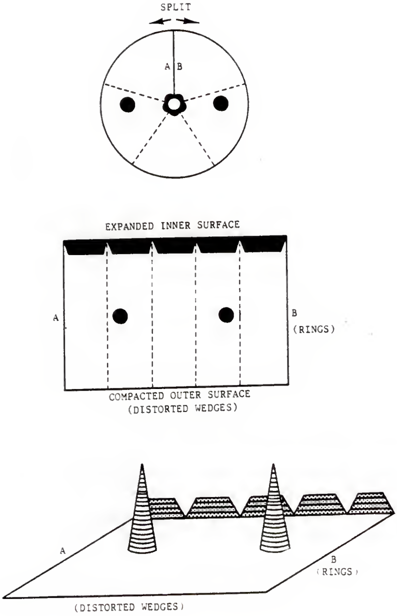

Figure 3.25 Rectangular representation of three-dimensional surface plot of Fourier transform power spectrum data.

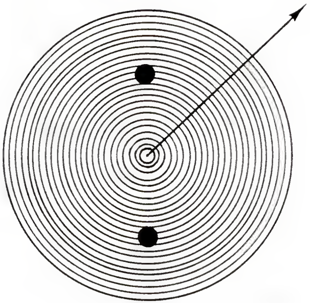

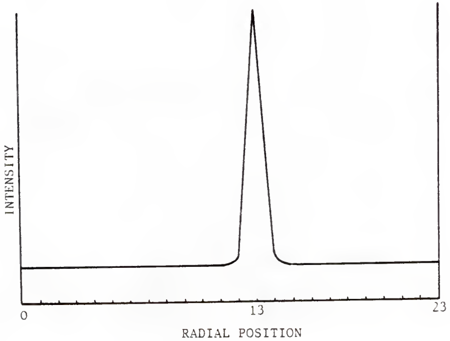

Figure 3.26 Radial plot sampling of Fourier transform power spectrum data.

two data spikes and a set of concentric rings. If the contents of each ring is summed and plotted with respect to radial position, a radial signature curve results. The radial plot, as shown at the bottom of Figure 3.26, clearly indicates the presence of data spikes at ring 13. The plot provides no information about orientation of the data however. The radial plot may also be displayed in the log-data format. The first difference of the log radial plot displays the slope of the curve and emphasizes inflections due to outer high frequency spikes in the data.

3.2.5.4 Ring plot

The ring plot, as shown in Figure 3.27, is a technique of displaying the Fourier transform power spectrum data for a specific frequency. It is simply the result of making a rotational scan through one of the data rings of the Fourier transform power spectrum and plotting the contents of the ring as a function of angular position. Figure 3.27 shows a sample spectrum with two opposing data points. The ring plot shows two spikes due to the two peaks, located at opposing positions. The 3D surface plot provides similar information in that the image is composed of a collection of ring plots. Each ring location is simply the distance from the inner surface of the 3D plot. For a given ring number, the ring plot can be evaluated by examination of the 3D surface plot.

3.2.5.5 Wedge plot

The wedge plot is a frequency insensitive technique for displaying the Fourier transform power spectrum data. It is similar

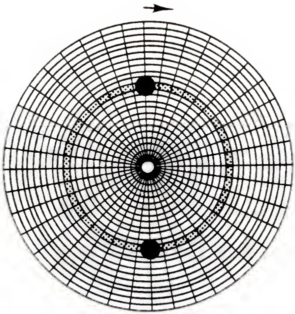

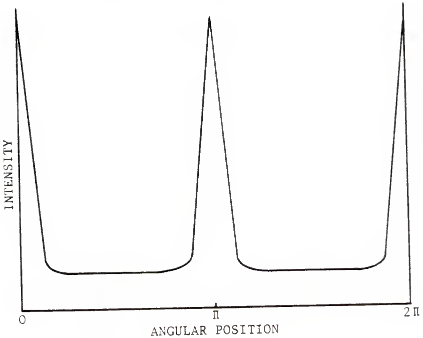

Figure 3.27 Ring plot sampling of Fourier transform power spectrum data.

to the ring plot except that all the sectors with the same sector number are summed. The wedge plot, as shown in Figure 3.28, provides a directional description of the input image that is independent of spatial frequency.

The combination of the Fourier transform power spectrum display and sampling patterns provides a means of classifying and characterizing the various types of input fractographic images.

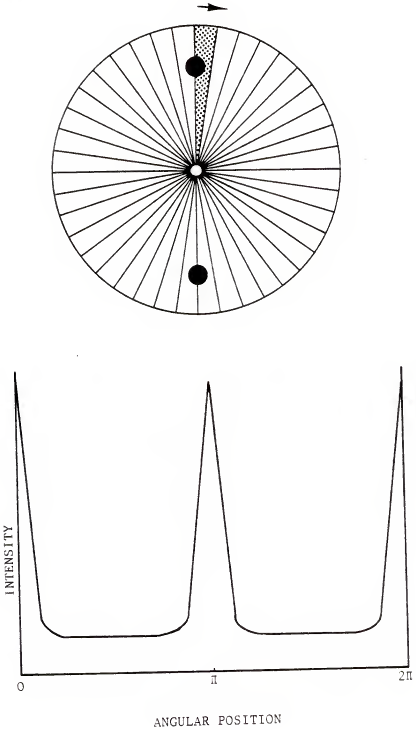

Figure 3.28 Wedge plot sampling of Fourier transform power spectrum data.

CHAPTER 4

RESULTS AND DISCUSSION

The data analyzed by the digital Fourier transform imaging procedures fell into four categories: data for analysis of the window function, data for analysis of instrumentation variables from the SEM, data for dimensional calibration of the input patterns and data from the actual fractographs. The data for the window function will be considered first.

4.1 Data Window Function Analysis

The tapered window used for imaging all the data is shown in Figure 4.1a with no data present. The resulting Fourier transform power spectrum is shown in Figure 4.1b. The Fourier transform spectrum for the window was limited to a small region at the center of the spectrum. The central spot (dc power spike) was the transform of the tapered window. It had four minor lobes centered at 45 degrees to the horizontal and vertical axes. The window function was carefully evaluated to determine its alteration of the character of data being analyzed. Figure 4.2 shows a surface plot of the tapered window power spectrum data. The wall of spikes to the rear of the surface plot corresponded to the outer edge of the dc power spike in

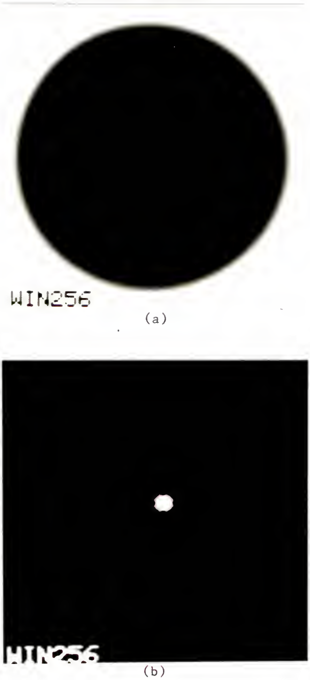

Figure 4.1 Circular window/Fourier transform pair.
(a) Tapered window with no data present and
(b) resulting Fourier transform power spectrum.

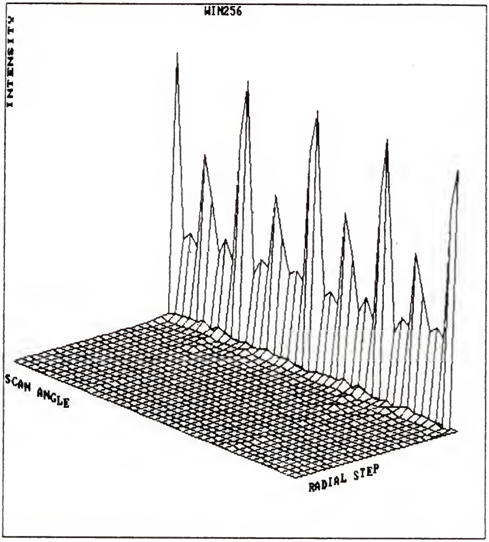

Figure 4.2 Surface plot of Fourier transform power spectrum from tapered data window.

the transform image. The surface plot was generated by sectioning the transform at the right horizontal position and opening the transform pattern in a counterclockwise manner as described in the experimental procedure section. Figure 4.3 shows a radial plot of the tapered window power spectrum. The log of intensity was plotted vs. the radial position from the center of the transform expressed as ring numbers. The curve descended rapidly to near zero intensity. However, the presence of some data beyond the central spike area was indicated. To determine the nature of the data, a log surface plot was prepared, as shown in Figure 4.4. The plot indicated that the window transform had nonuniform data content, even to the last outer ring. Because the transform of the window is convolved with the transform of the data, the window used should have minimal data content beyond the dc spike. The window used had the least amount of data and least effect of altering the input data of all the windows evaluated. There were no indications that the tapered window seriously affected any of the fractographic patterns in the study.

4.2 Scanning Electron Microscope Variable Analysis

Changes in the nature of the SEM image were evaluated by examination of corresponding effects in the Fourier transform power spectrum. Figure 4.5a shows an input image of a gold test grid used for SEM image calibration with the image produced under normal fractographic imaging conditions. Figure 4.5b shows the resulting Fourier transform power spectrum. The equally spaced grid pattern in the input image produced an equally spaced pattern of spots in the

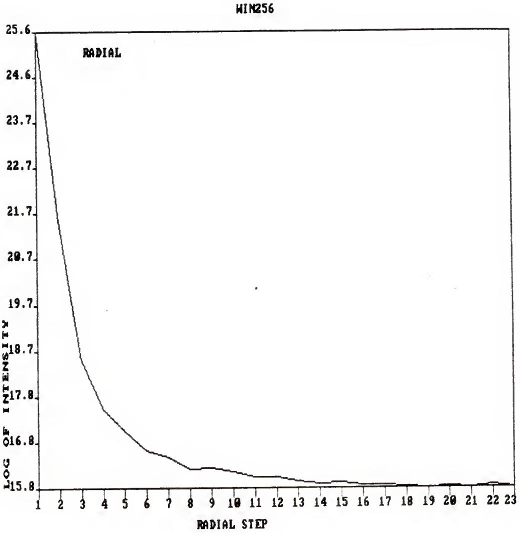

Figure 4.3 Radial plot of Fourier transform power spectrum from tapered data window.

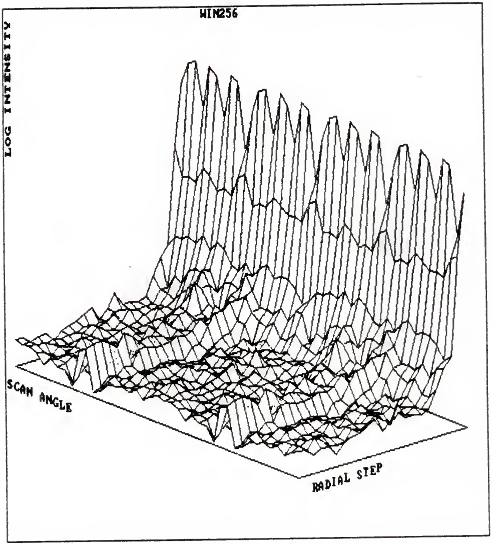

Figure 4.4 Log surface plot of Fourier transform power spectrum from tapered data window.

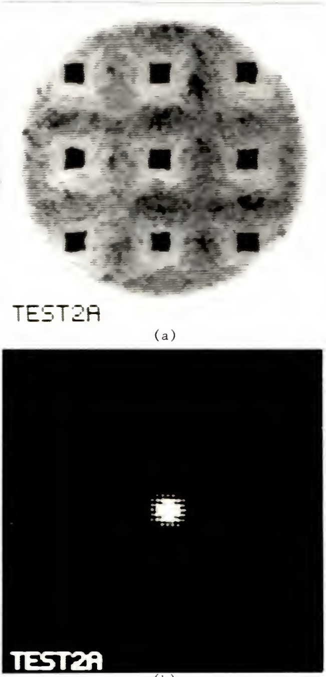

(a)

(b)

Figure 4.5 Test grid/Fourier transform pair.
(a) Input image of gold test grid under normal SEM imaging conditions and
(b) resulting Fourier transform power spectrum.

Fourier transform output image. The input grid spacing was inversely related to the output spot spacing. The SEM operating variable effects were evaluated by their effects on the wedge plot of the transform power spectrum. Figure 4.6 shows the wedge plot for the transform of the normal test grid image. The wedge plot scan began at the right horizontal axis and proceeded counterclockwise, intercepting spots in the transform as it rotated. The wedge plot from the test grid was composed of four major spikes corresponding to the horizontally and vertically aligned rows of spots in the transform pattern. The smaller spikes in the wedge plot corresponded to the intermediate positions in the transform pattern where spot alignment was not as strong. The test grid micrograph imaged under normal conditions, the resulting transform pattern, and the wedge plot were established as a baseline for evaluating the effects of other SEM instrumental conditions such as brightness, contrast and electron beam probe size.

Increase in the brightness level of the test grid input image, as shown in Figure 4.7a, slightly increased the intensity of the spots in the transform pattern, Figure 4.7b, and increased the height of all of the peaks in the wedge plot, Figure 4.8. The increase in brightness caused the black-to-white transition in the input image to become more distinct, which improved the detectability of the input patterns. However, the increase in brightness also caused an oversaturation of the white level in the input image and resulted in loss of information content. Increase in brightness alone was not extremely beneficial for improvement of imaging analysis because it changed the average brightness of every feature.

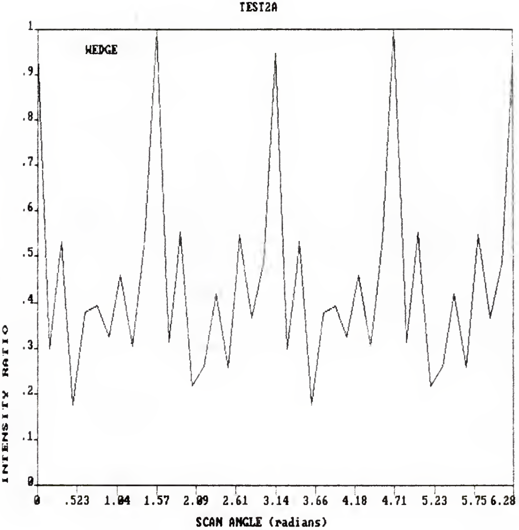

Figure 4.6 Wedge plot of Fourier transform power spectrum from gold test grid under normal imaging conditions.

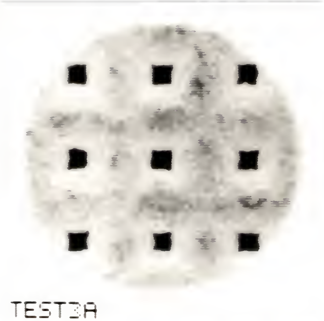

(a)

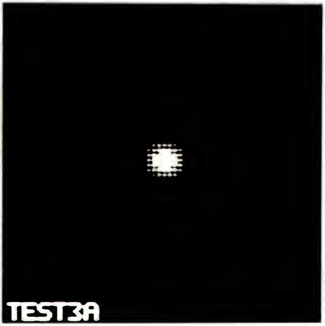

(b)

Figure 4.7 Test grid/Fourier transform pair.
(a) Input image of gold test grid under increased SEM brightness conditions and
(b) resulting Fourier transform power spectrum.

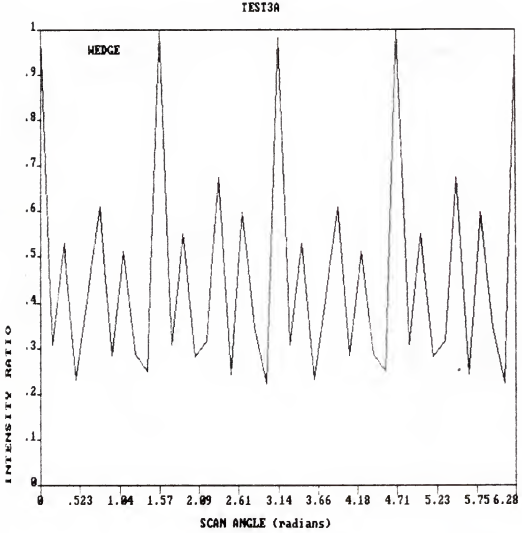

Figure 4.8 Wedge plot of Fourier transform power spectrum from gold test grid under increased brightness imaging conditions.

Decrease in brightness level of the image, as shown in Figure 4.9a, decreased the intensity of the spots in the transform pattern, Figure 4.9b, and decreased the height of the peaks in the wedge plot, Figure 4.10. The loss of brightness decreased the black to white transition in the input image which made the repeat patterns less detectable. Decrease in brightness level was not beneficial to feature detection sensitivity. The effects of minor changes in brightness had no major effect on the Fourier transform power spectrum.

Increase in contrast of the input image, as shown in Figure 4.11a, slightly increased the intensity of the spots in the transform pattern, Figure 4.11b, and resulted in the appearance of higher harmonic spots. The wedge plot, Figure 4.12, showed that the peak at the horizontal and vertical positions was significantly enhanced due to the addition of additional harmonic spots. Thus increased contrast was beneficial for feature detection sensitivity.

Decrease in contrast of the input image, as shown in Figure 4.13a, significantly decreased the intensity of the spots in the transform pattern, Figure 4.13b, and greatly reduced the signal-to-noise ratio as shown by the wedge plot, Figure 4.14. The reduction in contrast decreased the black to white transition in the input image, making the repeat patterns less distinct. It had the most serious negative effect on the transform pattern of any of the variables evaluated. Contrast is critical in the SEM fractograph but extreme loss of contrast is required to degrade the transform pattern.

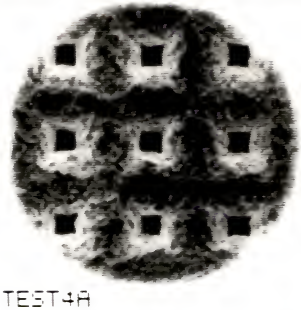

(a)

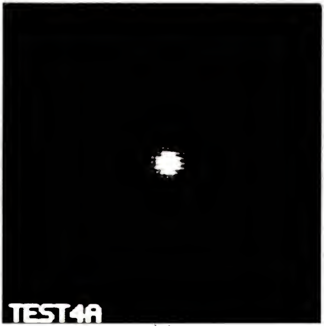

(b)

Figure 4.9 Test grid/Fourier transform pair.
(a) Input image of gold test grid under decreased SEM brightness conditions and
(b) resulting Fourier transform power spectrum.

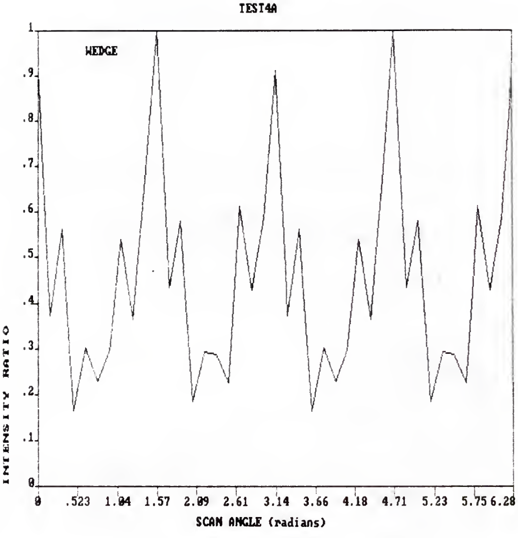

Figure 4.10 Wedge plot of Fourier transform power spectrum from gold test grid under decreased brightness imaging conditions.

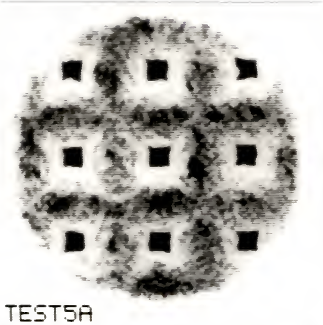

(a)

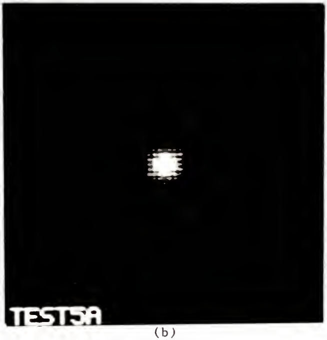

(b)

Figure 4.11 Test grid/Fourier transform pair.
(a) Input image of gold test grid under increased SEM contrast conditions and
(b) resulting Fourier transform power spectrum.

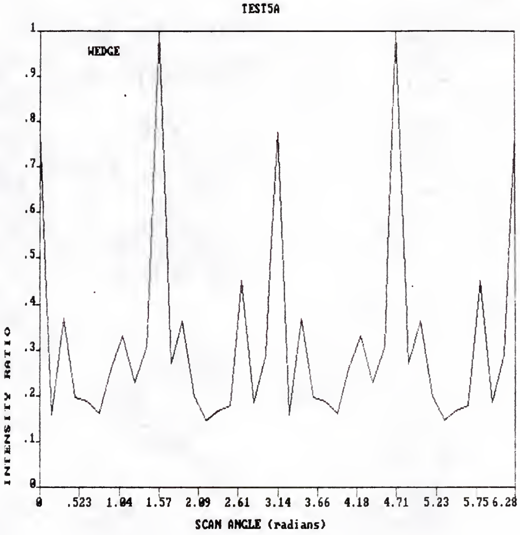

Figure 4.12 Wedge plot of Fourier transform power spectrum from gold test grid under increased contrast conditions.

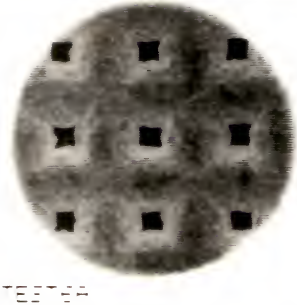

(a)

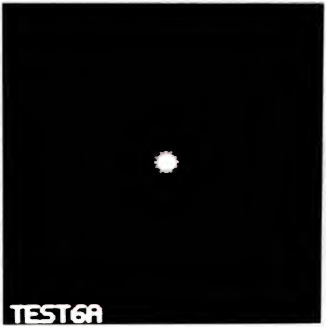

(b)

Figure 4.13 Test grid/Fourier transform pair.
(a) Input image of gold test grid under decreased SEM contrast conditions and
(b) resulting Fourier transform power spectrum.

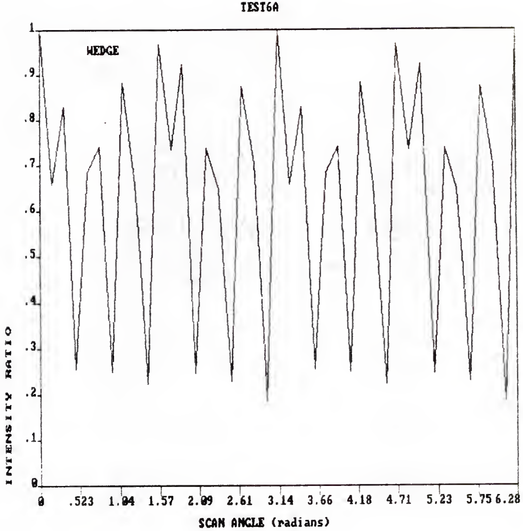

Figure 4.14 Wedge plot of Fourier transform power spectrum from gold test grid under decreased contrast conditions.

Increase in condenser current, which decreases the electron beam probe size and specimen electron emission, had little effect on the input image, as shown in Figure 4.15a. It caused a decrease in outer spot intensity in the transform pattern, Figure 4.15b, and a decrease in intensity between peaks in the wedge plot, Figure 4.16. In general, a reduction of the beam size will create an increase in image noise level because of reduced specimen electron emission. At low magnifications (less than 5000X), no benefit will be obtained in the image from the smaller beam size. At high magnifications (greater than 5000X), the smaller beam size allows finer features to be resolved and thus improves the image resolution. At the magnifications used with the test grids, and with all but one of the fractographs, an increase in condenser current offered no advantage, but also did not significantly degrade the feature detection ability of the Fourier transform. A decrease in condenser lens current, which had the effect of increasing specimen emission, increased image quality, as shown in Figure 4.17a, by improving the signal-to-noise ratio. The effect on the transform pattern, Figure 4.17b, was to increase the spot intensity. The wedge plot, Figure 4.18, showed no significant differences from the baseline pattern. Thus, decreasing the condenser lens current had little effect on the feature detection ability of the Fourier transform.

The SEM instrument variables that had the greatest effect on the Fourier transform power spectrum pattern were brightness and contrast. Because the negative image was utilized, an increase in brightness or contrast resulted in a greater separation of the black

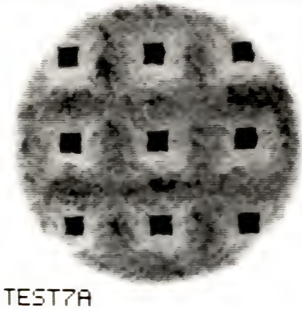

(a)

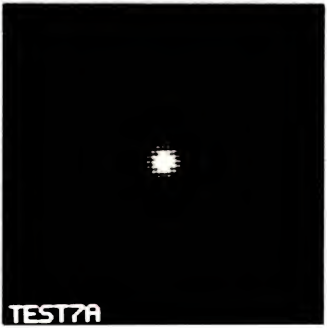

(b)

Figure 4.15 Test grid/Fourier transform pair.
(a) Input image of gold test grid under increased condenser lens current conditions and
(b) resulting Fourier transform power spectrum.

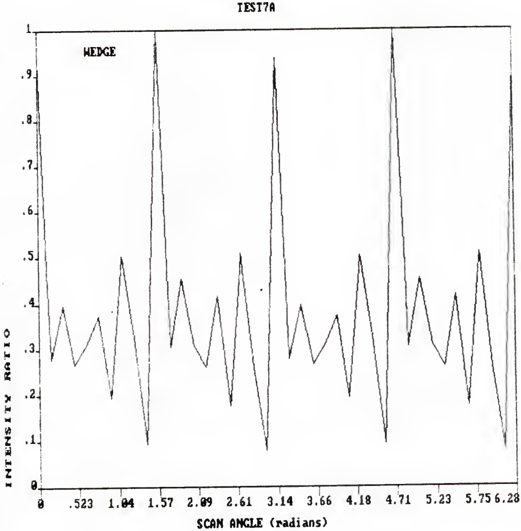

Figure 4.16 Wedge plot of Fourier transform power spectrum from gold test grid under increased condenser lens current conditions.

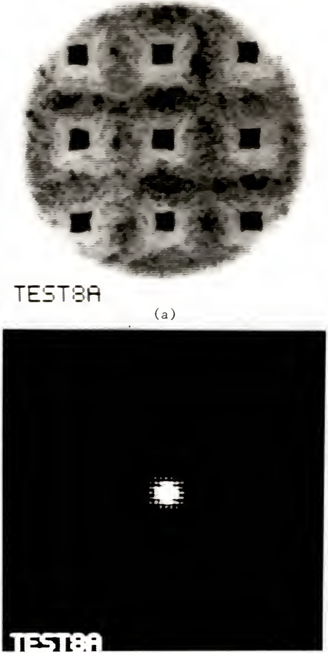

(a)

(b)

Figure 4.17 Test grid/Fourier transform pair.
(a) Input image of gold test grid under decreased condenser lens current conditions and
(b) resulting Fourier transform power spectrum.

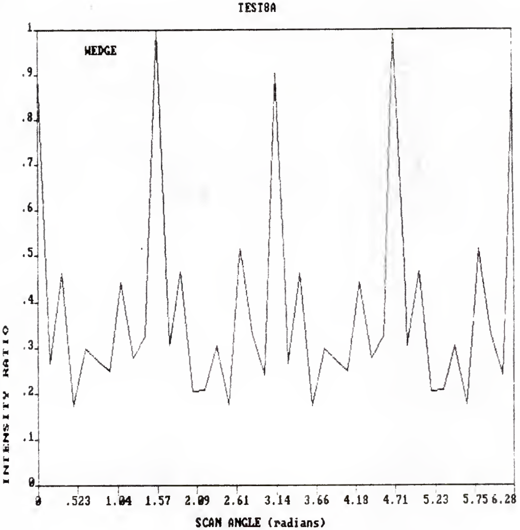

Figure 4.18 Wedge plot of Fourier transform power spectrum from gold test grid under decreased condenser lens current conditions.

and white levels, causing adjacent features with different gray levels to be more easily distinguished.

The impact of the use of the negative input image was evaluated by examination of the Fourier transform power spectrum of both a positive and negative test grid image. Figure 4.19a shows the input image of the test pattern at a lower magnification than previously shown and Figure 4.19b shows the resulting Fourier transform power spectrum. Figure 4.20a shows the inverse pattern of the grid input image and Figure 4.20b shows the resulting transform power spectrum. Comparison of the two transform patterns revealed no significant differences. For fractographs the result would be similar except that the gray level of the input image would increase the size of the central dc spike in the transform power spectrum.

The gold grid pattern used to evaluate SEM instrumental variables was also used to correlate input image repeat dimensions to Fourier transform power spectrum spot spacing. The input pattern shown in Figure 4.5a is 3-1/3 times larger than the pattern shown in Figure 4.19a. The transform patterns showed expected reciprocal type changes in dimensions. The decrease in magnification of the input image resulted in an increase in spot spacing of the corresponding Fourier transform power spectrum patterns. The test grid was also evaluated at other lower magnifications, for a total of four magnifications. The highest magnification image, Figure 4.5a, had a two-dimensional repeat spacing of 23 mm in the photograph. The Fourier transform had a two-dimensional spot spacing of 1.4 mm which corresponded to the first ring in the circularly arranged transform data. The next highest magnification, Figure 4.19a, had an input

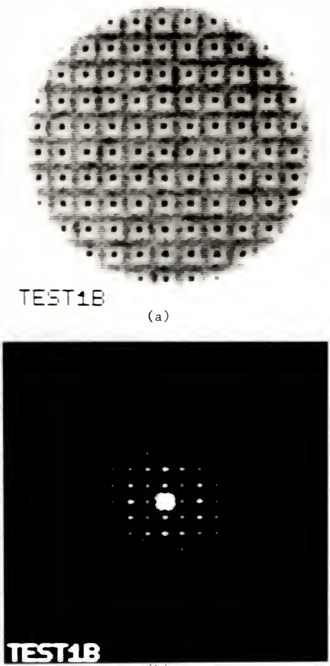

(a)

(b)

Figure 4.19 Test grid/Fourier transform pair.
(a) Input image of gold test grid under normal SEM imaging conditions with lower magnification and
(b) resulting Fourier transform power spectrum.

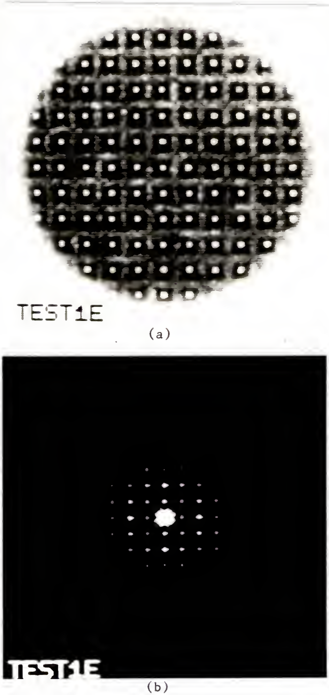

Figure 4.20 Test grid/Fourier transform pair.
(a) Input image of gold test grid under normal SEM conditions but complement of image and
(b) resulting Fourier transform power spectrum.

spacing of 6.8 mm and a transform spot spacing of 4.6 mm corresponding to the second ring of data. The third and fourth decreasing magnifications had input spacings of 3.4 and 2.3 mm. The transform patterns had spacings of 9.0 and 13.0 mm corresponding to rings 5 and 7. The results will be shown graphically combined with results from the theoretical fracture feature patterns in the following section.

4.3 Fractographic Image Feature Calibration

The two classes of theoretical fracture feature models, parallel lines, and multifaceted cellular patterns, were used to evaluate the ability of the digital Fourier transform to produce the expected transform power spectrum patterns. They were also used to calibrate the input image repeat spacing with the spot spacing for the transform pattern. The data from the test grid at various magnifications and the theoretical fracture feature models at various magnifications were combined to establish calibration curves for analysis of repeat features in the fractographic images.

A set of dual frequency straight parallel lines at a repeat spacing of 2 mm and 20 mm are shown in the input image of Figure 4.21a. The resulting Fourier transform power spectrum is shown in Figure 4.21b. For the two sets of lines in the input image the repeat spacing along the horizontal axis resulted in a row of frequency spots in the transform pattern also along the horizontal axis. The finer lines in the input image resulted in the two highest intensity spots and their first harmonic, located twice the distance

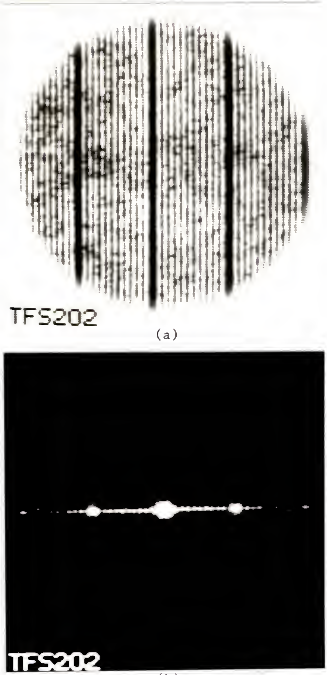

(a)

(b)

Figure 4.21 Parallel lines/Fourier transform pair.
(a) Input image of theoretical fatigue as two repeat frequency bands of straight parallel lines and
(b) resulting Fourier transform power spectrum.

from the dc spike. The coarse lines resulted in the row of multiple equally spaced spots, consisting of the principal spot adjacent to the dc spike and multiple harmonics of the primary repeat frequency. Figure 4.22 shows the surface plot of the transform spectrum, again opened at the right horizontal position and displayed so that the central dc spike was located at the back row of smaller spikes. The two large outer spikes in the transform image were two halves of a single spike which was split where the transform pattern was sectioned at the right horizontal position. The two large spikes are the two outer spots in the transform pattern due to the fine line repeat spacing. The two spikes at the back row of the surface plot located adjacent to the dc spike in the transform power spectrum were caused by the coarse lines in the input image. The location of the spots adjacent to the dc spike indicated that 24 mm was approximately the largest input repeat feature that could be successfully analyzed. Figure 4.23 shows a radial plot of the log intensity of the transform power spectrum. The radial plot is directionally insensitive and only reflects the input image repeat frequencies. The spikes close to the dc spike were contained in ring 1 and the midscale large spikes were contained in ring 10. A harmonic of the spikes at ring 10 was located at ring 21. The input image had repeat spacings of 2 and 24 mm. The transform pattern had spacings of 19.2 and 1.6 mm, corresponding to the radial plot rings 10 and 1. Figure 4.24 shows the wedge plot of the transform power spectrum from the dual frequency parallel lines. The wedge plot is frequency insensitive, showing only the angular location of the power in the Fourier transform power spectrum. Its primary use is to reveal

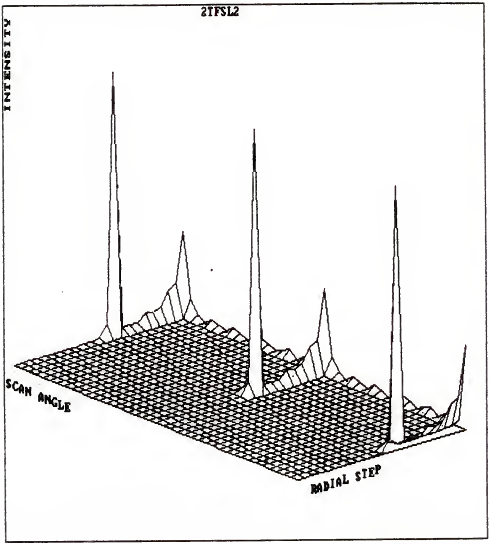

Figure 4.22 Surface plot of Fourier transform power spectrum from theoretical straight line fatigue at two repeat frequencies.

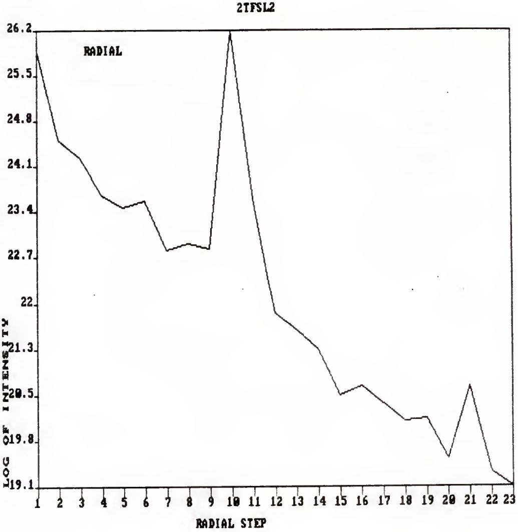

Figure 4.23 Radial plot of Fourier transform power spectrum from theoretical straight line fatigue at two repeat frequencies.

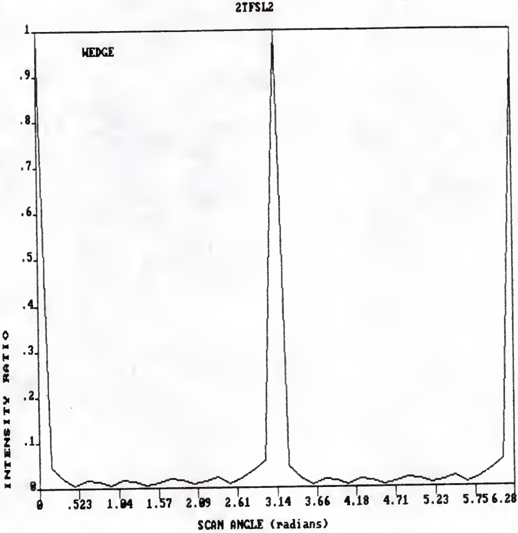

Figure 4.24 Wedge plot of Fourier transform power spectrum from theoretical straight line fatigue at two repeat frequencies.

directionality in the input image. The wedge plot for the dual frequency straight parallel lines contained two spikes located at the outer axes and one at the midpoint on the scan angle scale. The two outer spikes were the two halves of one spike. The wedge plot, as the surface plot, began at the right horizontal position of the transform power spectrum and proceeded counterclockwise. The horizontal row of spots on the right side of the transform power spectrum formed the initial spike at the zero scan angle position. As the wedge was scanned to the 180 degree (3.14 radian) position, the opposing symmetry row of spots was encountered and the center wedge plot spike resulted. Continued rotational scan of the wedge to the 360 degree (6.28 radian) position caused the row of spots at the right horizontal position to be encountered again, forming the second half of the outer spike in the wedge plot.

The dual frequency straight lines were also used as an input image at half the magnification shown in Figure 4.21a. The results were used to calibrate the high frequency limits of the transform power spectrum. The one millimeter repeat spacing for the fine lines in the input image was near the limit of the Fourier analysis system for high frequency data.

The effect of curvature in the input pattern of parallel lines was evaluated for two different curvatures. Figure 4.25a shows the input image pattern with a single frequency spacing of 2 mm and a small degree of curvature. The corresponding Fourier transform power spectrum is shown in Figure 4.25b. The center spot in the spectrum was due to the circular window and was nearly identical to the transform spectrum with no data present, Figure 4.1b. The two high

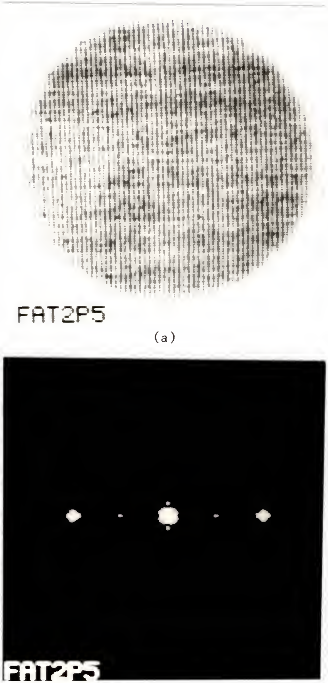

(a)

(b)

Figure 4.25 Parallel line/Fourier transform pair.
(a) Input image of theoretical fatigue as single curvature parallel lines and
(b) resulting Fourier transform power spectrum.

intensity spots on the horizontal axis were due to the 2 mm spaced input lines. The vertical spread of the spots was due to curvature of the lines in the input image. The two small spots on the horizontal and vertical axes was due to repeat defects in the input image. The parallel lines were computer generated at a 1 mm spacing and the plotter was incapable of accurately reproducing the fine detail. Some of the parallel lines joined, creating a second, coarser, repeat frequency composed of wider lines. This coarser frequency resulted in spots located closer to the optical axis on the horizontal axis. The vertical spots were due to repeat noise in the input image in the form of parallel lines with an even coarser spacing. The surface plot, Figure 4.26, showed the central spike and two halves of an outer spike. The high intensity of the major spikes caused the minor spikes to be barely visible. The major spikes were spread as in the transform image due to curvature of the input lines. The radial plot, Figure 4.27, showed that the major spikes, located at ring 13, were also elongated. The input image had a spacing of 2 mm and a transform spacing of 25 mm, corresponding to the ring 13 position. The minor spikes and the beginning of a harmonic from the major spike were also shown in the radial plot. The wedge plot, Figure 4.28, showed two major spike halves at the beginning and end of the scan and the single spike at the midpoint. The two spots on the vertical axis in the transform image appeared as two small spikes located midway between the two major spikes. The remaining data in the wedge plot was due to the window and the central dc spike.

A similar set of single curvature lines with greater curvature is shown as the input image in Figure 4.29a. The resulting Fourier

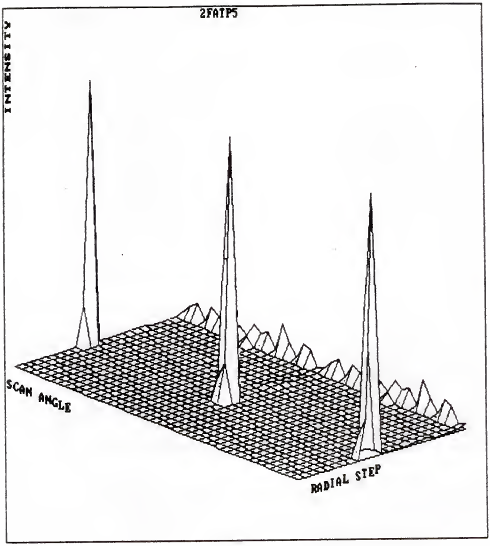

Figure 4.26 Surface plot of Fourier transform power spectrum from theoretical single curvature fatigue.

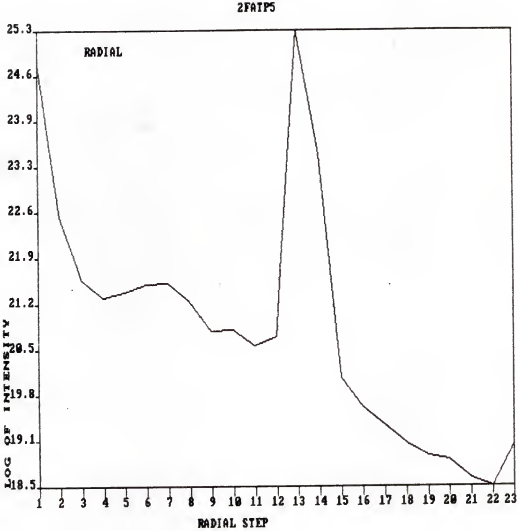

Figure 4.27 Radial plot of Fourier transform power spectrum from theoretical single curvature fatigue.

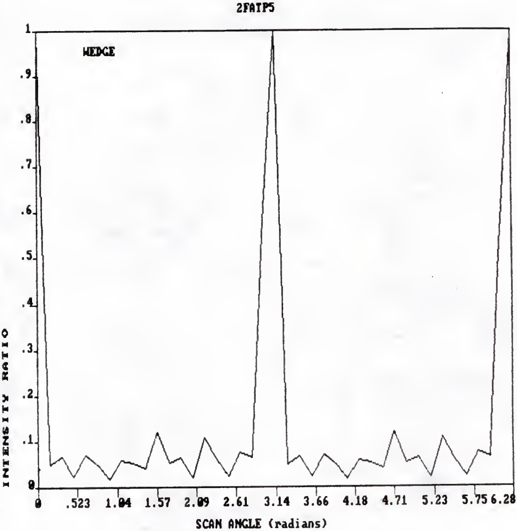

Figure 4.28 Wedge plot of Fourier transform power spectrum from theoretical single curvature fatigue.

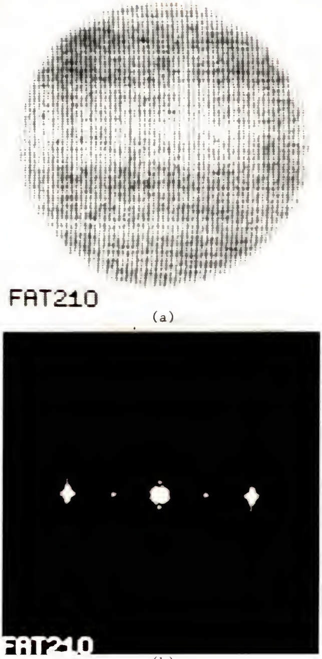

Figure 4.29 Parallel line/Fourier transform pair.
(a) Input image of theoretical fatigue as single curvature parallel lines with greater single curvature and
(b) resulting Fourier transform power spectrum.

transform power spectrum pattern is shown in Figure 4.29b. The resulting two high intensity spikes showed greater vertical spread due to the higher degree of curvature. The secondary spots were again present, due to the same input image defects in the previous example. The surface plot in Figure 4.30 was nearly identical to the previous surface plot in Figure 4.26, except for greater spread in the spikes from the input image curvature. The radial plot, Figure 4.31, reflected the increased spread. The input image had a spacing of 1.5 mm and the transform pattern had a spacing of 24.5 mm, corresponding to ring 13 on the radial plot. The wedge plot, Figure 4.32, was also very similar to the previous example.

A final input image of parallel lines, with double curvature, is shown in Figure 4.33a. The Fourier transform power spectrum, Figure 4.33b, showed extensive elongation of the outer spots. The spots nearer the dc spike were the primary spots from the parallel, double curved lines. The outer spots were harmonics of the two primary spots. The surface plot, Figure 4.34, showed the spread of the spikes from the curvature of the parallel lines. The radial plot, Figure 4.35, illustrated the spread and the radial position of the primary and secondary spikes. The input image had a spacing of 2.0 mm which resulted in a transform spacing of 17.2 mm, corresponding to the spike at ring 9 in the radial plot. The wedge plot, Figure 4.36, also showed the spread in the spikes due to the input image curvature.

The parallel line input images were models of various types of fatigue fracture striations. A fatigue crack front is often bowed, creating parallel lines with single curvature. The crack front may

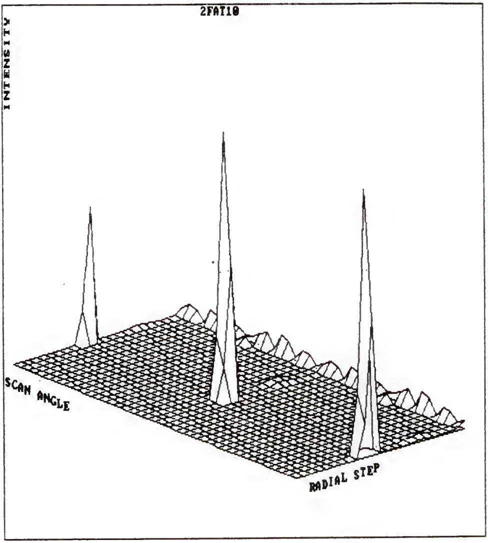

Figure 4.30 Surface plot of Fourier transform power spectrum from theoretical single curvature fatigue with greater curvature

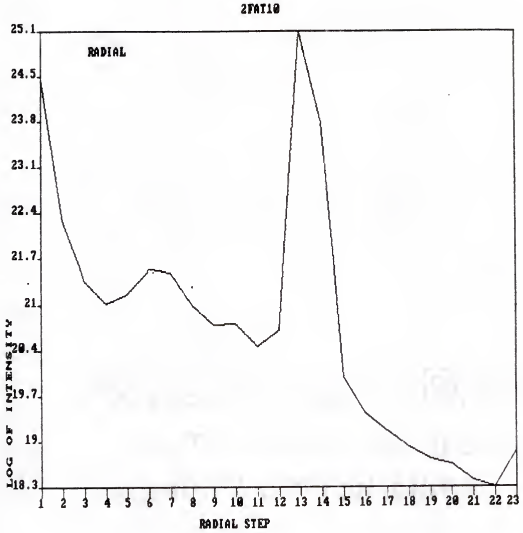

Figure 4.31 Radial plot of Fourier transform power spectrum from theoretical single curvature fatigue with greater curvature.

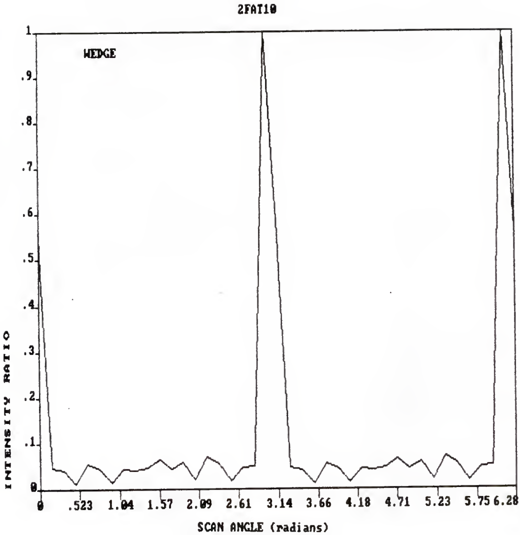

Figure 4.32 Wedge plot of Fourier transform power spectrum from theoretical single curvature fatigue with greater curvature.

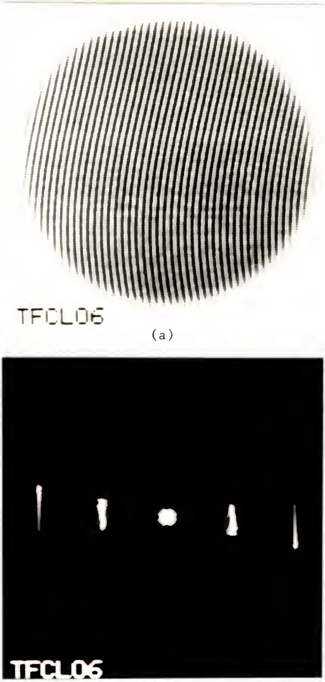

(a)

(b)

Figure 4.33 Parallel line/Fourier transform pair.
(a) Input image of theoretical fatigue as double curvature parallel lines and
(b) resulting Fourier transform power spectrum.

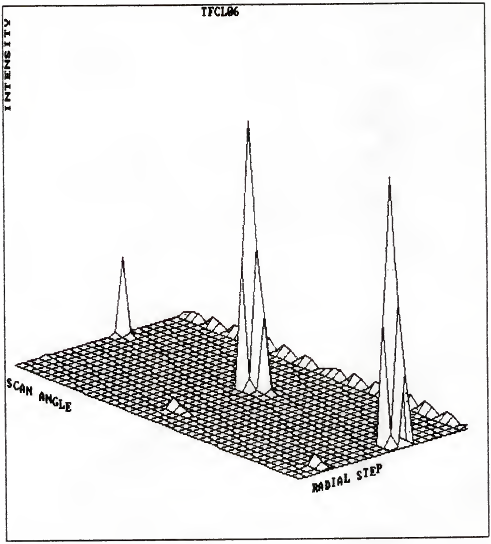

Figure 4.34 Surface plot of Fourier transform power spectrum from theoretical double curvature fatigue.

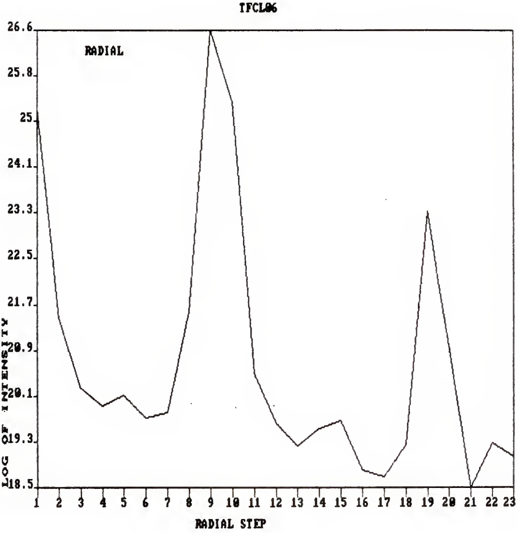

Figure 4.35 Radial plot of Fourier transform power spectrum from theoretical double curvature fatigue.

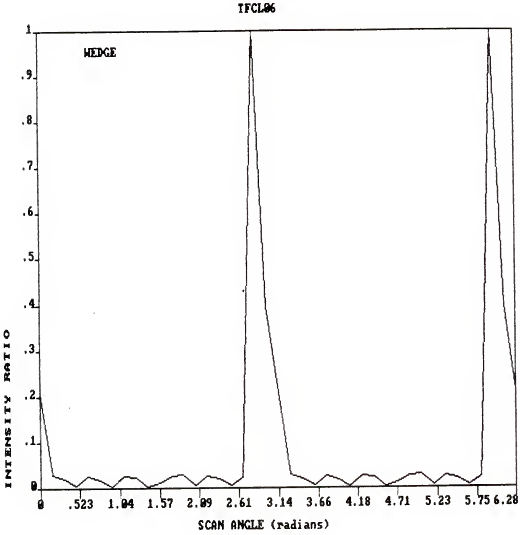

Figure 4.36 Wedge plot of Fourier transform power spectrum from theoretical double curvature fatigue.

be retarded by intercept of microstructural constituents such as inclusions, resulting in a crack front with double curvature. Thus the three types of lines represented several types of fatigue fracture. The remaining theoretical models examined were composed of equiaxed cellular structures (ASTM grain size charts) to simulate the equiaxed features that occur in dimple rupture, cleavage, and intergranular fractures.

The input image shown in Figure 4.37a is the digitized ASTM grain size 2 chart with an average feature spacing of 18 mm. The resulting Fourier transform power spectrum is shown in Figure 4.37b. The spot pattern was essentially uniform with most of the spots clustered about the dc spike. The surface plot, Figure 4.38, revealed the uniformity of the equiaxed input structure. The radial plot, Figure 4.39, showed a steeply decreasing curve with minor inflections present. The wedge plot, Figure 4.40 revealed the presence of a small degree of preferred orientation in the input image. The two valleys in the plot indicated that a lower number of grain boundary lines were aligned with a perpendicular repeat direction oriented 1.57 and 4.71 radians (±90 degrees) from the right horizontal axis. Examination of the input image in Figure 4.37a showed a decreased number of horizontal grain boundary lines. The preferred orientation was probably due to the subjectiveness of the individual who drew the charts.

Figure 4.41a shows the ASTM grain size 4 chart input image, with an average feature spacing of 9 mm. The corresponding Fourier transform power spectrum is shown in Figure 4.41b with a ring of spots arranged around the dc spike. The ring was due to a uniform

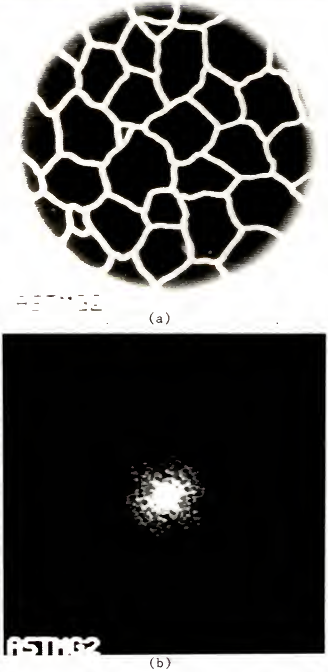

Figure 4.37 Cellular structure/Fourier transform pair.
(a) Input image of theoretical multifaceted cellular structure as ASTM grain size 2 chart and
(b) resulting Fourier transform power spectrum.

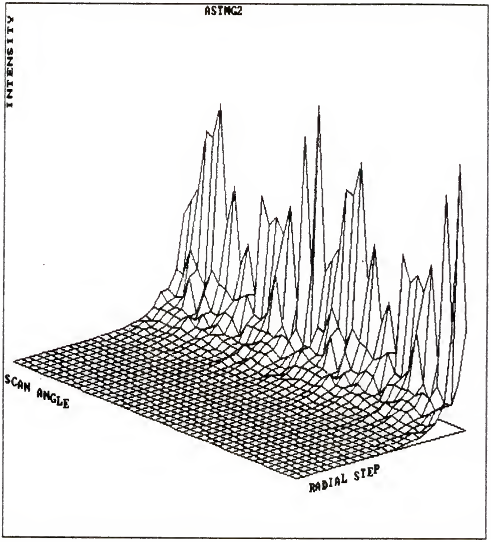

Figure 4.38 Surface plot of Fourier transform power spectrum from ASTM grain size 3 chart.

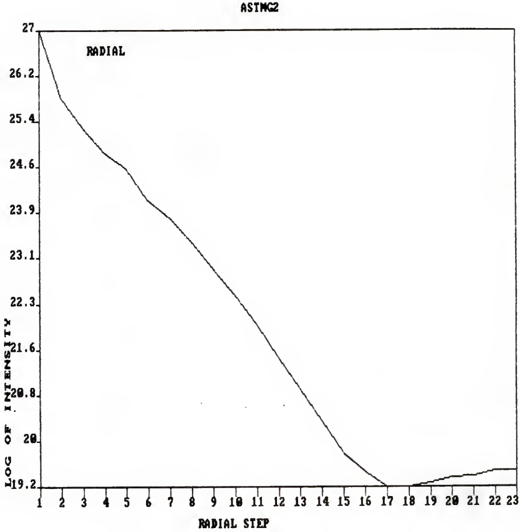

Figure 4.39 Radial plot of Fourier transform power spectrum from ASTM grain size 2 chart.

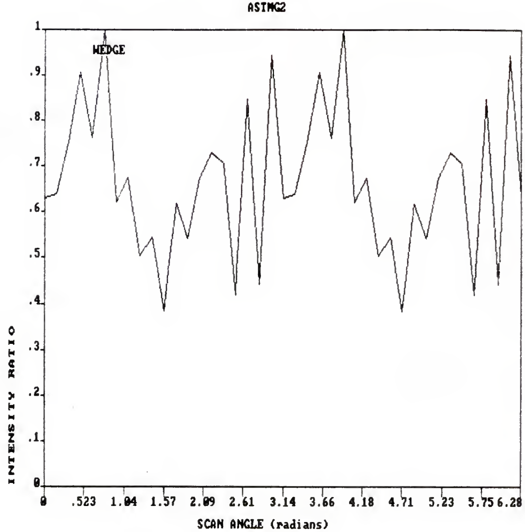

Figure 4.40 Wedge plot of Fourier transform power spectrum from ASTM grain size 2 chart.

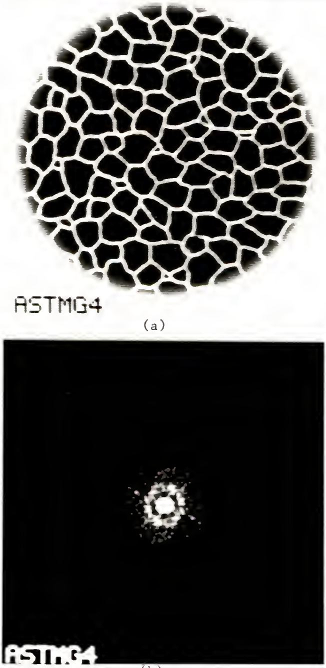

(a)

(b)

Figure 4.41 Cellular structure/Fourier transform pair.
(a) Input image of theoretical multifaceted cellular structure as ASTM grain size 4 chart and
(b) resulting Fourier transform power spectrum.

repeat dimension of equiaxed cells in the input image. The surface plot, Figure 4.42, reflected the uniformity of the input image repeat features and showed the ring of spots as a row of spikes located at the base of the back row spikes. The radial plot, Figure 4.43, showed that the average feature size of 9 mm in the input image resulted in a transform image with a ring of spots located approximately 4.4 mm from the center of the transform, corresponding to ring 2 of the radial plot. The wedge plot, Figure 4.44, indicated the presence of a small degree of preferred orientation. The spike located at approximately 1.04 radians (60 degrees) in the wedge plot indicated a repeat pattern direction approximately 1.04 radians (60 degrees) counterclockwise from the right horizontal position in the input. Examination of the input image revealed a significant number of lines in the grain size chart aligned almost parallel. This observation was enhanced by viewing the page at a low angle and rotating the image until the parallel lines become aligning with the viewing direction.

Figure 4.45a shows the ASTM grain size 6 chart input image with an average repeat feature size of approximately 4.5 mm. The Fourier transform power spectrum, Figure 4.45b, showed a ring of spots indicating a uniform distribution of repeat features. The surface plot, Figure 4.46, showed the row of spikes from the transform pattern. The radial plot, Figure 4.47, showed the row to be located at ring 5. The input image with an average spacing of 4.5 mm produced a transform pattern with a spacing of 8.5 mm that correspond to ring 5 in the radial plot. The wedge plot, Figure 4.48, showed no significant preferred orientation.

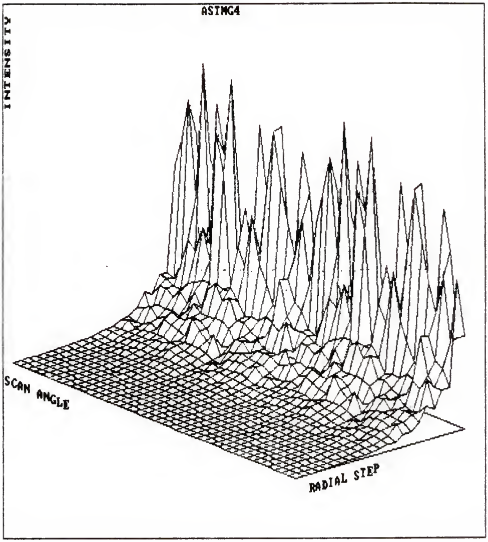

Figure 4.42 Surface plot of Fourier transform power spectrum from ASTM grain size 4 chart.

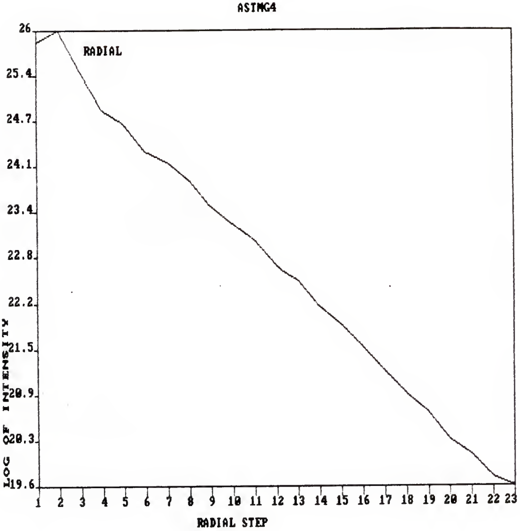

Figure 4.43 Radial plot of Fourier transform power spectrum from ASTM grain size 4 chart.

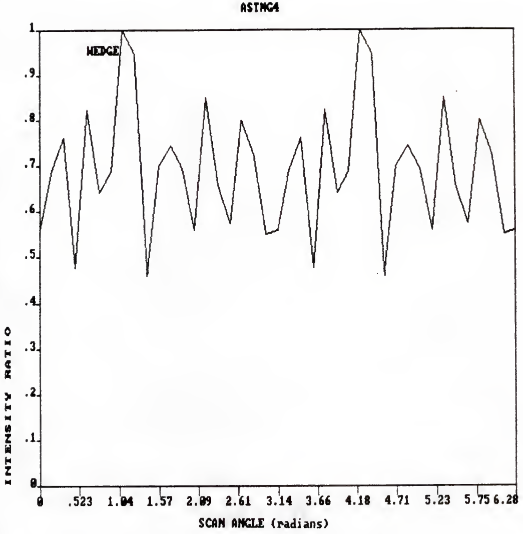

Figure 4.44 Wedge plot of Fourier transform power spectrum from ASTM grain size 4 chart.

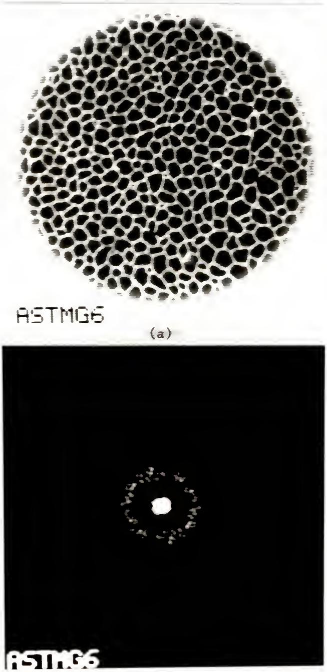

Figure 4.45 Cellular structure/Fourier transform pair.
(a) Input image of theoretical multifaceted cellular structure as ASTM grain size 6 chart and
(b) resulting Fourier transform power spectrum.

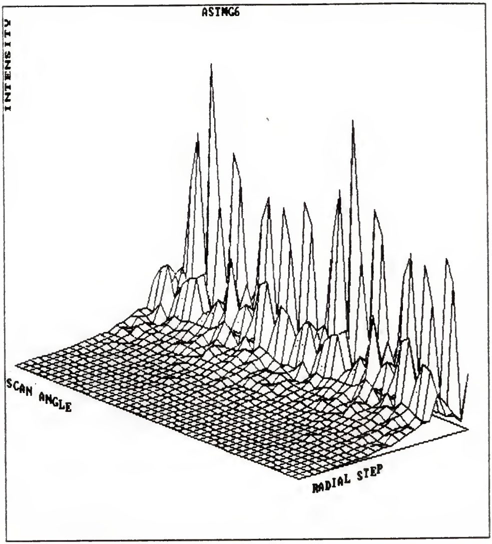

Figure 4.46 Surface plot of Fourier transform power spectrum from ASTM grain size 6 chart.

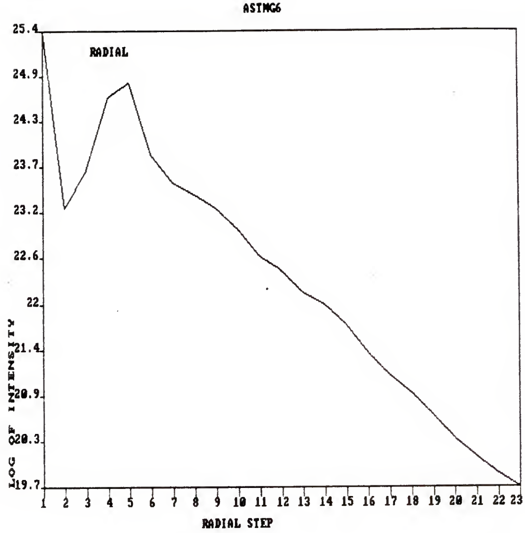

Figure 4.47 Radial plot of Fourier transform power spectrum from ASTM grain size 6 chart.

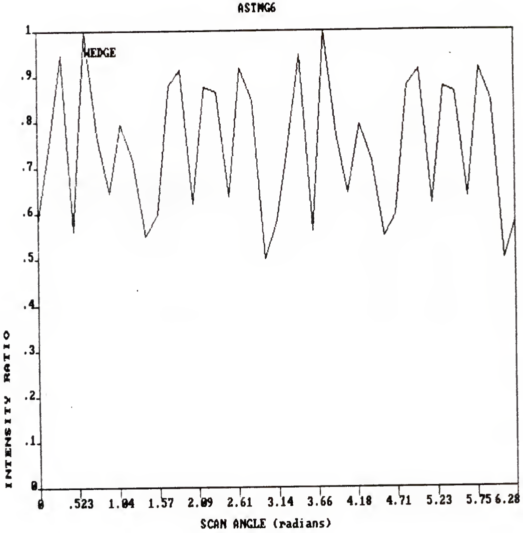

Figure 4.48 Wedge plot of Fourier transform power spectrum from ASTM grain size 6 chart.

Figure 4.49a shows the ASTM grain size 7 chart input image with an average repeat feature spacing of about 3.2 mm. The corresponding Fourier transform power spectrum, shown in Figure 4.49b, indicated significant preferred orientation in the input image. The surface plot, Figure 4.50, also indicated the preferred orientation by the presence of higher spikes with associated radial ridges. The radial plot, Figure 4.51, showed that the ring was located in ring position 7, which was 11.4 mm from the center of the transform, corresponding to the input image repeat spacing of 3.2 mm. The wedge plot, Figure 4.52, clearly showed the preferred orientation present in the input image. It indicated that the extra parallel lines in the input image had a repeat direction oriented approximately 2.6.radians (150 degrees) counterclockwise from the horizontal axis in the input image. Visual examination of the input image at a low angle of incidence at the 150 degree direction again revealed the parallel lines. Thus, the Fourier transform power spectrum and associated sampling techniques formed a powerful tool for image analysis that revealed image features not readily apparent to the observer.

Calibration of the Fourier transform power spectrum was performed by analysis of the test grid patterns, the parallel lines and the equiaxed cellular structures at a range of magnifications that extended over the limits of the transform power spectrum. The calibration was required to evaluate the feasibility of making quantitative measurements of fracture surface features. The photographs of the input image and transform patterns were all made to approximately the same magnification to allow measurements to be made directly from the photographs. The results from photographic

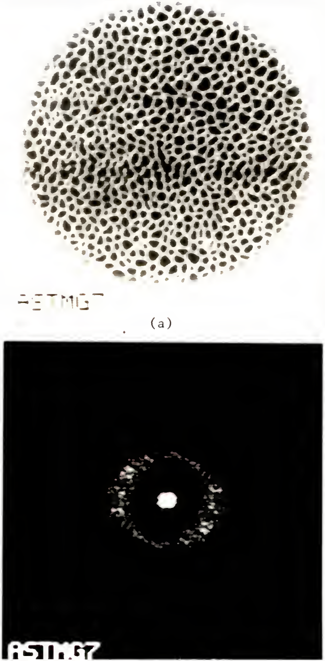

(a)

(b)

Figure 4.49 Cellular structure/Fourier transform pair.
(a) Input image of theoretical multifaceted cellular structure as ASTM grain size 7 chart and
(b) resulting Fourier transform power spectrum.

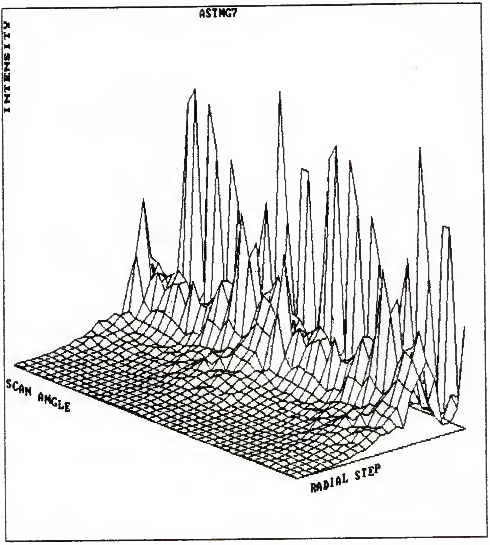

Figure 4.50 Surface plot of Fourier transform power spectrum from ASTM grain size 7 chart.

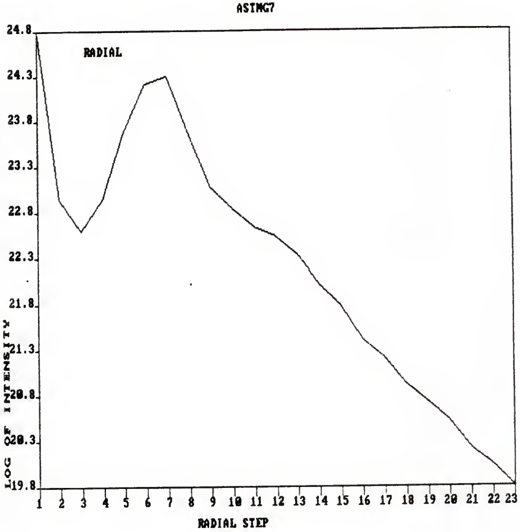

Figure 4.51 Radial plot of Fourier transform power spectrum from ASTM grain size 7 chart.

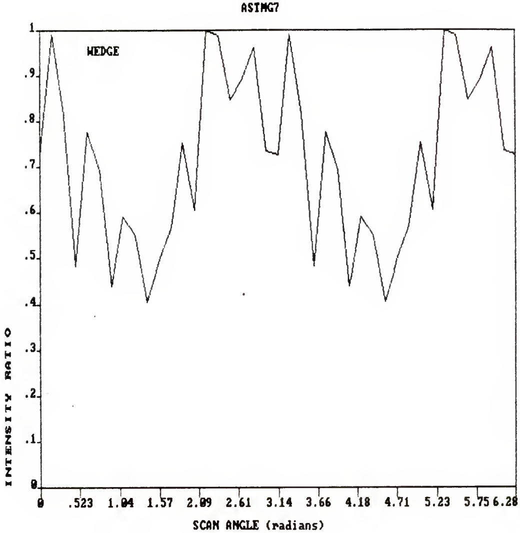

Figure 4.52 Wedge plot of Fourier transform power spectrum from ASTM grain size 7 Ochart.

measurements were compared to the generated plotted radial plots. Identical correlations resulted. Figure 4.53 shows a plot of the input pattern repeat dimension in pixels compared to the input dimension in millimeters. The correlation was made by relating the circular window, with a 256 pixel diameter, to the measured diameter of the window. This approach allowed measurements of repeat feature dimensions in each input image photograph to be expressed as pixels, avoiding errors from photographic magnification variations. The correlation plot for input repeat dimension expressed as millimeters or pixels led to a correlation of approximately 3.2 pixels per millimeter for the input image photographs.

A further correlation between the input pattern repeat dimension and the Fourier transform power spectrum spot spacing was made. For each feature of interest in each of the input theoretical model images, the repeat spacings were correlated to the spot distance from the transform center. Some of the theoretical model patterns were analyzed at half magnification to extend the correlation for fine features. Figure 4.54 shows the correlation with the input feature dimension and the transform spot pattern location both expressed in millimeters. For very small input pattern dimensions the transform pattern has extremely high sensitivity; a change in input spacing from one to two millimeters causes the corresponding spot pattern to change from approximately 20 mm to approximately 10 mm. For very large input pattern dimensions the transform pattern has extremely low sensitivity; a change in input spacing from 10 mm to 20 millimeters results in a spot location change from about 2 to 1 millimeters. The correlation curve in Figure 4.54 showed the optimum

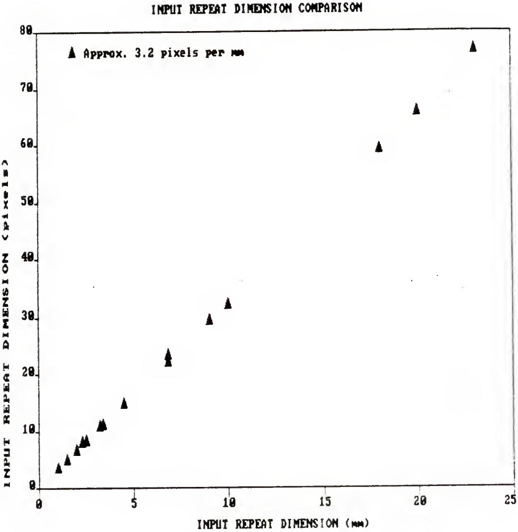

Figure 4.53 Correlation of input pattern repeat dimension to number of pixels.

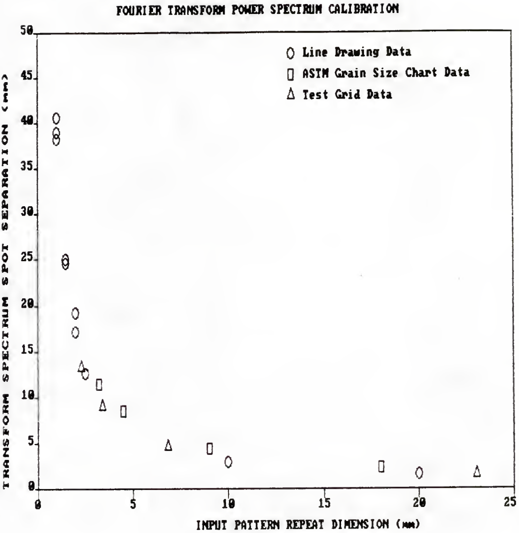

Figure 4.54 Correlation of input image repeat dimension to Fourier transform power spectrum spot separation.

range of input feature spacings to be from one to ten millimeters. The plot is also shown in Figure 4.55 with the transform pattern spot location plotted as ring position. Instead of measuring the spot location on the photograph for each image, the ring position was taken from the radial plot. Thus the plot in Figure 4.55 is less dependent of photographic measurements while retaining the identical form of the curve produced from photographic measurements in Figure 4.54. The correlation of spot location in the transform pattern in millimeters to the ring position is shown in Figure 4.56. The measurements led to a correlation of about 1.8 mm spacing in the transform image photograph per ring position in the radial plot. Figure 4.57 shows the input-output correlation plot with the input image spacing expressed in pixels and the transform pattern spot location expressed as ring number. Again, the correlation was identical to the previous input-output correlations.

4.4 Digital Fractographic Pattern Classification

In order to evaluate the ability of the Fourier transform power spectrum to classify the primary classes of fracture features, four representative fractographs were selected. A single magnification was used for the analysis of each of the fractographs. The magnification was chosen after evaluation of ten fracture specimens at four magnifications each, with as many as four areas of the fractograph sampled at each magnification. Evaluation of the resulting patterns indicated that for the specimens used, an input image magnification of 250X produced features that had a sufficient

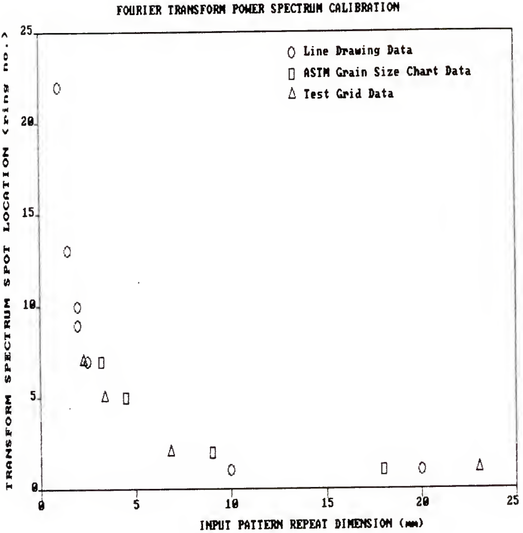

Figure 4.55 Calibration of input image repeat dimension in millimeters to Fourier transform power spectrum spot location ring number.

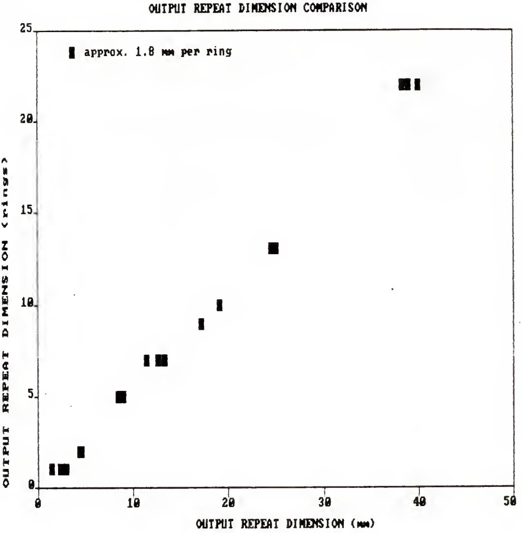

Figure 4.56 Correlation of output pattern repeat dimension to ring number.

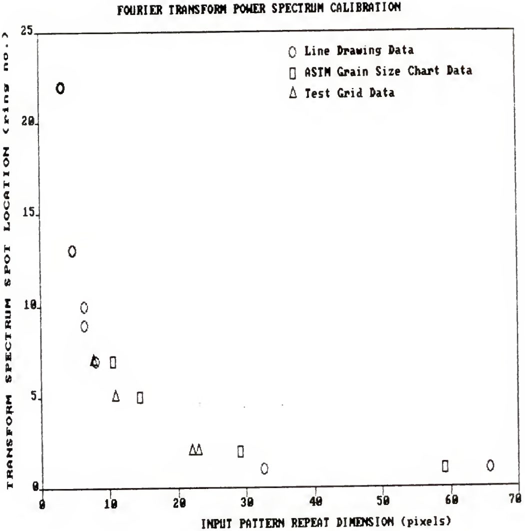

Figure 4.57 Calibration of input image repeat dimension in pixels to Fourier transform power spectrum spot location ring number.

number of repeat units to allow Fourier transform comparison and classification. Other magnifications that were evaluated revealed different fracture surface features in a similar manner to fractal analysis which produces different dimensional measurements for different magnifications. To objectively evaluate the potential of the digital fractographic imaging analysis technique, the single magnification was utilized in the study. The four fractographs selected demonstrated typical features for microvoid coalescence, cleavage, fatigue, and decohesive rupture. For each fractograph the input image, the resulting Fourier transform power spectrum, the surface plot, radial plot, first difference of the radial plot, ring plot and wedge plot were generated. Each transform pattern and associated plots provide an objective description of the input image repeat feature pattern.

4.4.1 Microvoid Coalescence Dimples

The specimen that best typified tensile dimples resulting from microvoid coalescence was the 4340 quenched and tempered steel tailhook from the attack aircraft. Figure 4.58a shows the input image composed of dimples of various sizes arranged in pockets. The corresponding Fourier transform power spectrum, shown in Figure 4.58b, indicated a uniform structure with no strong indications of directionality or specific strong repeat frequency in the input image. The surface plot, Figure 4.59, was also uniform. The radial plot, Figure 4.60, was almost linear from the edge of the dc spike to the outermost ring. To amplify the slope changes in the radial curve, the first difference curve was plotted as shown in Figure

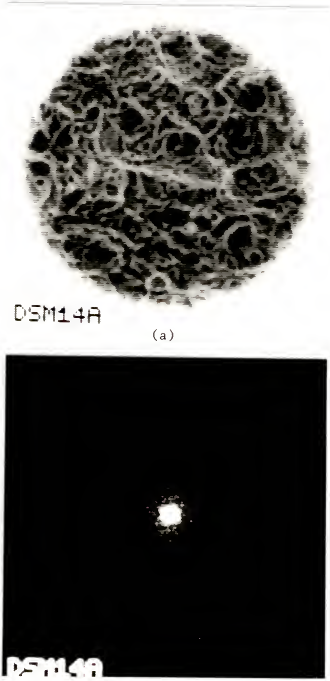

(a)

(b)

Figure 4.58 Tensile dimple image/Fourier transform pair.
(a) Input image of fine tensile dimples from tailhook and
(b) resulting Fourier transform power spectrum.

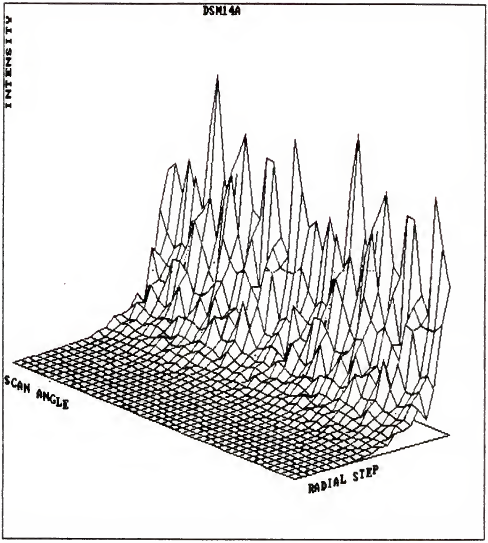

Figure 4.59 Surface plot of Fourier transform power spectrum from fine tensile dimples.

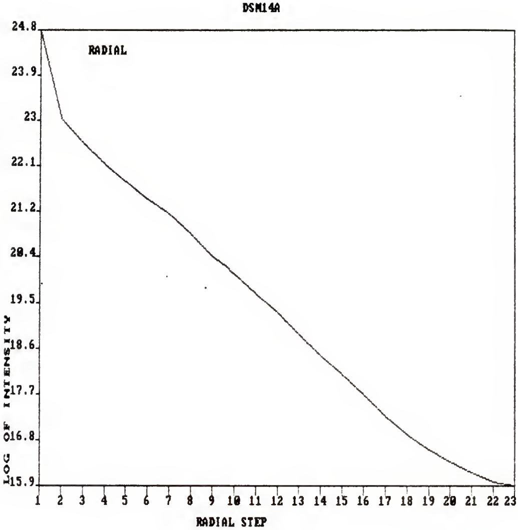

Figure 4.60 Radial plot of Fourier transform power spectrum from fine tensile dimples.

4.61. The curve reached a constant negative slope at the second ring and remained constant to almost the last ring. The slope changes in the radial plot caused by the presence of repeat frequencies are shown as inflections in the first difference plot. The plot in Figure 4.61 showed inflections at ring 8, 10 and 20. Examination of the calibration curve in Figure 4.55 revealed an input image spacing of 2.4 mm, 2.2 mm and 1.1 mm. The transform image also had low frequency spots near the dc spike which corresponded to a spacing of 10 mm. The fine spacings (1 to 3 mm) were the approximate sizes of the dimples in the input image and the coarse spacing (10 mm) was the approximate size of the pockets of dimples. The generally high slope indicated by the radial difference plot reflected the presence of a full range of repeat sizes in the input image. The ring plot from the seventh ring is shown in Figure 4.62. The scan was initiated at the right horizontal position and proceeded counterclockwise, as with the wedge plot. It indicated the presence of minor preferred orientation in the input image. The wedge plot, Figure 4.63, also indicated the presence of orientation effects in the input image by the two frequency spikes with an initial angle of 1.04 radians (60 degrees). The spikes were located in the transform image, Figure 4.58b, near the dc spike. They were a result of the fracture ridges between pockets of dimples in the input image.

The features that appear to classify dimples are a uniform surface plot and a high slope in the radial plot indicating the uniform presence of a range of frequency components. The ring plot and wedge plot showed no directional effects for equiaxed dimples.

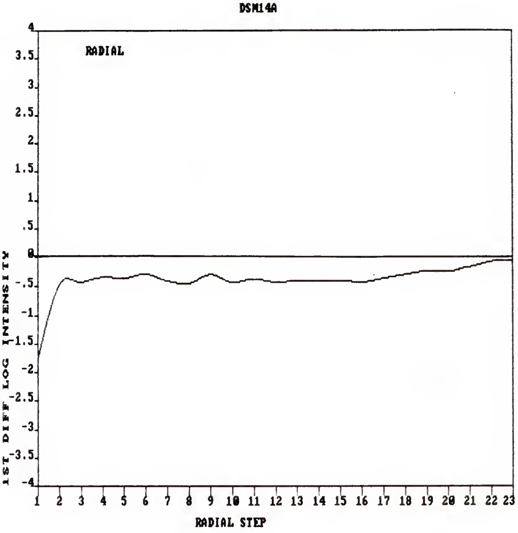

Figure 4.61 First difference of radial plot of Fourier transform power spectrum from fine tensile dimples.

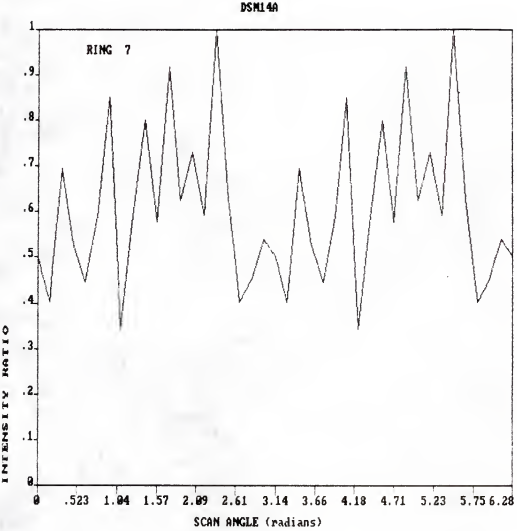

Figure 4.62 Ring plot of 7th ring of Fourier transform power spectrum from fine tensile dimples.

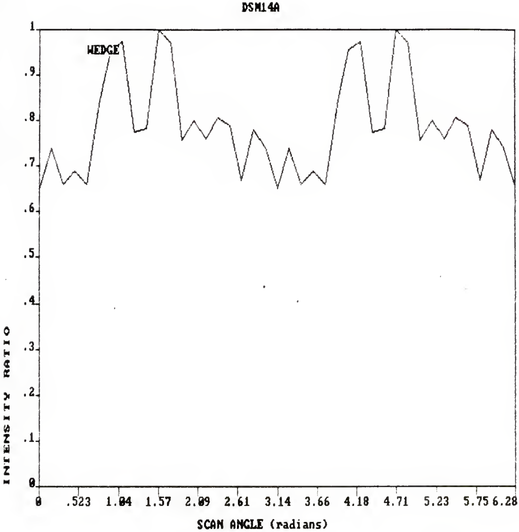

Figure 4.63 Wedge plot of Fourier transform power spectrum from fine tensile dimples.

4.4.2 Cleavage Planes

The specimen used to represent cleavage planes was the plain carbon steel specimen from the Florida Keys Bridge fractured at rifle velocity. The input image, shown in Figure 4.64a, contained cleavage river patterns on flat cleavage facets. The resulting Fourier transform power spectrum is shown in Figure 4.64b. The transform pattern indicated the presence of coarse features, by the presence of spots close to the dc power spike and directionality in the input image by the spread in the transform pattern. The surface plot, Figure 4.65, clearly demonstrated the directionality that was present. There were four major spikes indicating two primary repeat directions. The radial plot, Figure 4.66, showed greater curvature than the previous radial plot for dimples, indicating the absence of some higher frequency components. Figure 4.67, the first difference of the radial plot, showed specific inflections at rings 5, 9, 14 and 22 corresponding to an input image spacing ranging from 3.4 to 1.0 mm. Coarse features of approximately 10 mm spacing were also indicated by the spots in the transform power spectrum image close to the dc spike. Each of the spacings corresponded to the spacings of the river patterns at certain positions. The radial difference plot showed a slowly rising slope. The ring plot, Figure 4.68, and the wedge plot, Figure 4.69, both indicated the presence of multiple directional features. Spikes were located at approximately 0.5, 0.8, 1.4, 1.9, 2.5 and 2.7 radians (29, 46, 80, 109, 143, 155 degrees) counterclockwise from the right horizontal axis. Two of the spikes were paired to form larger spikes which were oriented at approximately 143 and 155 degrees from the right horizontal axis.

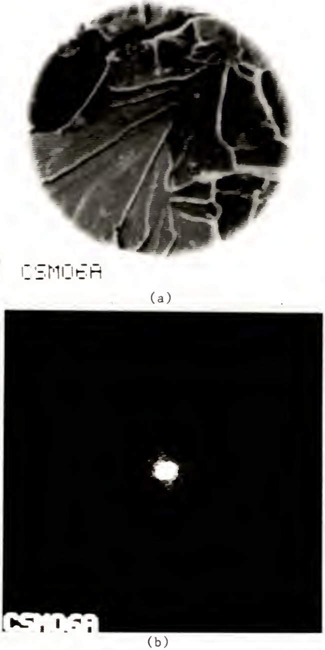

Figure 4.64 Cleavage facet image/Fourier transform pair.
(a) Input image of cleavage facets from Florida Keys Bridge steel and
(b) resulting Fourier transform power spectrum.

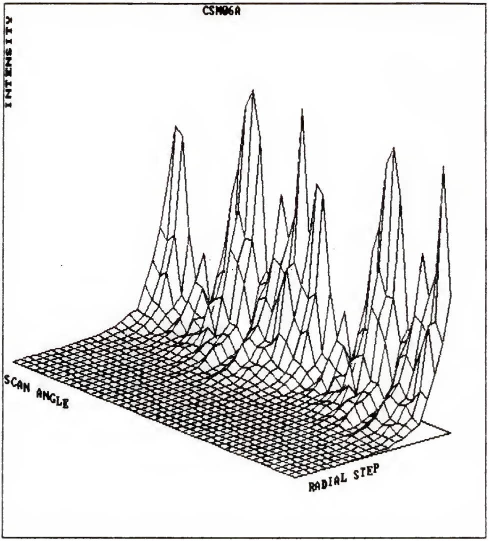

Figure 4.65 Surface plot of Fourier transform power spectrum from cleavage facets.

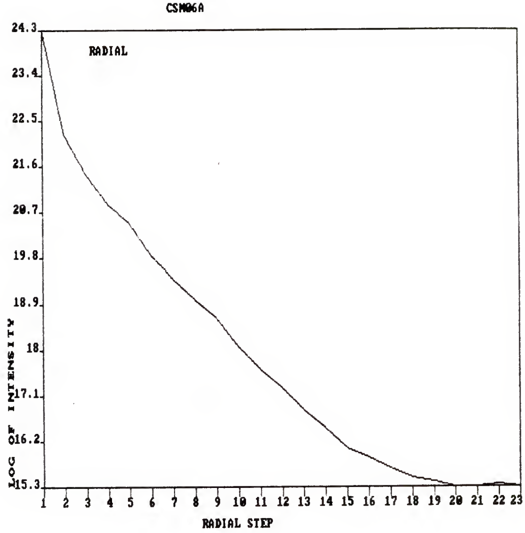

Figure 4.66 Radial plot of Fourier transform power spectrum from cleavage facets.

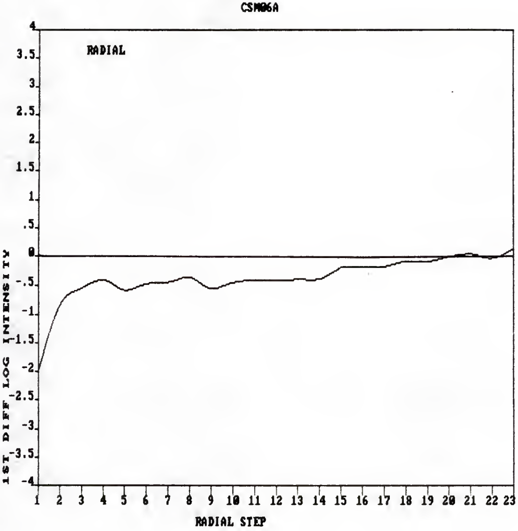

Figure 4.67 First difference of radial plot of Fourier power spectrum from cleavage facets.

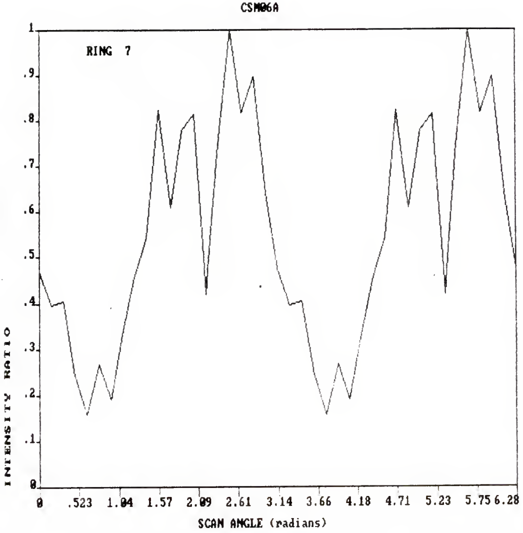

Figure 4.68 Ring plot of 7th ring of Fourier transform power spectrum from cleavage facets.

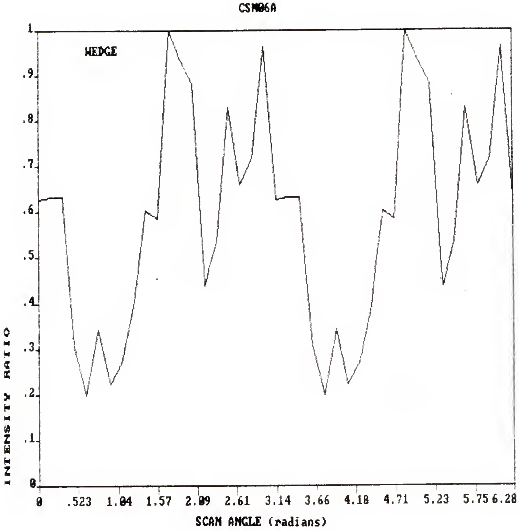

Figure 4.69 Wedge plot of Fourier transform power spectrum from cleavage facets.

Their repeat directions corresponded to the directions of the two primary river pattern angles in the input image. The Fourier transform analysis was able to detect the presence of river patterns and their angular orientation for a cleavage fracture. At a lower magnification the transform will reveal the cleavage facet size.

The primary features for classifying cleavage fracture were large multiple spikes in the surface plot and wedge plot and a slowly rising negative slope in the radial plot.

4.4.3 Fatigue Striations

The specimen used to represent fatigue striations was the 2024 aluminum hydraulic cylinder which failed in fatigue. The input image of the fatigue fracture is shown in Figure 4.70a. The fatigue striations were equally spaced and had multiple curvature. The Fourier transform power spectrum is shown in Figure 4.70b. The pattern showed the central dc spike from the tapered window and two outer spikes that represented the fatigue striations. The two spikes were elongated horizontally indicating the presence of curvature in the input image parallel lines. The surface plot, Figure 4.71, showed two extremely distinct spikes. The radial plot, Figure 4.72, showed the presence of the principal spike at ring 4. This corresponded to an input feature spacing of approximately 4 mm. Measurement of the striation spacing in the input image revealed a repeat spacing of 4 mm. The radial difference plot, Figure 4.73, showed inflections at rings 4, 8, 14 and 16. The fourth ring corresponded to a spacing of 5.0 mm, the striation spacing. The other rings corresponded to features with spacings of 2.5 to 1.4 mm.

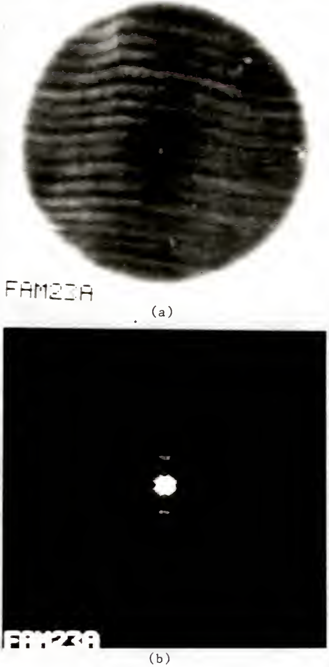

Figure 4.70 Fatigue striation image/Fourier transform pair. (a) Input image of fatigue striations from aluminum hydraulic cylinder and (b) resulting Fourier transform power spectrum.

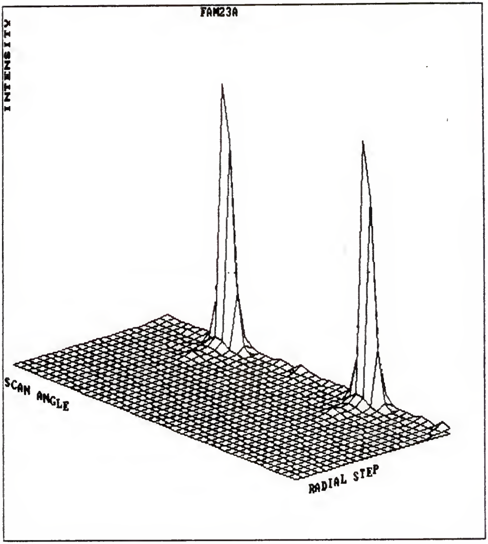

Figure 4.71 Surface plot of Fourier transform power spectrum from fatigue striations.

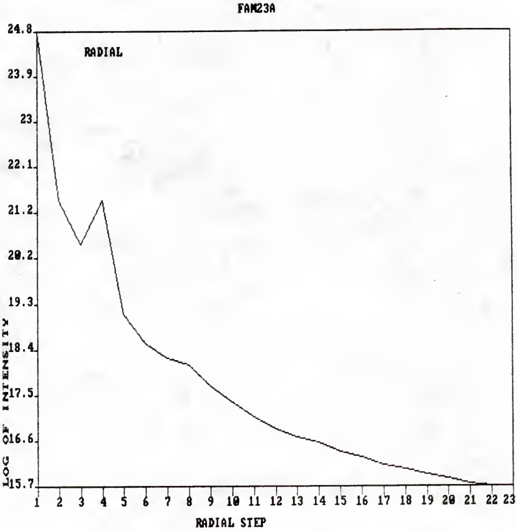

Figure 4.72 Radial plot of Fourier transform power spectrum from fatigue striations.

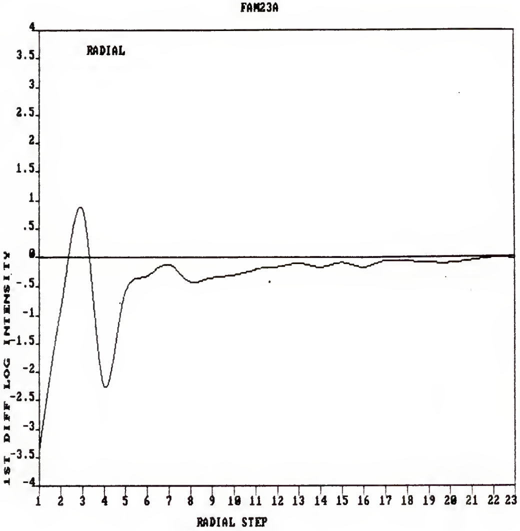

Figure 4.73 First difference of radial plot of Fourier transform power spectrum from fatigue striations.

These fine spacings were not readily apparent in the input image and it is probably that they were actually due to harmonic spots in the transform pattern due to the large primary spikes. The ring plot, Figure 4.74, and the wedge plot, Figure 4.75, showed the two principal spikes and the spread in the spikes due to curvature of the striations.

The Fourier transform power spectrum for fatigue was the most unique for all the fracture modes and was the easiest to classify by the dual spots in the transform pattern or dual spikes in the surface plot. Fatigue also showed strong curvature in the radial plot due to the absence of a full range of frequency components. The Fourier transform had the ability to detect the presence of striations, to automatically measure the striation spacing, and to isolate frequency components produced by random loading.

4.4.4 Intergranular Facets

The specimen used to represent intergranular fracture was the 4340 quenched and tempered steel helicopter axle fractured by hydrogen assisted cracking. The input image is shown in Figure 4.76a and the corresponding Fourier transform power spectrum is shown in Figure 4.76b. The transform pattern indicated the presence of coarse features in the input image as evidenced by the collection of spots close to the dc power spike. The transform pattern also indicated directionality by the collection of spots at the top and bottom of the dc power spike. The surface plot, Figure 4.77, indicated no strong orientation effects or repeat features. The radial plot, Figure 4.78, showed moderate curvature. The radial difference plot,

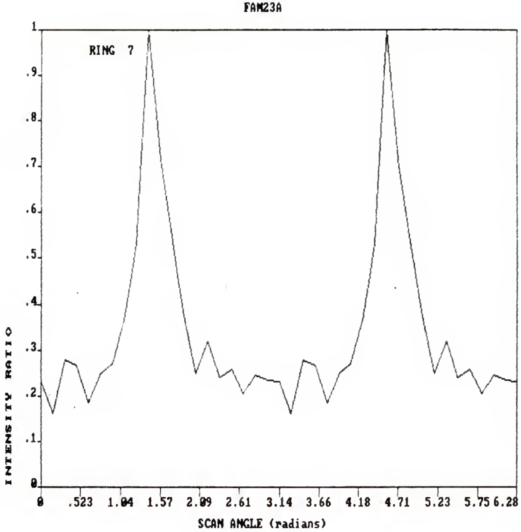

Figure 4.74 Ring plot of 7th ring of Fourier transform power spectrum from fatigue striations.

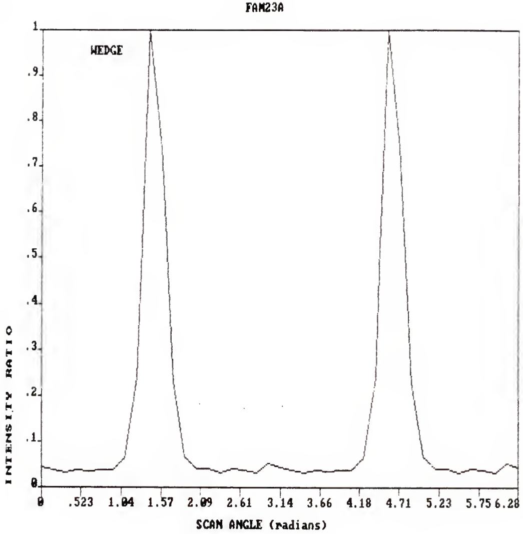

Figure 4.75 Wedge plot of Fourier transform power spectrum from fatigue striations.

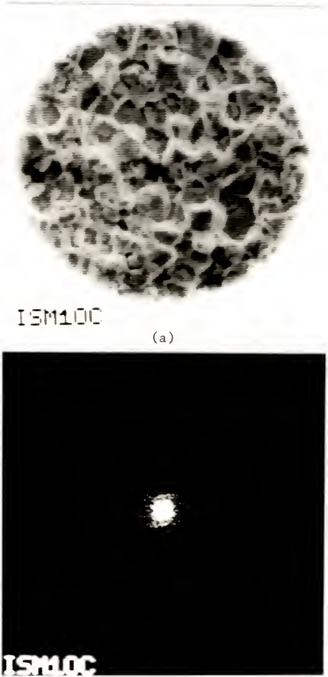

(a)

(b)

Figure 4.76 Intergranular facet image/Fourier transform pair.
(a) Input image of intergranular fracture from hydrogen assisted cracking in axle and
(b) resulting Fourier transform power spectrum.

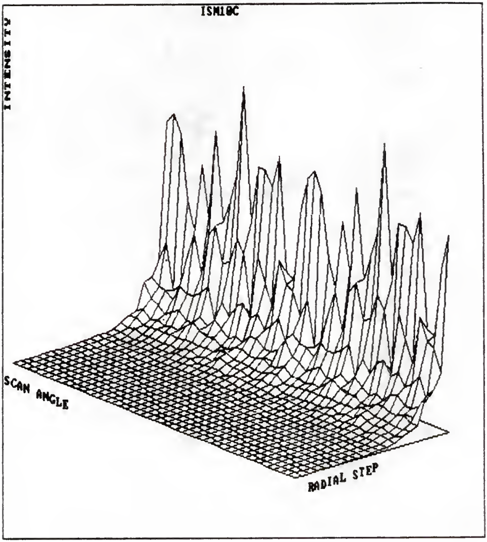

Figure 4.77 Surface plot of Fourier transform power spectrum from intergranular hydrogen assisted cracking facets.

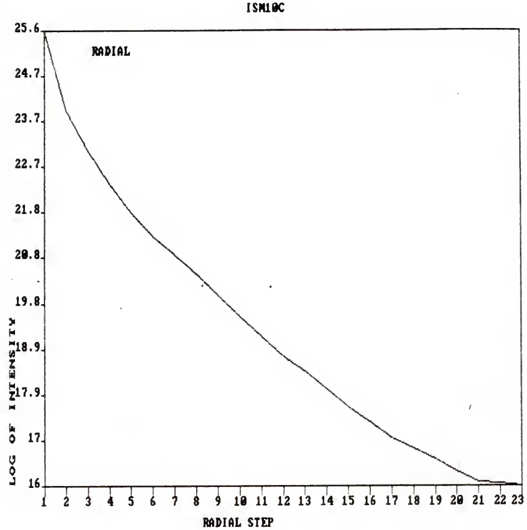

Figure 4.78 Radial plot of Fourier transform power spectrum from intergranular hydrogen assisted cracking.

Figure 4.79, showed a slowly changing negative slope with minor inflections. The size of the minor inflections indicated a limited number of repeat units for the size classes. A small inflection was present between rings 4 and 5 which corresponded to an input repeat pattern spacing of about 5 mm. Low frequency components were contained in the transform pattern near the dc spikes with a spacing of 3.5 mm, corresponding to an input image spacing of 10.0 mm. The intergranular facets in the input image had a projected diameter of approximately 10.0 mm. Other facets in the input image had projected diameters of approximately 5 mm. Smaller facets were also present as indicated by the outlying inflections in the radial difference curve. The ring plot, Figure 4.80, showed some directionality in the input image but the wedge plot, Figure 4.81, showed less indication of directionality. The directionality was apparently stronger in the facets with a size corresponding to ring 7 as represented by the ring plot. The directionality was a result of grain elongation from the forging process used to manufacture the axle.

The features used to classify intergranular fracture were a uniform pattern in the surface plot, moderate curvature of the radial plot and a few outlying inflections in the radial difference plot. Intergranular fracture transform features were similar to dimple rupture fracture features. A primary difference was the lower slope of the radial plot due to fewer high frequency components present in the intergranular fracture images. The Fourier transform analysis was able to determine the size of facets, the proportion of facets within a given size class and the presence of grain elongation.

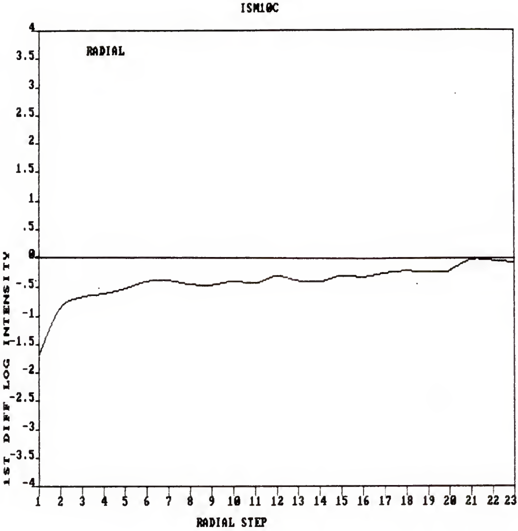

Figure 4.79 First difference of radial plot of Fourier transform power spectrum from intergranular hydrogen assisted cracking facets.

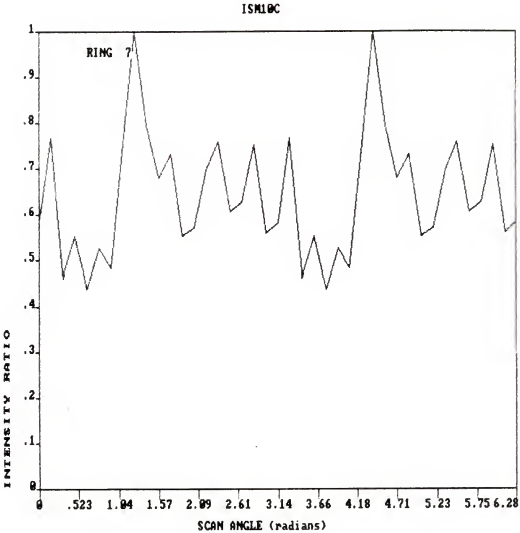

Figure 4.80 Ring plot of 7th ring of Fourier transform power spectrum from intergranular hydrogen assisted cracking facets.

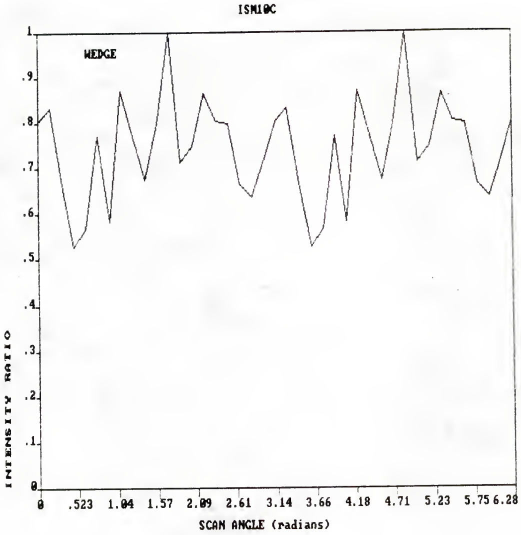

Figure 4.81 Wedge plot of Fourier transform power spectrum from intergranular hydrogen assisted cracking facets.

4.5 Digital Fractographic Pattern Characterization

The two-dimensional Fourier transform has the potential for fractographic feature classification of specific patterns and for characterization of descriptive information concerning a certain pattern. The characterization can produce information on feature orientation, feature size, and quantity of features of a given size, class and spacing.

4.5.1 Fatigue Striation Density

The fatigue fracture example given in section 4.4.3 clearly demonstrated the potential of Fourier transform analysis to extract striation frequency data from the input image. However, the striations in that example were nearly perfect. A less than perfect fatigue fractograph is shown in Figure 4.82a. The specimen was the 2014-T6 helicopter main rotor blade spar that failed in fatigue and separated in flight. The striations were extremely fine and thus the magnification required to resolve the striations prior to digitization was 13,500X. The fracture pattern had indications of a mixed load cycle with varying load amplitude. Counting striations in the SEM fractograph was extremely difficult. The Fourier transform analysis was applied to the fractograph to extract the striation spacing information. The resulting Fourier transform power spectrum, Figure 4.82b, showed an orientation of spots corresponding to the repeat direction in the input image. Figure 4.83 shows the surface plot for the transform power spectrum. The two distinct spikes corresponded to the spots in the transform pattern. The radial

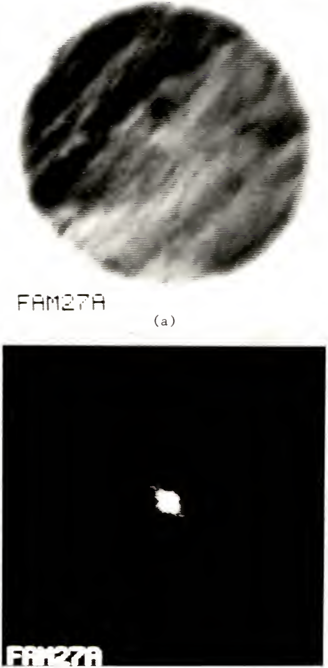

(a)

(b)

Figure 4.82 Fine fatigue striation image/Fourier transform pair.
(a) Input image of fatigue fracture with fine striations from helicopter spar at high magnification and
(b) resulting Fourier transform power spectrum.

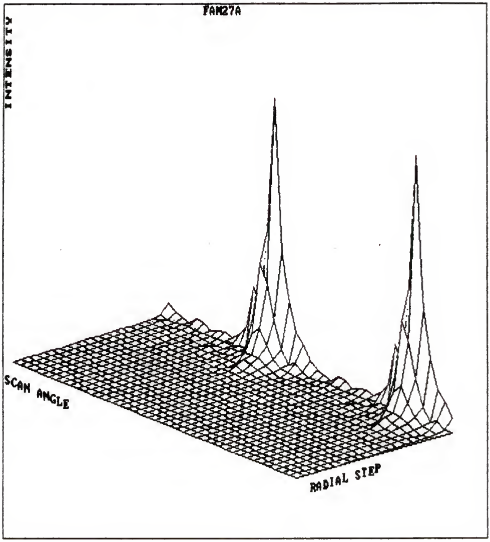

Figure 4.83 (a) Surface plot of Fourier transform power spectrum from fine striations and (b) resulting Fourier transform power spectrum.

difference plot, Figure 4.84, had 6 significant inflections at rings 7, 9, 12, 14, 16 and 18. The ring locations in the power spectrum corresponded to input repeat patterns spacings of 2.5 to 1.2 mm. Each of these striation widths may be measured in the input image. Examination of the original (undigitized) fractograph as shown in Figure 3.14b is beneficial in this case. Assuming an average fatigue striation spacing of 2 mm allows a striation analysis to be performed. The input image as shown in Figure 4.82a is at a magnification three times the undigitized image, or 40,500X. Thus the actual striation spacing on the part was 0.049 microns or 20.25 striations per micron. Conversion to English units resulted in a spacing of 514,350 striations per inch, a realistic striation density for the load cycle applied in the failure. The ring plot in Figure 4.85 and wedge plot in Figure 4.86 both revealed the presence and nature of the two spikes shown in the surface plot. Both plots showed nearly straight sided peaks which is an indication of parallel striations with no curvature. This was verified by examination of the input pattern.

4.5.2 Dimple Rupture Shear Component

The effect of dimple elongation is demonstrated to different extents in the following three examples. Figure 4.87a shows a dimple rupture pattern from the plain carbon steel bolt insert. Dimples of various sizes were present. Most of the larger dimples were elongated in one direction, probably from application of a bending load during the failure process. The corresponding Fourier Transform power spectrum is shown in Figure 4.87b. Most of the spots were

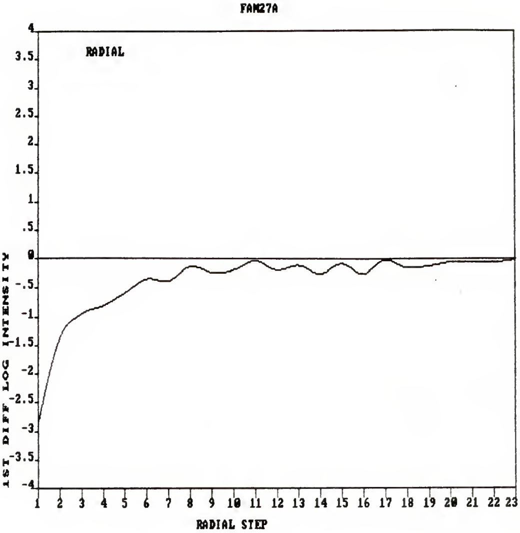

Figure 4.84 First difference of radial plot of Fourier transform power spectrum from fine striations.

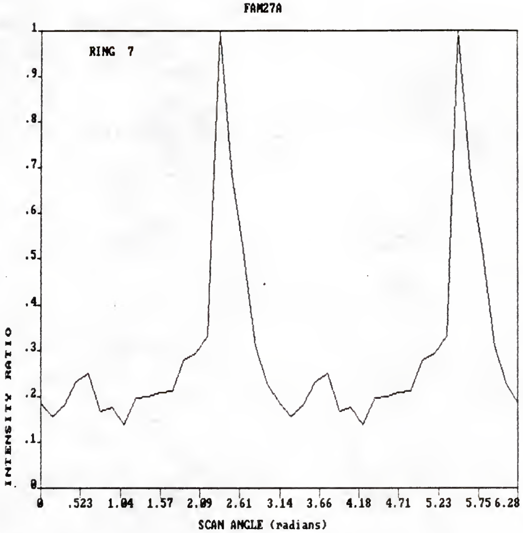

Figure 4.85 Ring plot of 7th ring of Fourier transform power spectrum from fine striations.

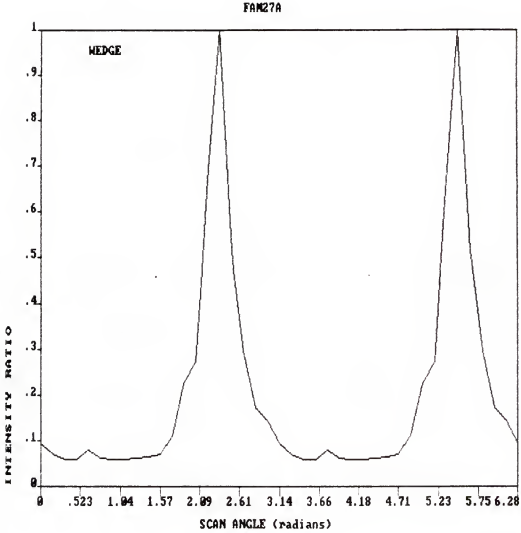

Figure 4.86 Wedge plot of Fourier transform power spectrum from fine striations.

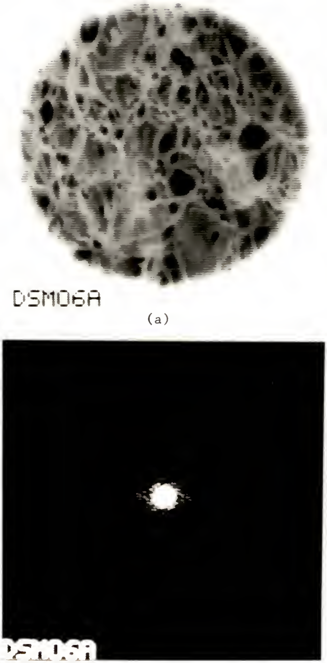

(a)

(b)

Figure 4.87 Coarse dimple image/Fourier transform pair. (a) Input image of coarse oval tensile dimples from bolt insert and (b) resulting Fourier transform power spectrum.

grouped near the central dc spike. The surface plot, Figure 4.88, showed the presence of directionality in the transform power spectrum and input image. The radial difference plot, Figure 4.89, showed several sizes of repeat patterns, corresponding to rings 5, 14, 17.5, and 20. These spacings corresponded to input dimensions of 3.4 mm to 1.1 mm. The transform power spectrum also showed spots located 4 mm from the center of the spectrum which corresponded to a input dimension of approximately 8.75 mm. Examination of the input pattern revealed that dimples of the three size classes were present. The ring plot, Figure 4.90, and the wedge plot, Figure 4.91, both revealed significant amounts of directionality in the input image. The repeat dimension was aligned over a range of 2.3 to 3.7 radians (131 to 212 degrees) counterclockwise from the right horizontal axis. This indicated smearing of the dimples along the vertical axis which was verified by examination of the input image.

A tear dimple pattern was analyzed as shown in Figure 4.92a, from the plain carbon steel bolt insert but from the edge of the specimen. The Fourier transform power spectrum, Figure 4.92b, showed no strong indication of directionality. The surface plot, Figure 4.93, also showed no strong indications of directionality. The radial difference plot, Figure 4.94, showed inflections at rings 4, 11.5, and 20, which corresponded to input spacings of 5 mm, 2.0 mm and 1.1 mm. The transform power spectrum also showed spots located 3 mm from the center of the spectrum indicating a spacing of 7 mm in the input image. Examination of the input image revealed two zones, one with large tear dimples ranging in size from 5 to 10 mm and the other zone with fine tear dimples with a size of 1 to 2 mm. The ring

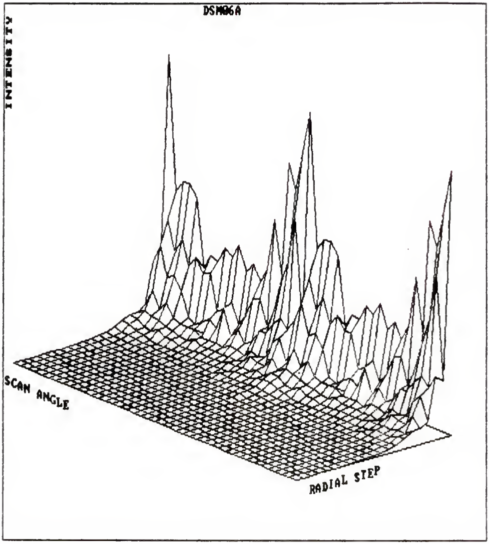

Figure 4.88 Surface plot of Fourier transform power spectrum from coarse oval dimples.

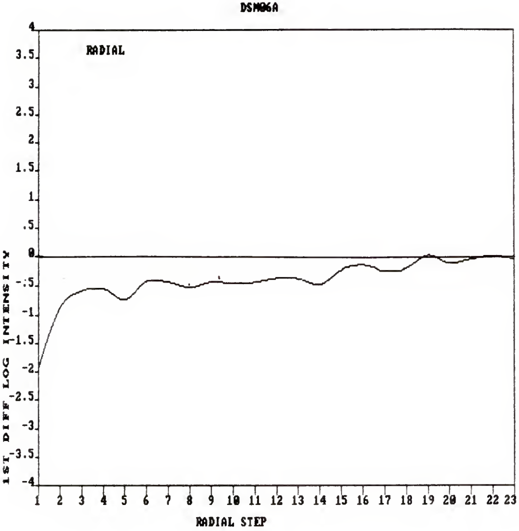

Figure 4.89 First difference of radial plot of Fourier transform power spectrum from coarse oval dimples.

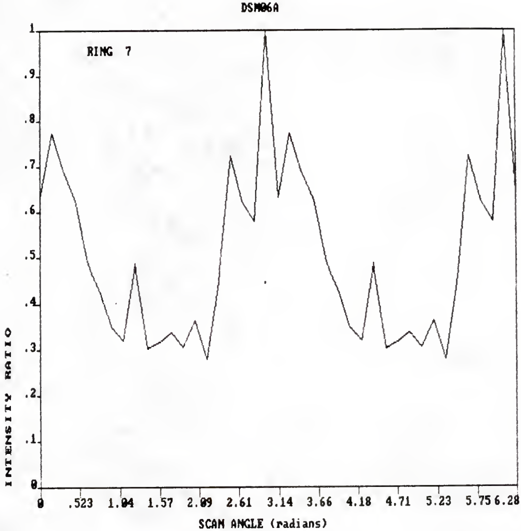

Figure 4.90 Ring plot of 7th ring of Fourier transform power spectrum from coarse oval dimples.

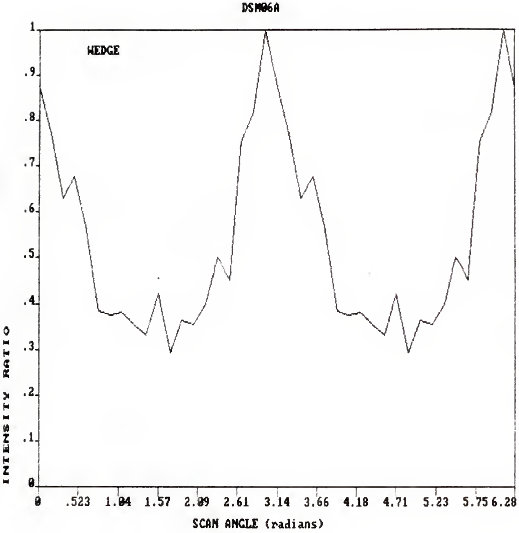

Figure 4.91 Wedge plot of Fourier transform power spectrum from coarse oval dimples.

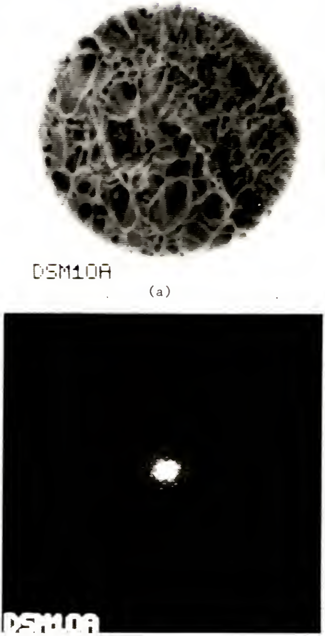

(a)

(b)

Figure 4.92 Tear dimple image/Fourier transform pair.
(a) Input image of tear dimples from bolt insert and
(b) resulting Fourier transform power spectrum.

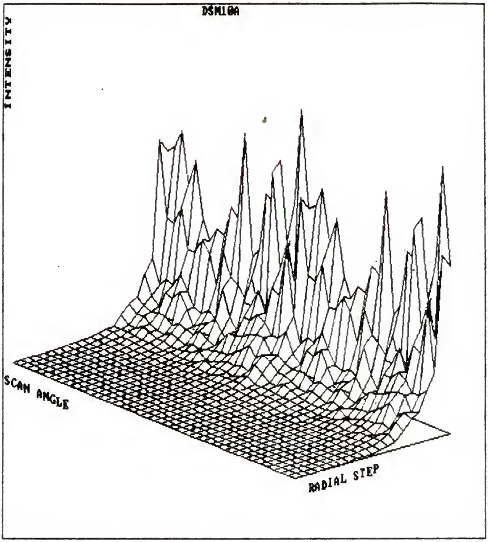

Figure 4.93 Surface plot of Fourier transform power spectrum from tear dimples.

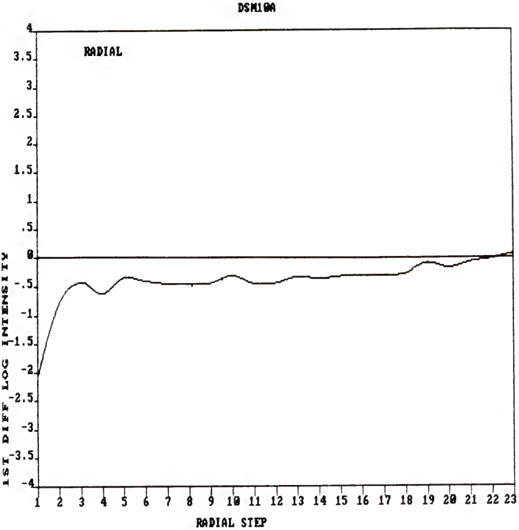

Figure 4.94 First difference of radial plot of Fourier transform power spectrum from tear dimples.

plot, Figure 4.95, and the wedge plot, Figure 4.96, both indicated directionality in the input image with the repeat direction oriented 2.6 radians (149 degrees) counterclockwise from the right horizontal axis. This direction corresponded to the repeat pattern formed by the parallel edges of the elongated tear dimples.

A shear dimple pattern, shown in Figure 4.97a, from the plain carbon steel wood screw that failed in torsional overload was also analyzed. The resulting Fourier transform power spectrum, Figure 4.97b, showed a spread of spots oriented in a direction that corresponded to the edges of the shear dimples. The surface plot, Figure 4.98, showed two primary broad spikes that corresponded to the shear dimple edges. The radial difference plot, Figure 4.99, showed inflections at ring 3, 5.5, 8, 11.5, 15, and 18. These corresponded to input feature spacings of approximately 7.0 mm to 1.3 mm. Ring 3 corresponded to the first spot from the dc spike so the 6 mm spacing is the largest in the input image. Features of each of the 5 size classes were isolated in the input image. The ring plot, Figure 4.100, and the wedge plot, Figure 4.101, both reflected the directionality in the input image due to the shear dimples. The two spikes in the ring and wedge plots were located at 0.4 radians (22 degrees) counterclockwise from the right horizontal axis. This direction corresponded to the repeat pattern formed by the edges of the shear dimples. The heights of the peaks indicated strong orientation effects in the input image. The wedge plots for the three examples of elongated dimples, including the oval dimple, the tear dimple, and the shear dimple, illustrated the power of the Fourier transform imaging analysis to characterize fracture features

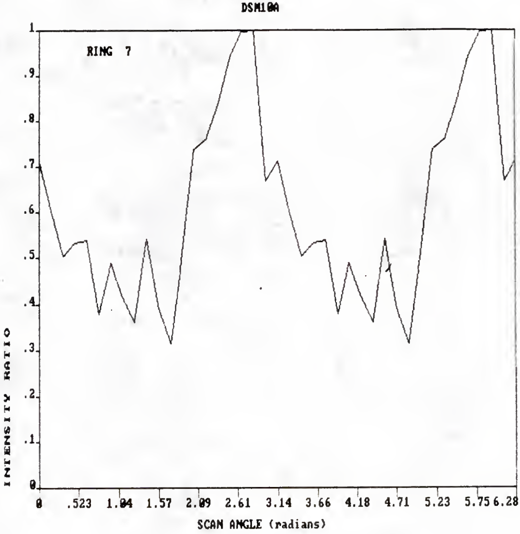

Figure 4.95 Ring plot of 7th ring of Fourier transform power spectrum from tear dimples.

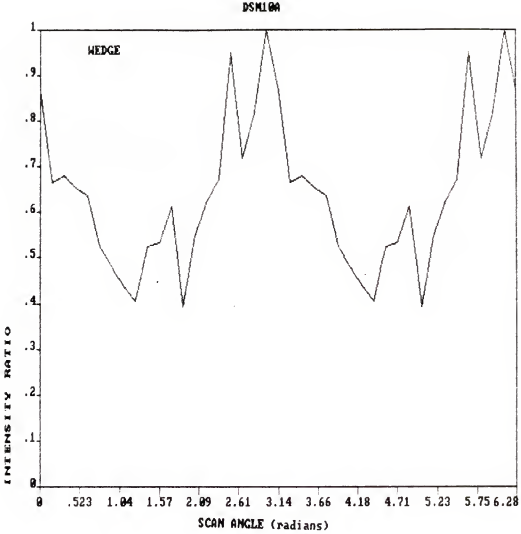

Figure 4.96 Wedge plot of Fourier transform power spectrum from tear dimples.

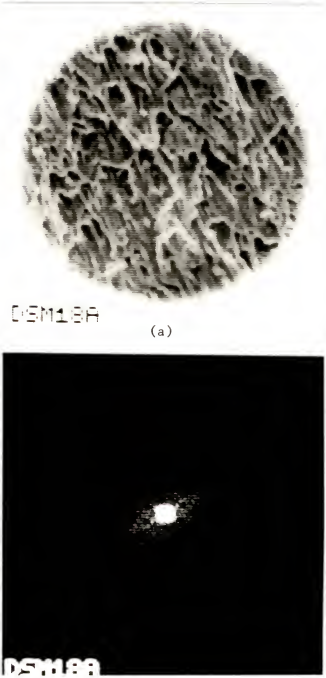

Figure 4.97 Shear dimple image/Fourier transform pair.
(a) Input image of shear dimples from wood screw and
(b) resulting Fourier transform power spectrum.

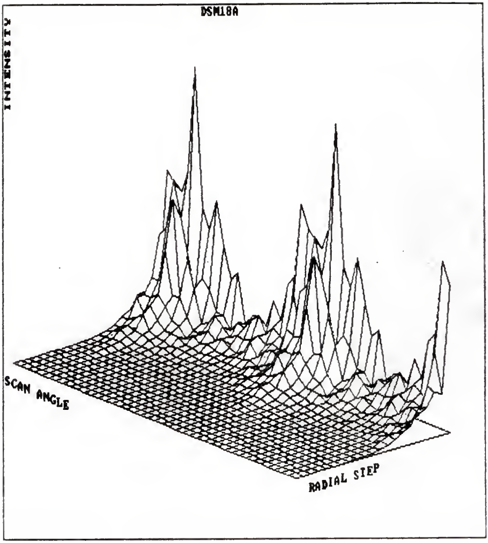

Figure 4.98 Surface plot of Fourier transform power spectrum from shear dimples.

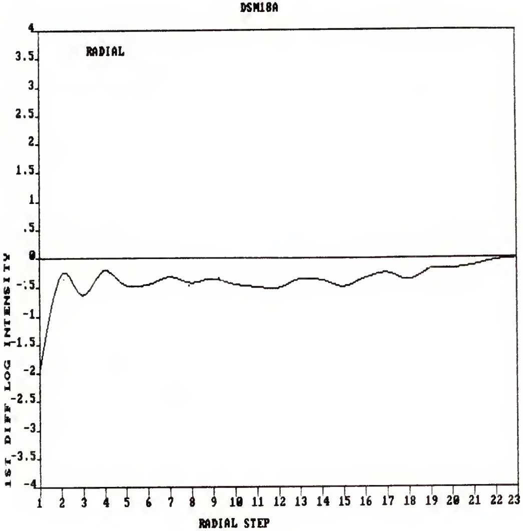

Figure 4.99 First difference of radial plot of Fourier transform power spectrum from shear dimples.

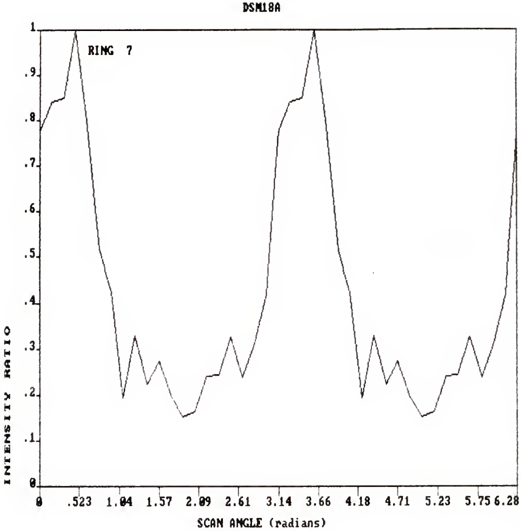

Figure 4.100 Ring plot of 7th ring of Fourier transform power spectrum from shear dimples.

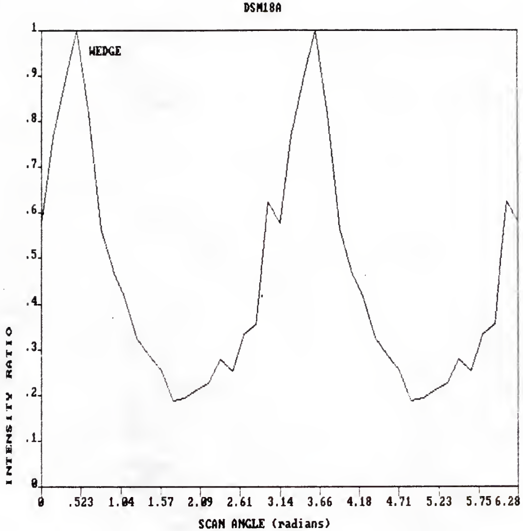

Figure 4.101 Wedge plot of Fourier transform power spectrum from shear dimples.

within a given class. The sampled Fourier transform power spectrum was capable of revealing the orientation direction for each type dimple fracture. The degree of orientation was also indicated by the peak to background heights of the wedge plot.

4.5.3 Cleavage vs. Quasicleavage

The example of cleavage presented in section 4.4.2 is usually the type fracture that occurs in steels with high transition temperatures or at high velocities. Quasicleavage occurs more often in the fracture of high strength steels. A quasicleavage specimen, the 17-4 PH stainless steel helicopter control stick, was analyzed to determine similarities to the cleavage fracture. Figure 4.102a shows the input image composed of micro-quasicleavage facets. The corresponding Fourier transform power spectrum pattern is shown in Figure 4.102b. Most of the spots in the transform pattern were grouped near to the dc spike. The surface plot, Figure 4.103, appeared uniform with a small amount of directionality indicated. The radial difference plot, Figure 4.104, showed inflections at ring 3, 6, 12, 14, and 20 which corresponded to an input spacing of 7 mm to 1.1 mm. Examination of the transform pattern also showed spots at 3.5 mm which corresponded to an input spacing of 10.0 mm. Examination of the input pattern showed large features with a 10.0 mm diameter and smaller features that corresponded to the other sizes listed. The ring plot, Figure 4.105, showed minor orientation effects. The wedge plot, Figure 4.106, showed no significant overall orientation effects such as those in the cleavage fracture. The Fourier transform analysis was able to differentiate cleavage from

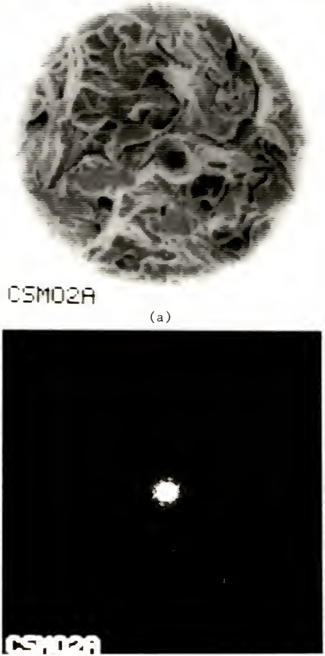

(a)

(b)

Figure 4.102 Quasicleavage facet image/Fourier transform pair.
(a) Input image of micro-quasicleavage from collective control stick and
(b) resulting Fourier transform power spectrum.

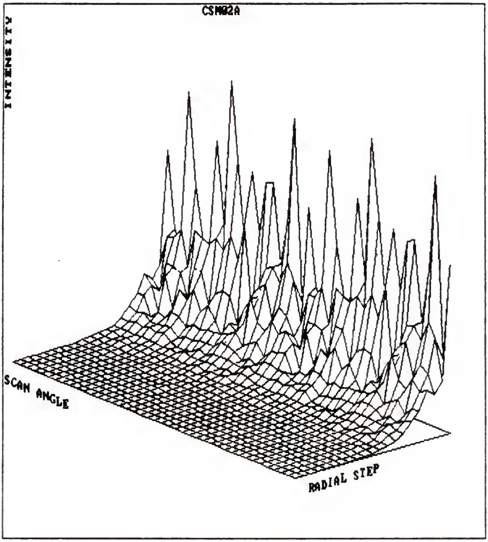

Figure 4.103 Surface plot of Fourier transform power spectrum from micro-quasicleavage facets.

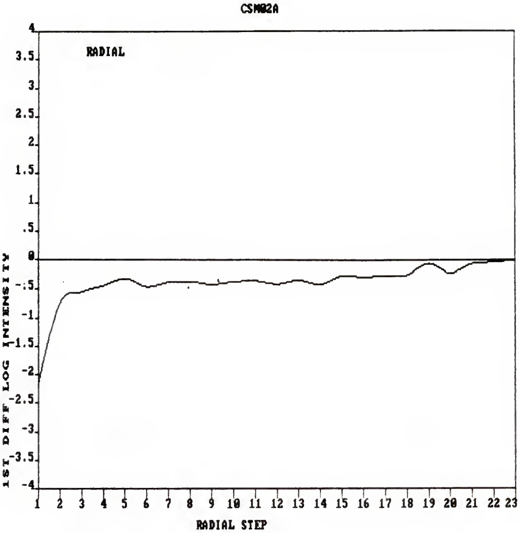

Figure 4.104 First difference of radial plot of Fourier transform power spectrum from micro-quasicleavage facets.

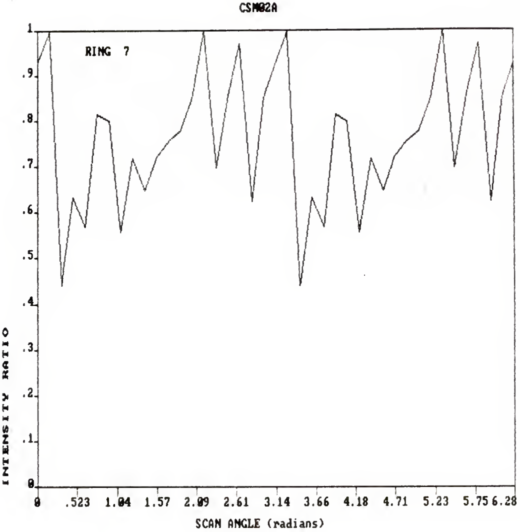

Figure 4.105 Ring plot of 7th ring of Fourier transform power spectrum from micro-quasicleavage.

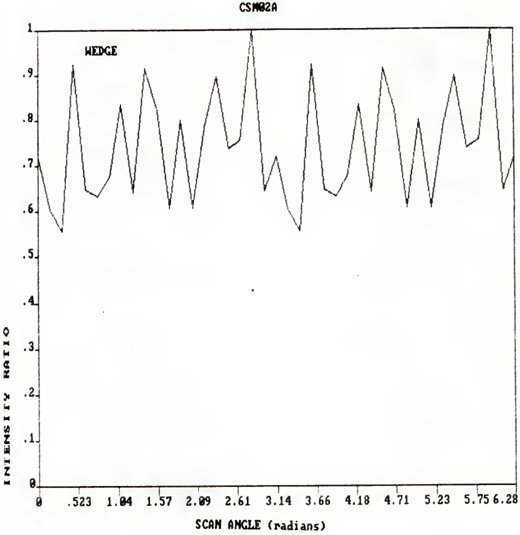

Figure 4.106 Wedge plot of Fourier transform power spectrum from micro-quasicleavage facets.

quasicleavage based on the presence or absence of river patterns. The river patterns that occurred in cleavage fracture resulted in strong directional patterns in the ring and wedge plots. The quasicleavage fracture showed a greater number of high frequency components as revealed by the radial difference plot, due to the presence of small facets in the input image.

4.5.4 Hydrogen Assisted Cracking vs. Stress Corrosion Cracking

The example of intergranular fracture in Section 4.4.4 was due to hydrogen assisted cracking. Two examples of stress corrosion cracking will now be considered. Figure 4.107a shows the input image of the 4340 quenched and tempered steel tailhook. The Fourier transform power spectrum, Figure 4.107b, showed spots centered around the dc spike. The surface plot, Figure 4.108, showed indications of directional detail in the input image. The radial difference plot, Figure 4.109, showed inflections at rings 4, 12, 15, and 17 which corresponded to input image spacings of 3.2 mm to 1.3 mm. Spots located near the dc spike in the transform pattern had a spacing of 3.5 mm which corresponded to an input pattern spacing of 10.0 mm. The large facets in the input image appeared to be approximately 5 mm in diameter and the remaining facets were finer. The large black spaces corresponded to the 9.5 mm spacing obtained from the spots in the transform image. The ring plot, Figure 4.110 and the radial plot, Figure 4.111, showed minor orientation effects, due to grain boundary elongation from the forged tailhook. There were no significant features in the stress corrosion fracture analysis that would distinguish it from the hydrogen assisted cracking fracture.

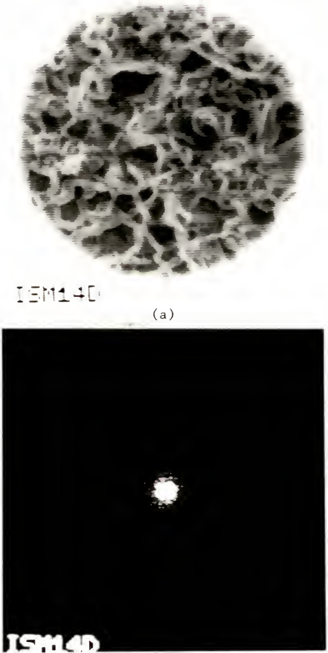

(a)

(b)

Figure 4.107 Intergranular facet image/Fourier transform pair. (a) Input image of intergranular stress corrosion facets in steel tailhook and (b) resulting Fourier transform power spectrum.

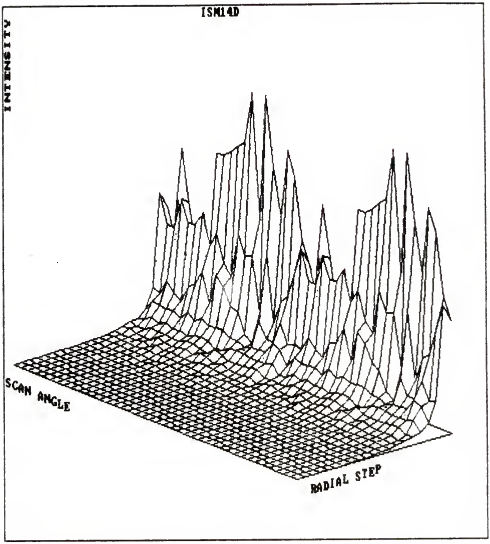

Figure 4.108 Surface plot of Fourier transform power spectrum from stress corrosion intergranular facets.

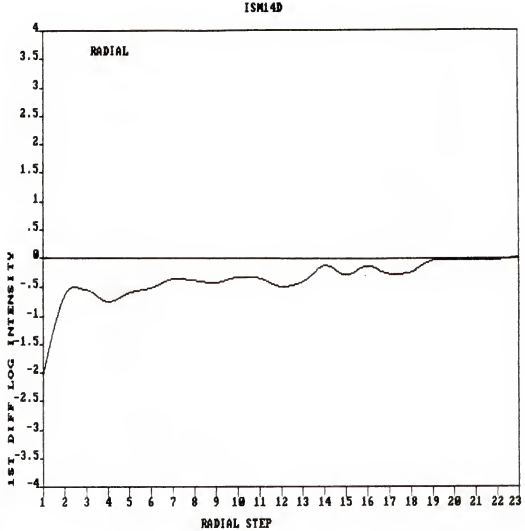

Figure 4.109 First difference of radial plot of Fourier transform power spectrum from stress corrosion intergranular facets.

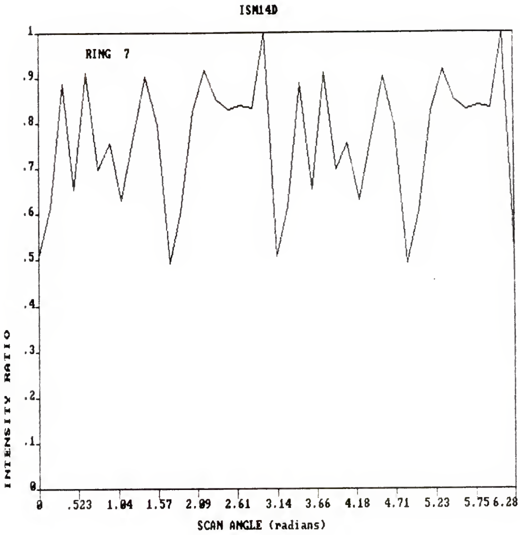

Figure 4.110 Ring plot of 7th ring of Fourier transform power spectrum from stress corrosion intergranular facets.

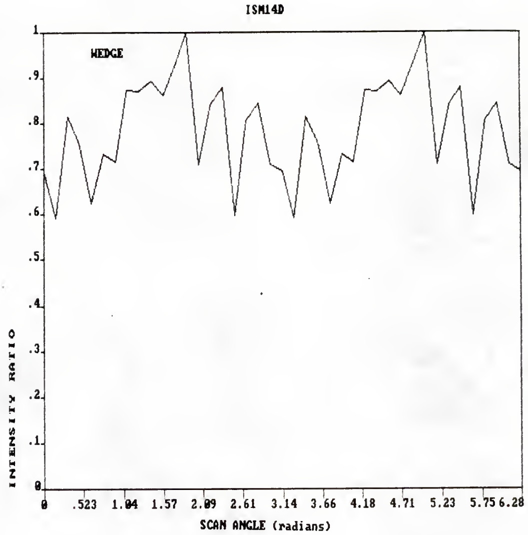

Figure 4.111 Wedge plot of Fourier transform power spectrum from stress corrosion intergranular facets.

A second stress corrosion cracking fractograph from the H-11 tool steel washer is shown in Figure 4.112a. The input pattern showed greater directional effects than in the previous stress corrosion cracking fracture. The corresponding Fourier transform power spectrum is shown in Figure 4.112b. The transform pattern showed the presence of a greater number of high frequency spots than in the previous intergranular fracture examples. The surface plot, Figure 4.113, showed a uniform pattern with minor indications of directionality. The radial difference plot, Figure 4.114, showed inflections at rings 5, 7, 10, 14, 18, and 21 which corresponded to input image spacings of 3.4 mm to 1.0 mm. Spots were also present in the transform image at approximately 3.5 mm from the spectrum center which corresponded to an input image spacing of 10.0 mm. The range of sizes of features indicated by the radial difference plot were identified in the input image. The ring plot, Figure 4.115, and the wedge plot, Figure 4.116, both showed strong directional effects oriented at approximately 2.3 radians (131 degrees) counterclockwise from the right horizontal axis. That direction corresponded to the pattern formed by grain edges of elongated grains in the washer. Again, there were no significant features in the analysis of the stress corrosion fracture that would distinguish it from the hydrogen assisted cracking fracture. In the case of stress corrosion fracture with significant amounts of fracture surface corrosion product, differences in the two fractures would probably be observed in the Fourier transform power spectrum.

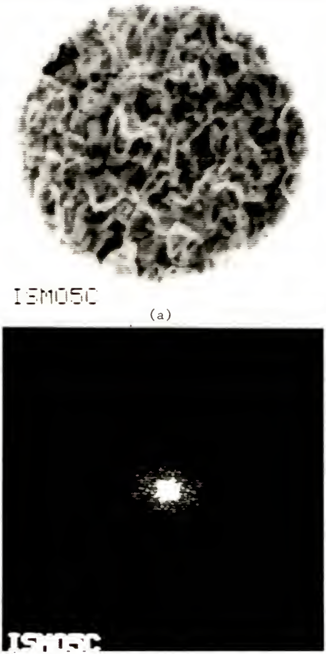

(a)

(b)

Figure 4.112 Intergranular facet image/Fourier transform pair.
(a) Input image of elongated intergranular stress corrosion facets in tool steel washer and
(b) resulting Fourier transform power spectrum.

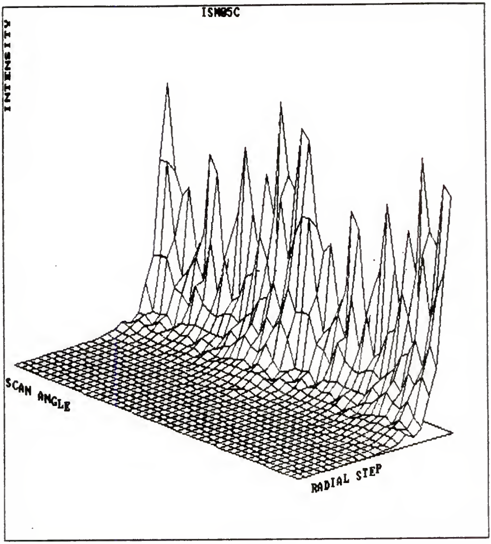

Figure 4.113 Surface plot of Fourier transform power spectrum from elongated intergranular stress corrosion facets.

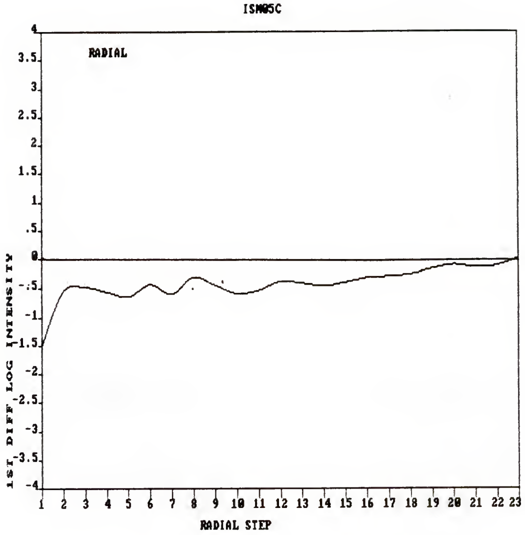

Figure 4.114 First difference of radial plot of Fourier transform power spectrum from elongated intergranular stress corrosion facets.

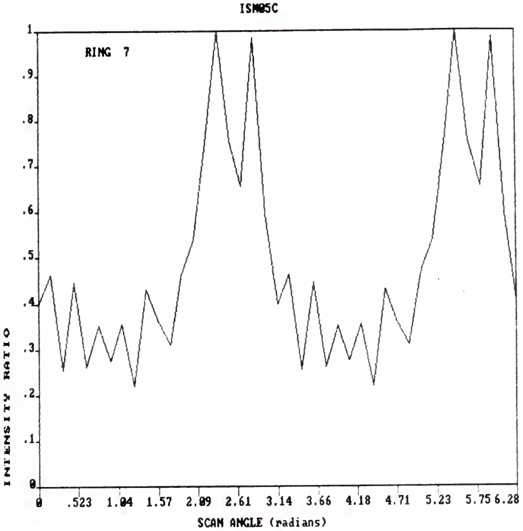

Figure 4.115 Ring plot of 7th ring of Fourier transform power spectrum from elongated intergranular stress corrosion facets.

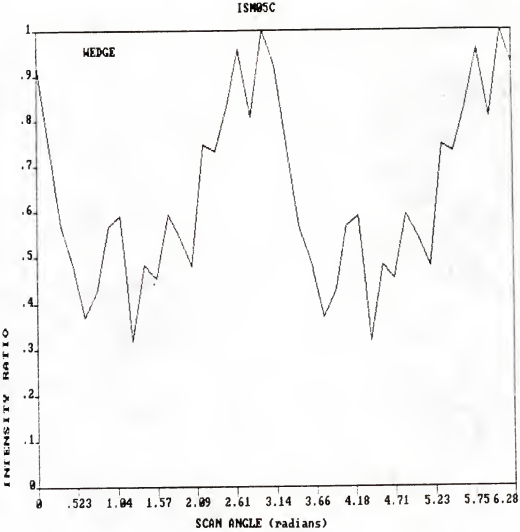

Figure 4.116 Wedge plot of Fourier transform power spectrum from elongated intergranular stress corrosion facets.

CHAPTER 5

CONCLUSIONS AND RECOMMENDATIONS

Digital fractographic imaging analysis using the Fourier transform has been demonstrated to be a useful technique for classifying and characterizing fractographic images. For four primary fracture modes, microvoid coalescence, cleavage, fatigue, and decohesive rupture, the digital imaging analysis technique was able to distinguish and classify the spatial frequency character of each type of fracture surface. The microvoid coalescence fracture had a wide range of repeat frequency components related to dimple size and a uniform distribution of frequency content. The cleavage fracture had river patterns that created a narrow range of directional repeat frequency effects in the transform power spectrum. The fatigue fracture had uniform striations of a single frequency that produced distinct spots in the Fourier transform pattern. The decohesive rupture fractures produced intergranular facets with a range of facet sizes that typically lacked higher frequency component content. It also showed minor directional effects due to elongated grain shape.

Many of the subclasses of patterns were more difficult to distinguish and classify because of similarity of features. However, the Fourier transform was able to extract useful information from subclasses concerning the nature of the fracture surface. Some of the features measured were the repeat spacing of striations, dimples, and grain facets. Size classes of repeat features were determined and the extensiveness of the size class was evaluated. Orientation effects were easily determined using the wedge sampled Fourier transform pattern and the direction of orientation was evaluated for many of the fractures. The technique was even able to detect orientation effects in ASTM grain size charts which was completely unexpected. The digital fractographic imaging analysis technique is not expected to replace the fractographer, but to assist the fractographer in making qualitative and quantitative assessments of fracture surface features.

Recommendations for future work suggest improvements in fractographic input image acquisition, improvements in digital Fourier transform analysis, and evaluation of the optical Fourier transform for fractographic analysis. The input image should be further evaluated to determine if more suitable magnifications exist for fractographic comparisons. Improvements in feature detection should be obtainable by use of an automatic contrast level for the digitized image. Expansion of the image gray levels so that black is fully black and white is fully white should improve feature detection by enhancement of the black-to-white transitions.

The inverse digital image should be evaluated for production of a smaller dc power spike. This should cause the low frequency image components which are located close to the dc spike to be more easily distinguished. Large matrix sizes, such as a 512 x 512 pixels, should also be evaluated for improved image resolution.

The digital fractographic imaging analysis technique should also be investigated for incorporation into an existing digital imaging system such as offered by x-ray microanalysis system manufacturers. The present computer systems with hard disk capability could easily perform the Fourier transform calculation. A hardware array processor could even be used to significantly reduce the calculation time. The availability of the Fourier transform for feature analysis alone would be a tremendous aid in fractographic investigations.

The use of the optical transform for fractographic analysis should also be investigated. The optical transform has the advantage of tremendous speed and high resolution. The use of an array light sensor with computerized transform pattern sampling would make the system comparable to the one in this study, without the problems of limited digital resolution and excessive calculation time.

Digital fractographic imaging analysis using the two-dimensional Fourier transform offers a new and creative approach to fracture surface feature analysis that is worthy of further investigation. It has the ability to draw the Fractographer's attention to subtle characteristics in a fracture surface pattern, to classify the pattern, and to extract quantitative information concerning the nature of the pattern. With the further development of digital imaging analysis applications for scanning electron microscopy, digital fractographic imaging analysis should become an instrumentation option readily available to the fractographer.

APPENDIX

COMPUTER PROGRAMS

<u>HARM Fast Fourier Transform Program</u>

```
      SUBROUTINE HARM(A,M,INV,S,IFSET,  IFERR)
      INTEGER*4 NT,NTSQ
      DIMENSION A(1),INV(1),S(1),N(3),M(3),NP(3),W(2),W2(2),W3(2)
      EQUIVALENCE (N1,N(1)),(N2,N(2)),(N3,N(3))
   10 IF( IABS(IFSET) - 1) 900,900,12
   12 MTT=MAX0(M(1),M(2),M(3)) -2
      ROOT2 = SQRT(2.)
      IF (MTT-MT ) 14,14,13
   13 IFERR=1
      RETURN
   14 IFERR=0
      M1=M(1)
      M2=M(2)
      M3=M(3)
      N1=2**M1
      N2=2**M2
      N3=2**M3
   16 IF(IFSET) 18,18,20
   18 NX= N1*N2*N3
      FN = NX
      DO 19 I = 1,NX
      A(2*I-1) = A(2*I-1)/FN
   19 A(2*I) = -A(2*I)/FN
   20 NP(1)=N1*2
      NP(2)= NP(1)*N2
      NP(3)=NP(2)*N3
      DO 250 ID=1,3
      IL = NP(3)-NP(ID)
      IL1 = IL+1
      MI = M(ID)
      IF (MI)250,250,30
   30 IDIF=NP(ID)
      KBIT=NP(ID)
      MEV = 2*(MI/2)
      IF (MI - MEV )60,60,40
   40 KBIT=KBIT/2
      KL=KBIT-2
      DO 50 I=1,IL1,IDIF
      KLAST=KL+I
      DO 50 K=I,KLAST,2
      KD=K+KBIT
      T=A(KD)
      A(KD)=A(K)-T
      A(K)=A(K)+T
      T=A(KD+1)
      A(KD+1)=A(K+1)-T
   50 A(K+1)=A(K+1)+T
      IF (MI - 1)250,250,52
   52 LFIRST =3
      JLAST=1
      GO TO 70
   60 LFIRST = 2
      JLAST=0
   70 DO 240 L=LFIRST,MI,2
      JJDIF=KBIT
      KBIT=KBIT/4
      KL=KBIT-2
      DO 80 I=1,IL1,IDIF
      KLAST=I+KL
      DO 80 K=I,KLAST,2
      K1=K+KBIT
      K2=K1+KBIT
      K3=K2+KBIT
      T=A(K2)
      A(K2)=A(K)-T
      A(K)=A(K)+T
      T=A(K2+1)
      A(K2+1)=A(K+1)-T
      A(K+1)=A(K+1)+T
      T=A(K3)
      A(K3)=A(K1)-T
      A(K1)=A(K1)+T
      T=A(K3+1)
      A(K3+1)=A(K1+1)-T
      A(K1+1)=A(K1+1)+T
      T=A(K1)
      A(K1)=A(K)-T
      A(K)=A(K)+T
      T=A(K1+1)
      A(K1+1)=A(K+1)-T
      A(K+1)=A(K+1)+T
      R=-A(K3+1)
      T = A(K3)
      A(K3)=A(K2)-R
      A(K2)=A(K2)+R
      A(K3+1)=A(K2+1)-T
   80 A(K2+1)=A(K2+1)+T
      IF (JLAST) 235,235,82
   82 JJ=JJDIF    +1
      ILAST= IL +JJ
      DO 85 I = JJ,ILAST,IDIF
      KLAST = KL+I
      DO 85 K=I,KLAST,2
      K1 = K+KBIT
      K2 = K1+KBIT
      K3 = K2+KBIT
      R =-A(K2+1)
      T = A(K2)
      A(K2) = A(K)-R
      A(K) = A(K)+R
      A(K2+1)=A(K+1)-T
      A(K+1)=A(K+1)+T
      AWR=A(K1)-A(K1+1)
      AWI = A(K1+1)+A(K1)
      R=-A(K3)-A(K3+1)
      T=A(K3)-A(K3+1)
      A(K3)=(AWR-R)/ROOT2
      A(K3+1)=(AWI-T)/ROOT2
      A(K1)=(AWR+R)/ROOT2
      A(K1+1)=(AWI+T)/ROOT2
      T= A(K1)
      A(K1)=A(K)-T
      A(K)=A(K)+T
      T=A(K1+1)
      A(K1+1)=A(K+1)-T
      A(K+1)=A(K+1)+T
      R=-A(K3+1)
      T=A(K3)
      A(K3)=A(K2)-R
      A(K2)=A(K2)+R
      A(K3+1)=A(K2+1)-T
   85 A(K2+1)=A(K2+1)+T
```

```
      IF(JLAST-1) 235,235,90
   90 JJ= JJ + JJDIF
      DO 230 J=2,JLAST
   96 I=INV(J+1)
   98 IC=NT-I
      W(1)=S(IC)
      W(2)=S(I)
      I2=2*I
      I2C=NT-I2
      IF(I2C)120,110,100
  100 W2(1)=S(I2C)
      W2(2)=S(I2)
      GO TO 130
  110 W2(1)=0.
      W2(2)=1.
      GO TO 130
  120 I2CC = I2C+NT
      I2C=-I2C
      W2(1)=-S(I2C)
      W2(2)=S(I2CC)
  130 I3=I+I2
      I3C=NT-I3
      IF(I3C)160,150,140
  140 W3(1)=S(I3C)
      W3(2)=S(I3)
      GO TO 200
  150 W3(1)=0.
      W3(2)=1.
      GO TO 200
  160 I3CC=I3C+NT
      IF(I3CC)190,180,170
  170 I3C=-I3C
      W3(1)=-S(I3C)
      W3(2)=S(I3CC)
      GO TO 200
  180 W3(1)=-1.
      W3(2)=0.
      GO TO 200
  190 I3CCC=NT+I3CC
      I3CC = -I3CC
      W3(I)=-S(I3CCC)
      W3(2)=-S(I3CC)
  200 ILAST=IL+JJ
      DO 220 I=JJ,ILAST,IDIF
      KLAST=KL+I
      DO 220 K=I,KLAST,2
      K1=K+KBIT
      K2=K1+KBIT
      K3=K2+KBIT
      R=A(K2)*W2(I)-A(K2+1)*W2(2)
      T=A(K2)*W2(2)+A(K2+1)*W2(1)
      A(K2)=A(K)-R
      A(K)=A(K)+R
      A(K2+1)=A(K+1)-T
      A(K+1)=A(K+1)+T
      R=A(K3)*W3(1)-A(K3+1)*W3(2)
      T=A(K3)*W3(2)+A(K3+1)*W3(1)
      AWR=A(K1)*W(1)-A(K1+1)*W(2)
      AWI=A(K1)*W(2)+A(K1+1)*W(1)
      A(K3)=AWR-R
      A(K3+1)=AWI-T
```

```
     A(K1)=AWR+R
     A(K1+1)=AWI+T
     T=A(K1)
     A(K1)=A(K)-T
     A(K)=A(K)+T
     T=A(KI+1)
     A(KI+1)=A(K+1)-T
     A(K+1)=A(K+1)+T
     R=-A(K3+1)
     T=A(K3)
     A(K3)=A(K2)-R
     A(K2)=A(K2)+R
     A(K3+1)=A(K2+I)-T
220  A(K2+I)=A(K2+1)+T
230  JJ=JJDIF+JJ
235  JLAST=4*JLAST+3
240  CONTINUE
250  CONTINUE
     NTSQ=NT*NT
     M3MT=M3-MT
350  IF(M3MT) 370,360,360
360  IGO3=I
     N3VNT=N3/NT
     MINN3=NT
     GO TO 380
370  IGO3=2
     N3VNT=I
     NTVN3=NT/N3
     MINN3=N3
380  JJD3 = NTSQ/N3
     M2MT=M2-MT
450  IF (M2MT)470,460,460
460  IGO2=1
     N2VNT=N2/NT
     MINN2=NT
     GO TO 480
470  IGO2 = 2
     N2VNT=1
     NTVN2=NT/N2
     MINN2=N2
480  JJD2=NTSQ/N2
     M1MT=MI-MT
550  IF(M1MT)570,560,560
560  IGO1=I
     N1VNT=NI/NT
     MINNI=NT
     GO TO 580
570  IGO1=2
     N1VNT=I
     NTVNI=NT/NI
     MINN1=NI
580  JJD1=NTSQ/N1
600  JJ3=I
     J=1
     DO 880 JPP3=1,N3VNT
     IPP3=INV(JJ3)
     DO 870 JP3=1,MINN3
     GO TO (610,620),IGO3
610  IP3=INV(JP3)*N3VNT
     GO TO 630
620  IP3=INV(JP3)/NTVN3
```

```
630 I3=(IPP3+IP3)*N2
700 JJ2=1
    DO 870 JPP2=1,N2VNT
    IPP2=INV(JJ2)+I3
    DO 860 JP2=1,MINN2
    GO TO (710,720),IGO2
710 IP2=INV(JP2)*N2VNT
    GO TO 730
720 IP2=INV(JP2)/NTVN2
730 I2=(IPP2+IP2)*N1
800 JJ1=1
    DO 860 JPP1=1,N1VNT
    IPP1=INV(JJ1)+I2
    DO 850 JP1=1,MINN1
    GO TO (810,820),IGO1
810 IP1=INV(JP1)*N1VNT
    GO TO 830
820 IP1=INV(JP1)/NTVN1
830 I=2*(IPP1+IP1)+1
    IF (J-I) 840,850,850
840 T=A(I)
    A(I)=A(J)
    A(J)=T
    T=A(I+1)
    A(I+1)=A(J+1)
    A(J+1)=T
850 J=J+2
860 JJ1=JJ1+JJD1
870 JJ2=JJ2+JJD2
880 JJ3 = JJ3+JJD3
890 IF(IFSET)891,895,895
891 DO 892 I = 1,NX
892 A(2*I) = -A(2*I)
895 RETURN
900 MT=MAX0(M(1),M(2),M(3)) -2
    MT = MAX0(2,MT)
904 IF (MT-18) 906,906,13
906 IFERR=0
    NT=2**MT
    NTV2=NT/2
910 THETA= 7853981634
    JSTEP=NT
    JDIF=NTV2
    S(JDIF)=SIN(THETA)
    DO 950 L=2,MT
    THETA=THETA/2.
    JSTEP2=JSTEP
    JSTEP=JDIF
    JDIF=JSTEP/2
    S(JDIF)=SIN(THETA)
    JC1=NT-JDIF
    S(JC1)=COS(THETA)
    JLAST=NT-JSTEP2
    IF(JLAST - JSTEP) 950,920,920
920 DO 940 J=JSTEP,JLAST,JSTEP
    JC=NT-J
    JD=J+JDIF
940 S(JD)=S(J)*S(JC1)+S(JDIF)*S(JC)
950 CONTINUE
960 MTLEXP=NTV2
    LM1EXP=1
```

```
      INV(1)=0
      DO 980 L=1,MT
      INV(LM1EXP+1) = MTLEXP
      DO 970 J=2,LM1EXP
      JJ=J+LM1EXP
  970 INV(JJ)=INV(J)+MTLEXP
      MTLEXP=MTLEXP/2
  980 LM1EXP=LM1EXP*2
  982 IF(IFSET)12,895,12
      END
```

REFERENCES

Abelkis, P. R. (1978). "Use of Microfractography in the Study of Fatigue Crack Propagation Under Spectrum Loading," in Fractography and Failure Analysis, ASTM STP 645, B. M. Strass and W. H. Cullen, Jr., Eds., American Society for Testing and Materials, Philadelphia, Pa., p. 213.

Aggarwal, R. K., Geokezas, M., and Soland, D. E. (1980). "Autonomous Target Screeners," in Image and Sensor Data Processing for Target Acquisition and Recognition, AGARD-CP-290, NATO, p. 34.1.

Agricola, G. (1556). De Re Metallica, H. Froben, Basel.

Alex, F. (1972). "Interpreting Electron Fractographs of Stress Corrosion in Aluminum Alloys," Metals Engineering Quarterly, Vol. 12, No. 3, p. 48.

Almond, E. A., King, J. T., and Embury, J. D. (1970). "Interpretation of SEM Fracture Surface Detail Using a Sectioning Tech," Metallography, Vol. 3, No. 3, p. 379.

Andrews, H. C. (1970). Computer Techniques in Image Processing, Academic Press, New York, N.Y.

Application of Electron Microfractography to Materials Research (1971). ASTM STP 493, American Society for Testing and Materials, Philadelphia, Pa.

Ashbury, F. E., and Baker, C. (1967). "Metallurgical Applications of the Scanning Electron Microscope," Metals and Materials, Vol. 1, No. 10, p. 323.

Au, J. J., and Ke, J. S. (1981). "Correlation Between Fatigue Crack Growth Rate and Fatigue Striation Spacing," in Fractography and Materials Science, ASTM STP 733, L. N. Gilbertson and R. D. Zipp, Eds., American Society for Testing and Materials, Philadelphia, Pa., p. 202.

Bajcsy, R. (1972). Computer Identification of Textured Visual Scenes, Stanford University Department of Computer Science Report No. STAN-CS-76-321, Stanford Univ., Stanford, Ca.

Banerji, K., and Underwood, E. E. (1983). "Quantitative Analysis of Fractographic Features in a 4340 Steel," Acta Stereol, Vol. 2, No. 1, p. 65.

Barnett, W. J., and Troiano, A. R. (1959). "Crack Propagation in the Hydrogen Induced Brittle Fracture of Steels," Trans. AIME, Vol. 209, p. 486.

Bastien, M. P. (1972). L'Hydrogene dans les Metaux, Science et Industrie, Paris.

Bastien, P., and Azou, P. (1951). "Effect of Hydrogen on the Deformation and Fracture of Iron and Steel in Simple Tension," Proc. First World Metall. Congress, American Society of Metals, Metals Park, Ohio, p. 535.

Beachem, C. D. (1962a). Characterizing Fractures by Electron Fractography. Part V. Several Fracture Modes and Failure Conditions in Four Steel Specimens, NRL Memorandum Report 1352, Naval Research Laboratory, Washington, D.C.

Beachem, C. D. (1962b). An Electron Fractographic Study of the Mechanism of Ductile Rupture in Metals, NRL Memorandum Report 5871, Naval Research Laboratory, Washington, D.C.

Beachem, C. D. (1962c). Characterizing Fractures by Electron Fractography. Part IV. The Slow Growth and Rapid Propagation of a Crack Through a Notched Type 410 Stainless Steel Wire Specimen, NRL Memorandum Report 1297, Naval Research Laboratory, Washington, D.C.

Beachem, C. D. (1963). "An Electron Fractographic Study of the Influence of Plastic Strain Conditions Upon Dimple Rupture Processes in Metals," Trans. ASM, Vol. 56, No. 3, p. 318.

Beachem, C. D. (1965). Electron Microscope Fracture Examination to Characterize and Identify Modes of Fracture, NRL Report 6293, AFML-TR-64-408, Naval Research Laboratory, Washington, D.C.

Beachem, C. D. (1966a). The Interpretation of Electron Microscope Fractographs, NRL Report 6360, Naval Research Laboratory, Washington, D.C.

Beachem, C. D. (1966b). "The Formation of Cleavage Tongues in Iron," Report of NRL Progress, Feb., Naval Research Laboratory, Washington, D.C., p. 19.

Beachem, C. D. (1966c). "Origin of Fatigue Tire Tracks," Report of NRL Progress, May, Naval Research Laboratory, Washington, D.C., p. 22.

Beachem, C. D. (1967). "Microscopic Fatigue Features and the Influence of Propagation Angle upon their Formation," Trans. ASM, Vol. 60, p. 325.

Beachem, C. D. (1969). "Microscopic Fracture Processes," in Fracture, Vol. I, Academic Press, New York, N.Y.

Beachem, C. D. (1972). "A New Model for Hydrogen-Assisted Cracking (Hydrogen-"Embrittlement")," Met. Trans., Vol. 3, p. 437.

Beachem, C. D. (1975). "The Effects of Crack Tip Plastic Flow Directions Upon Microscopic Dimple Shapes," Met. Trans., Vol. 6A, p. 377.

Beachem, C. D. (Ed.) (1977). Hydrogen Damage, American Society for Metals, Metals Park, Ohio.

Beachem, C. D. (1978). "Microscopic Analysis of Cleavage Mechanisms (Cohesion vs. Cleavage)," in Proceedings of the Second International Conference of Mechanical Behavior of Materials, American Society for Metals, Metals Park, Ohio.

Beachem, C. D. (1979). "Some Recent Improvements in Electron Fractographic Analyses," in Application of Fracture Mechanics to Design, J. J. Burke and V. Weiss, Eds., Plenum, New York, N.Y.

Beachem, C. D., Brown, B. F., and Edwards, A. J. (1963). Characterizing Fractures by Electron Fractography, Part XIII, Illustrated Glossary. Section I. Quasi-Cleavage, NRL Memorandum Report 1432, Naval Research Laboratory, Washington, D.C.

Beachem, C. D., and Meyn, D. A. (1964). Illustrated Glossary of Fractographic Terms. Section II. Glide Plane Decohesion, Serpentine Glide, Ripples, Stretching, Microvoid Coalescence, NRL Memorandum Report 1547, Naval Research Laboratory, Washington, D.C.

Beachem, C. D., and Meyn, D. A. (1968). "Fracture by Microscopic Plastic Deformation Processes," in Electron Fractography, ASTM STP 436, American Society for Testing and Materials, Philadelphia, Pa., p. 59.

Beachem, C. D., and Pelloux, R. M. N. (1965). Electron Fractography--A Tool for the Study of Micromechanisms, ASTM STP 381, American Society for Testing and Materials, Philadelphia, Pa.

Beachem, C. D., and Pelloux, R. M. N. (1964). "Electron Fractography--A Tool for the Study of Micromechanisms of Fracturing Processes," in Fracture Toughness Testing and Its Applications, ASTM STP 381, American Society for Testing and Materials, Philadelphia, Pa., p. 210.

Beachem, C. D., and Warke, W. R. (Eds.) (1976). Fractography-Microscopic Cracking Processes, ASTM STP 600, American Society for Testing and Materials, Philadelphis, Pa.

Beck, W., Jankowsky, E. J., and Fischer, P. (1971). Hydrogen Stress Cracking of High Strength Steels, NADC-MA-7140, Naval Air Development Center, Warminster, Pa.

Beddow, J. K. (Ed.) (1984). Particle Characterization in Technology. Volume I. Applications and Microanalysis, Volume II. Morphological Analysis, CRC Press, Boca Raton, Fl.

Beddow, J. K., and Meloy, T. P. (Eds.) (1980). Advanced Particulate Morphology, CRC Press, Boca Raton, Fl.

Bergland, G. D. (1967). "The Fast Fourier Transform Recursive Equations for Arbitrary Length Records," Math Compt., Vol. 21, p. 236.

Bergland, G. D. (1968a). "A Fast Fourier Transform Algorithm Using Base 8 Iterations," Math Compt., Vol. 22, p. 275.

Bergland, G. D. (1968b). "A Fast Fourier Transform Algorithm for Real-Valued Series," Commun. Assoc. Comput. Mach., Vol. 11, p. 703.

Bergland, G. D. (1969). "A Guided Tour of the Fast Fourier Transform," IEEE Spectrum, July, p. 41.

Bernstein, I. M., and Thompson, A. W. (Eds.) (1974). Hydrogen in Metals, American Society for Metals, Metals Park, Ohio.

Berry, J. M. (1959). "Cleavage Step Formation in Brittle Fracture Propagation," Trans. ASM, Vol. 51, p. 556.

Bezdek, J. C., and Solomon, K. H. (1984). "Shape Prediction Using Prototypes and Membership Interpolation," in Particle Characterization in Technology, Vol. II Morphological Analysis, J. K. Beddow, Ed., CRC Press, Boca Raton, Fl., p. 113.

Bhattacharyya, S., Johnson, V. E., Agarwal, S., and Howes, M. A. H. (1979). IITRI Fracture Handbook, Failure Analysis of Metallic Materials by Scanning Electron Microscopy, Metals Research Division, IIT Research Inst., Chicago, Il.

Bilby, B. A., and Hewitt, J. (1962). "Hydrogen in Steel--The Stability of Microcracks," Acta. Metall., Vol. 10, p. 587.

Biringuccio, V. (1540). De La Pirotechnia, N.P., Venice.

Bowen, D. K., and Hall, C. R. (1975). Microscopy of Materials, Wiley and Sons, New York, N.Y.

Bowles, C. Q., and Broek, D. (1972). "On the Formation of Fatigue Striations," Int. J. Fracture Mechanics, Vol. 8, p. 75.

Bowles, C. Q., and Schijve, J. (1973). "The Role of Inclusions in Fatigue Crack Initiation in an Aluminum Alloy," Int. J. Fracture Mechanics, Vol. 9, p. 171.

Boyer, H. E., and Gall, T. L. (Eds.) (1985). Metals Handbook Desk Edition, American Society for Metals, Metals Park, Ohio.

Brenner, N. M. (1967). Three Fortran Programs That Perform the Cooley-Tukey Fourier Transform, Tech Note 1967-2 Lincoln Laboratory, MIT, Lexington, Mass.

Broek, D. A. (1969). "The Effect of Intermetallic Particles on Fatigue Crack Propagation in Aluminum Alloys," Fracture, Chapman and Hall, U.K., p. 754.

Broek, D. (1970). "A Critical Note on Electron Fractography," Eng. Fracture Mechanics, Vol. 1, p. 691.

Broek, D. (1971). A Study on Ductile Fracture, Ph.D. Diss., Nat. Aerospace Inst., Amsterdam.

Broek, D. (1972). Some Contributions of Electron Fractography to the Theory of Fracture, TR.72029 Nat. Aerospace Inst., Amsterdam.

Broek, D. (1973). The Role of Inclusions in Ductile Fracture and Fracture Toughness," Eng. Fracture Mechanics, Vol. 5, p. 55.

Broek, D. (1974). "Some Contributions of Electron Fractography to the Theory of Fracture," Intl. Metallurgical Rvws., Vol. 19, p. 135.

Broek, D. (1982). Elementary Engineering Fracture Mechanics, Martinus Nijhoff Publishers, The Hague.

Brown, B. F. (1972). "A Preface to the Problem of Stress Corrosion Cracking," in Stress Corrosion Cracking of Metals--A State of the Art, ASTM STP 518, American Society for Testing and Materials, Philadelphia, Pa., p. 3.

Burghard, H. C., and Davidson, D. L. (1965). "Fracture Mechanisms and Fracture Surface Topography," in Proceedings of the First International Conference on Fracture, Sendai, Japan, September, p. 571.

Burghard, H. C., and Stoloff, N. S. (1968). "Cleavage Phenomena and Topological Features," in Electron Fractography, ASTM STP 436, American Society for Testing and Materials, Philadelphia, Pa., p. 32.

Chen, C. H. (1982). Digital Waveform Processing and Recognition, CRC Press, Boca Raton, Fl.

Chermant, J. L., and Coster, M. (1979). "Review Quantitative Fractography," J. of Materials Science, Vol. 14, p. 509.

Chiao, T. T., and Schuster, D. M. (1976). "Failure Modes in Composites, Vol. III," The Met. Soc. of AIME, New York, N.Y.

Ching, M. L. (1981). "True Three-Dimensional Nuclear Magnetic Resonance Imaging by Fourier Reconstruction Zeugmatography," J. Appl. Physics, Vol. 52, p. 1141.

Coffin, L. F., Jr. (1972). "Fatigue," in Annual Review of Materials Science, Vol. 2, p. 313.

Cole, M. (1971). "Instrument Errors in Quantitative Image Analysis," Microscope, Vol. 19, p. 87.

Coleman, E. G., Weinstein, D., and Rostoker, W. (1961). "On a Surface Energy Mechanism for Stress Corrosion Cracking," Acta Metallurgica, Vol. 9, p. 491.

Cooley, J. W. (1966a). "Harmonic Analysis Complex Fourier Series," SHARE Doc 3425.

Cooley, J. W. (1966b). "Complex Finite Fourier Transform Subroutine," SHARE Document 3465.

Cooley, J. W., and Tukey, J. W. (1965). "An Algorithm for the Machine Calculation of Complex Fourier Series," Math. Compt., Vol. 19, p. 297.

Cornie, J. A., and Crossman, F. W. (1979). Failure Modes in Composites, Vol. IV, The Met. Soc. of AIME, New York, N.Y.

Coster, M., and Chermant, J. L. (1983). "Recent Developments in Quantitative Fractography," International Metals Reviews, Vol. 28, p. 228.

Cottrell, A. H., and Hull, D. (1957). "Extrusion and Intrusion by Cyclic Slip in Copper," Proc. Royal Society, Vol. A 242, p. 211.

Craig, H. L., Jr. (Ed.) (1972). Stress Corrosion Cracking of Metals--A State of the Art, ASTM STP 518, American Society for Testing and Materials, Philadelphia, Pa.

Craig, H. L., Jr. (Ed.) (1976). Stress Corrosion - New Approaches, ASTM STP 610, American Society for Testing and Materials, Philadelphia, Pa.

Crowther, R. A., and Klug, A. (1975). "Structural Analysis of Macromolecular Assemblies by Image Reconstruction from Electron Micrographs," Annual Review of Biochemistry, Vol. 44, p. 161.

Crussard, C., Plateau, J., Tamhankar, R., LaJeunesse, D. (1959). "A Comparison of Ductile and Fatigue Fractures," in Fracture, John Wiley and Sons, New York, N.Y., p. 524.

Dahlberg, E. P. (1962). "Characteristics of Twinnning on Fracture Surfaces of Single and Polycrystalline Tungsten," in Proceedings of Fifth International Congress for Electron Microscopy, S. S. Breese, Jr., Ed., Academic Press, New York, N.Y.

Dahlberg, E. P., and Beachem, C. D. (1963). Fractography Part XV. Some Artifacts Possible with the Two-Stage Plastic Carbon Replication Technique, Memorandum Report 1457, Naval Research Laboratory, Washington, D.C.

Danity, R. V. (1984). "Use of "Marker Blocks" as an Aid in Quantitative Fractography in Full Scale Aircraft Fatigue Testing: A Case Study," in Fractography of Ceramic and Metal Failures, J. J. Mecholsky, Jr. and S. R. Powell, Eds., ASTM STP 827, American Society for Testing and Materials, Philadelphia, Pa., p. 285.

DeHoff, R. T. (1968a). "Quantitative Microstructural Analysis," in Fifty Years of Progress in Metallographic Techniques,ASTM STP 430, American Society for Testing and Materials, Philadelphia, Pa., p. 63.

DeHoff, R. T. (1968b). "Quantitative Metallography Techniques of Metals Research," Vol. II, Pt. 1, Interscience Publishers, Division of John Wiley and Sons, New York, N.Y., p. 221.

DeHoff, R. T., and Rhines, F. N. (Eds.) (1968). Quantitative Microscopy, McGraw-Hill Book Co., New York, N.Y.

De Kazinczy, F. A. (1954). "The Nature of Hydrogen Embrittlement," J. Iron Steel Inst., Vol. 177, p. 85.

de Reaumur, R. A. F. (1722). L'Art de Convertir le Fer Forge en Acier, et L'Art d'Adoucir, le Fer Fondu, M. Brunet, Paris.

Dix, E. H., Jr. (1940). "Acceleration of the Rate of Corrosion by High Constant Stresses," Trans. AIME, Vol. 137, p. 11.

Dix, E. H., Jr. (1950). "Aluminum-Zinc-Magnesium Alloys Their Development and Commercial Production," Trans. ASM, Vol. 42, p. 1057.

Duke, D. B., Fryer, A. J., and Bird, P. A. (1980). "Research into Methods of Image Processing for Target Enhancement and Detection," in Image and Sensor Data Processing for Target Acquisition and Recognition, AGARD-CP-290, NATO, p. 18.1

Dundurs, J., and Mura, T. (1969). "Interaction Between an Edge Dislocation and a Circular Inclusion," J. Mech. Phys. Solids, Vol. 12, p. 177.

Dykes, G. W. (1985). "Automated Inspection of Food Jars for Glass Fragments," Presented at Vision 85, Society of Manufacturing Engineers, March 25-28, Detroit, Mich.

Ehrlich, R., and Full, W. E. (1984). "Fourier Shape Analysis - A Multivariate Pattern Recognition Approach," in Particle Characterization in Technology, Vol. II. Morphological Analysis, J. K. Beddow, Ed., CRC Press, Boca Raton, Fl., p. 89.

El-Soudani, S. M. (1974). "Theoretical Basis for the Quantitative Analysis of Fracture Surfaces," Metallography, Vol. 7, p. 271.

El-Soudani, S. M. (1978). "Profilometric Analysis of Fracture," Metallography, Vol. 11, p. 247.

El-Soudani, S. M., and Pelloux, R. M. N. (1973). "Influence of Inclusion Content on Fatigue Crack Propagation in Aluminum Alloys," Met. Trans., Vol. 4, p. 519.

Electron Fractography (1968). ASTM STP 436, American Society for Testing and Materials, Philadelphia, Pa.

Electron Microfractography (1968). ASTM STP 453, American Society for Testing and Materials, Philadelphia, Pa.

Elliott, D. E., and Rao, K. R. (1982). "Fast Transforms, Algorithms, Analyses, Applications," Academic Press, Orlando, Fl.

Engel, L., and Klingele, H. (1981). "An Atlas of Metal Damage," Printece-Hall, Englewood Cliffs, N.J.

Engel, L., Klingele, H., Ehrenstein, G., and Schaper, H. (1981). "An Atlas of Polymer Damage," Prentice-Hall, Englewood Cliffs, N.J.

Ercker, L. (1574). Beschreibung allerfurnemisten mineralischen Ertzt und Berckwercksanten, 1st Edition, G. Schwartz, Prague

Erickson, H. P., and Klug, A. (1971). "Measurements and Composition of Defocusing and Abberations by Fourier Processing of Electron Micrographs," Phil. Trans. of the Royal Soc. of London, Vol. 261, Series B, p. 105.

Ewalds, H. L., and Wanhill, R. J. H. (1984). "Fracture Mechanics," Edward Arnold Ltd., London.

Exner, H. E. (1978). "Programmable Semiautomatic Instruments for Quantitative Structural Analysis and Other Geometric Evaluations in the Materials Laboratory," Prakt. Metallogr., Vol. 15, p. 15.

Exner, H. E., and Hougardy, H. (1981). Quantitative Analysis of Metallic Microstructures, Qberursel, Deutsche Geseuschaft Fur Metallkunde.

Eylon, D., and Kerr, W. R. (1978). "Fractographic and Metallographic Morphology of Fatigue Initiation Sites," in Fractography in Failure Analysis, ASTM STP 645, B. M. Strauss and W. H. Cullen, Jr., Eds., American Society for Testing and Materials, Philadelphia, Pa., p. 235.

Failure Analysis and Prevention (1975). Metals Handbook, Vol. 10, 8th Edition, American Society for Metals, Metals Park, Ohio.

Finello, D., Park, Y. H., Schmerling, M., and Marcus, H. L. (1984). "Fractography of Metal Matrix Composites," in Fractography of Ceramic and Metal Failures, ASTM STP 827, J. J. Mecholsky and S. R. Powell, Jr., Eds., American Society for Testing and Materials, Philadelphia, Pa., p. 387.

Fitch, J. T., and Holmes, K. C. (1967). "Structural Studies of Viruses," in Methods in Virology, K. Maromorosch and H. Koprowski, Eds., Academic Press, New York, N.Y., p. 351.

Fleck, J. N., and Mehan, R. N. (1974). Failure Modes in Composites, Vol. II, The Met. Soc. of AIME, New York, N.Y.

Fong, J. T. (Ed.) (1979). Fatigue Mechanisms, ASTM STP 675, American Society for Testing and Materials, Philadelphia, Pa.

Ford, F. P. (1984). "Current Understanding of the Mechanisms of Stress Corrosion and Corrosion Fatigue," in Environment-Sensitive Fracture: Evaluation and Comparison of Test Methods, ASTM STP 821, American Society for Testing and Materials, Philadelphia, Pa., p. 32.

Forsyth, P. J. E. (1961). "A Two Stage Process of Fatigue Crack Growth," in Proceedings of the Crack Propagation Symposium, Cranfield, Sept., Vol. I, p. 76.

Forsyth, P. J. E. (1963). "Fatigue Damage and Crack Growth in Aluminum Alloys," Acta Met., Vol. 11, p. 703.

Forsyth, P. J. E., and Ryder, D. A. (1961). "Results of the Examination of Aluminum Alloy Specimen Fracture Surfaces," Metallurgia, Vol. 63, p. 117.

Forsyth, P. J. E., Ryder, D.A., Smale, A. C., and Wilson, R. N. (1959). "Some Further Results Obtained from the Microscopic Examination of Fatigue, Tensile, and Stress Corrosion Surfaces," Tech Note Met 312, Royal Aircraft Establishment, U.K.

Forsyth, P. J. E., Stubbington, C. A., and Clark, D. (1961). "Cleavage Facets Observed on Fatigue-Fracture Surfaces in an Aluminum Alloy," Tech Note No. 47, J.I.M., Vol. 90, p. 238.

Forty, A. J., and Humble, P. (1963). "The Influence of Surface Tarnish on the Stress Corrosion of Alpha Brass," Philosophical Magazine, Vol. 8, p. 247.

Fox, L. (1980). "The Application of Landsat Remote Sensing Technology to Natural Resources Management," NASA Science Grant 2341, National Aeronautics and Space Administration, Washington, D.C.

Fractography and Atlas of Fractographs (1974). Metals Handbook, Vol. 9, 8th Edition, American Society for Metals, Metals Park, Ohio.

Frechette, V. D. (1984). "Markings on Crack Surfaces of Brittle Materials: A Suggested Unified Nomenclature," in Fractograph of Ceramic and Metal Failures, ASTM STP 827, American Society for Testing and Materials, Philadelphia, Pa., p. 104.

French, R. S. (1978). Evaluation of the Two-Dimensional Fourier Transform Applied to Acoustic Image Pattern Measurements, Naval Ocean Systems Center Report No. NOSC/TR-354, San Diego, Ca.

Fridge, A., Lee, J., Jr., and Walker, R. (1984). "Machine Vision Automates Inspection of Hybrids and PCBs," Test and Measurement World, Oct., p. 203.

Friedel, J. (1959). "Propagation of Cracks and Work Hardening," in Fracture, Proceedings of the Swampscott Conference, B. L. Averbach, D. K. Felbeck, G. T. Hahn, and D. A. Thomas, Eds., Technology Press and Wiley and Sons, New York, N.Y., p. 498.

Fu, K. S. (Ed.) (1982). Applications of Pattern Recognition, CRC Press, Boca Raton, Fl.

Gahm, J. (1973). "Instruments for Stereometric Analysis with the Microscope--Their Application and Accuracy of Measurement," in Advances in Optical and Electron Microscopy, Vol. 5, Academic Press, New York, N.Y., p. 115.

Gellert, C. E. (1750). Anfangsgrunde der Metallurgischen Chemie, J. Wendler, Leipzig.

Gibala, R., and Hehemann, R. F. (Eds.) (1984). Hydrogen Embrittlement and Stress Corrosion Cracking, American Society for Metals, Metals Park, Ohio.

Gilbertson, L. N., and Zipp, R. D. (Eds.) (1981). Fractography and Materials Science, ASTM STP 733, American Society for Testing and Materials, Philadelphia, Pa.

Ginsburg, A. P. (1976). Method and Apparatus for Pattern Analysis, U. S. Patent No. 3,993,976, 23 Nov.

Goldstein, J. I., Newbury, D. E., Echlin, P., Joy, D. C., Fiori, C., and Lifshin, E. (Eds.) (1981). Scanning Electron Microscopy and X-Ray Microanalysis, Plenum, New York, N.Y.

Goldstein, J. I., Yakowitz, H., Newbury, D. E., Lifshin, E., Colby, J. W., and Coleman, J. R. (Eds.) (1975). Practical Scanning Electron Microscopy, Plenum, New York, N.Y.

Good, I. J. (1958). "The Interaction Algorithm and Practical Fourier Series," J. R. Statist. Soc., Section B, Vol. 20, p. 361.

Govila, R. K., Beardmore, P., and Kinsman, K. R. (1981). "Strength Characterization and Nature of Crack Propagation in Ceramic Materials," in Fractograph and Materials Science, ASTM STP 733, L. N. Gilbertson and R. D. Zipp, Eds., American Society for Testing and Materials, Philadelphia, Pa., p. 225.

Grosskreutz, J. C. (1971a). "The Mechanisms of Metal Fatigue (I)," Phys, Stat. Sol., Vol. 47, p. 11.

Grosskreutz, J. C. (1971b). "The Mechanisms of Metal Fatigue (II)," Phys. Stat. Sol., Vol. 47, p. 359.

Grosskreutz, J. C., and Shaw, C. (1969). "Critical Mechanisms in the Development of Fatigue Cracks in 2024-T4 Aluminum," in Fracture, Chapman and Hall, U.K., p. 620.

Gurland, J. and Plateau, J. (1963). "The Mechanism of Ductile Rupture of Metals Containing Inclusions," Trans. ASM, Vol. 56, p. 442.

Hall, E. L. (1979). Computer Image Processing and Recognition, Academic Press, New York, N.Y.

Hancock, J. R. (Ed.) (1975). Fatigue of Composite Materials, ASTM STP 569, American Society for Testing and Materials, Philadelphia, Pa.

Hannigan, J. W. (1980). Method and Apparatus for Camouflage Signature Measurement, United States Patent 4,223,345, 16 Sept.

Harmon, L. D. (1974). The Recognition of Faces in Image, Object and Illusion, Readings from Scientific American, p. 101.

Harris, K. L., Sandland, P., and Singleton, R. M. (1984). "Automated Inspection of Wafer Patterns with Applications in Stepping, Projection and Direct Write Lithography," Solid State Technology, Feb., p. 159.

Heady, R. B. (1977). "The Petch-Stables Theory of Hydrogen Embrittlement," Corrosion, Vol. 33, p. 441.

Hertzberg, R. W., and Manson, J. A. (1980). Fatigue of Engineering Plastics, Academic Press, New York, N.Y.

Hertzberg, R. W., and Mills, W. J. (1976). "Character of Fatigue Fracture Surface Micromorphology in the Ultra-Low Growth Rate Regime," in Fractography-Microscopic Cracking Processes, ASTM STP 600, C. D. Beachem and W. R. Warke, Eds., American Society for Testing and Materials, Philadelphia, Pa., p. 220.

Hines, J. G., and Hoar, T. P. (1958). "Stress Corrosion Cracking of Austenetic Stainless Steels with Applied E.M.F.," J. of Applied Chemistry, Vol. 8, p. 764.

Hirth, J. P., and Johnson, H. H. (1976). "Hydrogen Problems in Energy Related Technology," Corrosion, Vol. 32, p. 3.

Hoar, T. P. (1963). "Stress Corrosion Cracking,", Corrosion, Vol. 19, p. 331.

Hoar, T. P. (1971). "Stress Corrosion Cracking: Some Electrochemical Contributions," Proced. of NATO Conf., Ericiera Portugal, J. C. Scully, Ed., p. 106.

Hoar, T. P., and West, J. M. (1962). "Mechano-Chemical Anodic Dissolution of Austenitic Stainless Steel in Hot Chloride Solution," Proc. Royal Society, Vol. A268, p. 304.

Hougardy, H. P. (1974). "Instrumentation in Automatic Image Analysis," Microscope, Vol. 22, p. 5.

Hougardy, H. P. (1975). "Measurement of the Performance of Quantitative Image Analysing Instruments," Prakt. Metallogr., Vol. 12, p. 624.

Hougardy, H. P. (1976). "Recent Progress in Automatic Image Analysis Instrumentation," Microscope, Vol. 24, p. 7.

Huang, T. S. (1979). Trends in Digital Image Processing Research," in Advances in Digital Image Processing Theory, Application, Implementation, P. Stucki, Ed., Plenum, New York, N.Y., p. 21.

Hutchins, F. R., and Unterweiser, P. M. (1981). "Failure Analysis--The British Engine Technical Reports," American Society for Metals, Metals Park, Ohio.

Johari, O. (1968). "Comparison of Transmission Electron Microscopy and Scanning Electron Microscopy of Fracture Surfaces," J. Metals, p. 26.

Jones, A. V., and Smith, K. C. A. (1978). "Image Processing for Scanning Microcopists," Scanning Electron Microscopy, Vol. 1, p. 13.

Kaye, B. H. (1984). "Fractal Description of Fine Particle Systems," in Particle Characterization in Technology. Vol. I Applications and Microanalysis, J. K. Beddow, Ed., CRC Press, Boca Raton, Fl., p. 81.

Kerr, W. R., Eylon, D., and Hall, J. A. (1976). "On the Correlation of Specific Fracture Surface and Metallographic Features by Precision Sectioning in Titanium Alloys," Met. Trans., Vol. 7A, p. 1477.

Kikuta, Y., Araki, T., and Kuroda, T. (1978). "Analysis of Fracture Morphology of Hydrogen-Assisted Cracking in Steel and its Welds," in Fractography in Failure Analysis, ASTM STP 645, B. M. Strauss and W. H. Cullen, Eds., American Society for Testing and Materials, Philadelphia, Pa., p. 107.

Kim, C., Phillips, W. L., and Weimer, R. J. (1981). "Fracture of Tungsten Wire in Metal Matrix Composites," in Fractography and Materials Science, ASTM STP 733, L. N. Gilbertson and R. D. Zipp, Eds., American Society for Testing and Materials, Philadelphia, Pa., p. 314.

Kinsinger, R. E. (1984). "Medical Imaging," Research and Development, Vol. 26, No. 6, p. 228.

Kitajima, K., and Futagami, K. (1969). "Fractographic Studies on the Cleavage Fracture of Single Crystals of Iron," in Electron Microfractography, ASTM STP 453, American Society for Testing and Materials, Philadelphia, Pa., p. 33.

Klug, A., and Berger, J. E. (1964). "An Optical Method for the Analysis of Periodicities in Electron Micrographs and Some Observations on the Mechanism of Negative Staining," J. of Molecular Biology, Vol. 10, p. 564.

Knoll, M. (1935). "Static Potential and Secondary Emission of Bodies Under Electron Irradiation," Z. Tech. Phys., Vol. 11, p. 467.

Kobayashi, T., Irwin, G. R., and Zhang, X. J. (1984). "Topographic Examination of Fracture Surfaces in Fibrous Cleavage Transition," Behavior, in Fractography of Ceramic and Metal Failures, ASTM STP 827., J. J. Mecholsky, Jr. and S. R. Powell, Jr., Eds., American Society for Testing and Materials, Philadelphia, Pa., p. 234.

Kobayashi, T., and Shockey, D. A. (1984). Environmentally Accelerated Cyclic Crack Growth Mechanisms in Reactor Steel Determined from Fracture Surface Topography, Pourter Laboratory Tech. Rpt. 002-84, SRI International, Marlo Park, Ca.

Koterazawa, R., Mori, M., Matsuiti, T., and Shimo, D. (1973). "Fractographic Study of Fatigue Crack Propagation," Trans. ASME, J. of Engr. Matls. and Tech., Vol. 95, p. 202.

Laird, C. (1979). "Mechanisms and Theories of Fatigue," p. 141 in Fatigue and Microstructure, American Society for Metals, Metals Park, Ohio, p. 141.

Laird, C., and Smith, G. C. (1962). "Crack Propagation in High Stress Fatigue," The Philosophical Magazine, Vol. 7, p. 847.

Lankford, J., Davidson, D. L., Morris, W. L., and Wei, R. P. (Eds.) (1983). "Fatigue Mechanisms: Advances in Quantitative Measure of Physical Damage," ASTM STP 811, American Society for Testing and Materials, Philadelphia, Pa.

LeMay, I. (1978). "Failure Mechanisms and Metallography: A Review," p. 1 in Metallography in Failure Analysis, J. L. McCall and P. M. French, Eds., Plenum, New York, N.Y., p. 1.

Lendaris, G. G., and Stanley, G. L. (1970). "Diffraction-Pattern Sampling for Automatic Pattern Recognition," Proceedings of the IEEE, Vol. 58, No. 2, p. 198.

Lenth, R. V. (1984). "Smoothing a Digitized Particle Profile in Particle Characterization Technology," in Vol. II. Morphological Analysis, J. K. Beddow, Ed., CRC Press, Boca Raton, Fl., p. 103.

Lieberman, A. (1984). "Fine Particle Characterization Methods in Liquid Suspensions," in Particle Characterization in Technology. Vol. I. Applications and Microanalysis, J. K. Beddow, Ed., CRC Press, Boca Raton, Fl., p. 187.

Lieberman, L. (1979). "Model-Driven Vision for Industrial Automation," in Advances in Digital Image Processing, Theory, Application and Implementation, P. Stucki, Ed., Plenum, New York, N.Y.

Liechti, K. M., Masters, J. E., Ulman, D. A., and Lehman, M. W. (1982). SEM/TEM Fractography of Composite Materials, AFWAL-TR-82-4085, Wright Patterson AFB, Ohio.

Lifshin, E., Morris, W. G., and Bolon, R. B. (1969). "The Scanning Electron Microscope and its Application in Metallurgy," J. Metals, Vol. 21, No. 12, p. 43.

Limb, H. R., and McNeil, J. F. (1964). "Cleavage Fracture in Wrought High-Purity Chromium: A Description of the Fracture-Surface Characteristics," JIM, Vol. 93, p. 297.

Lipson, H. (Ed.) (1972). Optical Transforms, Academic Press, London.

Lipson, H., and Taylor, C. A. (1958). Fourier Transforms and X-Ray Diffraction, G. Bell and Sons, Ltd., London.

Logan, H. L. (1952). "Film Rupture Mechanism of Stress Corrosion," J. of Res. of the National Bureau of Standards, Vol. 48, p. 99.

Logan, H. L. (1966). The Stress Corrosion of Metals, Wiley and Sons, New York, N.Y.

Low, J. R. (1959). "A Review of the Microstructural Aspects of Cleavage Fracture," in Fracture, Proceedings of the Swampscott Conference, B. L. Averback, D. K. Felbeck, G. T. Hahn, and D. A. Thomas, Eds., Technology Press and Wiley and Sons, New York, N.Y., p. 68.

Luerkens, D. W., Beddow, J. K., and Vetter, A. F. (1984). "Theory of Morphological Analysis," in Particle Characterization in Technology, Vol. II. Morphological Analysis, J. K. Beddow, Ed., CRC Press, Boca Raton, Fl., p. 3.

Lynch, S. P. (1979). "Mechanisms of Hydrogen-Assisted Cracking," Met. Forum, Vol. 2,3, p. 189.

Madeyski, A., and Albertin, L. (1978). "Fractographic Method of Evaluation of the Cyclic Stress Amplitude in Fatigue Failure Analysis," in Fractography in Failure Analysis, ASTM STP 645, B. M. Strauss and W. H. Cullen, Jr., (Eds.), American Society for Testing and Materials, Philadelphia, Pa., p. 73.

Mallet, R. (1856). Physical Conditions Involved in the Construction of Artillery, N.P., London.

Mandelbrot, B. (1977). Fractals, Form, Chance, and Dimension, W. H. Freeman and Co., San Francisco, Calif.

Markham, R., Frey, S., and Hills, G. J. (1963). "Methods for the Enhancement of Image Detail and Accentuation of Structure in Electron Micrographs," Virology, Vol. 20, p. 88.

Martens, A. (1878a). "The Microscopical Examination of Iron," Z. Ver. Dent. Ing., Vol. 21, p. 11.

Martens, A. (1878b). "Uber die Mikroskopische Untersuchung des Eisens," Z. Deut. Ing., Vol. 22, p. 11.

Martens, A. (1887). "Ueber das Kleingefuge des Schmiedbaren Eisens," Stahl Eisen, Vol. 7, p. 235.

Mason, J. B. (1977). "Optical Fourier Transform Analysis of Satellite Cloud Imagery," in Advances in Laser Technology for the Atmos. Sci., SPIE, Bellingham, Wash., p. 77.

Maxwell, J. (1892). A Treatise on Electricity and Magnetism, Clarendon Press, Oxford.

McCall, J. L. (1972). Fracture Analysis by Scanning Electron Microscopy, Metals and Ceramics Information Center, Report MCIC 72-12, Battelle, Columbus Laboratories, Columbus, Ohio.

McEvily, A. J., and Boettner, R. C. (1963). "On Fatigue Crack Propagation in FCC Metals," Acta Met., Vol. 11, p. 725.

McEvily, A. J., and Bond, A. P. (1967). "Effect of Thermal-Mechanical Processing on the Fatigue and Stress Corrosion Properties of an Al-Zn-M Alloy," Trans. ASM, Vol. 60, p. 661.

McGrath, J. T., Buchanan, J. G., and Thurston, R. C. A. (1962). "A Study of Fatigue and Impact Fractures with the Scanning Electron Microscope," J. Inst. Metals, Vol. 91, p. 34.

McHargue, W. R. (1976). An Algorithm for Recognition of Russian Characters Using Correlation, Air Force Inst. of Tech. School of Engineering Report No. AFIT/GE/EE-76-35, Wright Patterson AFB, Ohio.

McMillian, J. C., and Pelloux, R. M. N. (1962). The Analysis of Fracture Surfaces by Electron Microscopy," Boeing Report DI-82-0169.

McMullan, D. (1953). "An Improved Scanning Electron Microscope for Opaque Specimens," Proc. Inst. Elec. Engr., Pt. II, Vol. 100, p. 245.

Mears, R. B., Brown, R. H., and Dix, E. H., Jr. (1945). "A Generalized Theory of Stress Corrosion of Alloys," Stress Corrosion Cracking of Metals, in Stress Corrosion Cracking of Metals, ASTM STP 64, American Society for Testing and Materials, Philadelphia, Pa., p. 323.

Mecholsky, J. J., and Freiman, S. W. (1981). "Fractographic Analysis of Delayed Failure in Ceramics," in Fractography and Materials Science, ASTM STP 733, American Society for Testing and Materials, Philadelphia, Pa., p. 246.

Mecholsky, J. J., Freiman, S. W., and Rice, R. W. (1978). "Fractographic Analysis of Ceramics," in Fractography in Failure Analysis, ASTM STP 645, B. M. Strauss and W. H. Cullen, Jr., Eds., American Society for Testing and Materials, Philadelphia, Pa., p. 363.

Mecholsky, J. J., and Rice, R. W. (1984). "Fractographic Analysis of Biaxial Failure in Ceramics," in Fractography of Ceramic and Metal Failures, ASTM STP 827, J. J. Mecholsky, Jr. and S. R. Powell, Jr., Eds., American Society for Testing and Materials, Philadelphia, Pa., p. 185.

Meny, L., Maillard, A., Henry, G., Champigny, M., and Legrand, J. (1970). "Microfractographic Applications of Conventional and Scanning Electron Microscopes," Metaux-Corrosion-Ind., Vol. 45, No. 542, p. 343.

Meyn, D. A. (1967). Comparison of Fatigue Crack Propagation in Air and Vacuum for 2024 Aluminum, Report of NRL Progress, May, Naval Research Laboratory, Washington, D.C.

Michalske, T. A. (1984). "Fractography of Slow Fracture in Glass," in Fractography of Ceramic and Metal Failures, ASTM STP 827, J. J. Mecholsky, Jr. and S. R. Powell, Jr., Eds., American Society for Testing and Materials, Philadelphia, Pa., p. 121.

Moik, J. G. (1980). Digital Processing of Remotely Sensed Images, NASA SP-431, National Aeronautics and Space Administration, Washington, D.C.

Moody, M. F. (1971). "Application of Optical Diffraction to Helical Structures in the Bacteriophage Fail," Phil. Trans. of the Royal Soc. of London, Series B, 261, p. 181.

Moore, G. A. (1972). "Recent Progress in Automatic Image Analysis," J. Microsc., Vol. 95, Part 1, p. 105.

Moss, R. H., Robinson, C. M., and Poppelbaum, W. J. (1983). "On-Line Recognition (OLREC): A Novel Approach to Visual Pattern Recognition," Pattern Recognition, Vol. 16, No. 6, p. 535.

Mott, F. A. (1958). "A Theory of the Origin of Fatigue Cracks," Acta Met., Vol. 6, p. 195.

Mundy, J. L., and Jarvis, J. F. (1982). "Automatic Visual Inspection," in Applications of Pattern Recognition, K. S. Fu, Ed., CRC Press, Boca Raton, Fl., p. 121.

Murr, L. E. (1970). Electron Optical Applications in Materials Science, McGraw Hill, New York, N.Y.

Murr, L. E. (1982). Electron and Ion Microscopy and Microanalysis Principles and Application, Marcel Dekker, New York, N.Y.

Nelson, H. G. (1983). "Hydrogen Embrittlement," in Treatise on Materials Science and Technology, Vol. 25, Academic Press, New York, N.Y., p. 275.

Neumann, P. (1973). "On the Mechanism of Crack Advance in Ductile Materials," 3rd ICF Conference, Vol. III, p. 233.

Oatley, C. W., Nixon, W. C., and Pease, R. F. (1965). Advances in Electronics and Electron Physics, Vol. 21, Academic Press, New York, N.Y., p. 181.

Oriani, R. A. (1978). "Hydrogen Embrittlement in Steels," Ann. Rev. Mat. Sci., Vol. 8, p. 327.

Oriani, R. A., and Josephic, P. H. (1974). "Equilibrium Aspects of Hydrogen-Induced Cracking of Steels," Acta Met., Vol. 22, p. 1065.

Passoja, D. E., and Psioda, J. A. (1981). "Fourier Transform Techniques - Fracture and Fatigue," in Fractography and Materials Science, ASTM STP 733, L. N. Gilbertson and R. D. Zipp, Eds., American Society for Testing and Materials, Philadelphia, Pa., p. 355.

Pease, M. C. (1968). "An Adaptation of the Fast Fourier Transform for Parallel Processing," J. Assoc, Comput. Mach., Vol. 15, p. 252.

Pelloux, R. M. N. (1964). "Fractographic Analysis of the Influence of Constituent Particles on Fatigue Crack Propagation in Aluminum Alloys," Trans. ASM, Vol. 57, p. 511.

Pelloux, R. M. N. (1969). "Mechanisms of Formation of Ductile Striations," Trans. ASM., Vol. 62, p. 281.

Pelloux, R. M. N. (1970). "Crack Extension by Alternating Shear," Engineering Fracture Mechanics, Vol. 1, p. 697.

Pelloux, R. M., Erhardt, K., and Grant, N. J. (1970). "Application of the Scanning Microscope to Electron Fractography," Proceedings of the Third Annual Scanning Electron Microscope Symposium, IIT Research Institute, Chicago, Il.

Percy, J. (1861). Metallurgy, John Murray, London.

Petch, N. J. (1955). "The Cleavage Strength of Polycrystals," J. of the Iron and Steel Institute, Vol. 174, p. 25.

Petch, N. J. (1956). "The Lowering of Fracture Stress Due to Surface Adsorption," Philosophical Magazine, Vol. 1, p. 331.

Petch, N. J., and Stables, P. (1952). "Delayed Fracture of Metals Under Static Load," Nature, Vol. 169, p. 842.

Peterson, R. A., and Dobrin, M. B. (1966). A Pictorial Digital Atlas, United Geophysical Corp., Pasadena, Ca.

Phillips, A., Kerlins, V., Rowe, B. A., and Whiteson, B. V. (1966). "Electron Fractography Handbook, Suppl. I.," AFML-TDR-64-416, Wright Patterson AFB, Dayton, Ohio.

Phillips, A., Kerlins, V., and Whiteson, B. V. (1965). "Electron Fractography Handbook," AFML-TDR-64-416, Wright Patterson AFB, Dayton, Ohio.

Pincus, H. J. (1969). "Sensitivity of Optical Data Processing to Changes in Fabric," Intl. J. Rock. Mech., Vol. 6, p. 259.

Pincus, H. J. (1978). "Optical Diffraction Analysis in Microscopy," in Advances in Optical and Electron Microscopy, V. E. Cosslett and R. Barer, Eds., Academic Press, New York, N.Y.

Plateau, J., Henri, G., and Friedel, J. (1965). "Cleavage Crack Propagation," in Proceedings of the First International Conference on Fracture, Vol. II, p. 597.

Power, P. C., Jr. (1973). Optical Diffraction Analysis of Petrographic Thin Sections, MS Thesis, University of Wisconsin-Milwaukee, Milwaukee, Wis.

Prebus, A., and Hillier, J. (1939). "The Construction of a Magnetic Electron Microscope of High Resolving Power," Can. J. Research, Vol. A17, p. 49.

Preston, K., Jr. (1979). "Biomedical Image Processing," in Advances in Digital Image Processing, Theory, Application, Implementation, Ed. P. Stucki, Ed., Plenum, New York, N.Y., p. 125.

Preston, K., Jr. (1982). "Application of Pattern Recognition to Medical Data Analysis," in Application of Pattern Recognition, K. S. Fu, Ed., CRC Press, Boca Raton, Fl., p. 169.

Pugh, E. N. (1971). "Mechanisms of Stress Corrosion Cracking of Alpha-Brass in Aqueous Ammonia," in Theory of Stress Corrosion Cracking, J. L. Scully, Ed., Proceedings of NATO Conference, March, Ericiera, Portugal, p. 418.

Puttick, K. E. (1959). "Ductile Fracture in Metals," Philosophical Magazine, Vol. 4, p. 964.

Rhines, F. N. (1979). "Quantitative Microscopy and Fatigue Mechanisms," in Fatigue Mechanisms, ASTM STP 675, J. T. Fong, Ed., American Society for Testing and Materials, Philadelphia, Pa., p. 22.

Rice, R. W. (1984). "Ceramic Fracture Features, Observations, Mechanisms, and Uses," in Fractography of Ceramic and Metal Failures, ASTM STP 827, J. J. Mecholsky, Jr. and S. R. Powell, Jr., Eds., American Society for Testing and Materials, Philadelphia, Pa., p. 5.

Richard, C. W., Jr., and Hemami, H. (1972). Identification of Three-Dimensional Objects Using Fourier Descriptors of the Boundary Curve, Ohio State Univ. Dept. of Electrical Engr., Contract No. AF-AFOSR-2048-71, Columbus, Ohio.

Riederer (1979). Case Histories in Failure Analysis, American Society for Metals, Metals Park, Ohio.

Rimnac, C. M., Hertzberg, R. W., and Manson, J. A. (1981). "Fatigue Fracture Surface Micromorphology in Poly(vinyl chloride)," in Fractograph and Materials Science, ASTM STP 733, American Society for Testing and Materials, Philadelphia, Pa., p. 291.

Rogers, H. C. (1960). "The Tensile Fracture of Ductile Metals," Trans. AIME, Vol. 218, p. 498.

Russ, J. C. (1971a). "Comparison of Fractographic Techniques, Part I," Microstructures, Vol. 2, Dec/Jan, p. 19.

Russ, J. C. (1971b). "Comparison of Fractographic Techniques, Part II," Microstructures, Vol. 2, Feb/Mar, p. 13.

Sailors, R. H. (1976). "Fracture Feature Anisotropy in a Martensitic Steel Plate," in Fractography-Microscopic Cracking Processes, ASTM STP 600, C. D. Beachem and W. R. Warke, Eds., American Society for Testing and Materials, Philadelphia, Pa., p. 172.

Saltykov, S. A. (1958). Stereometric Metallography, 2nd Edition, Metallurgizdat, Moscow.

Schardin, H. (1954). "Velocity Effects in Fracture," in Fracture I, Proceedings of the Swampscott Conference, B. L. Acarback, D. K. Felbeck, G. T. Hahn, and D. A. Thomas, Eds., MIT Press, Cambridge, Mass.

Scully, J. C. (1968). "Electrochemical Parameters of Stress-Corrosion Cracking," Corrosion Science, Vol. 8, p. 513.

SEM/TEM Fractography Handbook (1975). Metals and Ceramics Information Center, MCIC-HB-06, Batelle, Columbus Laboratories, Columbus, Ohio.

Shepherd, B. F. (1923). "Carburization of Steel," Trans ASST., Vol. 4, p. 171.

Shepherd, B. F. (1924). "A Few Notes on the Shimer Hardening Process," Trans. ASST., Vol. 5, p. 485.

Skaggs, F. L. (1984). "Machine Vision System Speeds PCB Inspection and Increases Measurement Efficiency," Test and Measurement World, Vol. 4, No. 6, p. 94.

Smith, E. (1966). "The Nucleation and Growth of Cleavage Microcracks in Mild Steel," in Proceedings of the Conference on the Physical Basis of Yield and Fracture, Institute of Physics and Physical Society, Oxford, p. 36.

Smith, K. C. A., and Oatley, C. W. (1955). "The Scanning Electron Microscope and its Fields of Application," Brit. J. Appl. Phys., Vol. 6, p. 391.

Speiser, J. M., and Whitehouse, H. J. (1976). "Apparatus For the Generation of a Two-Dimensional Discrete Fourier Transform," United States Patent 3,952,186, 20 April.

Spitzig, W. A., Pellissier, G. E., Beachem, C. D., Brothers, A. J., Hill, M. and Warke W. R. (1968). "A Fractographic Analysis of the Relationship Between Fracture Toughness and Surface Topography in Ultra-high Strength Steels," in Electron Fractography, ASTM STP 436, American Society for Testing and Materials, Philadelphia, Pa., p. 17.

Staehle, R. W. (1971). "Theory of Stress-Corrosion Cracking of Alloys," Proceedings of NATO Conf., Ericiera, Portugal, J. C. Scully, Ed., p. 223.

Staehle, R. W., Hockmann, J., McCright, R. D., and Slater, J. E. (Eds.) (1977). "Stress-Corrosion Cracking and Hydrogen Embrittlement of Iron-Base Alloys," Proceedings of NACE Conference, Firminy, France.

Steward, E. G. (1983). Fourier Optics: An Introduction, Ellis Horwood, Ltd., Div. of Wiley & Sons, New York, N.Y.

Stinchcomb, W. W., and Reifsnider, K. L. (1979). "Fatigue Damage Mechanisms in Composite Materials: A Review," in Fatigue Mechanisms, ASTM STP 675, J. T. Fong, Ed., American Society for Testing and Materials, Philadelphia, Pa., p. 762.

Stoloff, N. S., and Duquette, D. J. (1979). "Fatigue Mechanisms in Nickel and Cobalt-Base Eutectic Composites," in Fatigue Mechanisms, ASTM STP 675, J. T. Fong, Ed., American Society for Testing and Materials, Philadelphia, Pa., p. 788.

Strauss, B. M., and Cullen, W. H., Jr. (1978). "Fractography in Failure Analysis," ASTM STP 645, American Society for Testing and Materials, Philadelphia, Pa.

Stucki, P. (Ed.) (1979). "Image Processing for Document Reproduction," in Advances in Digital Image Processing Theory, Application, Implementation, Plenum Press, New York, N.Y., p. 177.

Taylor, C. A., and Lipson, H. (1951). "Optical Methods in Crystal Structure Determination," Nature, Vol. 167, p. 809.

Taylor, C. A., and Lipson, H. (1964). Optical Transforms, G. Bell and Sons, Ltd., London.

Taylor, C. A., and Lipson, H. (1965). Optical Transforms, Cornell Univ. Press, Ithaca, N.Y.

Taylor, R. W., and Rehkugler, G. E. (1985). "Development of a System for Automated Detection of Apple Bruises," Presented at Vision 85, Society of Manufacturing Engineers, March 25-28, 1985, Detroit, Mich.

Tejeda, J., and Dominguez, J. M. (1985). "Computer Processing of High-Resolution Electron Micrographs," American Laboratory, p. 131.

Tetelman, A. S., and McEvily, A. J. (1967). Fracture of Structural Materials, Wiley & Sons, New York, N.Y.

Tetelman, A. S., and Robertson, W. D. (1962). "The Mechanism of Hydrogen Embrittlement Observed in Iron-Silicon Single Crystals," Trans. AIME, Vol. 224, p. 775.

Thompson, N., Wadsworth, N., and Louat, N. (1956). "The Origin of Fatigue Fracture in Copper," Phil. Mag., Vol. 1, p. 12.

Tipper, C. F., Dagg, D. I., and Wells, O. C. (1959). "Surface Fracture Markings on Alpha Iron Crystals, J. Iron and Steel Institute, Oct., p. 133.

Toth, I. (Ed.) (1973). Failure Modes in Composites, Vol. I, The Met. Soc. of AIME, New York, N.Y.

Tou, J. T. (1980). "Computer-Based Particle Shape Analysis for Classification, Recognition, Utilization," in Advanced Particulate Morphology, J. K. Beddow and T. P. Meloy, Eds., CRC Press, Boca Raton, Fl., p. 165.

Tovey, N, K., and Wong, K. Y. (1978). "Optical Techniques for Analysing Scanning Electron Micrography," Scanning Electron Microscopy, Vol. 1, p. 381.

Triendl, E. E. (1979). "Landsat Image Processing," in Advances in Digital Image Processing, Theory, Application, Implementation, P. Stucki, Ed., Plenum, New York, N.Y., p. 165.

Troiano, A. R. (1960). "The Role of Hydrogen and Other Interstitials in the Mechanical Behavior of Metals," Trans. ASM, Vol. 52, p. 54.

Tunner, P. (1858). Das Eisenhuttenwesen im Schweden, Engelhardt, Freiberg.

Ulig, H. H. (1959). Physical Metallurgy of Stress Corrosion Fracture, T. H. Rondin, Ed., Interscience, New York, N.Y., p. 11.

Ullman, J. R. (1982). "Advances in Character Recognition," in Application of Pattern Recognition, K. S. Fu, CRC Press, Boca Raton, Fl., p. 197.

Underwood, E. E. (1970). Quantitative Stereology, Addison Wesley Publ. Co., Inc., Reading, Mass.

Underwood, E. E. (1974). "Stereology in Automatic Image Analysis," Microscope, Vol. 22, p. 69.

Underwood, E. E., and Chakrabortty, S. B. (1981). "Quantitative Fractography of a Fatigued Ti-28V Alloy," in Fractography and Materials Science, ASTM STP 733, L. N. Gilbertson and R. D. Zipp, Eds., American Society for Testing and Materials, Philadelphia, Pa., p. 337.

Underwood, E. E., and Starke, E. A., Jr. (1979). "Quantitative Stereological Methods for Analyzing Important Microstructural Features in Fatigue of Metals and Alloys," in Fatigue Mechanisms, ASTM STP 675, J. T. Fong, Ed., American Society for Testing and Materials, Philadelphia, Pa., p. 633.

Underwood, E. E., and Underwood, E. S. (1982). "Quantitative Fractography by Computer Simulation," Acta Stereol., Proc. 3rd Eur. Symp Stenol., 2nd Part, p. 89.

Van Ness, H. C., and Dodge, B. F. (1955). "Effects of Hydrogen at High Pressures on the Mechanical Properties of Metals," Chem. Eng. Prog., Vol. 51, p. 266.

Van Stone, R. H., and Cox, T. B. (1976). "Use of Fractography and Sectioning Techniques to Study Fracture Mechanisms," in Fractography-Microscopic Cracking Processes, ASTM STP 600, C. D. Beachem and W. R. Warke, Eds., American Society for Testing and Materials, Philadelphia, Pa., p. 5.

Vander Voort, G. F. (1984). Metallography Principles and Practice, McGraw-Hill, New York, N.Y.

Vermilyea, D. A. (1972). "A Theory for the Propagation of Stress Corrosion Cracks in Metals," J. of the Electrochemical Society, Vol. 119, p. 405.

von Ardenne, M. (1938a). "The Scanning Electron Microscope: Practical Construction," Z. Tech. Phys., Vol. 19, p. 407.

von Ardenne, M. (1938b). "The Scanning Electron Microscope: Theoretical Fundamentals," Z. Physics, Vol. 109, p. 553.

von Borries, B., and Ruska, E. (1939). "Aufbau and Leistung des Siemens-Ubermikroskopes," Z. Wiss Mikroskopie, Vol. 56, p. 317.

Warke, W. R., and McCall, J. L. (1964). Using Electron Microscopy to Study Metal Fracture, SAE Paper 828D, Society of Automotive Engineers, Warrendale, Pa.

Warke, W. R., and McCall, J. L. (1965). Fractography Using the Electron Microscope, ASM Tech. Rpt. No. W-3-2-65, American Society for Metals, Metals Park, Ohio.

Wells, O. C. (1974). Scanning Electron Microscopy, McGraw-Hill, New York, N.Y.

Westlake, D. G. (1969). "A Generalized Model for Hydrogen Embrittlement," Trans. ASM, Vol. 62, p. 1000.

Wiebel, E. R. (1980). Stereological Methods, Vol. I. Practical Methods for Biological Morphometry. Vol. II. Theoretical Foundations, Academic Press, London.

Wood, W. A. (1958). "Recent Observations on Fatigue Fracture in Metals," in Basic Mechanisms of Fatigue, ASTM STP 237, American Society for Testing and Materials, Philadelphia, Pa., p. 110.

Wood, T. W, and Daniels, R. D. (1965). "The Influence of Hydrogen on the Tensile Properties of Columbium," Trans. AIME, Vol. 233, p. 898.

Wright, K., and Karlsson, B. (1983). "Fractal Analysis and Stereological Evaluation of Microstructures," J. Microsc., Vol. 120, No. 2, p. 185.

Wulpi, D. J. (1985). Understanding How Components Fail, American Society for Metals, Metals Park, Ohio.

Yarne, R. (1968). "An Economical Method for Calculating the Discrete Fourier Transform," 1968 Fall Joint Computer Conf., IFIPS Proc., Vol. 33, p. 115, Washington, D.C.

Yokota, Y., Tomita, M., Hashimoto, H., and Endon, H. (1981). "Construction of an On-Line System for FFT Processing and Analysis of Atomic Resolution Microscopic Images and its Applications," Ultramicroscopy, Vol. 6, No. 4, p. 313.

Yoshino, K., and McMahon, C. J. (1974). "The Cooperative Relation Between Temper Embrittlement and Hydrogen Embrittlement in a High Strength Steel," Met. Trans., Vol. 5, p. 363.

Young, T. (1802). "The Theory of Light and Coulour," Phil. Trans. of the Royal Soc. of London, Vol. 92, p. 12.

Zapffe, C. A., and Clogg, M., Jr. (1945a). "Fractography - A New Tool for Metallurgical Research," Trans. ASM, Vol. 34, p. 71.

Zapffe, C. A., and Clogg, M., Jr. (1945b). "Cleavage Structures of Iron-Silicon Alloys," Trans. ASM, Vol. 34, p. 103.

Zapffe, C. A., and Landgraf, F. K. (1949). "Fractographic Examination of Tungsten," Trans. ASM, Vol. 41, p. 396.

Zapffe, C. A., and Moore, G. A. (1943). "A Microfractographic Study of the Cleavage of Hydrogenized Ferrite," Trans. AIME, Vol. 154, p. 335.

Zapffe, C. A., and Sims, C. E. (1941). "Hydrogen Embrittlement, Internal Stress, and Defects in Steel," Trans. AIME, Vol. 145, p. 225.

Zapffe, C. A., and Worden, C. O. (1951). "Fractographic Registration of Fatigue," Trans. ASM, Vol. 43, p. 958.

Zapffe, C. A., Landgraf, F. K., and Worden, C. O. (1948). "Transgranular Cleavage Facets in Cast Molybdenum," Metal Progress, Vol. 54, p. 328.

Zapffe, C. A., Worden, C. O., and Landgraf, F. K. (1948). "Cleavage Patterns Disclose "Toughness" of Metals," Science, Vol. 108, p. 440.

Zworykin, V. K., Hiller, J., and Snyder, J. (1942). "A Scanning Electron Microscope," Proc. Inst. Radio Engineers, Vol. 30, p. 255.

BIOGRAPHICAL SKETCH

Richard Horace McSwain, son of Howard Horace and LaBelle (Henderson) McSwain, was born in Greenville, Alabama, on September 27, 1949. He attended public schools in Brewton, Alabama, and graduated from T. R. Miller High School in 1967. He attended Jefferson Davis Junior College and Auburn University where he received the Bachelor of Materials Engineering in 1972. He entered Graduate School at Auburn University in 1972 and received a Master of Science degree in 1974 in materials engineering. Research for the master's degree was performed at Southern Research Institute in Birmingham, Alabama, in the area of surface phenomena and the mechanism of solidification of gray and ductile iron. He continued as metallurgist at Southern Research Institute until 1977 when he accepted his current position as metallurgist at the Naval Air Rework Facility, Pensacola, Florida. Presently he is senior metallurgist heading the failure analysis group.

In 1982 he began a long-term training program sponsored by the Navy and entered the University of Florida. He completed the Ph.D. coursework in 1983. This research was then performed simultaneously in Pensacola and at the University of Florida.

He married the former Wanda Lynn Hare of Atmore, Alabama, in June 1972. They have two children, Rachel Lynn, born February 17, 1977, and John Angus, born June 1, 1981.

He is a registered professional engineer in the State of Florida and an elder in the Northeast Presbyterian Church, Pensacola, Florida.

I certify that I have read this study and that in my opinion it conforms to acceptable standards of scholarly presentation and is fully adequate, in scope and quality, as a dissertation for the degree of Doctor of Philosophy.

Robert W Gould

Robert W. Gould, Chairman
Professor of Materials Science
and Engineering

I certify that I have read this study and that in my opinion it conforms to acceptable standards of scholarly presentation and is fully adequate, in scope and quality, as a dissertation for the degree of Doctor of Philosophy.

Robert T. DeHoff

Robert T. DeHoff
Professor of Materials Science
and Engineering

I certify that I have read this study and that in my opinion it conforms to acceptable standards of scholarly presentation and is fully adequate, in scope and quality, as a dissertation for the degree of Doctor of Philosophy.

Martin A.

Martin A. Eisenberg
Professor of Engineering Sciences

I certify that I have read this study and that in my opinion it conforms to acceptable standards of scholarly presentation and is fully adequate, in scope and quality, as a dissertation for the degree of Doctor of Philosophy.

John J. Hren
Professor of Materials Science
and Engineering

I certify that I have read this study and that in my opinion it conforms to acceptable standards of scholarly presentation and is fully adequate, in scope and quality, as a dissertation for the degree of Doctor of Philosophy.

Ellis D. Verink, Jr.
Distinguished Service Professor
of Materials Science and
Engineering

This dissertation was submitted to the Graduate Faculty of the College of Engineering and to the Graduate School, and was accepted as partial fulfillment of the requirements for the degree of Doctor of Philosophy.

August 1985

Hubert A. Bevis
Dean, College of Engineering

Dean, Graduate School